Doctoral theses at NTNU, 2020:260

Adrian Lervik

Microstructural Characterisation of Features Related to Grain Boundary Corrosion Phenomena in Aluminium Alloys

Doctoral thesis

NTNU
Norwegian University of Science and Technology
Thesis for the Degree of
Philosophiae Doctor
Faculty of Natural Sciences
Department of Physics

NTNU
Norwegian University of
Science and Technology

Adrian Lervik

Microstructural Characterisation of Features Related to Grain Boundary Corrosion Phenomena in Aluminium Alloys

Thesis for the Degree of Philosophiae Doctor

Trondheim, September 2020

Norwegian University of Science and Technology
Faculty of Natural Sciences
Department of Physics

NTNU
Norwegian University of
Science and Technology

NTNU
Norwegian University of Science and Technology

Thesis for the Degree of Philosophiae Doctor

Faculty of Natural Sciences
Department of Physics

ISBN 978-82-326-4868-9 (printed ver.)
ISBN 978-82-326-4869-6 (electronic ver.)
ISSN 1503-8181

Doctoral theses at NTNU, 2020:260

Printed by NTNU Grafisk senter

Abstract

In order to understand intergranular corrosion (IGC) and stress corrosion cracking (SCC) in aluminium (Al) alloys, a detailed understanding of the microstructure is required. Finding ways to improve corrosion problems, while maintaining high strength, will enable Al alloys to become more applicable in components in the automotive and aerospace industries. An experimental tool enabling studies of the microstructure at the required length scales is the (scanning) transmission electron microscope ((S)TEM). This is the main experimental tool used in this work.

The results of this thesis is presented as six research papers. The three first concerns Al-Mg-Si-Cu alloys and IGC properties, and the final three concerns Al-Zn-Mg alloys and SCC properties.

Paper I investigates the influence of the α-Al(Fe,Mn,Cu)Si particles on IGC, by comparing two Al-Mg-Si-Cu alloys with- and without the presence of these particles. Both alloys were IGC tested for 1 to 120 h. Microstructures were studied using scanning electron microscopy (SEM), (S)TEM, and electron backscatter diffraction (EBSD). Presence of α-particles yields significantly more uniform IGC attacks and higher corrosion rates. The maximum depth of IGC attacks become similar, in both alloys, after $\sim$20 h exposure. This is attributed to formation of Cu-rich particles at the corroded grain boundaries, which catalyses the cathodic reaction.

Paper II conducts a detailed analysis of grain boundaries in an extruded Al-Mg-Si-Cu alloy. EBSD demonstrates the presence of three main categories of grain boundaries in addition to sub-grain boundaries. These are systematically analysed using high-resolution STEM. IGC properties were statistically correlated with the same defined grain boundaries. A higher density of metastable Q′-phase grain boundary particles correlates with a reduction in Cu segregation at grain boundaries and an increased IGC resistance.

Paper III demonstrates a correlation between the amount of Cu incorporated in hardening precipitates and IGC resistance in an artificially aged Cu-containing

6005A alloy. Three mechanisms have been identified to increase Cu absorption in hardening precipitates: by increasing ageing temperature, by pre-deformation and by slow cooling from solution heat treatment (SHT).

Paper IV provides new information on the atomic structures of solute-rich clusters forming during natural ageing in Al-Zn-Mg alloys. Observations from high-angle annular dark-field (HAADF)-STEM images suggest a novel type of cluster unit of high Zn/Mg ratio to be the fundamental building block in all observed cluster configurations. The unit is essentially a partial substitution by Mg and Zn on the face-centered cubic Al cell and its surrounding truncated cube octahedral shell. A simple set of principles based on 'Frank-Kasper' structures can describe how the basic units arrange with respect to each other to form larger clusters. Density functional theory calculations, atom probe tomography and simulated diffraction patterns support the proposed atomic models.

Paper V investigates precipitation behaviour in an industrially extruded AA7003 alloy studied using (S)TEM together with differential scanning calorimetry. Air-cooling (AC) after SHT results in quench-induced heterogeneous precipitation of both β-Mg_2Si and η-$MgZn_2$ phases. Detailed (S)TEM characterisation of resulting nanoscale precipitates after artificial ageing, demonstrates that the orientation and size of the precipitates are different in the T6 and T7 temper. In addition, the T7 state forms 6xxx-type hardening precipitates only after a water-quench from SHT. Results presented here are expected to be relevant for any Si-containing 7xxx alloy and open new possibilities for development of hybrid 6xxx- and 7xxx series aluminium alloys.

Paper VI studies SCC using the double cantilever beam method and slow strain rate tensile tests for the same alloy and tempers as in Paper **V**. Microstructural features, including grain boundary particles, precipitate free zones and matrix precipitates have been studied using (S)TEM and SEM. A difference in the SCC properties is established between the two tempers. The dominating difference in microstructure is the size and orientation of hardening phases. Possible explanations between the microstructural observations and SCC properties are discussed.

The results presented in this thesis are expected to be relevant in further understanding microstructure, IGC and SCC in aluminium alloys.

Preface

This thesis is the result of the scientific work conducted between August 2016 and June 2020 at the Norwegian University of Science and Technology (NTNU), Department of Physics. It is submitted in partial fulfilment of the requirements for the degree of Philosophiae Doctor (Ph.D.).

The work has been conducted as a part of the competence building project entitled: 'Fundamentals of intergranular corrosion in aluminium alloys' (FICAL), supported by the Research Council of Norway, Norsk Hydro, Benteler Automotive Raufoss, Steertec Raufoss and Gränges, and with NTNU and SINTEF as research partners. Ambitions are to acquire fundamental insights into grain boundary corrosion processes, which require microstructural investigations at the nanoscale. Therefore, the work has mostly consisted of transmission electron microscopy (TEM) investigations carried out at the TEM Gemini Centre in Trondheim, Norway.

The thesis is divided into three parts. Part I provides the background and motivation for the thesis, introduction to aluminium, corrosion phenomena and methodology; and consists of 4 chapters. Part II contains the results presented as 6 journal publications. Part III is dedicated to a summary and outlook.

Papers Included in the Thesis

I

'Influence of α-Al(Fe,Mn,Cu)Si phase particles on intergranular corrosion in extruded AA6005 aluminium alloy'
A. Lervik, T. Danbolt, T. Furu, R. Holmestad, O. Lunder
To be submitted

II

'Grain boundary structures and their correlation with intergranular corrosion in an extruded Al-Mg-Si-Cu alloy'
A. Lervik, S. Wenner, C. D. Marioara, O. Lunder, R. Holmestad
Submitted to 'Materials Characterization' (14.05.2020)

III

'The correlation between intergranular corrosion resistance and copper content in the precipitate microstructure in an AA6005A alloy'
C. D. Marioara, A. Lervik, J. Grønvold, O. Lunder, S. Wenner, T. Furu, R. Holmestad
Metallurgical and Materials Transactions A. **49** (2018) 5146-5156.

IV

'Atomic structure of solute clusters in Al-Zn-Mg alloys'
A. Lervik, E. Thronsen, J. Friis, C. D. Marioara, S. Wenner, A. Bendo, K. Matsuda, R. Holmestad, S. J. Andersen
To be submitted

V

’Precipitation in an extruded AA7003 aluminium alloy: Observations of 6xxx-type hardening phases’
A. Lervik, C. D. Marioara, M. Kadanik, J. C. Walmsley, B. Milkereit, R. Holmestad
Materials & Design **186** (2020)

VI

’Stress corrosion cracking in an extruded Cu-free Al-Zn-Mg alloy’
A. Lervik, J. C. Walmsley, L. Lodgaard, C. D. Marioara, R. Johnsen, O. Lunder, R. Holmestad
In preparation

Other Scientific Contributions

Papers

- C. D. Marioara, O. Lunder, **A. Lervik**, S. Wenner, *Intergranular corrosion susceptibility of Si-rich Al-Mg-Si-(Cu) alloys*, In preparation
- A. Bendo, T. Maeda, K. Matsuda, **A. Lervik**, R. Holmestad, C. D. Marioara, K. Nishimura, N. Nunomura, H. Toda, M. Yamaguchi, K. Ikeda, T. Homma, *Characterisation of structural similarities of precipitates in Mg–Zn and Al–Zn–Mg alloys systems*, Philosophical Magazine vol. 99, no. 21, **(2019)**, 2619-2635, DOI:10.1080/14786435.2019.1637032
- A. Bendo, K. Matsuda, **A. Lervik**, T. Tsuru, K. Nishimura, N. Nunomura, R. Holmestad, C. D. Marioara, K. Shimizu, H. Toda, M. Yamaguchi, *An unreported precipitate orientation relationship in Al-Zn-Mg based alloys*, Materials Characterization, vol. 158, **(2019)**, 109958 DOI:10.1016/j.matchar.2019.109958

Presentations

Presenter underlined.

- **A. Lervik**, L. Lodgaard, C. D. Marioara, J. C. Walmsley, R. Holmestad, 'The effect of quench rate on stress corrosion cracking in a low Cu Al-Zn-Mg alloy', *8th Aluminium Surface Science & Technology Symposium*, Helsingør Denmark, 27th–30th May, 2018.
- **A. Lervik**, L. Lodgaard, C. D. Marioara, J. C. Walmsley, R. Holmestad, 'The effect of overaging on stress corrosion cracking in a low Cu Al-Zn-Mg alloy', *ICAA16 - International Conference on Aluminum Alloys*, Montreal Canada, 17th–21st June, 2018.
- **A. Lervik**, J. Friis, C. D. Marioara, S. J. Andersen, R. Holmestad, 'Co-precipitation in a Si containing 7xxx type Aluminum alloy', *19th international Microscopy Conference (IMC19)*, Sydney Australia, 9th–14th August, 2018.

Posters

- **A. Lervik**, C. D. Marioara, S. J. Andersen, J. Friis and R. Holmestad ,"Structure and interface of the η_1-$MgZn_2$ precipitate studied using TEM and DFT calculations", *The 61st Symposium of The Japanese Society of Microscopy*, Toyama Japan, 1st–3rd November 2018.

Acknowledgements

I would like to express my sincere gratitude to my supervisor Professor Randi Holmestad for giving me the possibility to pursue a PhD degree, and for her support, enthusiasm, genuine interest and great advice throughout the last 4 years. I have enjoyed both our scientific and non-scientific conversations, and I am extremely grateful that you have always made time for me in your otherwise hectic life. It is safe to say that without your guidance, this thesis would not have been realised.

I am grateful to my co-supervisor Dr. John C. Walmsley for his support, discussions, suggestions and for providing critical comments during my entire PhD study. Dr. Calin D. Marioara is highly acknowledged for all his support in all my projects and for teaching me everything there is to know about precipitates. Professor Otto Lunder is gratefully acknowledged for sharing his expertise and providing critical feedback. My sincere gratitude is extended to all my other co-authors and those who have supported me both directly and indirectly.

Without the funding for the project FICAL from the Research Council of Norway (RCN), and the partners SINTEF, Norsk Hydro, Benteler Automotive Raufoss, Steertec Raufoss and Gränges, none of this work could have happened. RCN is also greatly appreciated for supporting the NORTEM project that made the microscopes I have used available. I am grateful to everyone in the FICAL project for fruitful discussions, which has been important in realising this thesis. Working with industry has been an important and rewarding experience.

I am grateful to Professor Randi Holmestad and Professor Knut Marthinsen for sending me to Japan through the Norwegian-Japanese Aluminium Alloy Research Collaboration (INTPART project funded by RCN). I had the pleasure to experience working at UACJ corporation in Nagoya. Dr. Yoshihiko Kyo and Dr. Eng. Katsuhiro Sasaki are acknowledged for looking after me there.

I am gratefully to all the fantastic people associated with the TEM Gemini center in Trondheim. I thank the living encyclopedia on microscopes: Associate Professor

Per Erik Vullum for always having an answer to my questions. Our engineers Bjørn Gunnar Soleim and Dr. Ragnhild Sæterli are gratefully acknowledged for training me on the equipment and for all their trips down to U2 when I had problems on the microscope. I also want to thank Professor Antonius T. J. Van Helvoort for his creative ideas and challenging questions. To my colleagues for providing an excellent work environment: Tina, Jonas S, Elisabeth, Julie, Aleksander, Inger-Emma, Jonas F, Emil, Håkon, Christoph, Dipanwita, Simen and Kristoffer.

Thanks to my parents; Angenie and Øystein, and my brother Kevin, for their interest, motivation and support in every decision I have made. Last, but not least: to my dearest Athenna for her patience, understanding, support and love. Thank you for looking after me and our home while I have been busy and my mind been elsewhere, and for reminding me about all the important things in life.

Trondheim, June 2020
Adrian Lervik

List of Acronyms

AA artificial ageing.

ABF annular bright-field.

ADF annular dark-field.

APT atom probe tomography.

BF bright-field.

BSE backscattered electrons.

CSL coincident site lattice.

DCB double cantilever beam.

DFT density functional theory.

EBSD electron backscatter diffraction.

EDS energy-dispersive X-ray spectroscopy.

EELS electron energy-loss spectroscopy.

fcc face-centered cubic.

FIB focused ion beam.

GBPs grain boundary particles.

HAADF high-angle annular dark-field.

HRTEM high-resolution TEM.

IGC intergranular corrosion.

PFZ precipitate free zones.

RRA retrogression and reageing.

SADP selected area diffraction pattern.

SCC stress corrosion cracking.

SE secondary electrons.

SEM scanning electron microscope.

SHT solution heat treatment.

SPED scanning precession electron diffraction.

SSRT slow strain rate testing.

SSSS supersaturated solid solution.

STEM scanning transmission electron microscope.

TEM transmission electron microscope.

Contents

Part I

Background

Chapter 1

Introduction

1.1 Motivation

Aluminium (Al) alloys are among the most used medium-to-high strength materials in automotive and aerospace applications [1–4]. Properties such as high strength-to-weight ratio, formability and machinability, corrosion resistance, high thermal- and electrical conductivity, and the possibility of recycling, are all reasons aluminium production is increasing while finding its way into many new applications. It is of interest to replace heavy structural components of other metals in the transportation industry with lighter aluminium alloys to increase the distance travelled on the same amount of fuel without compromising on strength, effectively fulfilling the demand for reducing CO_2 emissions [5].

A large amount of energy ($\sim$17.000 kWh/ton) is required to produce primary aluminium [2, 6]. Due to the availability of clean hydropower, aluminium is one of Norway's most important export products, following the oil and gas, and fish farming industries [7, 8]. Nearly 75% of all aluminium produced up until today is still in its first use and has the possibility to be recycled [6]. This has huge economic and environmental savings, as recycling only require $\sim$5-7% of the energy used to produce the primary aluminium.

Alongside the positive properties of aluminium, certain alloy compositions and processing routes may result in unwanted corrosion phenomena. These may limit usage in certain applications. The corrosion phenomena studied here are called *intergranular corrosion (IGC)* and *stress corrosion cracking (SCC)*. To investigate such properties, detailed microstructural investigations at the nanoscale of all relevant microstructural features are required. An analytical tool enabling such studies is the *transmission electron microscope (TEM)*.

1.2 Objectives

This work is part of the larger competence building project 'fundamentals of intergranular corrosion in aluminium alloys' (FICAL). The overall aim is to obtain improved fundamental understanding of how corrosion susceptibility of aluminium alloys is connected to the microchemistry and microstructure, the bulk of grains, and particularly in the regions around grain boundaries [9]. The central objective is to understand the development of grain boundary microstructure and chemistry according to alloy composition and processing and, relate this to IGC susceptibility and its underlying mechanisms. This information is ultimately to be used in models that may predict the microstructure and its susceptibility to IGC [9].

1.3 Scope

It is important to state that there are limitations to the work presented in this thesis. First of all, the work is entirely experimentally oriented and mostly limited to scanning- and transmission electron microscopy. The purpose of this study is not to develop or establish a theory behind the corrosion processes taking place, but rather to provide fundamental microstructural information, which has important roles in such theories. Therefore, microstructural studies of features only accessible through state-of-the-art equipment is the main focus in this work. Following the industrial interest in the project, the thesis work is divided into two main parts: one part concerning Al-Mg-Si alloys and IGC, and a second part concerning Al-Zn-Mg alloys and SCC.

Chapter 2

Aluminium Alloys

This chapter is dedicated to give a brief summary of aluminium alloys, with special emphasis on the factors which may affect corrosion properties in the final product.

2.1 Classifying aluminium alloys

Aluminium alloys are classified as either cast- or wrought alloys. Cast alloys are directly cast into their final shape from the melt, while wrought alloys are produced as billets for subsequent forming by extrusion, drawing, forging or rolling. Wrought alloys are divided into groups, according to their main alloying element(s), as summarised in table 2.1. A four-digit nomenclature is commonly applied to classify them based on the principle element(s) and composition.

Table 2.1: General classification of wrought aluminium alloys. Modified from [2].

	Alloying elements	Heat treatable?	Applications
1xxx	None		Electrical conductors, architectural applications
2xxx	Cu, (Mg, Li)	Yes	Aerospace applications
3xxx	Mn, (Mg)		Heat exchangers, packaging, architectural applications
4xxx	Si		Architectural applications
5xxx	Mg		Automotive- and marine applications, packaging
6xxx	Mg, Si, (Cu)	Yes	Extruded and rolled products, automotive applications
7xxx	Zn, Mg, (Cu)	Yes	Aerospace- and automotive applications
8xxx	Various		

High purity aluminium exhibits a yield strength of only 7-11 MPa [2]. For this reason, it is alloyed with other elements to provide strength by introducing various *defects* in the aluminium lattice. The maximum solubility of selected elements are summarised in table 2.2. Mg and Zn demonstrate high solubilities, followed

by Cu and Si. Elements such as Fe, Mn, Cr and Zr have low solubility, but play important roles in processing of aluminium alloys as they form particles which influence grain structures and thus a range of the material properties.

Table 2.2: Solid solubility of common alloying elements in aluminium at the eutectic (E) or peritectic (P) temperature. The table is adapted from [2, 3].

		Maximum solid solubility	
Element	Temperature (°C)	at.%	wt.%
Cu	548 (E)	2.40	5.65
Fe	665 (E)	0.025	0.05
Mg	450 (E)	18.5	17.4
Mn	658 (E)	0.90	1.82
Si	577 (E)	1.59	1.65
Zn	443 (P)	66.4	82.8
Zr	660 (P)	0.08	0.28

2.2 Thermo-mechanical processing

Alloyed aluminium products are subjected to a *thermo-mechanical* processing route before reaching their final shape with specific properties. A typical processing route for age hardenable (heat treatable) alloys is schematically shown in figure 2.1.

Firstly, alloys are cast into billets by e.g. the direct chill (DC) casting method. During the solidification process, elements with low solubility, such as Fe, will form particles referred to as *primary particles*. A second heat treatment at temperatures below the melting point, called *homogenisation*, is conducted to even out concentration gradients of solutes formed during solidification. The primary particles are here (often) transformed into the α-phase in the process referred to as β to α transformation [10–12]. In addition, a new set of particles, called *dispersoids*, may form during homogenisation [13–16]. After homogenisation, the alloys are either extruded or rolled, before a possible subsequent forming process [17].

Prior to extrusion, the alloy is pre-heated to dissolve precipitates that may have formed to make the alloy as soft as possible, in order to limit the amount of force needed to push the billet through the forming die. During extrusion the microstructure typically develops into long fibrous grains along the extrusion direction, resulting in grains with defined orientations and a strong anisotropy in material properties. Following extrusion, the alloy is typically either air-cooled or water-quenched. Extruded profiles are typically stretched to make the profile

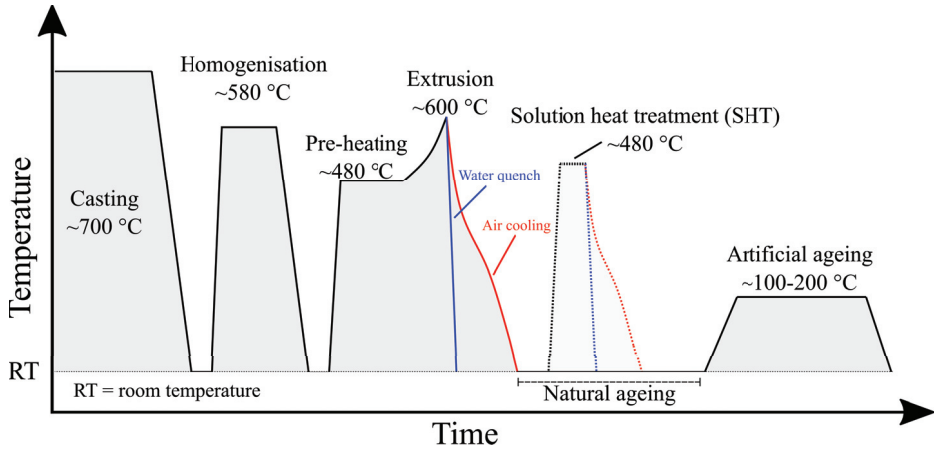

Figure 2.1: Schematic diagram of the thermo-mechanical processing of aluminium alloys, showing the most important steps from casting to an extruded product. The solution heat treatment (SHT) is shaded as many products are not subjected to this stage.

straight and/or release residual stresses in the material. Severe deformations are imposed during the forming process, resulting in a large dislocation density and high amounts of stored energy in the material. By heating the processed alloy, the dislocations can be annealed out through a process called *recovery* [18]. The dislocations move and arrange into sub-grain boundaries. At slightly higher temperatures, another process called *recrystallisation* occurs, in which some grains grow larger at the expense of others [18]. The dispersoids that formed during homogenisation reduces grain boundary migration and thus limit the recrystallisation behaviour. On the other hand, the primary particles are often associated with stimulating recrystallisation.

In many cases, yet another heat treatment called *solution heat treatment (SHT)* is conducted, with a following air-cooling or water-quench. A high concentration of vacancies will be present after a water-quench, which have important roles in the subsequent natural- and artificial ageing steps, as they increase the diffusion rate of solute elements, and are important in nucleation and growth of precipitates [19]. If the samples are slowly cooled after extrusion (or SHT), *heterogeneous nucleation* of particles may occur at grain boundaries or at other particles present in the microstructure [20–22]. After SHT (or extrusion) and before artificial ageing, the material is stored at room temperature and will experience an increase in hardness due to ordering (clustering) of solutes. This was first discovered by Alfred Wilm in the early 1900s [23]. Such clusters are today commonly referred to as 'GP-zones', as they were independently discovered in 1938 by Guinier and Preston [24–26]. This phenomenon is called *natural ageing*.

The final processing step is a heat treatment termed *artificial ageing (AA)*, in which metastable semi-coherent nanoscale *precipitates* are formed throughout the aluminium matrix. These contribute to the strength of the alloy as they obstruct dislocation movements during a deformation process. The time and temperature of this stage is tailored for each alloy in order to optimise strength, ductility, conductivity and even corrosion properties. The precipitation in 6xxx and 7xxx series aluminium will be explained in detail in sections 2.2.1 and 2.2.2.

2.2.1 Precipitation in Al-Mg-Si-Cu alloys

During artificial ageing, precipitates in the 6xxx series aluminium alloys nucleate and grow with a rod- or lath shape with one extended axis along $\langle 100 \rangle_{\mathrm{Al}}$. At maximum hardness, the needle shaped β''-$\mathrm{Mg_5Al_2Si_4}$ precipitate [27, 28], is present in high number densities [27, 29, 30]. The nucleation process starts from the supersaturated solid solution (SSSS) and is driven by a negative free energy change according to the classical nucleation theory (cf. equation 2.15). Rates of transformation and growth are governed by the interface- and volume energy associated with strain in the matrix. During transformation and growth, a range of phases are encountered with different degrees of coherency with the aluminium matrix. The precipitation sequence is most commonly written as [29, 31, 32]:

$$\begin{aligned} \text{SSSS} \rightarrow \text{Solute clusters} \rightarrow \text{GP-zones} \\ \rightarrow \beta'' \rightarrow \beta', \text{U1}, \text{U2}, \text{B}' \rightarrow \beta, \text{Si}, \end{aligned} \tag{2.1}$$

where the phases are described in table 2.3. Small additions of Cu are known to significantly affect the age hardening response [33–40], and several phases may form and develop during the artificial ageing stage [30, 32, 40]. With prolonged ageing, Cu is incorporated into the nanoscale precipitates and they develop to Q′-($\mathrm{Al_6Mg_6Si_7Cu_2}$) [41], or other hybrid structures [30, 40, 42]. All the metastable precipitates in the 6xxx system are structurally related through a common underlying projected Si-network [43]. The modified precipitation sequence is commonly written as:

$$\begin{aligned} \text{SSSS} \rightarrow \text{Solute clusters} \rightarrow \text{GP-zones} \\ \rightarrow \beta'', \text{L} \rightarrow \beta'_{\text{Cu}}, \text{Q}', \text{C}, \text{S} \rightarrow \text{Q}, \text{Si}, \end{aligned} \tag{2.2}$$

where the phases are explained in table 2.3. Other Cu-rich phases such as the E-, θ-, S- and T phases are typically found in the Al-Cu-Mg (2xxx) alloy series, and have not been reported to form in the typical 6xxx serious alloys. The effect of

minor addition of other elements (Ag, Au, Co, Ge, Li, Ni, Zn) has been reviewed by Saito *et al.* [32].

Although precipitate structures is not the main focus of this thesis, they are important to understand and account for in a study, as the solute incorporated into these phases may affect the overall solute distribution and thus the corrosion properties of the material. This is the topic of Paper **III**.

Table 2.3: Relevant precipitate phases in the Al-Mg-Si (6xxx) system represented with their composition, space group, lattice parameters and laterally coherent interface(s).

Phase	Composition	Space group	Lattice parameters	Coherent interface
Solute clusters [44–46]	Variable			
Pre-β'' [31, 47, 48]	$Al_{7-x-y}Mg_{2+x}Si_{2+y}$	C2/m	$a = 14.80$ Å $b = 4.05$ Å $c = 6.48$ Å $\beta = 105.3°$	
β'' [27, 28, 49]	$Al_2Mg_5Si_4$	C2/m	$a = 15.16$ Å $b = 4.05$ Å $c = 6.74$ Å $\beta = 105.3°$	$a_{\beta''}$//$[320]_{Al}$ $c_{\beta''}$//$[1\bar{3}0]_{Al}$
β' [50, 51]	$Mg_{1.8}Si$	$P6_3$	$a = b = 7.15$ Å $c = 4.05$ Å $\gamma = 120°$	None [52]
U1 [53]	Al_2MgSi_2	$P\bar{3}m1$	$a = b = 4.05$ Å $c = 6.74$ Å	a_{U1}//$[1\bar{3}0]_{Al}$
U2 [54]	AlMgSi	Pnma	$a = 6.75$ Å $b = 4.05$ Å $c = 7.94$ Å	a_{U2}//$[1\bar{3}0]_{Al}$
B′ [55]	$\sim Al_3Mg_9Si_7$	$P\bar{6}$	$a = b = 10.40$ Å $c = 4.05$ Å $\gamma = 120°$	$a_{B'}$//$[150]_{Al}$
L [36]	Variable	Disordered		
S (QP1) [36]	Variable		Variable	
β'_{Cu} (QC) [50, 56, 57]	$Al_3Mg_3Si_2Cu$	$P\bar{6}2m$	$a = b = 6.90$ Å $c = 4.05$ Å $\gamma = 120°$	$a_{\beta'_{Cu}}$//$[1\bar{3}0]_{Al}$
C [58]	$AlCu_{0.7}Mg_4Si_{3.3}$	$P2_1/m$	$a = 10.32$ Å $b = 4.05$ Å $c = 8.10$ Å $\beta = 100.9°$	c_C//$[010]_{Al}$
Q/Q′ [41, 59–62]	$Al_3Cu_2Mg_9Si_7$	$P\bar{6}$	$a = b = 10.32$ Å $c = 4.05$ Å $\gamma = 120°$	$a_{Q'}$//$[150]_{Al}$[†]
β [63]	Mg_2Si	$Fm\bar{3}m$	$a = 6.35$ Å	

[†] Only applies to the metastable Q′-phase precipitate.

2.2.2 Precipitation in Al-Zn-Mg-(Cu) alloys

A significant amount of work has previously addressed the precipitation sequence and structure of precipitates in the 7xxx series aluminium alloys. However, the overall understanding is still limited in comparison to the 6xxx series. Papers **IV** and **V** in this thesis mostly concern this topic, as hardening precipitates may have an influence on the SCC properties.

The general precipitation sequence from a SSSS following a SHT can be summarised as:

$$\mathrm{SSSS} \rightarrow \mathrm{GP(I)/GP(II)} \rightarrow \eta' + \eta_{(1-13)} \rightarrow \eta(\mathrm{MgZn_2}). \tag{2.3}$$

The different phases and labelling in the precipitation sequence 2.3 will be described in the following sections.

Clusters

At room temperature, coherent solute-rich clusters (Guinier-Preston (GP) zones), are formed from the SSSS during natural ageing [64–67]. The GP(I)-zones are made from Al, Mg and Zn, ordered on the aluminium face-centered cubic (fcc) lattice, and exhibit a well-defined selected area diffraction pattern (SADP) [65–74]. They have been described through an elongated anti-phase structure with alternating arrangement of Zn and Mg rich planes [60, 66, 74]. This suggested model has been deduced from collective SADPs and not from the structural information related to a single cluster. Thus, this description of the atomic ordering is limited, as will become clear in Paper **V**. These particular zones are important as they are known to exist in peak aged tempers if the material has been artificially aged under the temperature these clusters dissolve ('GP(I) solvus temperature') [64, 75–77].

GP(II) zones, often referred to as vacancy rich clusters, are described as Zn-rich layers on $\{111\}_{\mathrm{Al}}$. They have almost exclusively been observed directly using the high-resolution TEM (HRTEM) technique when viewing along $\langle 110\rangle_{\mathrm{Al}}$ [66, 70, 71, 78, 79], and usually following a rapid quenching from SHT temperatures [66, 70]. Li *et al.* found something which might have been the GP(II) zone in a high-angle annular dark-field (HAADF)-scanning transmission electron microscope (STEM) study, but did not argue for it [80]. Only once did we find something similar, which is shown in figure 2.2. If this is the GP(II) zone (seen by HAADF-STEM) is not discussed further in this thesis, but will be important to future works.

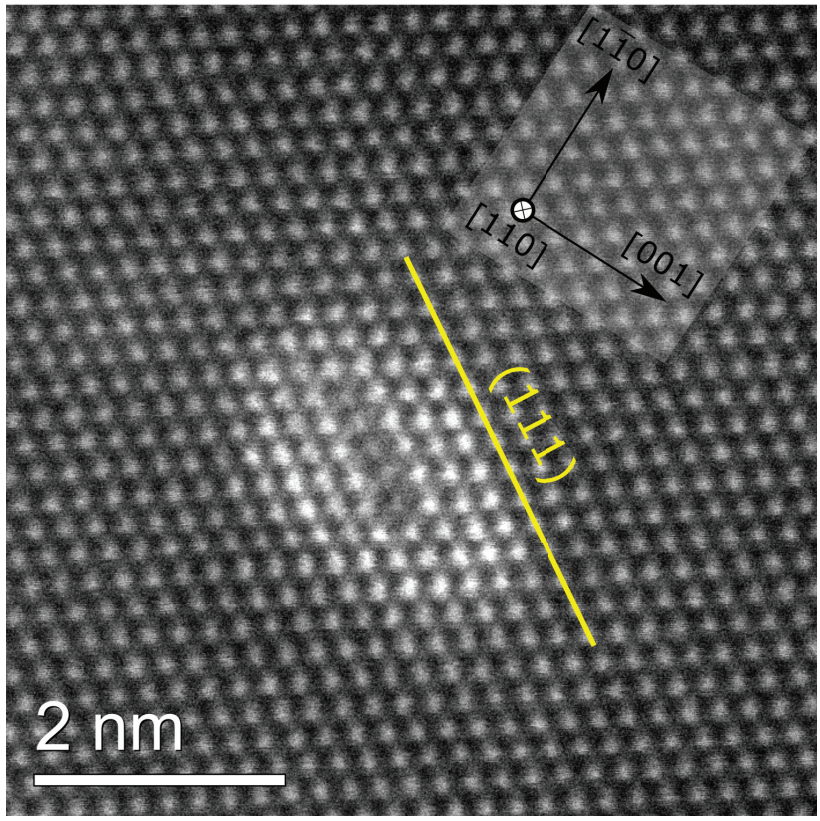

Figure 2.2: HAADF-STEM image of an unknown particle/GP-zone, lying on a $\{111\}_{\mathrm{Al}}$ plane. This was only observed once along $[110]_{\mathrm{Al}}$ in a peak aged Al-Zn-Mg alloy. It is not understood if this might be the 'GP(II) zone' (A. Lervik & A. Bendo: unpublished work).

Mg-Zn precipitates

The highest obtainable hardness in 7xxx series is associated with large number densities of the metastable η' precipitate phase forming on $\{111\}_{\mathrm{Al}}$ planes. This phase is described by stacking of a rhombohedral (R) and an orthorhombic (O) sub-unit resulting in a distinct thickness of $6\times\{111\}_{\mathrm{Al}}$ ($\sim$14.0 Å) [81].

The R-unit is found in the equilibrium hexagonal η-$MgZn_2$ phase with cell parameters $\mathrm{a} = 5.15$ Å and $\mathrm{c} = 8.48$ Å with space group $\mathrm{P6_3/mmc}$ (#194) known as the C14 Laves phase [82, 83]. This phase has been reported to form with 13 different orientations in the aluminium matrix, denoted as η_{1-13} [75, 84–88]. However, only a few of these have been reported in other studies than the ones they were originally proposed in. Only the η' [80, 81], η_1 [87, 89, 90] and η_2 [80, 81, 87], have been observed using HAADF-STEM. Studies have demonstrated these three

to be the most important phases present (with exception of η_4) in aged Al-Zn-Mg-(Cu) alloys [67, 70, 85, 91]. Note, these are not incoherent with the Al matrix, but rather semi-coherent metastable precipitates. As highlighted in the precipitation sequence 2.3, the different orientation relationships may exist simultaneously in an aged temper.

It was recently demonstrated that the η-$MgZn_2$ precipitates may incorporate an additional flattened hexagonal sub-unit giving rise to internal stacking faults [87, 89, 92]. This sub-unit can also be described through the O- and R-units [92], and is similar to a sub-unit found within the monoclinic Mg_4Zn_7 phase in Mg-Zn-X alloys [90, 93], if the O-unit replaces its internal Zn sites with Mg [81, 92]. Incorporation of these sub-units results in a quasicrystal-like internal structure giving uncommon morphologies, making it difficult to deduce their habit planes in a bright-field (BF)-TEM image. Therefore, many precipitates in both Al-Zn-Mg and Mg-Zn alloys can be found with large variations in their internal stacking due their relation to icosahedral fivefold and pseudo twofold symmetries [93]. This understanding only recently made possible through HAADF-STEM investigations, is likely the reason behind some of the confusion related to hardening phases in Al-Zn-Mg alloys. This sub-unit is described in more detail by A. Singh [93] and A. Bendo [90].

Transformations

One of the remaining unanswered questions in Al-Zn-Mg alloys is related to the transformation procedure from SSSS to hardening phases and the role of GP-zones in this process. More than $\sim$50 years after these questions were first addressed, there is still a serious need for modernised *in situ* heating studies (e.g. using STEM [94]) in order to fully understand how the transformation(s) are taking place.

It has been suggested that η' nucleates on sites such as GP-zones, vacancy rich clusters or impurity atoms [75]. However, Gjønnes & Simensen found no evidence for GP-zones preceding the η' phase [85]. Chung *et al.* demonstrated that η' nucleated away from the GP(II) zone by *in situ* heating HRTEM [78]. Several authors have suggested the reaction $\eta' \rightarrow \eta_2$ as a further transformation during coarsening [70, 78, 85, 95]. η_1 has, on the other hand, been suggested to nucleate directly from solid solution and not pass through an intermediate phase such as GP-zones or η' [85]. This phase is mostly found when aged at 'high' temperatures, meaning above the 'GP(I) solvus' temperature.

2.3 Mechanical properties

Tensile testing is a method commonly used to assess the mechanical properties of materials. This results in a *stress-strain curve* where one is schematically shown in

figure 2.3. A specimen with initial length, L_0, and cross-section area, A_0, becomes elongated when it is subjected to an applied load. The elongation can be normalised with respect to L_0 to give the *strain*, while the load can be normalised to the cross-section area to give the applied *stress*. At low stresses, there is a linear relationship between stress and strain, called the *elastic region*. Releasing the applied load will return the specimen to its original shape. At a certain stress, the material will start to yield at a point denoted the *yield strength (YS)*. The yield strength is the onset for dislocation movement and resulting *work hardening*. The material will in this region undergo *plastic deformation* and will no longer return to its original shape when relieved of its applied stress. Further increasing the applied load will reach the *ultimate tensile strength (UTS)*, which denotes the load required to initiate the processes leading to *fracture*.

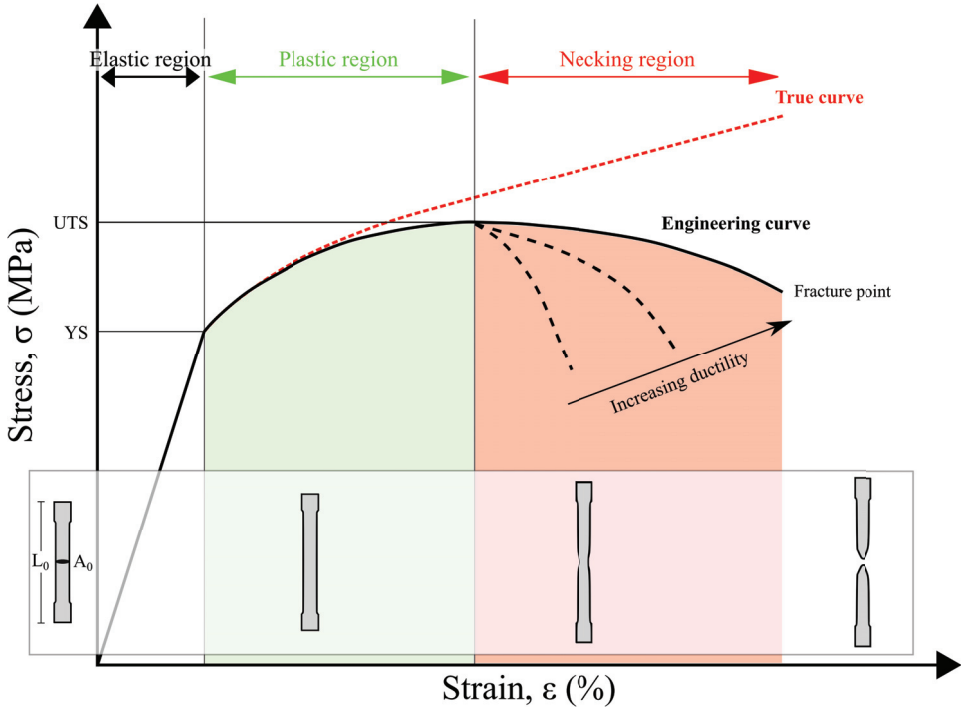

Figure 2.3: Schematic illustration of a stress-strain curve obtained from a tensile test. Both the engineering- and true stress-strain curves are indicated. The physical appearance of the specimen is illustrated in each of the different regimes.

One typically represents the stress-strain curve either as the engineering- or true curve. In the engineering curve, the reduction in cross-section area in the necking region is not considered when calculating the stress (force divided by load bearing area). In the true curve, the material will work harden all the way to its fracture

point, and not appear to soften as in the case of the engineering curve. This is also depicted in figure 2.3. The strain value reached prior to fracture is a measure of *ductility*, and the integrated area under the curve is a measure of *toughness*.

Plastic deformation in aluminium occurs by the propagation of small displacements and is referred to as *slip*. The line separating an unslipped and a slipped region is called a *dislocation line*. The magnitude and direction of the dislocations is called the *Burgers vector*. Both the magnitude and direction of the displacements, and the planes in which they propagate (glide plane), are restricted by the crystal structure. In aluminium, the slip will (usually) occur along the $\langle 110 \rangle_{\mathrm{Al}}$ directions on the close-packed $\{111\}_{\mathrm{Al}}$ planes. By the face-centered cubic symmetry a total of 12 different slip systems is generated.

2.3.1 Strengthening mechanisms

Dislocations will interact with different microstructural features (defects), as illustrated in figure 2.4, during plastic deformation. The defects can be point defects (vacancies, interstitial- or substitutional atoms), 1D (dislocations), 2D (grain boundaries, surfaces) or 3D (voids, precipitates). Hindering dislocation movement will increase the overall strength of the alloy, but hindering it too much will affect the ductility. The overall material response to plastic deformation and the strength-ductility trade-off is a complicated matter [96]. The total strength of the material is often expressed as a linear sum of the individual contributions to strength, which will only be introduced briefly here. More elaborate explanations are found elsewhere [2, 3, 97, 98].

A study of the relative contributions to strength was conducted by Teichmann *et al.* for a AA6060 alloy processed with and without a 10% pre-deformation step [99]. Solid solution strengthening contributed 30 MPa to the total strength and pre-deformation contributed 90 MPa. The small pre-deformation had a larger contribution to the overall strength than the contribution from precipitates (75 MPa). However, pre-deformation significantly reduced the ductility [99].

Solute strengthening

As illustrated in figure 2.4, a substituting atom (D), will generate a surrounding strain field according to its size misfit to Al [101], which will affect dislocation movement. The strength contribution from elements in solid solution can be expressed by the concentration of element C_j and a corresponding scaling factor k_j [102, 103]

$$\sigma_{\mathrm{ss}} = \sum_j k_j C_j^{2/3}. \tag{2.4}$$

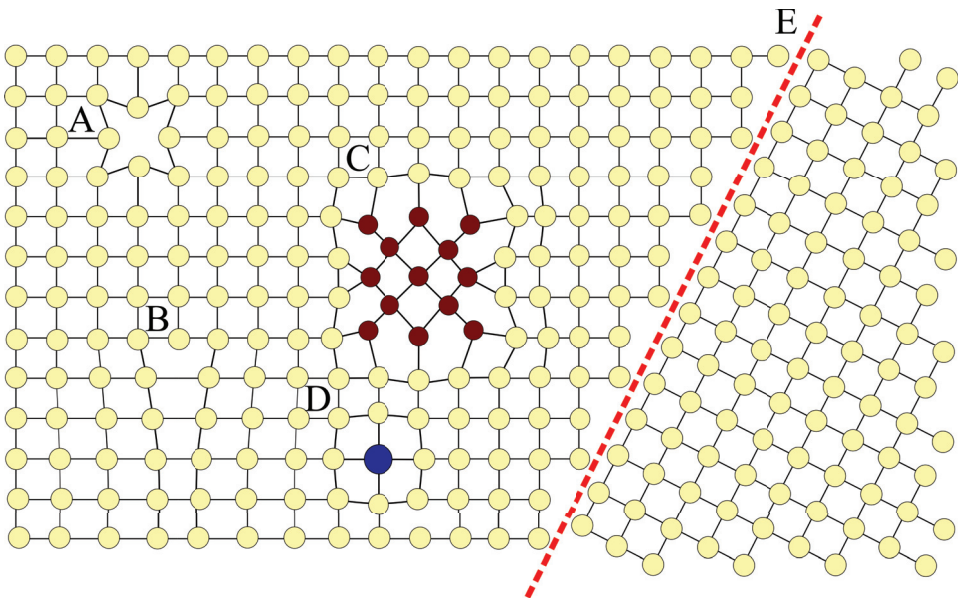

Figure 2.4: Schematic illustration of common lattice defects in a crystalline solid. **A**: vacancy, **B**: dislocation, **C**: precipitate phase, **D**: substitutional atom and **E**: grain boundary. Modified from [3, 100].

Dislocation strengthening

During work hardening, dislocations are generated which interact with one another when they move on the same slip system. Dislocation strengthening can be expressed as [103]:

$$\sigma_{\text{dis}} = \alpha M G b \sqrt{\rho} \tag{2.5}$$

where α is a constant, M is the Taylor factor, G is the shear modulus, b is the magnitude of the Burgers vector and ρ is the dislocation density.

Grain boundary strengthening

Reducing grain size can lead to an increase in strength, because grain boundaries may act as a barrier for dislocation movement. Dislocations become pinned at the grain boundary causing a stress build-up. This stress may activate new dislocation sources in the neighbouring grain and cause further deformation. Hence, a larger force will be required to propagate plastic flow, which is expressed by the 'Hall-Petch equation' [97, 103]:

$$\sigma_{\mathrm{gb}} = \sigma_0 + \frac{k}{\sqrt{d}} \tag{2.6}$$

where σ_0 is the material resistance to dislocation movement, k is a constant and d is the grain diameter. Geometrical limitations, such as the grain size, will limit the capacity for pileups. In 'normal' processed alloys the contribution from grain boundary strengthening is limited. In processing routes where ultrafine grains are produced this contribution becomes increasingly significant [104].

Precipitation strengthening

Strengthening of aluminium by precipitates is based on hindering the dislocation movement through the matrix by generating high number densities of nanoscale precipitates, with an associated strain field [105]. The phase boundary (particle-matrix interface) coherence is important for the strengthening properties and in addition to the cross-section area of the precipitate; these determines whether a particular precipitate becomes *sheared* or *bypassed*. The interface can either be fully coherent, semi-coherent or incoherent, which will subject the Al lattice to different degrees of strain. Only the coherent and semi-coherent interfaces make a substantial contribution to the strength.

If the particle is bypassed, it will leave behind a dislocation (Orowan loop) around the precipitate, while shearing will result internal defects and new interfaces as illustrated in figure 2.5. Small particles below a critical radius, r_{c}, will be subjected to shearing, whereas larger particle will undergo looping. The maximum strength increase will be obtained when mean particle radius is close to r_{c}, which is typically found close to the peak aged T6 temper. The interactions are complicated but can be estimated as:

$$\sigma_{\mathrm{p}} = \frac{M}{b\bar{r}} \left(2\beta G b^2\right)^{-1/2} \left(\frac{3f}{2\pi}\right)^{1/2} \bar{F}^{3/2}, \tag{2.7}$$

where β is a constant, M is the Taylor factor, b the magnitude of the Burgers vector, G the shear modulus, $\bar{r}$ is the mean particle size, f the particle volume fraction and $\bar{F}$ is the mean obstacle strength which is dependent on the particle size [102]. The mean particle strength, if the radius is less than r_{c}, can be expressed:

$$\bar{F} = 2\beta G b^2 \left(\frac{r}{r_{\mathrm{c}}}\right). \tag{2.8}$$

Particles with radius greater than r_{c} will have a constant $\bar{F}$, independent of the

radius, reducing equation 2.8 to $2\beta Gb^2$. According to Guyot & Cottignies, the decrease in yield strength due to precipitate coarsening was found to occur at the critical radius r_c = 3 nm for a 7xxx alloy [106].

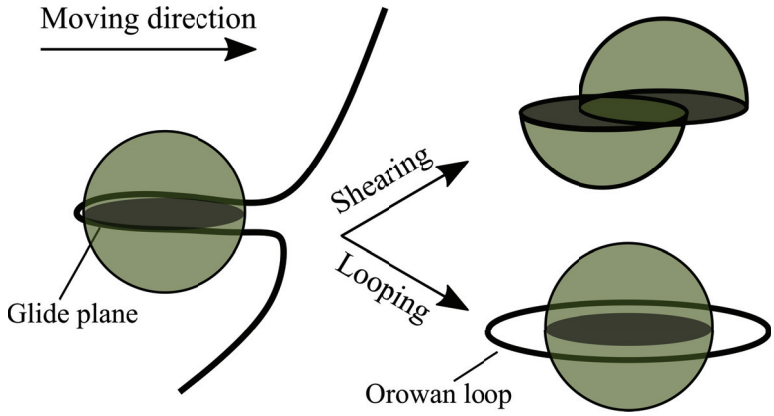

Figure 2.5: Schematic illustration of a moving dislocation interacting with a spherical precipitate. The dislocation will either shear or loop the precipitate. The figure is modified from [107].

2.4 Grain boundaries

This section is meant as an introduction to grain boundaries and is mostly based on the books by Lejček [108] and Priester [109], where more comprehensive explanations and topics can be found.

Grain boundaries exists in polycrystalline materials and are regions separating two grains (crystals) oriented differently, as illustrated in figure 2.4. The grain boundary can be considered as a transition region representing a crystallographic- and/or chemical discontinuity, typically distinguished by a width of less than two atomic diameters, but may in some cases extend to several atomic diameters [108].

A grain boundary is described by five independent macroscopic degrees of freedom (DOFs): 1 for the rotation angle (θ) between two crystals, 2 for the rotation axes (**o**) and 2 representing the grain orientation with respect to the grain boundary plane (represented by the grain boundary plane normal vector, **n**). By distinguishing them based on their relationship between the rotation axis and the grain boundary normal, one obtains the two definitions:

1. *Tilt boundaries*: where ($\boldsymbol{o} \perp \boldsymbol{n}$)
2. *Twist boundaries*: where ($\boldsymbol{o} \parallel \boldsymbol{n}$)

Three additional microscopic degrees of freedom exists which represent the rigid body translation between the grains. These translations are independent of macroscopic DOFs, but controlled by interface relaxation due to temperature, pressure and/or chemical composition.

Wolf & Lutsko suggested a classification scheme represented by the Miller indices of both contacting planes in a bicrystal and the twist angle, φ, summarised in table 2.4 [110]. If the boundary plane is described by the same Miller indices in both grains, it is a *symmetric* boundary and if not, it is called *asymmetric*. Depending on the twist angle, these are either tilt- or twist grain boundaries. If the grain boundary does not fit to any of these, it belongs to a class called *random* or *mixed* boundaries.

Table 2.4: Classification of grain boundaries based on the contacting plane $(h_i k_i l_i)$ in grains 1 and 2, and the twist angle, φ [108, 110].

Symmetric tilt grain boundary	$\{h_1k_1l_1\} = \{h_2k_2l_2\}$ & $\varphi = 0$
Asymmetric tilt grain boundary	$\{h_1k_1l_1\} \neq \{h_2k_2l_2\}$ & $\varphi = 0$
Twist grain boundary	$\{h_1k_1l_1\} = \{h_2k_2l_2\}$ & $\varphi \neq 0$
Random (mixed) grain boundary	$\{h_1k_1l_1\} \neq \{h_2k_2l_2\}$ & $\varphi \neq 0$

Low-angle grain boundaries

It is common to distinguish between *low-angle* and *high-angle* grain boundaries. The low-angle grain boundaries are described by a periodic row of discrete dislocations, which accommodate the misorientation [108]. The validity of such grain boundaries is up to a misorientation of $\sim$15°, which marks the typical transition from dislocations boundaries to high-angle grain boundaries according to Brandon's criterion [111]. The misorientation angle, θ, is related to the magnitude of the Burgers vector, $|\mathbf{b}|$, and the dislocation spacing, D, as:

$$\sin\frac{\theta}{2} = \frac{|\mathbf{b}|}{2D}. \tag{2.9}$$

The energy of these grain boundaries was demonstrated by Read & Shockley to follow the relation

$$E_{\mathrm{gb}} = \frac{\theta}{|\mathbf{b}|}\left[\frac{\mu\mathbf{b}^2}{4\pi(1-\nu)}\ln\frac{1}{\theta} + E_{\mathrm{c}}\right] = \theta(A - B\ln\theta), \tag{2.10}$$

where μ, ν and E_{c} are the shear modulus, Poisson's ratio and the energy of the

dislocation core, respectively [112]. The latter part of equation 2.10 is the typical form of what is commonly known as the 'Read-Shockley equation', with $A = E_c/|\mathbf{b}|$ and $B = \mu|\mathbf{b}|/4\pi(1-\nu)$. The energy of low-angle grain boundaries, based on this representation, is lower than for high-angle grain boundaries and increases with increasing misorientation angle.

The coincident site lattice

A special case of symmetric tilt boundaries is the coincident site lattice (CSL) boundaries, proposed by Kronberg & Wilson [113]. The assumption is that the grain boundary energy is at its lowest when the degree of coinciding atomic positions in both grains, is high. Thus, a high number of coinciding sites should be more thermodynamically stable than grain boundaries with highly perturbed structural configurations.

Assuming two grains are misoriented by an angle, θ, around the axis $\boldsymbol{o}$, the superposition of atoms from both grains are the *coincidence sites*, and gives the degree of fit, Σ, defined as:

$$\Sigma = \frac{\text{number of coincidence sites in an elementary cell}}{\text{total number of all lattice sites in an elementary cell}}. \tag{2.11}$$

In cubic systems, this may be determined directly from the Miller indices of the symmetrical tilt boundary plane as:

$$\Sigma = \delta(h^2 + k^2 + l^2), \tag{2.12}$$

where δ is either 1 or $1/2$ if $(h^2 + k^2 + l^2)$ is odd or even, respectively. As such, all Σ values are odd in cubic systems.

Note that the aforementioned theories only concern the symmetric tilt boundaries. There are few theories regarding random grain boundaries. It is likely that the atomic ordering at the grain boundary core consists of an arrangement of polyhedral atomic units built by the local relaxation of atoms to minimise the free energy, as first proposed by Ashby *et al.* [114]. A final quote summarising grain boundaries [109]:

> 'Let us first underline that there is no satisfying denomination of grain boundaries because it depends on the scale they are observed, i.e. of the observation tool. [...] The observations of the grain boundaries at different scales result in terminological ambiguities.'

2.4.1 Segregation and precipitation

Grain boundary segregation is a well-known phenomenon occurring in a range of materials. It plays important roles for corrosion- and mechanical properties in a range of metallic alloys [108, 115, 116].

Segregation

The driving force for *equilibrium* segregation is to reduce the Gibbs free energy of the system by redistribution of the solute elements. In the earliest thermodynamic models for interface segregation, grain boundary structure was not taken into account and were mostly based on a monolayer coverage i.e. similar to a bare surface (Gibbs adsorption model and the Langmuir-McLean segregation isotherm). More advanced models considers the atomic structure of grain boundaries (Seah & Hondros model) and the chemical interaction energies between solute elements (Fowler & Guggenheim model, and McLean & Guttmann). While interesting in themselves, these models and theories are not at the core of this thesis. More elaborate discussions can be found elsewhere [108, 109].

In the materials studied here, other factors introduced through the processing steps presented earlier will contribute to the segregation, which are included in *non-equilibrium* segregation theories. At the core of non-equilibrium segregation is flow of excess vacancies, formed during the rapid quench from SHT, to or from boundaries, which serves as sinks in order to accommodate the non-equilibrium vacancy concentration [117]. Two types of diffusion may occur depending on the solute-vacancy interaction. If there is a strong interaction between vacancies and solutes, the two species migrate together towards the grain boundary (solute drag). If the solute-vacancy interaction is weak, the solute and vacancy flux may be in opposite directions. These diffusion models account for the formation solute depleted zones (precipitate free zones (PFZ)) [109]. In addition, irradiation effects and grain boundary migration may influence segregation properties.

Complexion

There are numerous reports of segregated solute 'films', which follows the grain boundary core and are confined to very small widths (Å-nm). These films could be considered as separate phases with their own associated thermodynamic quantities. However, by arguing that the thermodynamic properties of intergranular phases are dependent on the neighbouring bulk phases, Tang *et al.* suggested the name *complexions* instead of phase transitions [118], as complexions do not satisfy the Gibbs definition of phase. Different grain boundaries having the same complexion may have different atomic structures, but have the same thermodynamic characteristics. The six defined and observed complexions are the clean, mono-, bi-, tri-, nano

and wetting layers. This term has not been used in this thesis although there are clear similarities with was is referred to as segregated layers in this work. More information can be found in the review by Cantwell *et al.* [119].

Precipitation

Having established that the grain boundary core consists of solutes, it may often further develop into particles which nucleate preferentially on intergranular defects, dislocations and/or steps. The diffusion rate of solutes along the grain boundaries are typically orders of magnitudes larger than that in the bulk [120]. This naturally makes the heterogeneously nucleated grain boundary particles (GBPs) larger than the those homogeneously distributed in the bulk.

The difference in the free energy, ΔG_T, for heterogeneous nucleation of a phase β on a phase α, may be expressed as [109]:

$$\Delta G_T = V\Delta G_V + \sum A_{\alpha/\beta}\gamma_{\alpha/\beta} - A_{\alpha/\alpha}\gamma_{\alpha/\alpha} \tag{2.13}$$

where ΔG_V is the difference in free enthalpy per unit volume, $A_{\alpha/\beta}$ is the area occupied by each interface between α/β, where $\gamma_{\alpha/\beta}$ is the interface energy per unit area. The latter term represents the energy released by forming a nucleus at the surface normally constituted by α. The first and the third terms are negative, thus favourable to nucleation; the second term is positive as it corresponds to a surface creation and is opposed to phase transformation.

In the case of a spherical particle (independent of interface orientation i.e. incoherent), depends on the radius, *r*, and the angle, ϕ, between the nucleus and grain boundary surface. The variation in free enthalpy for heterogeneous nucleation is a fraction of that of homogeneous nucleation, which can be expressed through the angle ϕ:

$$\Delta G_{\text{het}} = \left(\frac{1}{2}(2+\cos\phi)(1-\cos\phi)^2\right)\Delta G_{\text{hom}} \tag{2.14}$$

where:

$$\Delta G_{\text{hom}} = \frac{4}{3}\pi r^3\Delta G_V + 4\pi r^2\gamma_{\alpha/\beta} \tag{2.15}$$

is simply the *classic nucleation theory* expressed by a bulk and a surface term. It states that there is a critical radius, r_{crit}, that the growing nucleus must exceed in

order to overcome the associated energy barrier to form a stable nucleus. Differentiating equation 2.15 with respect to *r*, this radius becomes:

$$r_{\text{crit}} = -\frac{2\gamma_{\alpha/\beta}}{\Delta G_V}. \tag{2.16}$$

Evaluating equation 2.14 for different angles, the energy barrier for heterogeneous nucleation is lower than that of homogeneous nucleation. This formalism is not limited to grain boundaries but applies to any interface. An example of heterogeneous nucleation is shown in figure 2.6, where a Q-phase is nucleated on a α-phase dispersoid. Examples of heterogeneous nucleation on grain boundaries are found in Papers **I**, **II**, **III**, **V** and **VI**.

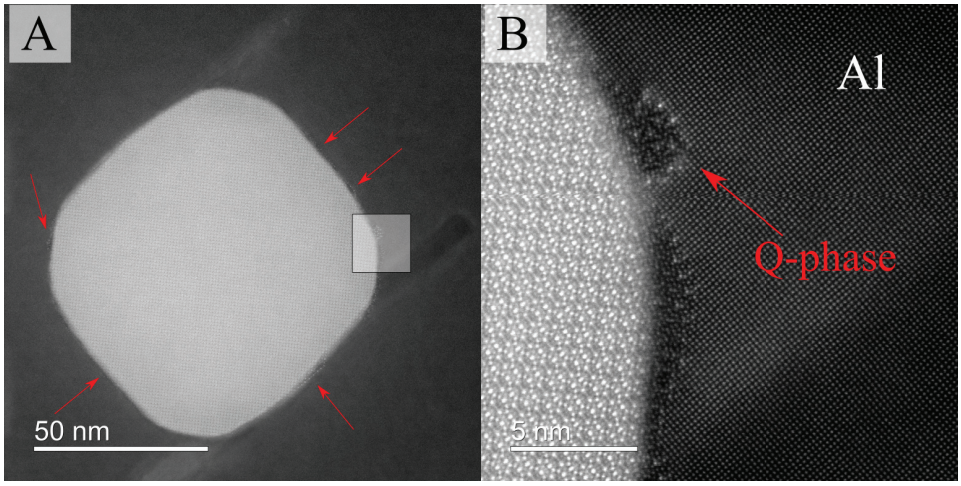

Figure 2.6: Heterogeneous nucleation of Q-phase particles on the interfaces of a α-Al(Fe,Mn)Si phase dispersoid in an Al-Mg-Si-Cu alloy. Red arrows indicate nucleation sites. A. Lervik, unpublished work.

This foregoing theory assumes that the nuclei are incoherent, which in the materials studied herein is a simplification. The heterogeneous nucleation process is more complicated than the foregoing theory suggests, as the particles are likely to have (at least) one coherent/semi-coherent interface. It is also likely dependent on how the lattice planes of the adjacent grains are aligned to one another. The grain boundary itself may also (probably always does) decompose into a range of faceted structures to minimise the free energy. The latter point was recently demonstrated by Zhao *et al.* in an Al-Zn-Mg alloy, leading to preferential segregation and precipitation along different facets due to different interface energies [121]. These points become evident when studying processed alloys, as one generally observe

a non-uniform particle distribution from one grain boundary to another, and even along the same grain boundary.

2.4.2 Precipitate free zones

The PFZs are formed as the vacancies and solute elements diffuse to the grain boundaries. Following the quench from SHT the excess vacancies rapidly diffuse to the grain boundary, resulting in a low vacancy concentration close to the grain boundary. The vacancy concentration together with the solute concentration, will be too low to facilitate nucleation and growth of precipitates during the subsequent artificial ageing [122]. This leaves behind a region depleted of solute and mostly consisting of Al [117, 122, 123]. This region is important for both the corrosion and mechanical properties of alloys. The absence of the hardening precipitates results in the PFZ becoming softer than the bulk material [124, 125]. Furthermore, it may lead to stress relaxation or strain localisation during deformation [126]. Depending on the electrochemical nature of the segregating elements to the grain boundary or the grain boundary particles, the PFZ may be either an anodic or cathodic region.

It was recently demonstrated by Matsuda *et al.* that solute clusters may form in the conventional PFZ, while 'normal' precipitates are formed in the bulk [127]. If this has importance in optimising strength and ductility, and maybe even SCC, is an interesting topic for future work. This particular work, however, demonstrates that PFZs needs to be carefully examined in future TEM studies, as the clusters are extremely small and easily missed.

Chapter 3

Corrosion Phenomena in Aluminium Alloys

3.1 Introduction

Pure aluminium has excellent corrosion resistance due to its high reactivity with oxygen, which passivates the metal by forming a protective oxide layer on the surface [128]. Even if the surface is damaged this oxide film will reform and limit corrosion [2]. Corrosion is a degradation process driven by electric current flowing between an *anodic*- and a *cathodic* region. The solute elements and particles associated with aluminium alloys have different electrochemical potentials than pure aluminium. These regions are in direct contact, and thus create a microgalvanic coupling, where one of the regions will preferentially corrode (dissolve). More fundamental introduction to corrosion can be found in e.g. [129].

Localised corrosion is most common in aluminium alloys, unless exposed to an environment where the oxide film is dissolved and uniform corrosion occurs. Common types of localized corrosion are pitting and intergranular corrosion (IGC). IGC is barely visible on the surface and will generally penetrate deep into the material along the grain boundaries, and be critical for the integrity of a profile. This is believed to be caused by elemental segregation to the grain boundaries and/or the presence of grain boundary particles, causing the galvanic coupling(s).

If the material is exposed to both a corrosive environment and an applied stress field, certain alloys may become susceptible to stress corrosion cracking (SCC). This phenomenon is typically reported in 2xxx, 5xxx and 7xxx alloys systems. It is believed to be associated with similar microgalvanic coupling(s) at grain boundaries, as in the case of IGC, in addition to hydrogen related failure mechanisms

which many have reported to play key role in this cracking behaviour.

3.2 Particle electrochemistry

In order to understand the electrochemical behaviour of various particle phases forming in aluminium alloys, much work has been dedicated to synthesising and characterising them. Although such studies are extremely valuable to obtain a general understanding of these phases, it is important to emphasise that what occurs within the tight grain boundary channels may be different than what is measured in these bulk measurements due to different chemical environments and mass-transport limitation.

Birbilis & Buchheit investigated the properties of common intermetallic phases in aluminium alloys [130], also as a function of pH [131]. A large review has been written by Li & Dang which discusses both Al solid solution and secondary particles [132]. Zhu *et al.* studied phases typically found in Al-Zn-Mg-Cu alloys [133]. The characteristics with respect to corrosion of phases encountered in this work are presented below.

Mg_2Si

Mg_2Si is a common phase often found on grain boundaries in both 6xxx and 7xxx series. It has a highly negative corrosion potential, making it one of the most anodic phases with respect to Al [130]. Regardless, its dissolution process is both complicated and pH dependent [131, 134]. It selectively dissolves Mg leading to Si enrichment. Si enrichment is cathodic with respect to Al, which in turn should reverse the process leading to Al dissolution. However, Si has a low catalytic activity with respect to sustaining the cathodic reactions and several authors have suggested it to be relatively inert in the corrosion process [133, 135]. Kairy & Birbilis demonstrated that the phase undergoes rapid selective dissolution of Mg and forms an amorphous SiO-rich phase at pH 2 [136]. Others have reported the Mg-Si remnants may increase the cathodic activity [137].

$MgZn_2$

The equilibrium phase in 7xxx alloys, $MgZn_2$, is typically found on grain boundaries. It has a very low corrosion potential and typically acts as anode in contact with the Al matrix [130]. Its corrosion potential has been demonstrated to be insensitive to pH [131]. In an alkaline solution (pH 10.1) Han & Ogle demonstrated a potential dependant dealloying mechanism for $MgZn_2$ [138]. Mg was found to preferentially dissolve with a resulting Zn oxide formation at the lower potentials and at higher potentials: congruent Zn and Mg dissolution was found.

Al_3Zr

Al_3Zr are important grain refining dispersoids in the 7xxx alloy series (also some 6xxx series). It is cathodic with respect to Al, but has limited cathodic activity and thus limited, if any, effect on corrosion properties [130].

α-Al(Fe,Mn,Cu)Si

The α-phase is found is found both as large primary particles and as smaller dispersoids. It is cathodic to the Al matrix, but has been demonstrate to rapidly undergo selective dissolution, leaving behind Cu-rich remnants [139, 140]. The effect of this particle on IGC is the topic of Paper **I**.

Q-$Al_6Mg_6Si_7Cu_2$

The Q-phase is a bulk hardening phase (metastable Q′) and is also found at grain boundaries in 6xxx series aluminium (with Cu) as either a metastable or stable equilibrium phase. Kairy *et al.* demonstrated that the Q phase is more noble than the Al matrix and in a very overaged aluminium alloy, evolution of Cu particles was found following a selective dissolution of the phase [141]. Ikeuba *et al.* demonstrated a pH dependent corrosion rate [142]. However, its role in intergranular corrosion remains somewhat uncertain as others have suggested it to be inert in this process [139, 140].

3.3 Intergranular corrosion

3.3.1 General considerations

Many independent corrosion studies have been performed on 6xxx alloys with different composition and heat treatment. Theories including preferential segregation of Cu at the grain boundaries [42, 135, 140, 143–147], formation of grain boundary particles [143, 145–152] and the formation of depletion zones around the grain boundaries [135, 143, 146, 147], have been published. These theories all agree that microgalvanic coupling between the grain boundary and its adjacent region has a first order effect.

Systematic studies with respect to Mg/Si content and Cu contents are limited. However, researchers at Monash university have explored how the Mg/Si ratio and Cu content effect the corrosion behaviour [147, 153]. Such studies are useful in order to paint a general understanding on corrosion behaviour in 6xxx alloys. Note: the alloys were tested in both 0.1 wt.% NaCl [153], and in an environment according to ASTM G110 [147]. Different tests may naturally yield different results [154]. Regardless, some general trends to be pointed out are:

- Naturally aged conditions have the lowest corrosion current density, which increases with ageing time. Naturally aged tempers of alloys with Cu demonstrate pitting corrosion irrespective of Mg/Si ratio.

- IGC develops in the underaged temper and persists until the overaged temper, but is highly dependent on the composition as to what extent.

- The severity of IGC is higher for Cu-containing alloys when compared with its Cu-free counterpart, for identical ageing conditions. Additionally, the extent increases with increasing Cu content and decreasing Mg/Si ratio.

- Alloys with high Mg/Si ratio (Mg excess) tend to be more corrosion resistant than alloys low Mg/Si.

Similar conclusion were drawn by Zou *et al.* [152]. Zhan *et al.* also demonstrated, by studying the same alloy while only varying the Cu content from 0.03-0.88 wt.%, that Cu content has the most dominant effect on the IGC properties [149].

In the comprehensive study conducted by Svenningsen *et al.*, the effect of artificial ageing, Cu content, quenching rate from SHT and step quenching in Cu-containing AA6005 was investigated [143, 148, 155, 156]. It was found that the IGC susceptibility is reduced by water-quenching after extrusion. IGC in air-cooled samples was reduced by ageing the sample to peak hardness. After water-cooling, an underaged temper exhibited susceptibility to IGC, while overageing lead to improved resistance to IGC, but susceptibility to pitting corrosion. In summary, they found that the best IGC properties were achieved when the extruded profiles were water-quenched after extrusion and aged to the peak aged condition.

3.3.2 Initiation

Recently, it has been demonstrated by Kumari *et al.* that IGC in a AA6005 alloy initiated on the α-Al(Fe,Mn,Cu)Si phase particles [140]. The α-phase dissolved rapidly in the acidified NaCl solution commonly used in assessing IGC susceptibility [139, 140]. Due to selective corrosion, Cu was found to remain on the outer surfaces, acting as an external cathode [140, 157]. Selective dissolution where the nobler element remains has been reported in other Cu-containing intermetallic particles [133, 141, 158, 159], and in other phases found in aluminium alloys [130–133, 160]. Larsen *et al.* showed that removing these surface particles, by etching in fluonitric acid ($HF + HNO_3$), resulted in significantly less IGC than in the case where they still were present on the surface [135].

3.3.3 Propagation

The local microgalvanic coupling found at the grain boundaries is related to Cu segregation, grain boundary particles and solute depleted zones (PFZ). However, the corrosion process is highly dynamic and there are limited, if any, studies concerning what is occurring *in situ* within an IGC filament.

It has been suggested that overageing has a positive influence on IGC as it disrupts the continuous Cu-film by the formation of Q-phase grain boundary particles. However, Q-phases have previously been shown to dissolve leaving behind Cu-rich remnants (in a very overaged alloy) [141]. With prolonged overageing, Li *et al.* demonstrated a return of IGC and attributed it to the Q-phases distributed continuously along grain boundaries [151]. Studying corroded grain boundaries has demonstrated that Cu-rich remnants can be found along grain boundaries [157, 161, 162]. Although their origin is complicated, these particles are important in sustaining the cathodic reactions.

There is a very limited amount of studies concerning which grain boundaries that are susceptible to IGC in the 6xxx system. Minoda *et al.* reported IGC susceptibility predominantly at high-angle grain boundaries due to the presence of PFZ and grain boundary particles, which were not found at the low-angle grain boundaries in an Al-Mg-Si alloy [163]. It has previously been shown that the special CSL grain boundaries have high resistance to IGC in pure Al [164]. Bałkowiec *et al.* reported a strong correlation between misorientation angle and IGC susceptibility in an AA2024 alloy, where the high-angle grain boundaries were more susceptible [165]. Similar observations were made by Chan *et al.* [166]. Grain boundary structures and their (statistical) correlation with IGC is the topic in Paper **III**.

3.4 Stress corrosion cracking

Many metals subjected to stresses (applied or residual) may in some corrosive environment experience SCC. The environment can be either aqueous solutions or moist air [167–169]. This phenomenon is not limited to aluminium alloys, but is encountered in metallic alloy system such as steels, nickel-, titanium and copper alloys. The effect can often be observed when e.g. conducting a tensile test, where the fracture point will typically be reached at lower strains (elongations) (cf. figure 2.3). The 7xxx alloy series are infamous for their susceptibility to SCC, which limits the use of these alloys in many applications [4, 170]. The work conducted in Paper **VI** concerns SCC in a commercial Cu-free Al-Zn-Mg alloy. In figure 3.1, the SCC has penetrated nearly through the entire cross-section of the profile. When the crack has gone through the profile, it will ultimately fail. This may happen spontaneously as the cracks are not clearly visible in the surface of the profile.

Many studies have been conducted in the last decades in order to both understand the underlying phenomenon and for finding ways of mitigating it. Especially for the commercial AA7050 and AA7075 alloys. There are also many review articles concerning the topic [169–174].

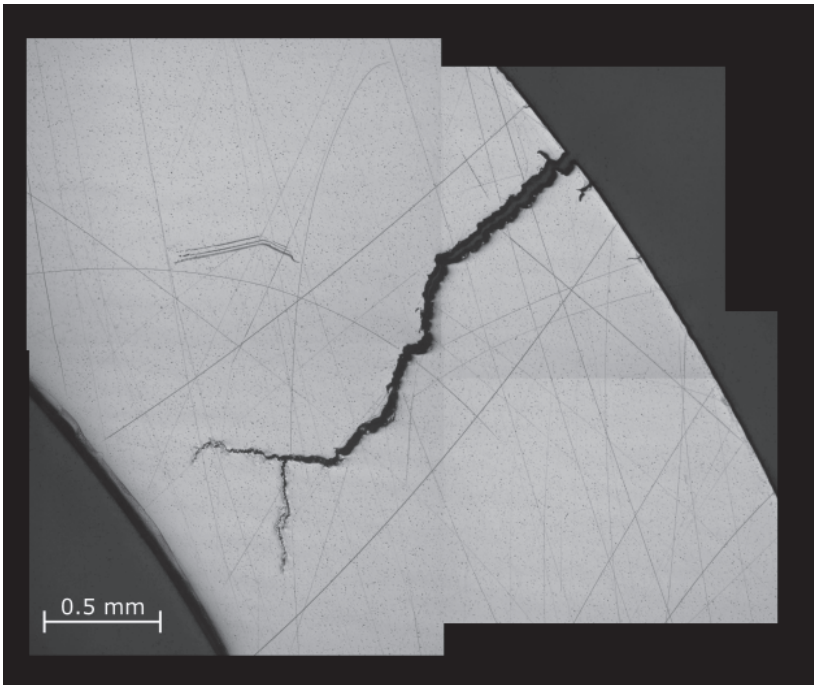

Figure 3.1: Optical microscopy image of a stress corrosion crack in the Al-Zn-Mg alloy studied in Papers **V** and **VI**. The crack has nearly penetrated through the entire cross-section of the profile.

In Cu-containing Al-Mg-Zn alloys, it has been demonstrated that the addition of 1-2 wt.% Cu has a positive effect in mitigating SCC, when compared to its Cu-free counterpart [175]. The generally accepted reason for this is due to the increased Cu content in the grain boundary $Mg(Zn,Al,Cu)_2$ particles (with overageing) [176–178]. This renders the particles less anodic with respect to the surrounding PFZ, and reduces the kinetics of the reactions occurring.

Mechanism

At the atomic level, there are numerous suggested theories for SCC with little consensus regarding one mechanisms for a given material in a certain environment. The theories can be roughly divided into three main classes: i) dissolution at the crack tip due to an active anodic path (particles or segregates), ii) formation of

oxide or de-alloyed protective films at crack tip, which may rupture when interaction with slip bands and iii) hydrogen related effects at or ahead of the crack tip. The theories concerning hydrogen's effect on SCC are manifested from: i) the possibility to generate hydrogen at the crack tip from the cathodic reaction, ii) the evident effect of hydrogen embrittlement (testing hydrogen charged samples or in hydrogen containing atmospheres) and iii) cracking behaviour in moist air (if other dissolution effects can be neglected). The hydrogen mechanisms behind SCC are essentially the same as those proposed for hydrogen embrittlement (HE) in other metals [179, 180]. The solute hydrogen may either weaken the atomic bonds and facilitate decohesion, or it may diffuse ahead of the crack tip and facilitate crack growth by a localised slip/microvoid-coalescence process. Both dissolution and embrittlement may, and probably does, influence each other [181]. These theories are explained in detail by S. P. Lynch [179, 182].

3.4.1 Microstructural aspects

The work presented in Paper **VI** considers a Cu-free Al-Zn-Mg alloy, thus work relating to such alloys are highlighted here. Regardless of the exact mechanism there are works suggesting that Cu-free Al-Zn-Mg alloys experience an accelerated cracking behaviour due to hydrogen [167, 183, 184]. Christodoulou & Flower suggested that hydrogen trapping can occur at the grain boundary particles if above a critical size of 20 nm, which would lead to an increased resistance towards embrittlement [185]. Similar ideas were suggested by Puiggali *et al.* [186]. This theory makes sense if hydrogen diffusion ahead of the crack tip is a requirement for cracking. On the other hand, hydrogen trapping at the grain boundary particles (and particularly at their interface) may lead to bond weakening and decohesion. This was demonstrated recently by Li *et al.* who used a modelling approach to show that a grain boundary containing a particle would experience a reduction in cohesive energy, with an even greater reduction if hydrogen was present [187]. This is in agreement with Wu *et al.*, although they also suggested that coarser bulk hardening precipitates will change the strain localisation at grain boundaries and improve SCC resistance [188]. Other have suggested the same concerning the bulk precipitates [175, 183, 189–192].

More recent work has demonstrate that in addition to grain boundaries, the matrix hardening precipitates can trap hydrogen [193–195]. This will in turn reduce the amount of hydrogen at the grain boundaries and increase the resistance towards cracking. Altering the bulk precipitate interface area and interface coherence, is typically related to overageing, and thus an improvement in SCC. Tsuru *et al.* demonstrated that the coherent precipitate-Al interface could trap more hydrogen than voids, grain boundaries and dislocations [195]. This resulted in a quasi-cleavage like fracture. Some have suggested that elemental segregation of Mg to

can influence the cracking behaviour by interaction with hydrogen and resulting in embrittlement [196–199].

In recent years, 3D *in situ* and *ex situ* work has emerged [195, 200–203]. Such studies enable new understanding of the cracking mechanisms occurring and how they evolve with respect to e.g. interaction with grain boundary particles. Singh *et al.* demonstrated that hydrogen bubble formation (within the crack tip) was associated with the anodic dissolution of the Mg_2Si particles in AA7075 alloy [200]. These studies are likely to become more important in the future. Especially linking 3D 'large scale' understanding to more detailed microstructural studies using TEM or atom probe tomography (APT), is a potential approach.

Quenching and residual stresses

Residual stresses in the material are often not accounted for, as they require X-ray diffraction or neutron scattering experiments to be evaluated. Large residual stressed ($\sim$100 MPa) has been reported in AA7075 following a water-quench from SHT [204]. Overageing demonstrated a stress relieving influence of 25-40% [204].

Chapter 4

Methodology

This chapter, briefly, describes the experimental methods utilised in this thesis.

4.1 Electron interaction with matter

A limitation with optical microscopy is in the obtainable resolution due to the wavelength of visible light. This limitation is called the *Rayleigh criterion* and limits the resolution to ∼200-500 nm, which is too big to resolve the phenomena occurring at the nanoscale which directly effects material properties. On the other hand, due to the properties of electrons, the wavelength may be tuned by accelerating the electrons in a potential field. This can be expressed through the equation for the relativistic electron wavelength:

$$\lambda = \frac{\mathrm{h}}{\sqrt{2\mathrm{m}_0\mathrm{e}V\left(1+\frac{\mathrm{e}V}{\mathrm{m}_0\mathrm{c}^2}\right)}} \tag{4.1}$$

where the terms h, m_0, e, c and V are the Planck's constant, electron rest mass, electron charge, vacuum speed of light and acceleration potential, respectively. Operating a typical scanning electron microscope (SEM) at 20 kV or a TEM at 200 kV, the resulting wavelengths are 8.59 and 2.51 pm, respectively. The wavelength is, however, not the obtainable resolution of the microscopes due to lens *aberrations*, as will be elaborated on in section 4.2.2.

The accelerated electrons generate a wide range of different signals upon interacting with the specimen as shown schematically in figure 4.1. The secondary electrons (SE) and backscattered electrons (BSE) are signals commonly associated with detectors in a SEM, and provides topological- and chemical information con-

trast, respectively. Auger electrons are detected in the Auger electron microscope and are typically used for near-surface critical studies. In the TEM, the detectors are placed below the specimen and detects the transmitted electrons which may be either elastically or inelastically scattered by the sample. X-rays are also generated and detected to provide chemical information using the energy-dispersive X-ray spectroscopy (EDS) detector.

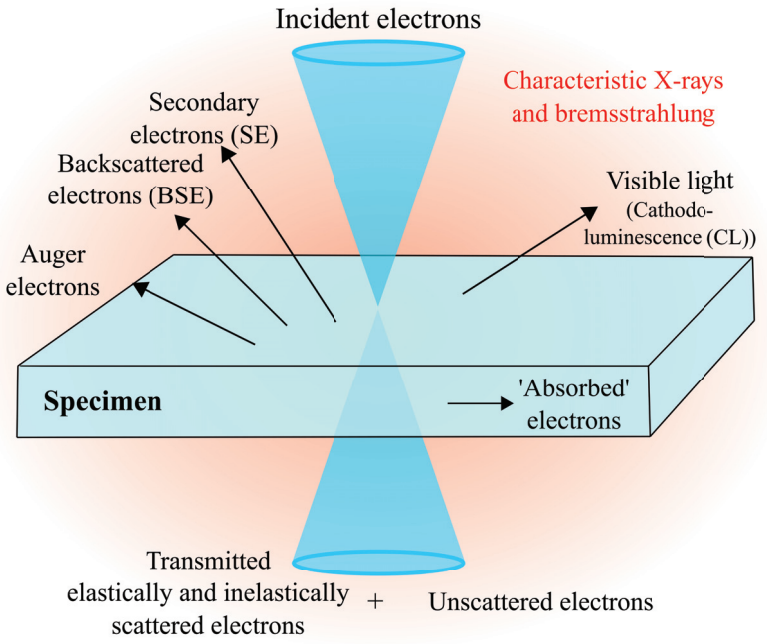

Figure 4.1: Schematic illustration of signals generated when an incident electron beam interacts with a specimen. The figure is adapted from [205].

4.2 (Scanning) Transmission electron microscopy

Following the invention by Max Knoll & Ernst Ruska in 1931, the TEM has been under constant development. Today, TEM is an essential tool for fundamental- and applied studies of materials in a wide variety of research fields. It is not limited to imaging, but can also simultaneously conduct various diffraction- and spectroscopic techniques from smaller regions than any other techniques - even all the way down to single atomic columns. The latter point has boosted research and knowledge concerning nanostructures. This was made possible through the development of aberration correctors, something which the developers Rose, Haider, Urban and Krivanek were acknowledged for by receiving the Kavli Prize in Nanoscience in May 2020 [206].

The TEM is either operated in a conventional TEM mode, where a parallel beam illuminates the sample, or in scanning TEM mode, where the electron beam is converged to a small probe which raster scans over the sample. In TEM mode, the images are generated by interference of electron wavelets scattered by the sample. In STEM mode, images are generated by recording and integrating signal generated in each pixel as the small probe scans across the sample. This can also be paired with spectroscopy techniques such as EDS, which enables chemical mapping at high spatial resolution pixel by pixel. The two modes are schematically illustrated in figure 4.2.

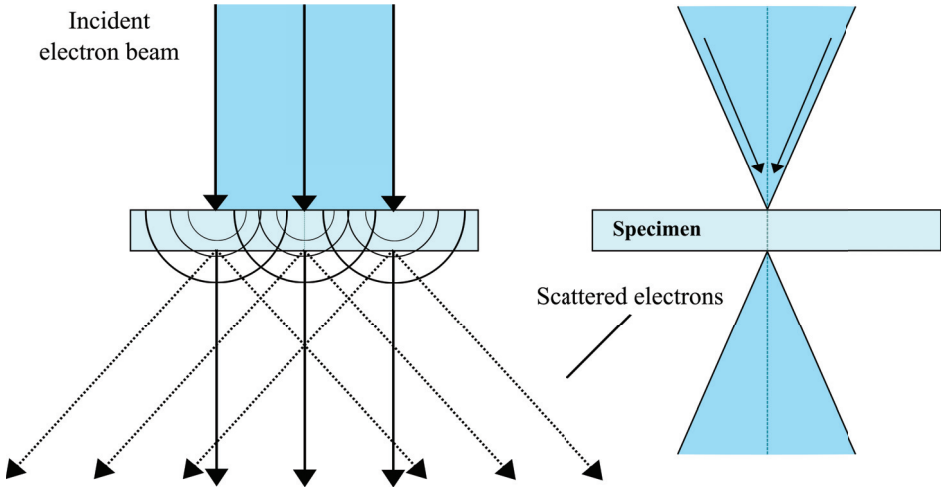

Figure 4.2: Schematic illustration highlighting the differences between the electron beam-specimen interaction in a conventional TEM (left) and in STEM (right).

STEM has been the emerging technique for the last 10 years and is the method predominantly used in this thesis. The fundamental physics of TEM will not be presented here and the reader is referred to other sources [205, 207–210].

4.2.1 STEM imaging

Accelerated electrons pass through a set of lenses, stigmators and apertures and a probe-corrector on its way from the electron source to the sample. A final aperture determines the convergence semi-angle, α, of the electron beam as shown schematically in figure 4.3. The electron beam is then focused to a probe which appear as Airy discs with a size according to the Rayleigh criterion given as:

$$\delta_D = 0.61\frac{\lambda}{\alpha} \tag{4.2}$$

where λ is the electron wavelength. As the probe is scanned across the specimen, the scattered electrons are detected below the sample on detectors situated at different collection angles. At each probe position on the specimen, the total intensity hitting the detectors is integrated. This is schematically shown in figure 4.3, where the typical detectors are situated at different collection semi-angles, β. The detectors are physically fixed at different positions, so in order to change the collection semi-angle one may change the camera length which is controlled by the post-specimen lenses.

At the highest scattering angles, an annular detector, referred to as the high-angle annular dark-field (HAADF) detector, is situated and mostly detects the Rutherford scattered electrons i.e. electrons scattered by interactions with the atomic nucleus. Ideally, the cross-section of Rutherford scattering depends on the unscreened scattering power of the nucleus, leading to a Z^2 dependent intensity [209]. For this reason, HAADF-STEM imaging is commonly referred to as 'Z-contrast imaging'. In practice, the intensity varies as approximately $Z^{1.8-2.0}$ depending on the inner collection angle and the scattering element [211]. The electrons are scattered incoherently, and the recorded intensity is expressed as:

$$I = |P(\vec{r})|^2 \otimes |\psi(\vec{r})|^2, \tag{4.3}$$

where $P(\vec{r})$ is the probe function, and the $\psi(\vec{r})$ is the object wavefunction. The probe function is again a function of the aperture function:

$$A(\vec{k}) = H(\vec{k}) \sin \chi(\vec{k}), \tag{4.4}$$

where $H(\vec{k})$ is due to the aperture and $\chi(\vec{k})$ is the aberration function [209]. By selecting other collection angles (by changing the camera length), one may change the recorded signal. At lower collection angles one typically refers to annular dark-field (ADF) imaging, which also show a Z-dependent contrast in addition to other effect such as strain contrast. Further reducing the collection angle, similar annular detectors can collect electrons without the Z-dependent often referred to as annular bright-field (ABF). This method is useful for imaging light elements such as Li or O [212]. The specific angles of the different detectors are not well-defined and also dependent on the convergence angle, α. However, some approximate numbers are: ABF 10-20 mrad, ADF 20-45 mrad and HAADF > 45 mrad. The BF detector includes the direct beam and is sensitive to Bragg scattered electrons. A full mathematical explanation is given by S. J. Pennycook in [209].

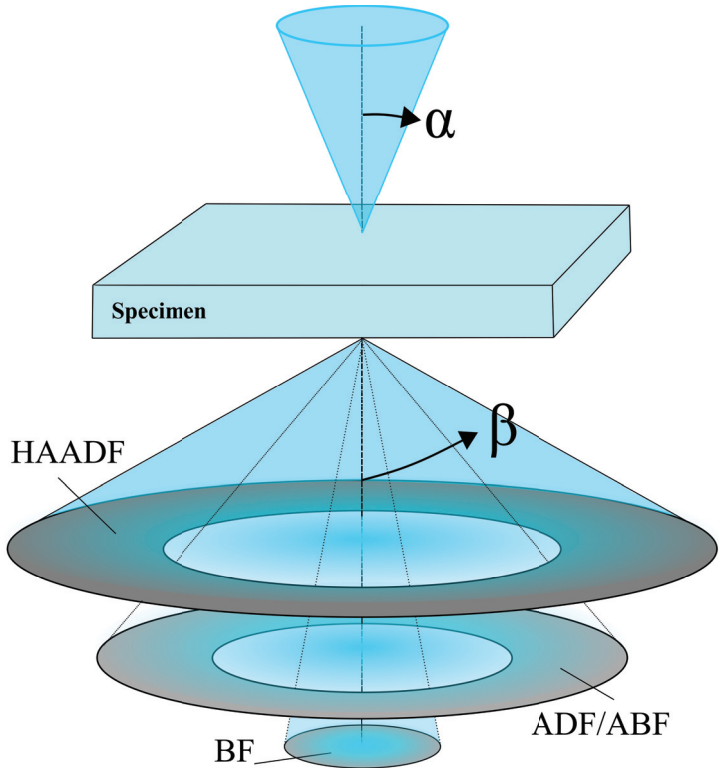

Figure 4.3: Schematic illustration of the STEM post-specimen detector geometry. The different detectors collect electrons scattered to different angles, β.

4.2.2 Aberrations

Lens aberrations are the limiting factor for achieving high-resolution. The most common aberrations are spherical- and chromatic aberrations. Spherical aberrations bring electron beams passing through the lens at different distances from the optical axis, to different focusing points in the image plane. This means that electron beams originating from one single point in the object plane, becomes a defined disc, *disc of least confusion*, in the image plane with radius:

$$r_{\mathrm{s}} = C_{\mathrm{s}}\alpha^3 \tag{4.5}$$

where $\mathrm{C_s}$ is the spherical aberration coefficient of the lens and α is the convergence semi-angle. Chromatic aberrations are caused by the energy spread in the accelerated electrons, ΔE, which causes electrons of different energies to be focused at different points in the image plane. This results in a disc of least confusion with

radius given as:

$$r_{\mathrm{c}} = C_{\mathrm{c}}\alpha\frac{\Delta E}{E_0} \tag{4.6}$$

where C_{c} is the chromatic aberration coefficient and E_0 is the nominal beam energy.

In reality there is an off-axial contribution which degrades the resolution, and a more sophisticated explanation is needed. An electron wave emerging from a position, w_0 in the object plane will intersect at ω in the aperture plane. If the electron beam is affected by aberrations, it will be focused at w_i' rather than w_i, in the image plane. The associated error is then $\Delta\mathrm{w}_i = \mathrm{w}_i' - \mathrm{w}_i$. Defining these positions as complex numbers $\omega = \theta_x + i\theta_y$ and $\mathrm{w}_0 = \mathrm{x}_i + i\mathrm{y}_0$, allows us to express the various aberrations in terms of ω and w. However, if imaging at high resolutions, the range of w_0 is small compared to the bore of the lens. In this case, the dependence of w_0 can be neglected in what is called the 'isoplanaric approximation'. Considering aberrations up to the 4$^{\mathrm{th}}$ order, the geometrical (i.e. excluding chromatic effects) aberration wavefunction reads:

$$\begin{aligned}\chi(\omega) = \Re\{A_0\bar{\omega} + \frac{1}{2}C_1\omega\bar{\omega} + \frac{1}{2}A_1\bar{\omega}^2 + B_2\omega^2\bar{\omega} + \frac{1}{3}A_2\bar{\omega}^3 \\ \frac{1}{4}C_3(\omega\bar{\omega})^2 + S_3\omega^3\bar{\omega} + \frac{1}{4}A_3\bar{\omega}^4 + ...\}\end{aligned} \tag{4.7}$$

where the coefficients are given in table 4.1. The notation here is according to [213]. Note that C_3 is the same as C_{s} presented in equation 4.5. Evidently, there is a large variation in the dependence of ω for the different aberrations. Modern high-resolution instruments are equipped with an aberration corrector which compensate the error introduced in the previous lenses up to a certain order [214]. In the present work, the high-resolution work conducted on the JEOL ARM-200CF is corrected for aberrations up to the 4$^{\mathrm{th}}$ order. Further explanations regarding aberrations can be found in the book by R. Erni [210].

4.2.3 Sample preparation

Samples for TEM needs to be "sufficiently thin" in order to let electrons traverse through the specimen. The required thickness depends on the intent of the study, but is generally in the range of 20-100 nm. Specimens for TEM, in this work, were mechanically ground to a thickness of $\sim$100 μm before they were electropolished at temperatures between -20 and -30 °C at a potential of 20 V, in an electrolyte

Table 4.1: Overview of the aberration coefficients up to the 4th order. Adapted from [210].

Symbol	Aberration
A_0	Beam shift
C_1	Defocus
A_1	Twofold astigmatism
B_2	Second-order axial coma
A_2	Threefold astigmatism
C_3	Third-order spherical aberration
S_3	Third-order star aberration
A_3	Fourfold astigmatism

made by 1/3 nitric acid (HNO_3) and 2/3 methanol (CH_3OH). This is, by far, the most common method to prepare Al thin foils as it provides many samples with relatively good quality in very little time. A limitation is that it is an aggressive electrochemical method, which may introduce unwanted effects. Particularly, selective dissolution of bulk precipitates and grain boundary particles, which is shown in figure 4.4, frequently occurs. In such cases, one simply finds another region unaffected by the electrolyte to study.

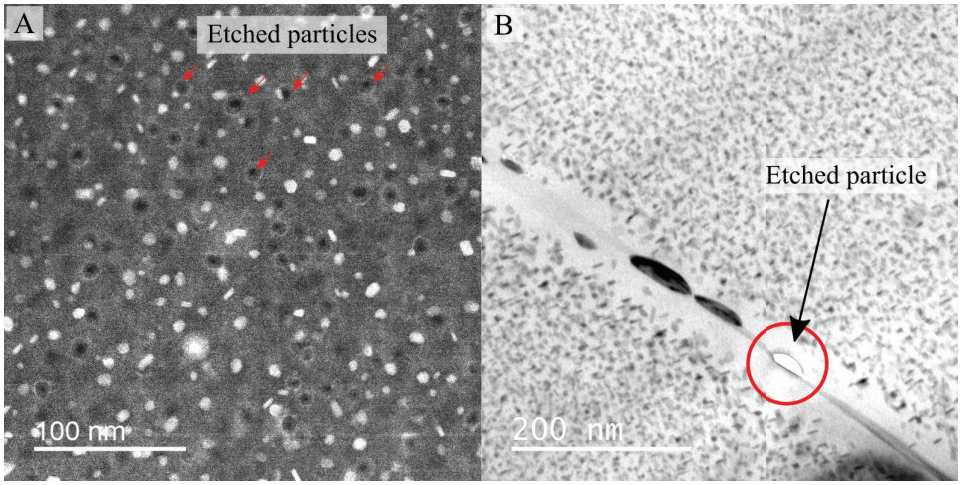

Figure 4.4: **A** HAADF-STEM image of a typical microstructure where large amounts of precipitates have been etched. **B** is a BF-STEM image showing a grain boundary particle which has been "dropped" due to selective etching. Both images are from an 7xxx Al alloy showing Mg-Zn type particles.

During the preparation of Paper **IV**, we observed that a Cu-free (< 0.01 at.%) alloy could form a small (1-2 nm) thick layer on the surface of the TEM specimen

during electropolishing, which consists of either Cu oxide and/or a Al-Cu phase. This gives an unwanted effect in the diffraction patterns. We also recognised the same layer in a large number of samples with different composition that were prepared similarly. An example of this is found in the supplementary to Paper **IV** in Appendix C. We suspect the reason for the unwanted layer to be either due to a 'dirty' electrolyte or that it forms due to the small amount of Cu in the alloy. This is investigated further in an ongoing study where more surface sensitive techniques (XPS, SIMS, AES) are applied. A similar layer has been reported by Wang *et al.* [215].

Some samples were subsequently subjected to a final Ar ion-thinning stage using a precision ion polishing system (PIPS) II instrument from Gatan. These samples were milled at 4 kV until changes in the TEM specimen were observed. Following this, a stepwise reduction in potential to 1 kV was conducted as a final polishing stage. Typical milling angles were $\pm 4^{\circ}$. No significant differences compared to the electropolished samples were observed.

Prior to all STEM work, the samples were plasma cleaned for 3 minutes in a Fischione 1020 plasma cleaner. This routine was found to significantly reduce buildup of carbon contamination during analysis.

4.2.4 Experimental challenges

The most common challenges encountered when working with STEM are sample contamination, beam damage, sample drift, scan noise and errors related to sample preparation. An example of scan noise likely due to magnetic disturbance is shown in figure 4.5**A**. In this case the microscope has been aligned to resolve the Al lattice along the $\langle 112 \rangle_{\mathrm{Al}}$ direction, but the two sudden distortions have ruined the image. In this case the only option is to try again and hope that the particle has not taken any beam damage and that no contamination has built up during the first scan. In figure 4.5**B**, a dispersoid particle has been imaged and analysed using EDS on multiple locations. The dark regions found all over the sample are carbon contamination formed during this analysis.

Drift problems usually occur when changing samples and/or moving across the specimen quickly. The easiest way to overcome the problem is to let the microscope stabilise. Another option frequently used in this thesis, is to record several ($\sim$20) images with low pixel dwell time, and thereafter align them to correct for the rigid and non-rigid distortions. This is implemented in the Smart Align software developed by L. Jones [216]. In the case of EDS mapping for several hours, most commercial packages have implemented a drift correction routine.

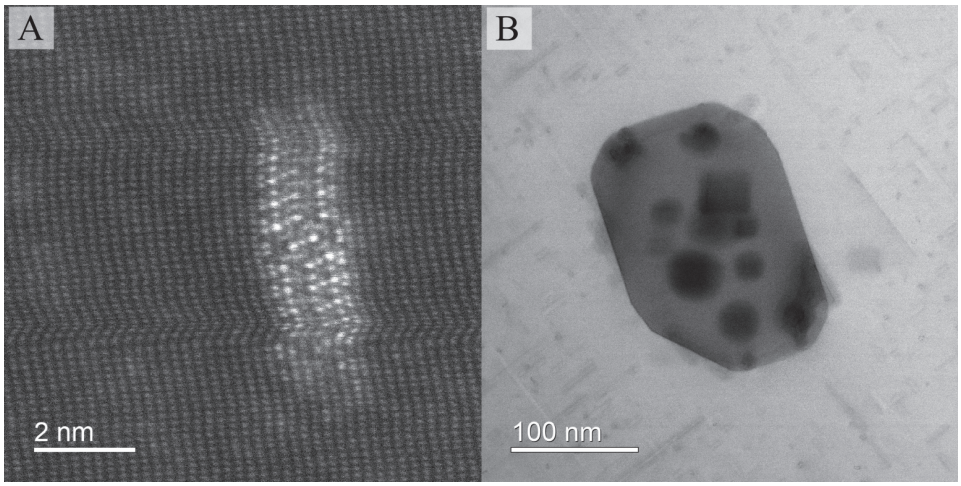

Figure 4.5: Example of scan noise in a high-resolution HAADF-STEM image in **A** and a BF-STEM image in **B**, with carbon contaminated regions on the particle.

4.3 Energy dispersive X-ray spectroscopy

X-rays are generated by the sample as illustrated in figure 4.1, and can be detected to provide chemical information about the sample. Electrons situated in different shells labelled K, L, M and N can be emitted if an incoming electron interacts with the core electron inelastically. An electron in a higher energy shell will relax to the lower energy shell, and in this process release an X-ray with energy according to difference between the two shells, as schematically illustrated in figure 4.6. The transitions are labelled according to the initial shell and the final shell. Alternatively, it may release an Auger electron. The ratio between generating an X-ray or Auger electrons is called the *fluorescence yield*, and for low Z elements the chance to release an Auger electron is higher [205].

The generated X-rays are recorded by a silicon drift detector together with the background Bremsstrahlung. The X-rays generate electron-hole pairs, which are assigned to specific energy channels. As depicted in figure 4.1, X-rays are generated in all direction. However, the detector is not a spherical shell recording all the emitted X-rays, but rather a small area with area described by the collection angle, Ω, which is dependent on the detector distance from the sample, active area of the detector and the angle between the specimen and the detector. Other artefacts includes X-ray absorption which is explained elsewhere [205].

When working with polycrystalline materials, one often needs to align the specimen to certain orientations prior to conducting the EDS scan. This may result in

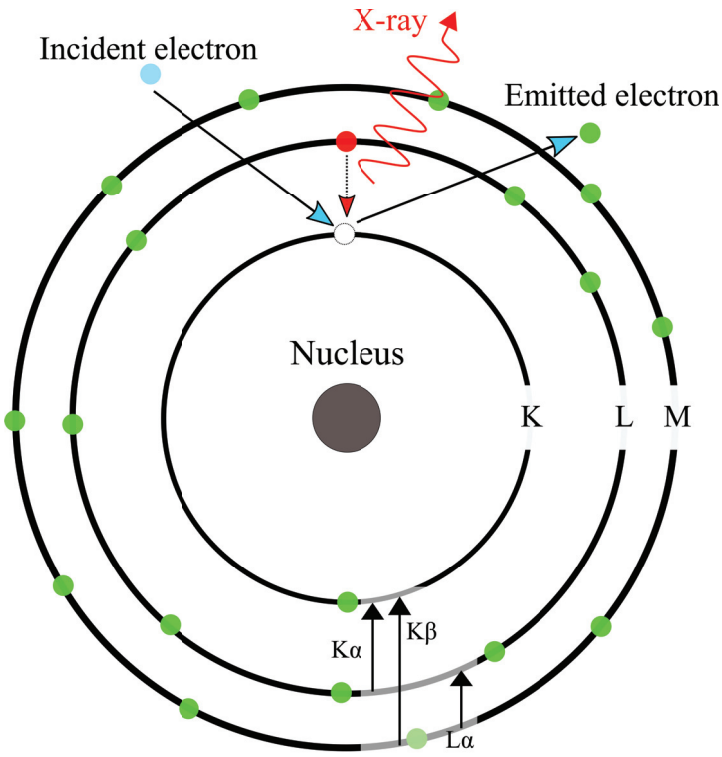

Figure 4.6: Schematic illustration of how a characteristic X-ray is generated. An incident electron excites a ground state electron, resulting in the relaxation of a higher energy electron situated in another shell. This relaxation process will release the characteristic X-ray with energy difference according to the difference between the shells.

the sample holder itself shading parts of the active area of the detector, resulting in a significant decrease in the measured intensity. This can be avoided by tilting the specimen towards the detector (if possible). The shadowing angle for the two microscopes used in this thesis has been measured to $+4.3$ and $+13.0$, for the 2100F and ARM, respectively [217].

The detected electrons are further quantified using pre-calibrated correction factors. This is almost exclusively done using the Cliff-Lorimer method [218], which relates the intensity of two X-ray energies through a sensitivity factor (k-factor). This is expressed as:

$$\frac{C_A}{C_B} = k_{AB}\frac{I_A}{I_B}, \tag{4.8}$$

where C_i is the composition of X-ray line i and I_i is the recorded intensity. The k-factor can be determined using a specimen with known composition or, as is most common, determined theoretically according to:

$$k_{AB} = \frac{Q_B \omega_B a_B \varepsilon_B M_A}{Q_A \omega_A a_A \varepsilon_A M_B}. \tag{4.9}$$

The terms Q, ω, a, ε and M in equation 4.9 are the ionisation cross-section, fluorescence yield, line weight (line transition probability), detector efficiency and atomic weight, respectively [205]. In this work, such pre-determined factors are used which are obtained from the supplier. More sophisticated quantification routines exists [219], but are difficult to practically implement in non-model systems.

In order to obtain an EDS spectra, one needs sufficient counts, i.e. there is a trade-off between specimen thickness, count and scan time. A thicker specimen will naturally result in more absorption effects. In addition, it will also increase the width of the probed region due to *beam broadening*. This theory usually assumes that the beam broadens according to a 2D Gaussian through the thickness of the specimen [220]. It was recently reviewed by J. D. Robson, who reported that a large probe size may result in an erroneous shape and in measured composition of segregated layers on the grain boundaries [221]. This of course depends on the width and composition of the segregated layer, in addition to the thickness of the specimen. As only the thickness in each pixel is required, this correction can be implemented in a system recording both the EDS and electron energy-loss spectroscopy (EELS) signal at the same time.

Most of the data in this work was acquired using a probe size of 1 nm, with a sampling rate close to 1:1, or slight oversampling. This means that the probe size has the same size as each pixel. The grain boundaries were typically found close to the center hole of the specimen, where the sample is at its thinnest. Grain boundaries were oriented parallel to the electron beam and the scan time varied according to the count rate and the resolution of the scan. In all cases, the EDS data had to be evaluated individually. A typical scan lasted from 2-4 hours.

4.4 Data analysis

The EDS data acquired in this thesis was post-processed using the open-source python package HyperSpy [222]. A least-square fitting procedure of the EDS spectra was performed for every pixel using a 6^{th} order polynomial as background and Gaussian peaks for each characteristic X-ray peak.

A simple methodology was developed for more statistically determining the con-

centration across the grain boundary. This is done by acquiring an EDS map across a grain boundary with (*n,m*) pixels. From this, a total of *m* linescans can be generated. These individual linescans are then represented as a single linescan using the mean value and corresponding standard error, for each element, at each position, *n*, across the grain boundary. Additionally, by inspecting the intensity of different elements, the larger GB particles and dispersoids can be masked using a threshold based on their intensity, enabling line profiles of elemental concentration only of the PFZ to be created. In some cases, this method is also applicable to the matrix composition, but the matrix precipitates cannot be removed unless they are sufficiently large, and even if they are large, beam broadening may still give contribution from the particles.

4.5 Scanning electron microscopy

The SEM is a separate microscope which has similar beam-forming optical system as the one previously introduced for the STEM system (without aberration corrector). The major differences are the use of a lower acceleration potential (1-20 kV) and that larger samples may be studied in the SEM. The detectors are placed above the sample to detect electrons emerging from the surface of the specimen after interacting with it, as illustrated in figure 4.1.

The backscattered electron (BSE) signal is caused by elastic scattering of the incident electrons with the atomic nucleus in the specimen. Different elements in the specimen will interact differently due to their nuclei sizes and thus BSE is commonly used as a way of imaging variations in composition [223]. The detector for this is typically placed directly above the sample. If the incident beam interacts inelastically with the specimen, it may knock a core electron out of it shell which generates a lower energy secondary electron (SE). These are attracted to a positively charged Faraday cage where a scintillator is placed within (Everhart-Thornley detector). The SE typically only originates close to the surface due to their low energy, and thus give topological information about the specimen.

4.5.1 Electron backscatter diffraction

The electron backscatter diffraction (EBSD) method is a routine characterisation technique, conducted in the SEM, which utilises the backscattered electrons that are diffracted due to the crystals' orientation. A phosphor screen is used as the detector, where diffraction patterns (Kikuchi patterns) are recorded for each scan pixel. The recorded patterns are subsequently indexed according to simulated patterns and the data can be post-processed to give a range of different information. The post-processing in this work was performed in MATLAB using the plugin MTEX [224]. This allows for texture analysis in polycrystalline material which

gives information with regards to grain orientation, phase orientation/distribution and grain boundary properties. EBSD provides the statistical understanding which is typically not acquired in the TEM. A detailed explanation of EBSD can be found in the book by Schwartz *et al.* [225].

4.6 Corrosion testing

Intergranular corrosion

The testing of IGC, included in Papers **I**, **II** and **III**, is based on the standard: ISO 11846 Method B. This involves a surface pre-treatment (degreasing in acetone ($(CH_3)_2CO$) and etching in 7.5 wt.% sodium hydroxide (NaOH) solution at 50-60 °C for 2.5 min, rinsing and desmutting in 68% concentrated nitric acid (HNO_3) for 2 min) before immersion in an aqueous solution containing 30 g/l sodium chloride (NaCl) and 10 ml/l concentrated hydrochloric acid (HCl) for 24 hours. Some modifications were applied in this work. In Paper **I**, the immersion time in the solution was varied from 1 to 120 hours to see how the corrosion process developed. In Paper **II**, the sample was exposed for only 2 hours in order to be able to conduct the study. In Paper **III**, the standard was followed. The author did not conduct the IGC testing in any of these works.

Stress corrosion cracking

The SCC properties in Paper **VI** were studied using double cantilever beam (DCB) and slow strain rate testing (SSRT). DCB test were based on the method described by M. V. Hyatt with specimen geometry shown in figure 4.7 [226]. Some modifications were applied. The V-notch was removed by spark erosion as it was suggested this was a better approach to measure the desired properties. Some samples were additionally fatigue pre-cracked, while others were not. This had no effect on the measured properties. The crack tip stress intensity was calculated using the formula:

$$K_{\mathrm{i}} = \frac{\Delta E h[3h(a+0.6h)^2 + h^3]^{1/3}}{4[(a+0.6h)^3 + h^2 a]} \tag{4.10}$$

where Δ, E, h, and a are the deflection at the load point, elastic modulus (70 GPa), half the specimen height and the crack length measured from the load point, respectively. An initial stress intensity of 25 MPa$\sqrt{\mathrm{m}}$ was used, as chosen based on previous experiences testing similar alloys. The crack tip was kept wet by dripping 3.5 wt.% NaCl solution, for a total duration of 1500 h. The crack evolution was monitored using an optical microscope. In order to study the fracture surfaces, specimens were cooled with liquid nitrogen and pulled apart by a tensile machine.

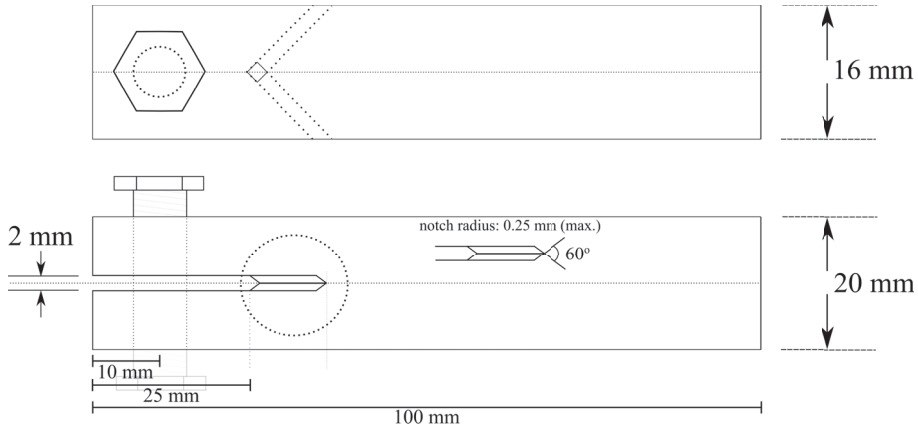

Figure 4.7: Schematic drawing of the DCB specimens used in this work.

SSRT experiments were conducted on samples machined according to figure 4.8 on a Cormet C-176 SSRT machine, shown in figure 4.9. In the latter figure, a sample is mounted in the liquid cell.

Samples were washed in ethanol in an ultrasonic bath for 2.5 minutes prior to testing. Test environments were air and 3.5 wt.% NaCl solution with neutral pH and pH 3. An initial strain rate of 1.2×10^{-8} ms^{-1} was applied in all cases. Plastic insulators were mounted between the clamps and the sample in order to prevent galvanic effects when testing in solution. The pH and open circuit potential were measured during and after each test. The fracture surfaces were observed in SEM and from such micrographs the reduction in area (RA) was estimated. The reduction in area ratio (RRA) was used as a measure deduce susceptibility to the environment. One tensile test for each temper in each environment was conducted.

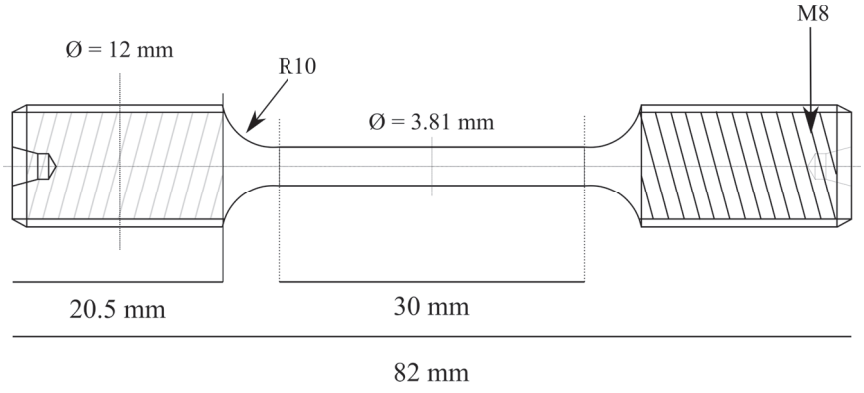

Figure 4.8: Schematic drawing of the SSRT specimens used in this work.

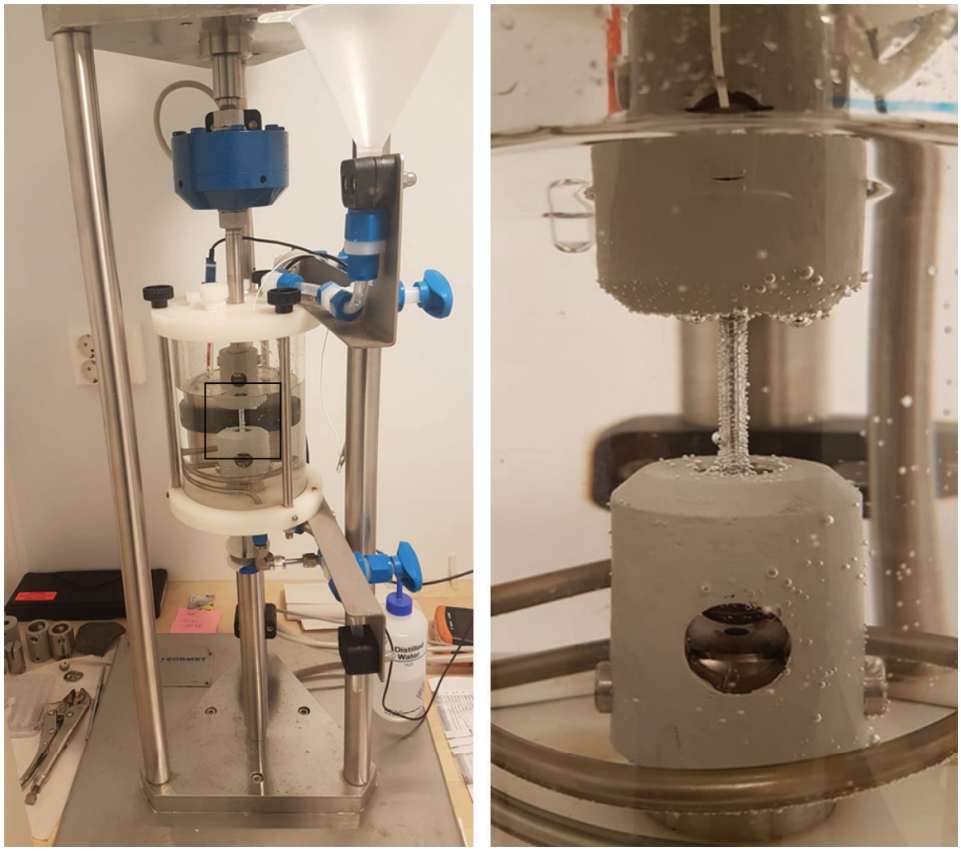

Figure 4.9: Images of the SSRT testing jig. A sample is mounted in the liquid cell, which is filled with the test solution (3.5 wt.% NaCl, pH $\approx$ 6.7).

Part II

Results

Chapter 5

Research Papers

I Influence of α-Al(Fe,Mn,Cu)Si phase particles on intergranular corrosion of extruded AA6005 aluminium alloy
A. Lervik, T. Danbolt, T. Furu, R. Holmestad & O. Lunder

Earlier works by our group have demonstrated that the α-Al(Fe,Mn,Cu)Si particles have clear influence on the IGC properties [135, 139, 140]. In this work, we further investigate how these particles affect IGC by comparing two alloys: one with- and one without the presence α-particles. The results demonstrate that the initial cathodic activity in the alloy is controlled by the presence of α-phase particles on the surface. Their importance as external cathodes for the propagation of IGC is gradually reduced as the particles dissolve in the IGC test solution. With increasing time of immersion, the cathodic activity increases considerably due to surface segregation of Cu, which becomes the dominating external cathode, regardless of the alloy. Removing the α-particles also demonstrates a delayed initiation of IGC, when testing according to the ISO standard. From a practical point of view, producing alloys without Fe and Mn is not feasible as (at least) Fe will be present in the primary alloy. It is more likely that a surface etch procedure to remove the surface particles could be relevant to IGC exposed components. The results are relevant to alloys forming similar primary particles.

O. Lunder and T. Furu suggested the study. T. Danbolt conducted the IGC tests and EBSD measurements. A. Lervik conducted all TEM experiments, analysed the EBSD data, acquired the SEM data and verified the IGC penetration depth. R. Holmestad supervised A. Lervik in the analysis. O. Lunder contributed significantly in interpreting the results. A. Lervik prepared all figures in the manuscript and wrote the manuscript with comments from all co-authors.

II Grain boundary structures and their correlation with intergranular corrosion in an extruded Al-Mg-Si-Cu alloy

A. Lervik, S. Wenner, O. Lunder, C. D. Marioara, & R. Holmestad

The motivation behind this work was to statistically correlate IGC properties with an understanding of the different grain boundary types that are present in the microstructure. Much of the work in literature assessing IGC presents only very limited descriptions regarding the nature of susceptible grain boundaries and often lacks statistics. In order to start a more statistical approach, we chose to investigate a highly textured Al-Mg-Si alloy along its extrusion direction, where the grains adapt predominantly two orientations. From the EBSD data we describe and characterise three main types of grain boundaries in addition to the very low-angle sub-grain boundaries. The corrosion data, based on 1396 grain boundaries, show that there is a preference for IGC to occur at the high-angle grain boundaries regardless of the adjacent grain's orientation. Grain boundaries with both grains oriented along $[100]_{Al}$ have a slightly lower fraction of corroded grain boundaries. We suspect the reason for this is related to a higher fraction of Q′-phase particles present at these grain boundaries. The particle densities along grain boundaries of the same type varies, most likely due to different interface termination planes and growth direction. The article demonstrates a statistical way in representing grain boundaries through the axis-angle rotation pairs, which should be implemented in future work.

C. D. Marioara and O. Lunder suggested the study. S. Wenner and O. Lunder conducted the corrosion tests. S. Wenner performed the EBSD measurements and developed the analysis of corroded grain boundaries. A. Lervik conducted all TEM experiments and performed the texture analysis from the EBSD data. R. Holmestad and C. D. Marioara supervised A. Lervik in the analysis. A. Lervik prepared all figures in the manuscript and wrote the manuscript with comments from all co-authors.

III The correlation between intergranular corrosion resistance and copper content in the precipitate microstructure in an AA6005A alloy

C. D. Marioara, A. Lervik, J. Grønvold, O. Lunder, S. Wenner, T. Furu & R. Holmestad

This work investigate ways to achieve reduced IGC susceptibility in the AA6005 alloy. It was observed that different combinations of cooling rates from SHT and artificial ageing temperatures resulted in similar Vickers hardness (HV) values, but different IGC properties. This is attributed to a change in the hardening pre-

cipitate phase(s), which incorporates large amounts of Cu, leaving less Cu in solid solution which otherwise might have segregated to grain boundaries. Introducing dislocations by a pre-deformation step (rolling), prior to artificial ageing, provides preferential nucleation sites for Cu-containing particles. These findings demonstrate possibilities to modify processing routes in order to produce Cu-containing Al-Mg-Si alloys with improved corrosion resistance.

C. D. Marioara and O. Lunder suggested the study. C. D. Marioara conducted the TEM experiments and finalised the paper with comments from all co-authors. J. Grønvold and S. Wenner conducted the work related to the deformed material, supervised by T. Furu and O. Lunder. A. Lervik analysed all EDS data with supervision from C. D. Marioara and R. Holmestad, and acquired EDS data from the deformed material. A. Lervik assisted in writing the draft of the article.

IV Atomic structure of solute clusters in Al-Zn-Mg alloys

A. Lervik, E. Thronsen, J. Friis, C. D. Marioara, S. Wenner, A. Bendo, K. Matsuda, S. J. Andersen & R. Holmestad

It is well known that Al alloys undergo natural ageing (NA) when left at room temperature. When Al-Mg-Zn alloys are naturally aged, or aged for shorter periods, very small ordered structures (clusters) in the bulk material can be observed by STEM imaging. After nearly two years of analysis, we demonstrate that the solute-rich clusters (also known as GP(I)-zones) adapt a novel type of cluster unit of high Zn/Mg ratio. This unit can be viewed as a partial substitution by Mg and Zn on an Al fcc unit cell and on its surrounding truncated cube octahedral shell. This is the fundamental unit found in all the larger cluster configurations observed, which connects via three different directions. The composition of these clusters was also measured using atom probe tomography and the stability of clusters assessed by density functional theory calculations. Nanobeam diffraction simulations of suggested structures match with what is obtained experimentally. This work provides new insights into a nearly 100 year old mystery regarding the structure of these clusters. We believe our results to be significant in further understanding and optimising age hardenable Al-Zn-Mg alloys. We also suspect the finding to be relevant to other Al alloy series which undergoes NA, such as Al-Cu (2xxx) and Al-Mg-Si (6xxx).

A. Lervik conducted the STEM experiments and wrote the initial draft. E. Thronsen assisted significantly in writing the initial draft and conducted the diffraction and image simulations. A. Bendo and K. Matsuda initiated the study and provided the lab cast alloy. J. Friis prepared the atomic models and conducted the dens-

ity functional theory (DFT) calculations. S. Wenner conducted the APT measurements. S. J. Andersen analysed the STEM data, deduced the structure of the clusters and assisted in writing the draft. C. D. Marioara analysed the STEM data and commented on the initial draft. R. Holmestad and S. J. Andersen supervised the study. All authors commented on the final manuscript.

V Precipitation in an extruded AA7003 aluminium alloy: Observations of 6xxx-type hardening phases

A. Lervik, C. D. Marioara, M. Kadanik, J. C Walmsley, B. Milkereit & R. Holmestad

This work studies a commercial Al-Mg-Zn alloy provided by Benteler Automotive AS. The motivation was to investigate microstructural differences caused by: i) difference in quench rate from SHT and ii) the artificial ageing parameters (T6 or T7). These conditions had different SCC properties based on an internal, non-standard test conducted by Benteler. Using the novel cooling differential scanning calorimetry (DSC) method (B. Milkereit and M. Kadanik) [20], we could assess whether quench-induced precipitation would occur over a range of different cooling rates. Studying the air-cooled material in TEM (in T4, T6 and T7) demonstrates clear heterogeneous nucleation of $MgZn_2$ and Mg_2Si phases at grain boundaries and primary/dispersoid particles. These findings are correlated with the DSC data. The hardening precipitate behaviour was further studied using HAADF-STEM. The important findings made are: i) the orientation (with respect to Al matrix) and size of hardening precipitates are different in the T6 and T7 temper. ii) When the material was water-quenched and aged to T7 (ageing at 170 °C), the formation of hardening phases commonly found in the Al-Mg-Si system was observed, even though the alloy contains very little Si (0.11 at.%). Both findings are important for the fundamental understanding of mechanical properties in such alloys. The latter finding is interesting as more and more recycled materials are used. The Si content in Al-Zn-Mg alloys might potentially be exploited in precipitation hardening, if one is able to optimise the thermo-mechanical treatment. The findings here make the foundation for Paper **VI**, where we investigate SCC properties.

A significant effort in order to deduce the interface structure of the η_1 hardening precipitate, which accounted for 50% of the phase fraction in the T7 tempers, was conducted. This work is yet too be concluded and has been extended in collaboration with Prof. Yong Jiang (CSU, China). It is particularly interesting whether this particle has the possibility to trap hydrogen at its interface in larger fractions than those particles found in the T6 temper. A poster regarding the interface structure

is attached in Appendix A of this thesis, for the interested reader.

A. Lervik conceptualised the study and suggested the collaboration with B. Milkereit and M. Kadanik, who conducted the DSC experiments. A. Lervik conducted all TEM experiments, analysed the data and prepared the figures. DSC results were interpreted by B. Milkereit and A. Lervik. C. D. Marioara, J. C. Walmsley and R. Holmestad assisted in interpreting the TEM data. A. Lervik wrote the manuscript with input from all co-authors.

VI Stress corrosion cracking in an extruded Cu-free Al-Zn-Mg alloy

A. Lervik, J. C. Walmsley, L. Lodgaard, C. D. Marioara, R. Johnsen, O. Lunder & R. Holmestad

Based on the findings in Paper **V**, two alloys with slightly different Si contents were extruded, and heat treated in a similar manner as before. Ideally, we wanted to use, and did order and prepare, a completely Si-free model alloy from a third party supplier. However, this material had a completely different grain structure (likely due to the lack of TiB grain refiner in their casting procedure) and thus different tensile properties than the industrial alloy. As such, this material could not be used in the study. The other materials were machined into specimens for both double cantilever beam (DCB) and slow strain rate tensile (SSRT) tests in order to assess the SCC properties. The DCB results establish a difference between the T6 and T7 tempers, and a subtle difference between water- and air-cooling. SSRT demonstrates a difference in the ratio in area reduction (RRA) when comparing a specimen elongated in air and in test solution. The T6 tempers additionally have presence of secondary cracks in the fracture surface, which may penetrate deep along the tensile axis. Such observations were not made in the T7 tempers.

Except for the difference in bulk hardening precipitates (cf. Paper **V**), there is no other significant difference in the microstructure which can be correlated with the measured SCC results. We suspect that the difference in precipitate microstructure may affect the slip characteristics and strain localised at grain boundaries during deformation. Consequently, the reduced stress concentration may limit the cracking process at the crack tip. This fits qualitatively with an increased SCC threshold intensity measured for the T7 tempers. In addition, the change in bulk microstructure may also impact hydrogen partitioning in the microstructure, which agrees with some of the recent work in literature. The work provides a deep understanding of the material's microstructure, and some interesting corrosion features were observed, but we were not able to fully understand the SCC properties in the selected material.

L. Lodgaard and A. Lervik initiated the study. A. Lervik conduct all experiments, analysed all the data, prepared all figures and wrote the initial draft of the manuscript. O. Lunder assisted in preparing the DCB samples and in analysing the DCB results. R. Johnsen supervised and analysed the SSRT experiments. R. Holmestad, C. D. Marioara and J. C. Walmsley assisted in analysing the data.

Paper I

Influence of α-Al(Fe,Mn,Cu)Si phase particles on intergranular corrosion of extruded AA6005 aluminium alloy

Adrian Lervik, Turid Danbolt, Trond Furu, Randi Holmestad, Otto Lunder

To be submitted

Influence of α-Al(Fe,Mn,Cu)Si phase particles on intergranular corrosion in extruded AA6005 aluminium alloy

A. Lervik[a,*], T. Danbolt[b], T. Furu[c,b], R. Holmestad[a], O. Lunder[d,b]

[a] *Department of Physics, Norwegian University of Science and Technology (NTNU), N-7491 Trondheim, Norway*
[b] *Department of Materials Science and Engineering, Norwegian University of Science and Technology (NTNU), N-7491 Trondheim, Norway*
[c] *Norsk Hydro ASA, Oslo, Norway*
[d] *SINTEF Industry, N-7465, Trondheim, Norway*

Abstract

The effect of α-Al(Fe,Mn,Cu)Si particles on intergranular corrosion (IGC) behaviour in an extruded Al-Mg-Si-Cu alloy is investigated by comparing a model alloy without Fe and Mn additions to a commercial AA6005 alloy. Both alloys were IGC tested for 1 to 120 h. Microstructures were studied using scanning- and transmission electron microscopy, and electron backscattered diffraction. The presence of α-Al(Fe,Mn,Cu)Si particles yields significantly more uniform IGC attacks and higher corrosion rates. The maximum depth of IGC attacks becomes similar after ∼20 h exposure. This is attributed to formation of Cu-rich particles along the corroded grain boundaries, which catalyses the cathodic reaction.

Keywords: Aluminium alloys, Intergranular corrosion, Electron microscopy, Grain boundaries, Microstructure,

1. Introduction

Extruded 6xxx series (Al-Mg-Si-(Cu)) aluminium alloys are extensively used in transportation industry due to their favorable properties such as high strength to weight ratio, extrudability and formability [1, 2]. These alloys achieve a significant hardness increase from heat treatments (artificial ageing) due to the formation of nanoscale semi-coherent and metastable precipitates. At maximum hardness the needle shaped β″-$Al_2Mg_5Si_4$ precipitate, growing along the $\langle 100 \rangle_{Al}$ directions, is present in high number densities [3–5]. Small additions of Cu is known to have effects on the age hardening response and the achievable strength [6–13]. Cu additions will also alter the metastable precipitate phases which form and develop during the artificial ageing stage [5, 13, 14]. With prolonged ageing, Cu incorporates into the nanoscale precipitates and develops them to Q′– ($Al_6Mg_6Si_7Cu_2$) [15], or other hybrid structures [5, 13, 16].

A limiting factor with these alloys which prevents usage in many applications is susceptibility to Intergranular Corrosion (IGC). IGC observed in Cu-containing Al-Mg-Si alloys with balanced Mg/Si ratio is believed to be associated with continuously segregated Cu along the grain boundaries, surrounding solute depleted zones and the presence of grain boundary particles [16–23]. Electrochemical properties and IGC susceptibility have been studied for numerous alloy compositions with different applied thermo-mechanical treatments [16, 17, 20, 21, 24–29]. In general, IGC is mostly present in under- and peak-aged tempers, while the over-aged temper is usually dominated by pitting corrosion. However, large variations are reported due to different alloy compositions in addition to variations in quenching- and artificial ageing conditions.

Large primary α-Al(Fe,Mn,Cu)Si phase particles are formed during casting and/or homogenisation through the β to α transformation [30–32], and have effect on the recrystallisation of new grains in the extruded profile after exiting the die. Smaller (<0.3 μm) α-Al(Fe,Mn,Cu)Si dispersoids are also formed at these stages by preferential nucleation on the β′ particles [33–36]. Larsen et al. demonstrated that removing such particles from the surface, by etching in fluonitric acid, resulted in significantly less IGC than in the case where the particles were still present on the

*Corresponding author at: Department of Physics, Norwegian University of Science and Technology (NTNU), N-7491 Trondheim, Norway
Email address: adrian.lervik@ntnu.no (A. Lervik)

surface [19]. It was demonstrated by Kumari et al. that IGC in an AA6005 alloy initiated at the α-Al(Fe,Mn,Cu)Si-phase particles at the surface [23]. The α-Al(Fe,Mn,Cu)Si phase dissolved rapidly in an acidified NaCl solution commonly used in assessing IGC susceptibility [23, 37]. Due to selective corrosion, Cu was found to enrich on the outer surfaces causing increased cathodic activity with the time of immersion [23]. Selective dissolution where the nobler element remains has been reported in other Cu containing intermetallic particles [38–42], and in other phases found in aluminium alloys [41, 43–46].

The purpose of this work is to further elucidate the role of α-Al(Fe,Mn,Cu)Si particles in the initiation and propagation of IGC. This is done by comparing AA6005 alloys with and without Fe and Mn additions, wherein the latter no α-Al(Fe,Mn,Cu)Si particles are present.

2. Material and methods

2.1. Material

Two variants of the AA6005 alloy were used in this study. A 'model alloy' without Mn and Fe addition was provided by American Elements, while the reference alloy is a commercial alloy provided by Hydro (further referred to as 'AA6005'). The composition of the two alloys is given in table 1. Note that the Si content in the model alloy is slightly lower in order to compensate for the Si which normally would be incorporated into the α-Al(Fe,Mn,Cu)Si primary constituents. The Si content was calculated using the Alstruc homogenization model [47].

The model alloy was homogenised at 550 °C for 30 min and water quenched, before being pre-heated to 480 °C and extruded into profiles with 3 mm thickness and 65 mm width at a ram speed of 5 mm/s. The extruded profile was subsequently water quenched. Artificial ageing was performed in a Nabertherm N15/65 air circulation furnace at 185 °C for 5 h to reach peak hardness. The AA6005 alloy was produced in a similar manner with the only difference being that the homogenization was conducted at 585 °C for 2.5 h due to a larger billet size.

Table 1: Alloy composition of the investigated alloys in at.% measured using optical emission spectroscopy.

	Cu	Fe	Mg	Mn	Si	Al
AA6005	0.06	0.09	0.63	0.07	0.61	Bal.
Model alloy	0.05	0.01	0.59	<0.01	0.56	Bal.

2.2. Corrosion testing

Three samples with an exposed area of 20x30 mm^2 were tested using the accelerated corrosion test ISO 11846 Method B. Before IGC testing, the samples were degreased in acetone and etched in 7.5 wt.% NaOH solution at 50-60 °C for 2.5 min, rinsed and desmutted in 68% concentrated HNO_3 for 2 min, then rinsed again in distilled water and air-dried. IGC testing was performed by immersing in a solution of 10 ml/l HCl and 30 g/l NaCl (further referred to as test solution), with ratio of 5 ml solution per cm^2 sample area. Immersion times were varied from 1 h to 120 h. Corrosion products were subsequently removed in concentrated HNO_3 solution. Samples were weighed before and after the accelerated test. The visible results from the corrosion tests were examined on cross-sections parallel to the extrusion direction using optical microscopy and on the corroded surfaces using Scanning Electron Microscopy (SEM).

Cathodic polarisation curves were acquired in the ISO 11846 test solution. Samples were pre-exposed for 5 min or 5 h in the solution prior to polarisation at a sweep rate of 1 mV/s, starting at the open circuit potential.

2.3. Electron Microscopy

Samples for SEM were initially ground using SiC abrasive paper down to 4000 grit. Subsequent polishing was done using 1 and 0.25 μm diamond spray and for Electron Backscatter Diffraction (EBSD) the samples were vibropolished as the final step. EBSD was performed on a Hitatchi SU-6600 FEG-SEM at 20 kV. Nordif3.0 was used to index the acquired patterns and the data were subsequently processed in MTEX [48]. Backscattered electron (BSE)-SEM images were acquired on a Zeiss Supra 55-VP FEG-SEM at 10 kV.

Transmission Electron Microscopy (TEM) specimens were prepared by grinding bulk specimens with SiC abrasive paper to ~100 μm thickness, punched into 3 mm discs and thereafter electropolished in an electrolyte consisting of 1/3 HNO_3 and 2/3 CH_3OH at temperatures between -30 and -20 °C at 20 V. Two TEM instruments were used in this study. A Cs-corrected JEOL ARM200CF operated at 200 kV with convergence semi-angle of 28 mrad and 35 mrad inner collector angle was used for high-resolution High-Angle Annular Dark Field (HAADF)-Scanning Transmission Electron Microscopy (STEM). A JEOL JEM-2100F operated at 200 kV in analytical STEM mode with a 1.0 nm probe size equipped with an Oxford X-max 80 detector with a solid angle of 0.23 sr for Energy-Dispersive X-ray Spectroscopy (EDS). Some high-resolution STEM images were acquired using Smart Align [49].

3. Results

3.1. Microstructure

Figure 1 shows representative BSE-SEM images of the microstructure in both alloys, acquired with the same magnification and experimental conditions. In the AA6005 alloy in figure 1**A**, there are particles present with an area coverage of ~0.65% composed of Al, Fe, Mn, Cu and Si as determined by EDS. These are the Fe-rich α-Al(Fe,Mn,Cu)Si primary constituents. In the model alloy shown in figure 1**B**, only a limited amount of particles are present. The few bright regions present are undissolved Si-rich Mg-Si eutectic phases.

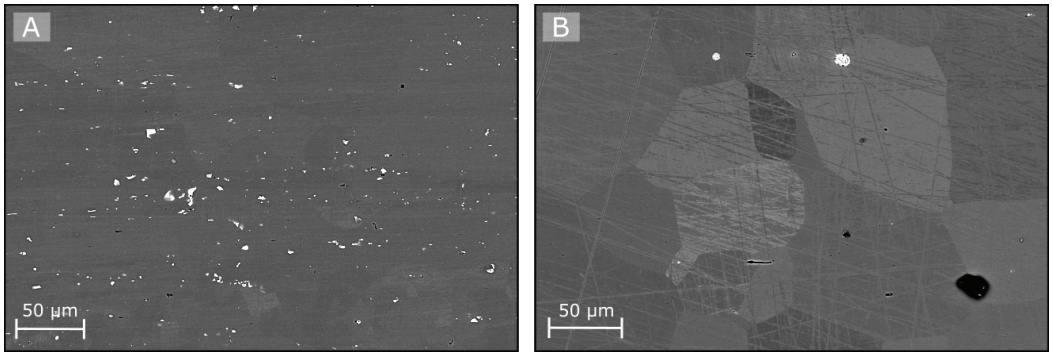

Figure 1: BSE-SEM images acquired at similar magnification for the AA6005 alloy in **A** and the model alloy in **B**.

EBSD was performed on the cross-section of the material covering a region from the surface and into the material as shown for the AA6005 and the model alloy in figures 2**A** and 2**B**, respectively. The grains are colour coded according the inverse pole figure shown in figure 2**B** and the grain boundaries according to their misorientation angle. A surface layer with larger grains extending approximately 450 μm into the material, where it reaches the interior composed of smaller grains, can be seen in the AA6005 alloy. Figures 2**C** and 2**D** show the normalised grain boundary misorientation angle from the surface (450 μm) and in the interior, for the AA6005 and model alloy, respectively. The fraction of high angle grain boundaries is greater in the surface layer. The distribution is compatible in both alloys. Due to the absence of grain controlling particles, the texture is slightly different as the model alloy exhibits larger grains and a more uniform distribution from the surface into the bulk, as demonstrated by figures 1 and 2.

Precipitate microstructures are similar for the two alloys as shown in figure 3 where a Bright Field (BF)-TEM image and typical precipitate microstructures obtained from HAADF-STEM are demonstrated. Precipitates are mostly β″ precipitates with some Cu inclusions, both in the precipitate and on its interface. This is deduced based on the high Z-contrast of the Cu containing atomic columns and the formation of the distinguishable Q′-phase sub-unit [14, 15].

3.2. Grain boundaries

A range of grain boundaries were studied using TEM-EDS, and they appeared both with- and without precipitates in both alloys. An example from the model alloy is shown in figure 4, where two segments of the same grain boundary

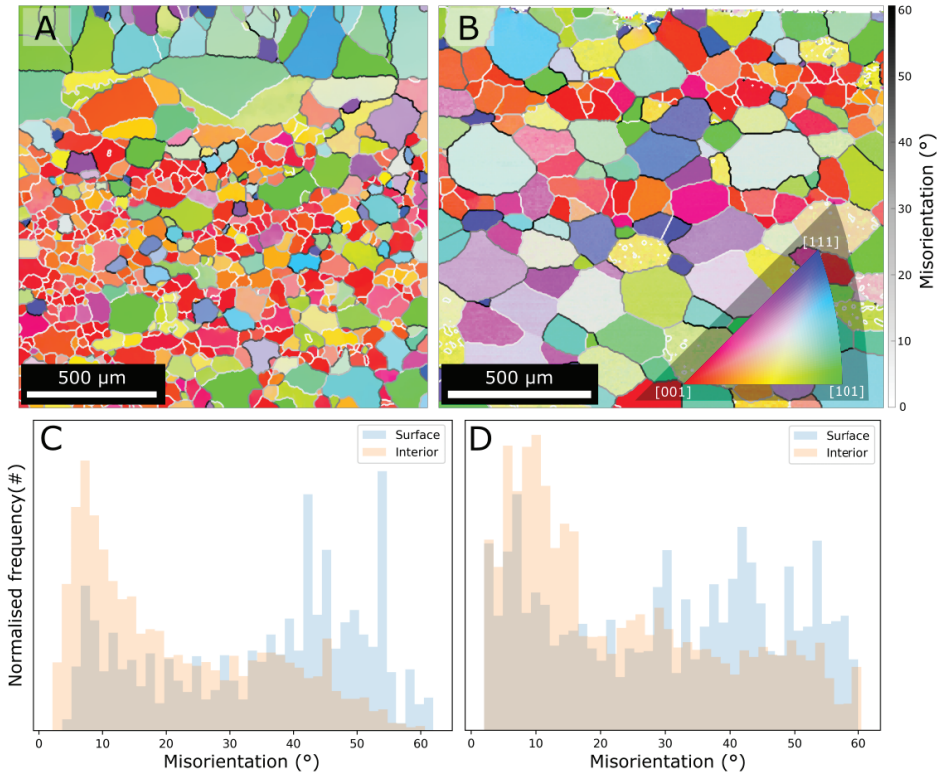

Figure 2: EBSD images of the cross-sections of the AA6005 and model alloy, in **A** and **B**, respectively. The surface is in the upper part of both figures. Grains are colour coded according to the inverse pole figure in (**B**) and grain boundaries are coloured based on their misorientation. **C** and **D** show the grain boundary misorientation angle for the AA6005 and model alloy, separated into the surface (first 450 µm) and the interior.

can be seen. They are defined by a similar misorientation angle of ~ 26° between the adjacent $[110]_{Al}$ and $[130]_{Al}$ oriented grains. Thes two segments are separated by a kink most likely caused by a pinning grain boundary precipitate. These two segments of the grain boundary are very different; one part has continuous precipitation of Q/Q'-phase particles and the other part has no precipitation. The upper segment is likely to have a more energetically favourable grain boundary plane allowing for nucleation, and does not demonstrate any clear indication of elemental segregation between the particles, while the lower segment does show segregation of Mg, Cu and Si.

Figure 5 shows a low-angle grain boundary in the AA6005 alloy. The adjacent grains are both oriented along the $[001]_{Al}$ axis. This is nearly a pure tilt boundary with a twist component of ~3° separating the grains to be simultaneously perfectly aligned parallel to the electron beam. A Precipitate Free Zone (PFZ) width of 70 nm is associated with this grain boundary, as marked in figure 5**B**. The grain boundary particles demonstrate a clear coherency with at least one of the grains which is seen by its interface plane of $(150)_{Al}$. These are the metastable Q′-phase as seen in the HAADF-STEM images in figures 5**C** and 5**D**. All particles on this grain boundary demonstrate this coherency. Figure 5**E** are the corresponding EDS maps of Al, Cu, Mg and Si. The grain boundary particles on these low-angle grain boundaries are smaller than those found on high-angle grain boundaries such as in figure 4.

PFZ widths were measured by orienting the grain boundary plane parallel to the electron beam and are on average 131±17 and 83±3 nm, for the model and AA6005 alloy, respectively. Apart from the measured PFZ widths, there were no apparent differences in the grain boundary characteristics in the two alloys.

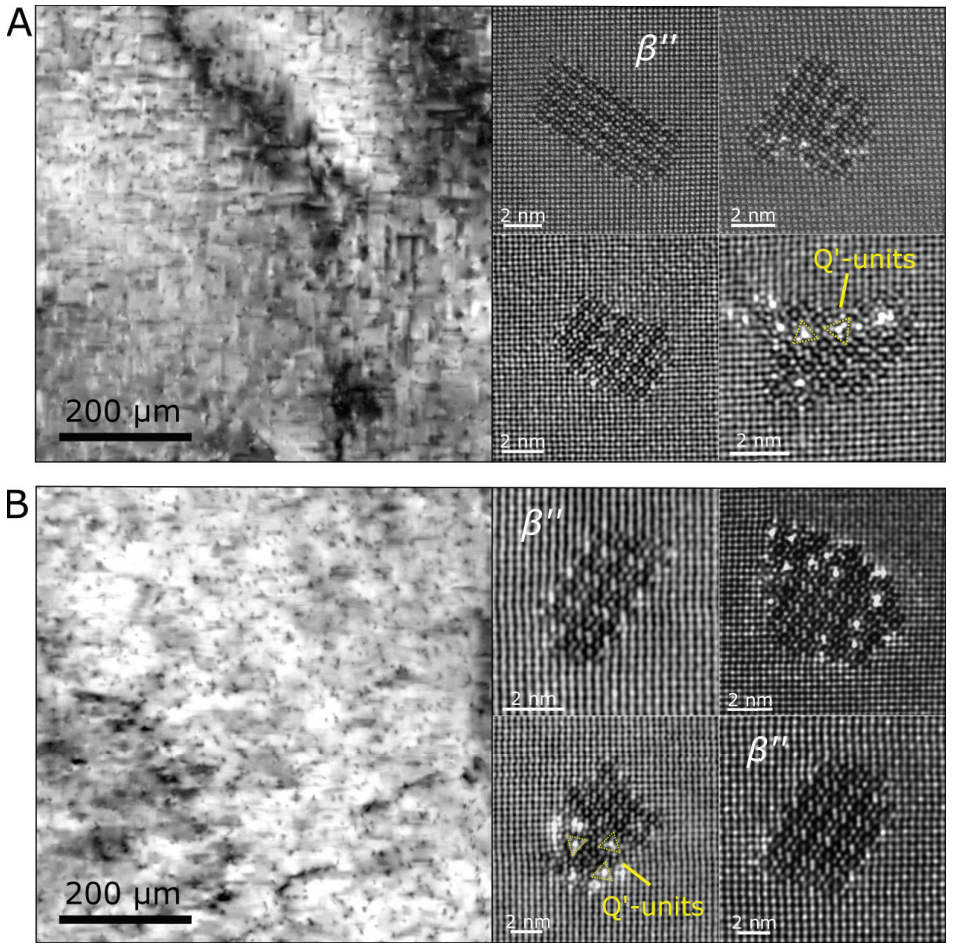

Figure 3: Bulk microstructures demonstrated by BF-TEM images taken along the $[001]_{Al}$ for the AA6005 and model alloy in **A** and **B**, respectively. Representative HAADF-STEM images of the hardening phases are presented are mostly β″ with some Cu inclusion on the interface or in the precipitate.

3.3. Corrosion properties

Maximum IGC penetration depth and mass reduction are shown as function of exposure time in figure 6. The initiation phase is delayed by ∼20 h for the model alloy compared to the AA6005 alloy, although they both reach comparable maximum penetration depths of 400-500 µm after prolonged exposure. The weight loss is significantly higher in the AA6005 alloy. Low magnification cross-sections images are shown in figure 7 after different exposure times. Less uniform attacks can be seen in the model alloy during the entire exposure, although the depths are comparable. After 48 h of exposure entire grains have detached from the surface of the AA6005 alloy.

Figure 8 shows Secondary Electron (SE)-SEM images of the corroded surfaces. Nearly all the surface α-particles on the AA6005 alloy were selectively dissolved during the first 5 hours of exposure, in accordance with previous observations [23, 37]. Only local IGC attacks can be seen in AA6005 after 5 h in figure 8**A**. After 24 h, these local attacks have developed into a near continuous network of corroded grain boundaries, where a few grains have

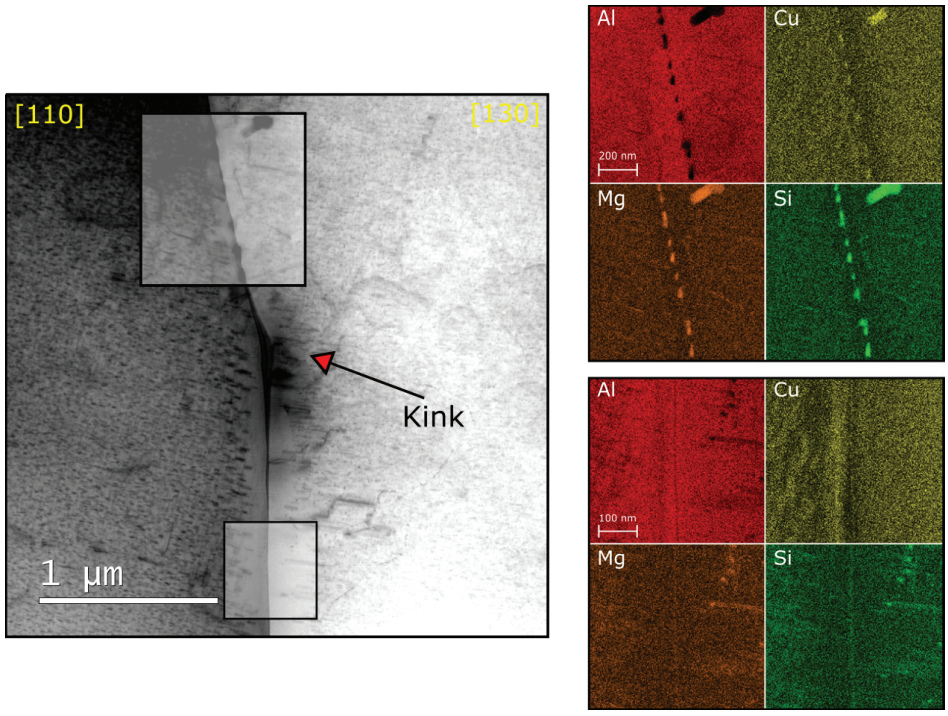

Figure 4: A grain boundary between two grains oriented along $[110]_{Al}$ and $[130]_{Al}$ in the model alloy, demonstrating different precipitation behaviour following the kink. The upper segment has continuous precipitation, while the bottom segment is free of precipitates.

detached. At 72 h, only remnants of the original surface are visible and the larger sub-surface grains demonstrated in figure 2 are clearly visible. In the model alloy, a few local IGC attacks are visible after 5 h exposure, which develop into localised networks after 24 and 72 h, where large regions are left unaffected in-between. In both alloys, corroded grains appear crystallographically etched after 5 h, while longer exposure develops these into pits.

After 24 h in the test solution Cu rich particles were observed along the grain boundaries, as demonstrated for the model alloy in figure 9. EDS mapping of the triple point shows a clear Cu signal associated with bright particles. An EDS spectrum acquired from the particle in figure 9 and from the surrounding grain, demonstrates clearly that Cu is associated with the particle. Similar observations were made in the AA6005 alloy.

3.3.1. Cathodic polarisation

Cathodic polarisation curves are shown in figure 10. Polarising after 5 min immersion demonstrates that the model alloy has the lowest current density, one order of magnitude lower than that of the AA6005 alloy. Exposing the samples for 5 h in the test solution prior to polarisation increases the current densities of both alloys to similar values.

4. Discussion

The present results confirm and supplement previous findings concerning the role of α-Al(Fe,Mn,Cu)Si phase particles in IGC [23, 50]. The IGC test results shown in figures 6, 7 and 8 demonstrate clear differences between the two materials when evaluating according to the ISO standard of 24 h exposure. The tested AA6005 alloy had a near continuous network of corroded grain boundaries, higher weight loss and slightly deeper maximum penetration depth than the model alloy. Only local IGC networks were observed in the model alloy for all hours tested. The

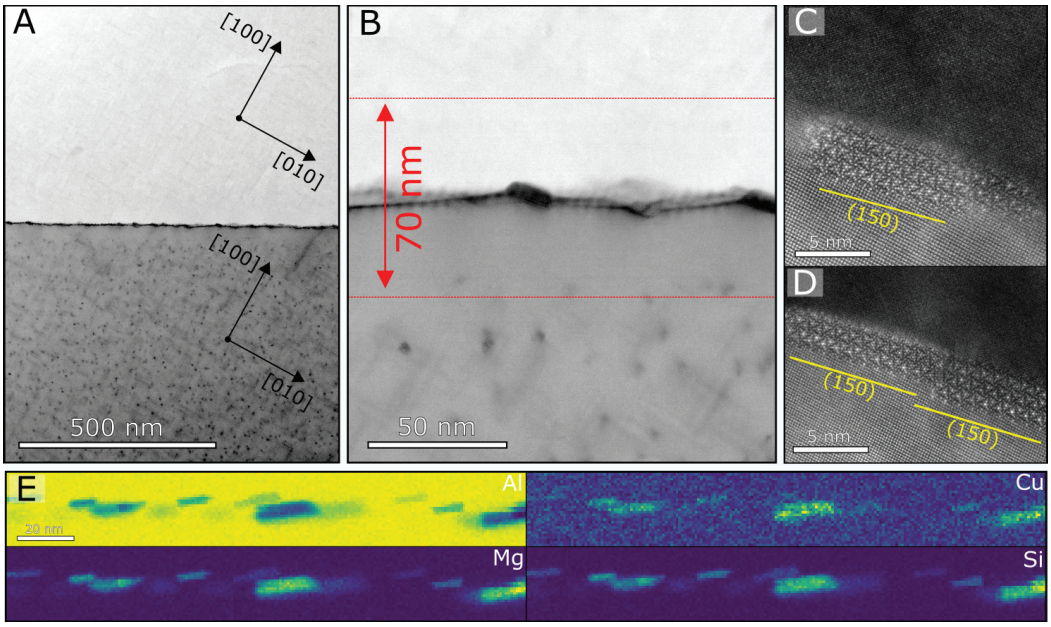

Figure 5: Low-angle grain boundary between two $[001]_{Al}$ oriented grains. BF-STEM at two different magnifications in **A** and **B**. High resolution HAADF-STEM images of grain boundary Q-phase particles in **C** and **D**. Corresponding EDS maps for Al, Cu, Mg and Si in **E**.

reason for this is believed to be due to lack of initiation sites in the form of α-Al(Fe,Mn,Cu)Si particles in connection to susceptible grain boundaries [23, 37, 50]. Due to the local IGC networks, the weight loss is lower than for the AA6005, which has more uniform corrosion resulting in the detachment of entire grains as shown in figures 7 and 8.

Surface α-Al(Fe,Mn,Cu)Si particles are also likely the reason for the measured difference in the initial cathodic current densities for the two alloys, as shown in figure 10. However, a large increase in cathodic current density was measured for the model alloy after 5 h exposure to the test solution. Figures 4 and 5 show that the grain boundaries have significant amounts of Q/Q′-phase particles present. The Q-phase has been demonstrated as a more noble particle than bulk aluminium, although it undergoes selective dissolution leaving behind Cu rich particles [40, 42]. As such, the increased cathodic current density in the model alloy may be caused by selective dissolution of such particles, as Cu-remnants were found on several grain boundaries as exemplified in figure 9. However, we cannot exclude enrichment of Cu at the surface due to uniform dealloying over the entire exposed surface [50]. Cu-rich remnants along corroded grain boundaries have been shown by others [20, 21]. Understanding the difference in kinetics of Q-phase dissolution along grain boundaries and its effect on IGC compared to continuously segregated Cu, is considered to be an important fundamental understanding which should be investigated further.

As demonstrated in figure 4, the same grain boundary defined by its misorientation angle may have different precipitation behaviour and thus different electrochemical nature. It is likely that there must exist certain grain boundary planes which facilitate precipitate growth. This has been demonstrated in the Al-Zn-Mg alloy system for the $MgZn_2$ phase [51]. A more comprehensive study correlating grain boundary precipitation, texture and corrosion properties is suggested as a future study.

For the industry, producing alloys free of α-Al(Fe,Mn,Cu)Si particles will not be practical as Fe is always present in primary aluminium and the particles are required to control grain size. It is more likely that a surface treatment to remove surface particles could be applied in components prone to IGC [19].

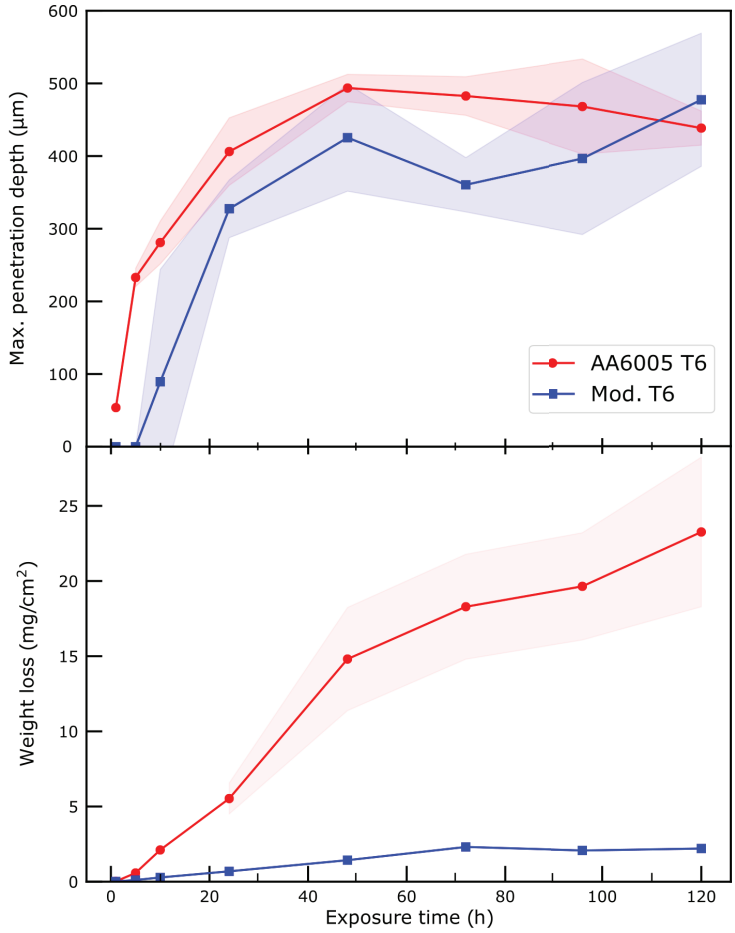

Figure 6: Maximum penetration depth (top) and average mass loss (bottom) as function of exposure time for the AA6005 and model alloys. Shaded region represents the standard deviation.

5. Conclusions

In this work, the effect α-Al(Fe,Mn,Cu)Si phase particles on IGC has been investigated. The most important findings are:

- α-Al(Fe,Mn,Cu)Si-phase particles play a key role in the initiation and distribution of IGC. Absence of the surface particles results in fewer, more locally, corroded grain boundaries.
- The initial cathodic activity on AA6005 is controlled by the presence of α-Al(Fe,Mn,Cu)Si particles on the surface. Their importance as external cathodes for the propagation of IGC is gradually reduced as the particles dissolve in the highly aggressive IGC test solution.
- With increasing time of immersion in the test solution the cathodic activity increases considerably due to surface segregation of Cu, which becomes the dominating external cathode.

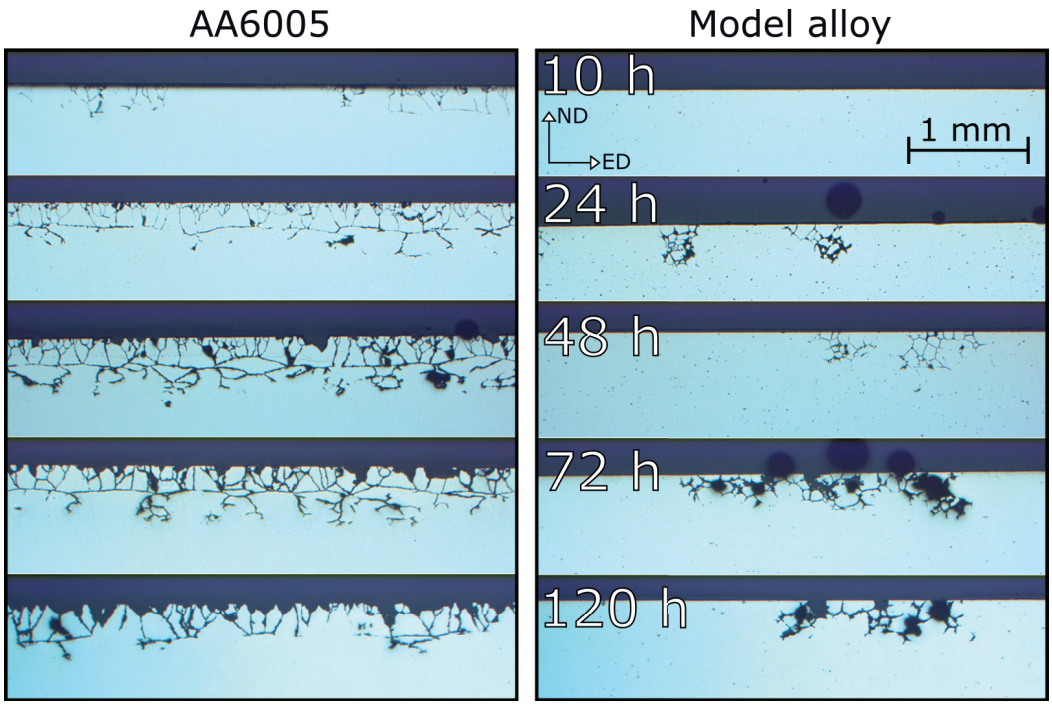

Figure 7: Optical microscopy images of cross-section of the AA6005 and model alloys after 10-120 h immersion in the accelerated IGC test solution.

- Cu rich remnants originating from grain boundary particles and/or grain boundary segregation decorate the corroded grain boundary and function as internal cathodes. This results in similar corrosion depths in the two alloys regardless of the initial surface conditions.

Acknowledgement

This work was supported by the KPN project 'FICAL' (NFR: 247598), co-financed by The Research Council of Norway (NFR), and the industrial partners Norsk Hydro ASA, Gränges, Benteler Automotive Raufoss AS and Steertec Raufoss. The (S)TEM work was conducted on the NORTEM (NFR: 197405) infrastructure at the TEM Gemini Centre, Trondheim, Norway. John Erik Lein (SINTEF Industry) is gratefully acknowledged for the polarisation measurements.

References

[1] O. Reiso, Extrusion of AlMgSi alloys, Materials Forum 28 (2004) 32–46.

[2] J. Hirsch, Recent development in aluminium for automotive applications, Transactions of Nonferrous Metals Society of China (English Edition) 24 (2014) 1995–2002. doi:10.1016/S1003-6326(14)63305-7.

[3] S. J. Andersen, H. W. Zandbergen, J. Jansen, C. Træholt, U. Tundal, O. Reiso, The crystal structure of the β″ phase in AlMgSi alloys, Acta Materialia 46 (1998) 3283–3298. doi:10.1016/S1359-6454(97)00493-X.

[4] H. S. Hasting, A. G. Frøseth, S. J. Andersen, R. Vissers, J. C. Walmsley, C. D. Marioara, F. Danoix, W. Lefebvre, R. Holmestad, Composition of β″ precipitates in AlMgSi alloys by atom probe tomography and first principles calculations, Journal of Applied Physics 106 (2009) 123527. doi:10.1063/1.3269714.

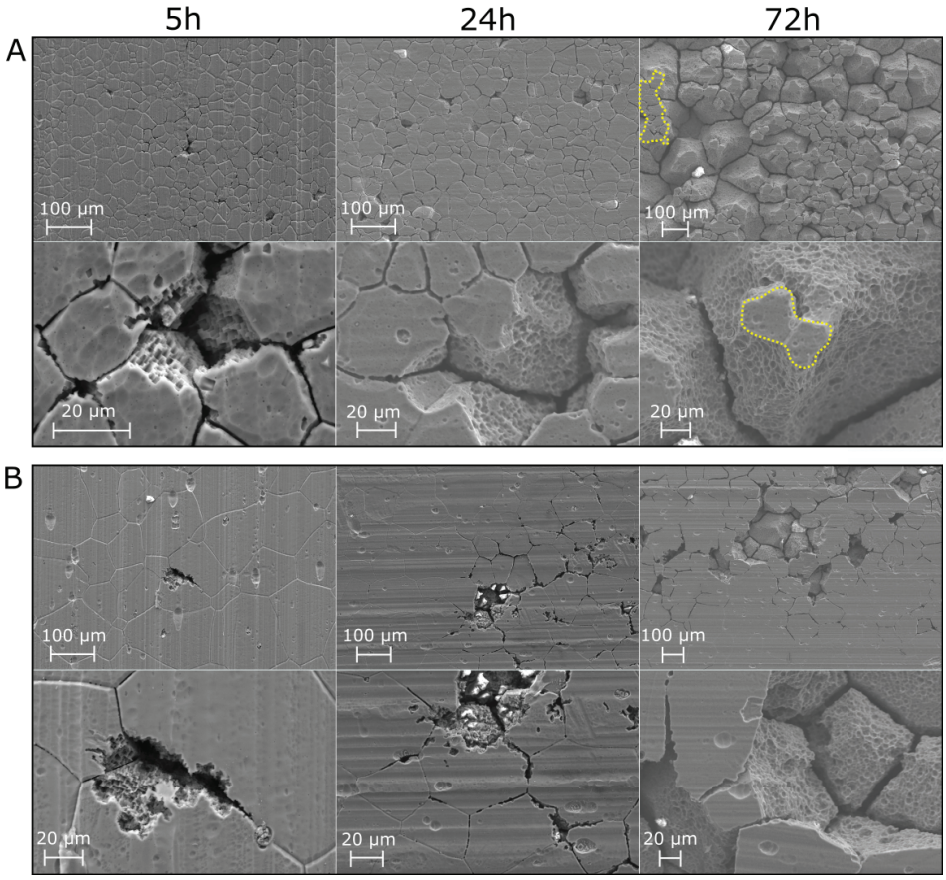

Figure 8: SE-SEM images of the corroded surface after 5, 24 and 72 h immersion in the accelerated IGC test solution for the AA6005 alloy and the model alloy, in **A** and **B**, respectively. Yellow dotted lines indicate the original surface, which is barely visible after 72 h exposure in the AA6005 alloy.

[5] J. K. Sunde, C. D. Marioara, A. T. van Helvoort, R. Holmestad, The evolution of precipitate crystal structures in an Al-Mg-Si(-Cu) alloy studied by a combined HAADF-STEM and SPED approach, Materials Characterization 142 (2018) 458–469. doi:10.1016/j.matchar.2018.05.031.

[6] W. F. Miao, D. E. Laughlin, Effects of Cu content and preaging on precipitation characteristics in aluminum alloy 6022, Metallurgical and Materials Transactions A 31 (2000) 361–371. doi:10.1007/s11661-000-0272-2.

[7] M. Murayama, K. Hono, W. Miao, D. E. Laughlin, The effect of Cu additions on the precipitation kinetics in an Al-Mg-Si alloy with excess Si, Metallurgical and Materials Transactions A 32 (2001) 239–246. doi:10.1007/s11661-001-0254-z.

[8] J. Man, L. Jing, S. G. Jie, The effects of Cu addition on the microstructure and thermal stability of an Al-Mg-Si alloy, Journal of Alloys and Compounds 437 (2007) 146–150. doi:10.1016/j.jallcom.2006.07.113.

[9] C. D. Marioara, S. J. Andersen, T. N. Stene, H. Hasting, J. Walmsley, A. T. J. Van Helvoort, R. Holmestad, The effect of Cu on precipitation in AlMgSi alloys, Philosophical Magazine 87 (2007) 3385–3413. doi:10.1080/14786430701287377.

[10] T. Saito, C. D. Marioara, J. Røyset, K. Marthinsen, R. Holmestad, The effects of quench rate and pre-deformation on precipitation hardening in Al-Mg-Si alloys with different Cu amounts, Materials Science and Engineering A 609 (2014) 72–79. doi:10.1016/j.msea.2014.04.094.

[11] M. W. Zandbergen, A. Cerezo, G. D. W. Smith, Study of precipitation in Al-Mg-Si Alloys by atom probe tomography II. Influence of Cu additions, Acta Materialia 101 (2015) 149–158. doi:10.1016/j.actamat.2015.08.018.

[12] Q. Xiao, H. Liu, D. Yi, D. Yin, Y. Chen, Y. Zhang, B. Wang, Effect of Cu content on precipitation and age-hardening behavior in Al-Mg-Si-xCu alloys, Journal of Alloys and Compounds 695 (2017) 1005–1013. doi:10.1016/j.jallcom.2016.10.221.

[13] J. K. Sunde, C. D. Marioara, R. Holmestad, The effect of low Cu additions on precipitate crystal structures in overaged Al-Mg-Si(-Cu) alloys,

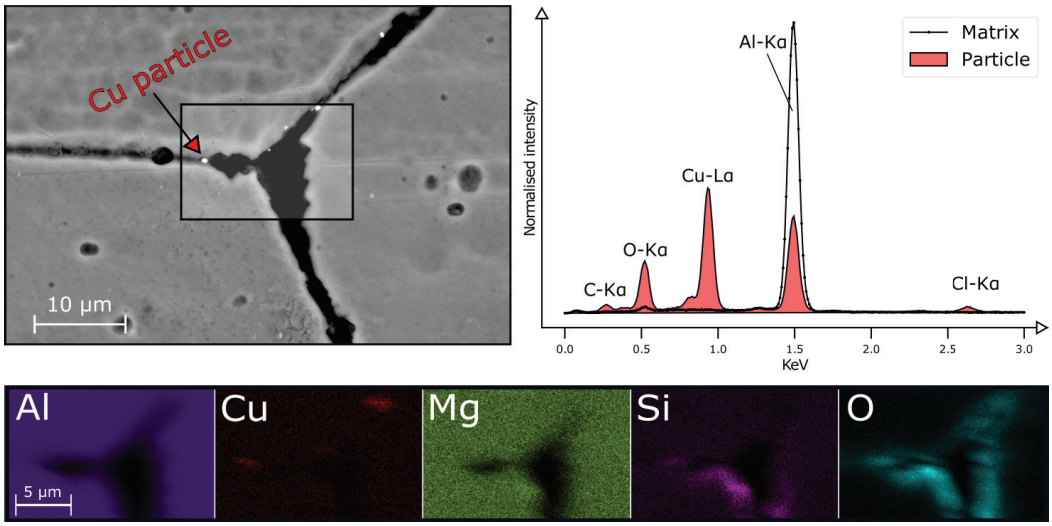

Figure 9: A triple point in the model alloy after 24 h immersion in the test solution, imaged using BSE-SEM. The bright particles are pure Cu particles as shown in the EDS spectrum and the corresponding maps.

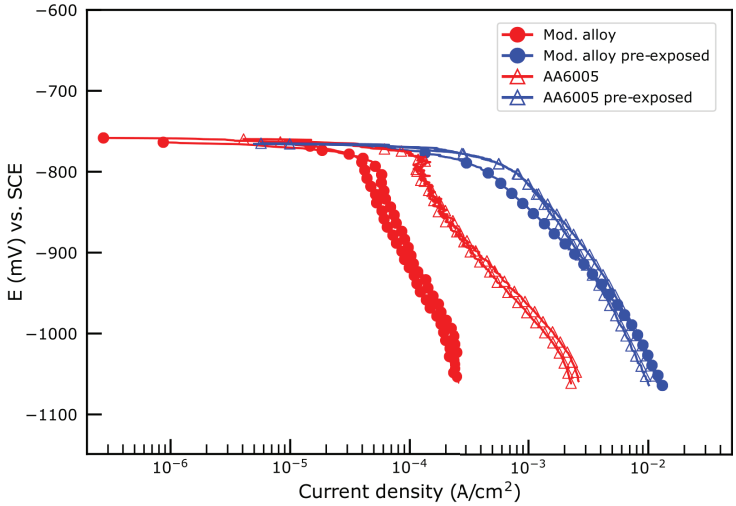

Figure 10: Cathodic polarisation curves for the two alloys after 5 min or 5 h immersion in the test solution prior to the scan.

Materials Characterization 160 (2020) 110087. doi:10.1016/j.matchar.2019.110087.

[14] T. Saito, E. A. Mørtsell, S. Wenner, C. D. Marioara, S. J. Andersen, J. Friis, K. Matsuda, R. Holmestad, Atomic Structures of Precipitates in Al-Mg-Si Alloys with Small Additions of Other Elements, Advanced Engineering Materials 1800125 (2018) 1–18. doi:10.1002/adem.201800125.

[15] S. Wenner, L. Jones, C. D. Marioara, R. Holmestad, Atomic-resolution chemical mapping of ordered precipitates in Al alloys using energy-dispersive X-ray spectroscopy, Micron 96 (2017) 103–111. doi:10.1016/j.micron.2017.02.007.

[16] C. D. Marioara, A. Lervik, J. Grønvold, O. Lunder, S. Wenner, T. Furu, R. Holmestad, The Correlation Between Intergranular Corrosion Resistance and Copper Content in the Precipitate Microstructure in an AA6005A Alloy, Metallurgical and Materials Transactions A 49

(2018) 5146–5156. doi:10.1007/s11661-018-4789-7.
[17] G. Svenningsen, M. H. Larsen, J. C. Walmsley, J. H. Nordlien, K. Nisancioglu, Effect of artificial aging on intergranular corrosion of extruded AlMgSi alloy with small Cu content, Corrosion Science 48 (2006) 1528–1543. doi:10.1016/j.corsci.2005.05.045.
[18] M. H. Larsen, J. C. Walmsley, O. Lunder, R. H. Mathiesen, K. Nisancioglu, Intergranular Corrosion of Copper-Containing AA6xxx AlMgSi Aluminum Alloys, Journal of The Electrochemical Society 155 (2008) C550. doi:10.1149/1.2976774.
[19] M. H. Larsen, J. C. Walmsley, O. Lunder, K. Nisancioglu, Effect of Excess Silicon and Small Copper Content on Intergranular Corrosion of 6000-Series Aluminum Alloys, Journal of The Electrochemical Society 157 (2010) C61–C68. doi:10.1149/1.3261804.
[20] D. Zander, C. Schnatterer, C. Altenbach, V. Chaineux, Microstructural impact on intergranular corrosion and the mechanical properties of industrial drawn 6056 aluminum wires, Materials and Design 83 (2015) 49–59. doi:10.1016/j.matdes.2015.05.079.
[21] C. Schnatterer, D. Zander, Influence of the grain boundary chemistry on the intergranular corrosion mechanisms of a high-strength Al-Mg-Si alloy, Surface and Interface Analysis 48 (2016) 750–754. doi:10.1002/sia.5859.
[22] S. K. Kairy, T. Alam, P. A. Rometsch, C. H. J. Davies, R. Banerjee, N. Birbilis, Understanding the Origins of Intergranular Corrosion in Copper-Containing Al-Mg-Si Alloys, Metallurgical and Materials Transactions A 47 (2016) 985–989. doi:10.1007/s11661-015-3296-3.
[23] S. Kumari, S. Wenner, J. C. Walmsley, O. Lunder, K. Nisancioglu, Progress in Understanding Initiation of Intergranular Corrosion on AA6005 Aluminum Alloy with Low Copper Content, Journal of The Electrochemical Society 166 (2019) C3114–C3123. doi:10.1149/2.0211911jes.
[24] G. Svenningsen, J. E. Lein, A. Bjørgum, J. H. Nordlien, Y. Yu, K. Nisancioglu, Effect of low copper content and heat treatment on intergranular corrosion of model AlMgSi alloys, Corrosion Science 48 (2006) 226–242. doi:10.1016/j.corsci.2004.11.025.
[25] G. Svenningsen, M. H. Larsen, J. H. Nordlien, K. Nisancioglu, Effect of thermomechanical history on intergranular corrosion of extruded AlMgSi(Cu) model alloy, Corrosion Science 48 (2006) 3969–3987. doi:10.1016/j.corsci.2006.03.018.
[26] G. Svenningsen, M. H. Larsen, J. H. Nordlien, K. Nisancioglu, Effect of high temperature heat treatment on intergranular corrosion of AlMgSi(Cu) model alloy, Corrosion Science 48 (2006) 258–272. doi:10.1016/j.corsci.2004.12.003.
[27] S. K. Kairy, P. A. Rometsch, K. Diao, J. F. Nie, C. H. J. Davies, N. Birbilis, Exploring the electrochemistry of 6xxx series aluminium alloys as a function of Si to Mg ratio, Cu content, ageing conditions and microstructure, Electrochimica Acta 190 (2016) 92–103. doi:10.1016/j.electacta.2015.12.098.
[28] S. K. Kairy, P. A. Rometsch, C. H. J. Davies, N. Birbilis, On the Intergranular Corrosion and Hardness Evolution of 6xxx Series Al Alloys as a Function of Si:Mg Ratio, Cu Content, and Aging Condition, Corrosion 9312 (2017) 1280–1296. doi:10.5006/2506.
[29] Y. Zou, Q. Liu, Z. Jia, Y. Xing, L. Ding, X. Wang, The intergranular corrosion behavior of 6000-series alloys with different Mg/Si and Cu content, Applied Surface Science 405 (2017) 489–496. doi:10.1016/j.apsusc.2017.02.045.
[30] S. Zajac, B. Hutchinson, A. Johansson, L.-O. Gullman, Microstructure control and extrudability of AlMgSi alloys microalloyed with manganese, Materials Science and Technology 10 (1994) 323–333. doi:10.1179/mst.1994.10.4.323.
[31] H. Tanihata, T. Sugawara, K. Matsuda, S. Ikeno, Effect of casting and homogenizing treatment conditions on the formation of Al-Fe-Si intermetallic compounds in 6063 Al-Mg-Si alloys, Journal of Materials Science 34 (1999) 1205–1210. doi:10.1023/A:1004504805781.
[32] N. C. Kuijpers, F. J. Vermolen, K. Vuik, S. Van Der Zwaag, A model of the β-AlFeSi to α-Al(FeMn)Si transformation in Al-Mg-Si alloys, Materials Transactions 44 (2003) 1448–1456. doi:10.2320/matertrans.44.1448.
[33] L. Lodgaard, N. Ryum, Distribution of Mn- and Cr-Containing Dispersoids in Al-Mg-Si-Alloys, Materials Science Forum 331-337 (2000) 945–950. doi:10.4028/www.scientific.net/msf.331-337.945.
[34] L. Lodgaard, N. Ryum, Precipitation of dispersoids containing Mn and/or Cr in AlMgSi alloys, Materials Science and Engineering: A 283 (2000) 144–152. doi:10.1016/s0921-5093(00)00734-6.
[35] R. Hu, T. Ogura, H. Tezuka, T. Sato, Q. Liu, Dispersoid formation and recrystallization behavior in an Al-Mg-Si-Mn alloy, Journal of Materials Science and Technology 26 (2010) 237–243. doi:10.1016/S1005-0302(10)60040-0.
[36] N. Bayat, T. Carlberg, M. Cieslar, In-situ study of phase transformation during homogenization 6005 and 6082 Al alloys, Journal of Alloys and Compounds 725 (2017) 504–509. doi:10.1016/j.jallcom.2017.07.149.
[37] K. Shimizu, K. Nisancioglu, High Resolution SEM Investigation of Intercrystalline Corrosion on 6000-Series Aluminum Alloy with Low Copper Content, ECS Electrochemistry Letters 3 (2014) C29–C31. doi:10.1149/2.0041409eel.
[38] S. Lebouil, J. Tardelli, E. Rocca, P. Volovitch, K. Ogle, Dealloying of Al_2Cu, Al_7Cu_2Fe, and Al_2CuMg intermetallic phases to form nanoparticulate copper films, Materials and Corrosion 65 (2014) 416–424. doi:10.1002/maco.201307550.
[39] S.-S. Wang, I.-W. Huang, L. Yang, J.-T. Jiang, J.-F. Chen, S.-L. Dai, D. N. Seidman, G. S. Frankel, L. Zhen, Effect of Cu Content and Aging Conditions on Pitting Corrosion Damage of 7xxx Series Aluminum Alloys, Journal of The Electrochemical Society 162 (2015) C150–C160. doi:10.1149/2.0301504jes.
[40] S. K. Kairy, P. A. Rometsch, C. H. J. Davies, N. Birbilis, On the electrochemical and quasi in-situ corrosion response of the Q-phase ($Al_xCu_yMg_zSi_w$) intermetallic particle in 6xxx series Al-alloys, Corrosion 73 (2017) 1–29. doi:10.5006/2249.
[41] Y. Zhu, K. Sun, G. S. Frankel, Intermetallic Phases in Aluminum Alloys and Their Roles in Localized Corrosion, Journal of The Electrochemical Society 165 (2018) C807–C820. doi:10.1149/2.0931811jes.
[42] A. I. Ikeuba, B. Zhang, J. Wang, E. H. Han, W. Ke, Electrochemical, TOF-SIMS and XPS studies on the corrosion behavior of Q-phase in NaCl solutions as a function of pH, Applied Surface Science 490 (2019) 535–545. doi:10.1016/j.apsusc.2019.06.089.
[43] K. Nisancioglu, Electrochemical Behavior of Aluminum-Base Intermetallics Containing Iron, Journal of The Electrochemical Society 137 (1990) 69. doi:10.1149/1.2086441.
[44] N. Birbilis, R. G. Buchheit, Electrochemical Characteristics of Intermetallic Phases in Aluminum Alloys An Experimental Survey and Discussion, Journal of The Electrochemical Society 152 (2005) B140–B151. doi:10.1149/1.1869984.
[45] N. Birbilis, R. G. Buchheit, Investigation and Discussion of Characteristics for Intermetallic Phases Common to Aluminum Alloys as a Function of Solution pH, Journal of The Electrochemical Society 155 (2008) C117–C126. doi:10.1149/1.2829897.
[46] J. Li, J. Dang, A Summary of Corrosion Properties of Al-Rich Solid Solution and Secondary Phase Particles in Al Alloys, Metals 7 (2017) 84. doi:10.3390/met7030084.
[47] A. L. Dons, The Alstruc homogenization model for industrial aluminum alloys, Journal of Light Metals 1 (2001) 133–149.

doi:10.1016/s1471-5317(01)00007-4.

[48] F. Bachmann, R. Hielscher, H. Schaeben, Texture Analysis with MTEX - Free and Open Source Software Toolbox, in: Texture and Anisotropy of Polycrystals III, volume 160 of *Solid State Phenomena*, Trans Tech Publications Ltd, 2010, pp. 63–68. doi:10.4028/www.scientific.net/SSP.160.63.

[49] L. Jones, H. Yang, T. J. Pennycook, M. S. J. Marshall, S. Van Aert, N. D. Browning, M. R. Castell, P. D. Nellist, Smart align - a new tool for robust non-rigid registration of scanning microscope data, Advanced Structural and Chemical Imaging 1 (2015) 8. doi:10.1186/s40679-015-0008-4.

[50] S. Kumari, S. Wenner, J. C. Walmsley, O. Lunder, K. Nisancioglu, Copper enriched by dealloying as external cathode in intergranular corrosion of aluminium alloy AA6005, Corrosion Science (2019) 108090. doi:10.1016/j.corsci.2019.07.014.

[51] H. L. P. Czurratis, R. Kroggel, Precipitation structure in an Al-2.0at.%Zn-1.0at.%Mg alloy within and close to the grain boundaries and its effects on mechanical properties, Czechoslovak Journal of Physics B 38 (1988) 444–456.

Paper II

Grain boundary structures and their correlation with intergranular corrosion in an extruded Al-Mg-Si-Cu alloy

Adrian Lervik, Sigurd Wenner, Calin Daniel Marioara, Otto Lunder, Randi Holmestad

Submitted *Materials Characterization* (14.05.2020)

Grain boundary structures and their correlation with intergranular corrosion in an extruded Al-Mg-Si-Cu alloy

A. Lervik[a,*], S. Wenner[b,a], O. Lunder[b], C.D. Marioara[b], R. Holmestad[a]

[a] *Department of Physics, Norwegian University of Science and Technology (NTNU), N-7491 Trondheim, Norway*
[b] *SINTEF Industry, N-7465, Trondheim, Norway*

Abstract

A detailed analysis of grain boundaries in a highly textured extruded Al-Mg-Si-Cu alloy is presented in this work. Electron backscattered diffraction demonstrates the presence of three main categories of grain boundaries in addition to sub-grain boundaries. These are systematically analysed using high resolution scanning transmission electron microscopy. Intergranular corrosion (IGC) properties were statistically correlated with the same defined grain boundaries. A higher density of metastable Q′-phase grain boundary particles correlates with a reduction in Cu segregation at grain boundaries and increased IGC resistance. Results herein are relevant in further understanding grain boundary structures in these alloys and their susceptibility to IGC, and can be implemented into modelling frameworks.

Keywords: Aluminium alloys, (Transmission) electron microscopy, Intergranular corrosion, Grain boundaries, Microstructure, Texture

1. Introduction

Extruded Al-Mg-Si-(Cu) (6xxx series) aluminium alloys are of great interest in transportation industry due to favourable properties such as high strength-to-weight ratio and formability [1, 2]. These alloys achieve a rapid increase in hardness after a short thermal treatment due to the formation of nanoscale metastable precipitate phases distributed throughout the Al matrix [3]. Small additions of Cu have influence on the precipitation kinetics and the mechanical properties of these alloys [4–11]. However, the addition of Cu is often associated with introducing susceptibility to intergranular corrosion (IGC) [12–17]. The reasons for this are related to microgalvanic coupling between Cu-segregation along grain boundaries, grain boundary particles (GBPs) and the adjacent precipitate free zones (PFZ) which are depleted of both solute elements and vacancies [12–18].

IGC is mostly reported in the under- and peak aged tempers, whereas overageing is usually associated with a change from IGC to pitting corrosion [12, 14]. This has previously been attributed to the transformation of segregated Cu along grain boundaries to the formation of discrete Q/Q′-$Al_6Mg_6Si_7Cu_2$ phase GBPs. At the same time, Cu redistribution by incorporation into matrix hardening phases in the form of the metastable Q′-phase, also has a positive influence on the IGC properties [16]. This typically occurs when overageing [3, 11].

It has previously been shown that the special coincident site lattice (CSL) grain boundaries have high resistance to IGC in pure Al [19]. Bałkowiec et al. reported a strong correlation between misorientation angle and IGC susceptibility in an AA2024 alloy, where the high-angle grain boundaries were more susceptible [20]. Similar observations were made by Chan et al. [21]. Minoda et al. reported IGC susceptibility predominantly at high-angle grain boundaries due to the presence of PFZ and GBPs, which were not found at the low-angle grain boundaries in an Al-Mg-Si alloy [22].

The Q and Q′ GBPs are similar in composition, but are distinguished by their coherency with the surrounding grains. Equilibrium Q-phase GBPs does not have any clear coherency with any of the grains and thus no defined

*Corresponding author at: Department of Physics, Norwegian University of Science and Technology (NTNU), N-7491 Trondheim, Norway
Email address: adrian.lervik@ntnu.no (A. Lervik)

shape. The metastable Q′-phase has clear coherency with at least one of the grains. Holmestad et al. demonstrated that low-angle grain boundaries had a high density of Q′-phase particles, while the high-angle grain boundaries consisted of fewer, but larger Q′-phase particles [18]. Kairy et al. demonstrated that Q′-phase particles were precipitated on grain boundaries, with an orientation relationship defined as $[0001]_{Q'}//[001]_{Al}$ and $(11\bar{2}0)_{Q'}//(510)_{Al}$ with at least one adjacent grain, in an under aged temper [15, 23]. Similar observations were made by Chrominski & Lewandowska [24]. It is interesting to note that this is the same interface plane as the metastable nanoscale Q′ hardening phase form within the bulk Al microstructure [25]. This suggests that on certain grain boundaries, particles have defined growth direction and/or nucleation planes. Yang et al. studied grain boundary precipitation in an extruded alloy with defined brass- and recrystallisation cube texture components, after artificial ageing for 30 min and 36 h at 175 °C [26]. High-angle grain boundaries, in the recrystallised cube texture, precipitated Q′-phase particles with the same $(11\bar{2}0)_{Q'}//(510)_{Al}$ orientation relationship with one of the grains. The low-angle grain boundaries, in the brass texture, consisted of phases only containing Mg and Si with a $\{310\}_{Al}$ interface plane, to which they suggested the precipitation sequence: pre-β″ → β′ → β. Understanding how these particles distribute at grain boundaries along with the Cu segregated layer, is essential in further understanding IGC mechanisms.

In this work a highly textured Al-Mg-Si-Cu alloy has been selected to conduct a thorough study of the precipitation behaviour on grain boundaries and its correlation to IGC. Defined crystallographic orientation relationships of grain boundaries are systematically investigated with respect to elemental segregation and precipitation, and correlated with a statistical analysis of the corroded grain boundaries.

2. Material and methods

2.1. Material

Table 1 gives the composition of the Al-Mg-Si-Cu alloy studied in this work. The material was extruded as a cylindrical bar with 20 mm diameter. A solution heat treatment (SHT) step at 530 °C for 30 min was conducted with a following water quench. More details about the processing steps and mechanical properties have been reported elsewhere under the alias 'K11' [27]. The alloy is studied in a T6 temper achieved by artificially ageing at 200 °C for 6 hours.

Table 1: Alloy composition (wt.% and at.%) measured using optical emission spectroscopy.

	Cu	Fe	Mg	Mn	Si	Al
wt.%	0.40	0.20	0.81	0.55	0.75	Bal.
at.%	0.17	0.10	0.90	0.27	0.72	Bal.

2.2. Electron microscopy

The material was exclusively imaged with the viewing direction parallel to the extrusion direction, as a strong texture is present and most grain boundaries are parallel to this direction. Samples for electron backscattered diffraction (EBSD) were ground and electropolished with the 'Struers A2' electrolyte. EBSD scans were conducted on a Hitachi SU-6600 FEG-SEM with a Nordif EBSD detector using a working distance of 24 mm, sample tilt of 70° and 0.1 µm step size. Nordif3.0 was used to index the acquired patterns and the data was thereafter processed in OIM TSL or MTEX [28]. The grain boundary axis-angle rotations are represented in the corresponding symmetry reduced fundamental zone [29].

Specimens for transmission electron microscopy (TEM) were first ground to ~100 µm thickness and punched into 3 mm discs, before they were electropolished in a solution of 1/3 HNO_3 and 2/3 CH_3OH at temperatures between -30 and -20 °C at 20 V. Two TEMs were used in this work. (i) A JEOL JEM-2100F operated at 200 kV equipped with an Oxford X-max 80 detector for energy-dispersive X-ray spectroscopy (EDS) analysis (solid angle: 0.23 sr). (ii) A double Cs-corrected JEOL ARM200CF operated in scanning transmission electron microscopy (STEM) mode

at 200 kV using a convergence semi-angle of 28 and 48 mrad inner collector angle, equipped with a Centurio EDS detector (solid angle: 0.98 sr). Some STEM images were acquired as image series, then aligned, distortion corrected and summed using Smart Align [30]. All EDS data was analysed using HyperSpy [31], and quantified using the Cliff-Lorimer method with theoretically calculated K-values.

2.3. Corrosion testing

The surface perpendicular to the extrusion direction was first electropolished with the electrolyte 'Struers A2' to obtain a smooth, clean surface. The samples were thereafter exposed to a HCl + NaCl solution, according to standard BS ISO 11846 method B, for durations ranging from 10 min to 24 h. A sample exposed for 2 hours was selected for EBSD analysis since its IGC attacks were of a suitable size to observe a good amount of grain boundaries, without the surface quality being significantly reduced. Preferential IGC along grain boundaries with certain misorientations could then be statistically investigated.

3. Results

3.1. Texture analysis

The material exhibits a well-defined fibrous texture that contains no recrystallized grains, as shown in the EBSD image in figure 1A where the grains are coloured according to the inverse pole figure. Most of the grains are oriented with the $\langle 111 \rangle_{Al}$ or $\langle 001 \rangle_{Al}$ directions close to the extrusion direction. A region highlighted in figure 1A is shown in figure 1B, where the grain boundaries are coloured according to their misorientation angle and the rotation axis is indicated by a solid black line. Evidently, most of the high-angle grain boundaries are associated with boundaries between grains oriented along $\langle 111 \rangle_{Al}$ and $\langle 001 \rangle_{Al}$, having misorientations around ~55°. Grain boundaries with lower misorientations are associated with grains oriented along the same axis, although these may appear over a range of misorientation angles (up to 45° for $[001]_{Al}$ and up to 30° for $[111]_{Al}$). The grain boundary axis-angle space is represented in the corresponding fundamental zone in figure 1C, where axis-angle pairs are mostly located along the two rotation axes: $\langle 100 \rangle_{Al}$ and $\langle 111 \rangle_{Al}$. These axis-angle pairs belong to grain boundaries where the adjacent grains are oriented along the same axis. The variation in misorientation is mainly caused by an in-plane rotation, as the rotation axes are parallel with the extrusion direction. A cluster of axis-angle pairs with high misorientation and more scattered axis is also present, and belongs to the high-angle grain boundaries between $[001]_{Al}//[111]_{Al}$ oriented grains. In addition, there exists a large number of sub-grain boundaries within individual grains, separated by misorientation angles of $\leq 3°$. These are clearly represented by the deviation from the average grain orientation, as shown in figure 1D. In the following section, we assign analysed grain boundaries into the categories [001]//[111], [001]//[001] and [111]//[111] based on the orientation of the neighbouring grains.

3.2. Grain boundaries

High-angle grain boundaries between two grains oriented along $[001]_{Al}$ and $[111]_{Al}$ typically only consist of a few large particles along their observable segment. One example is shown in the high-angle annular dark field (HAADF)-STEM image in figure 2A. A magnified view of the region indicated in figure 2A is shown in figure 2B. This, and all the other particles along the grain boundary adapt the $[0001]_{Q'}//[001]_{Al}$ orientation. However, the interface plane of the particle is not clearly defined in the $[001]_{Al}$ oriented grain, but in the $[111]_{Al}$ grain the interface appears more sharply defined. As such, it is uncertain whether the particle is coherent or incoherent, although the internal structure of the particle clearly is the Q/Q′-phase. Between the particles there is a clear layer of enhanced intensity at the grain boundary plane shown in detail in figure 2C where the grain on the right is oriented exactly along its $[001]_{Al}$ axis, while the grain on the left is tilted 7.5° away from its $[111]_{Al}$ axis. The enhanced intensity at the grain boundary plane is verified as segregated Cu in the corresponding EDS map. No other element shows any segregation here. Figure 2D is a composition profile constructed from the data within the enclosed region in the Al EDS map, showing the average value and its standard deviation for the labeled elements at different positions across the grain boundary. The observed Cu segregation reaches a peak value of ~8 at.% and is confined to a width of ~1.0 nm, which is likely overestimated due to beam-broadening effects [32]. The width of the PFZ associated with this grain boundary is measured to ~140 nm. All studied high-angle grain boundaries of this type demonstrate Cu segregation (and in some cases both Cu and Mg).

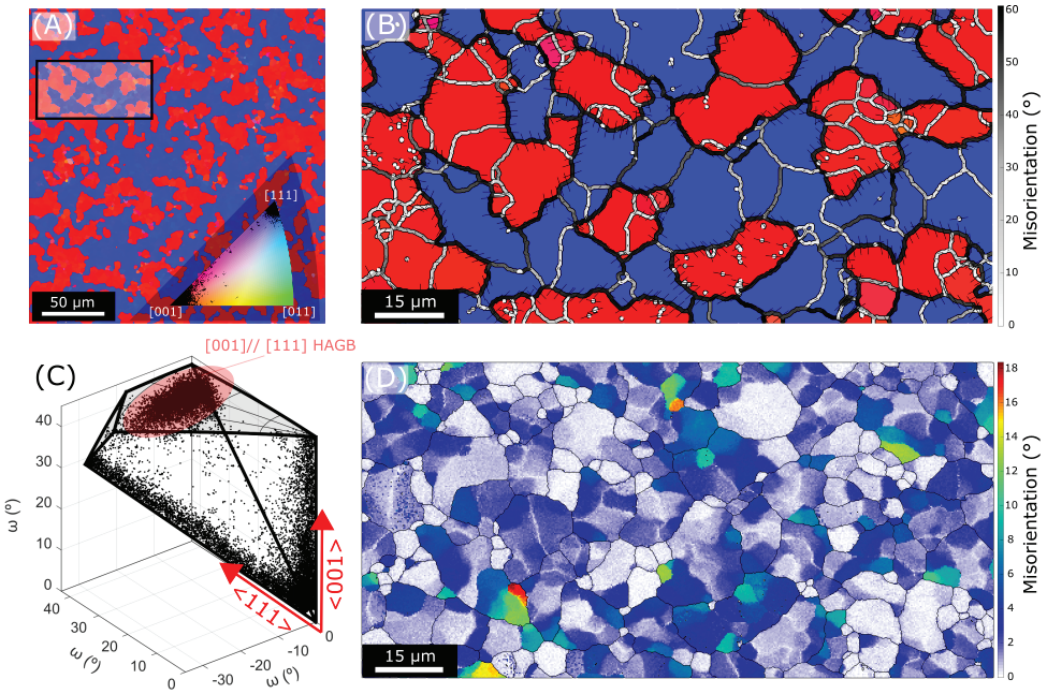

Figure 1: (A) EBSD map acquired parallel to the extrusion direction with grains coloured according to the inverse pole figure. (B) is a magnified view of the indicated region in (A) where the grain boundary misorientation is colour coded and the rotation axis is indicated as solid black lines. (C) Axis-angle rotation pairs of grain boundary segments represented in a fundamental zone. (D) In-grain misorientation of the same region as in (B), demonstrating a large amount of sub-grain boundaries within the individually defined grains.

High-angle grain boundaries between grains oriented along $[111]_{Al}$ varies greatly in appearance as demonstrated by figure 3. In figure 3A there are no GBPs present. A different grain boundary shown in figure 3B demonstrates both the presence of particles and segments where no particles are found. Figure 3C shows the grain boundary in figure 3A aligned parallel with the electron beam. As demonstrated by the EDS line profile and maps, Cu and Mg are found to segregate at this grain boundary. Tilting the same boundary slightly away from its parallel alignment with the electron beam, as shown in figure 3D, suppresses the signal from the segregated Mg and Cu in the EDS maps. Both these grain boundaries are high-angle with a misorientation of ~28°.

In figure 4, two grain boundaries between three grains oriented along $[001]_{Al}$ can be seen. The misorientation between grains 1-2 and 2-3 is ~15° and ~5°, respectively. Between grains 1-2 the grain boundary is oriented parallel to the electron beam and is close to a pure tilt boundary, where most of the misorientation is due to the in-plane rotation measured to 14°. The particles present are all the metastable Q′-phase with a defined interface plane $(510)_{Al}$, but also $(110)_{Al}$ and $(100)_{Al}$ planes as can be seen in figures 4B and 4C. The latter is often found in disordered structures such as the L-phase [27]. Between the particles there is little or no segregation observed in the corresponding EDS maps. The triple point where 'EDS 2' is acquired, show how the particles are aligned between grains 2-3 when the grain boundary becomes inclined with respect to the electron beam. A PFZ width of 115 nm is found on this grain boundary.

3.2.1. Sub-grain boundaries

An example of a sub-grain boundary within a $[001]_{Al}$ oriented grain is shown in figure 5. The misorientation associated with the sub-grain boundary is an in-plane rotation of <0.5°. As seen in the BF-TEM image in figure 5C

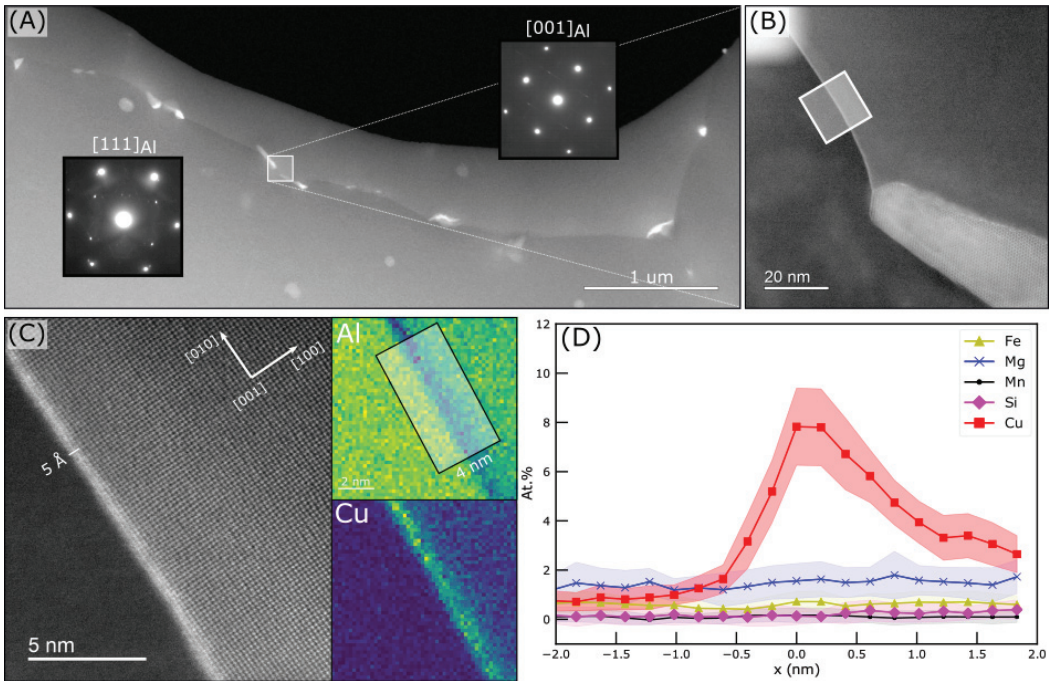

Figure 2: (A) HAADF-STEM image of a high-angle grain boundary between grains oriented along $[100]_{Al}$ and $[111]_{Al}$. (B) Magnification of the area indicated in (A) showing a large GBP and enhanced intensity at the grain boundary plane. (C) Magnification of the region in (B) with corresponding Al and Cu EDS maps, demonstrating clearly that Cu is segregated at the grain boundary interface. (D) A 2D EDS composition profile across the grain boundary.

dislocations are clearly associated with this grain boundary. In the BF-STEM image in figure 5A, the width of the associated PFZ is approximately 70 nm. EDS data acquired from the region indicated in figure 5A is presented in figure 5B and demonstrate that Cu, Mg and Si are found in the particles. The crystal structure of these particles is found to be the Q′-, L- and C-phase in addition disordered structures by the HAADF-STEM image shown in 5D.

An example of a sub-grain boundary within a $[111]_{Al}$ oriented grain with an associated misorientation of $< 1°$, is shown in figure 6. A PFZ of 100 nm separates the grain boundary from the bulk region. In figure 6A the grain boundary plane is rotated parallel to the electron beam and appears to have continuous segregation of Cu, Mg, and Si according to the EDS maps. In figure 6B the same grain boundary has been tilted and the presence of thin needles with growth direction along $[100]_{Al}$ can be seen. This is verified by following the direction of bulk precipitates on both sides of the interface. The grain boundary plane is close to $\{110\}_{Al}$, as can be seen from the diffraction pattern in figure 6A.

3.3. Corrosion

Discrete corrosion attacks typically extending 20–80 µm from single initiation points, were found across the surface of the 2 h corroded sample. EBSD inverse pole figure, grain misorientation and image quality maps, as well as secondary electron images of corrosion attacks were used to identify the type of grain boundaries and whether or not they had been corroded, as depicted in figure 7. Corroded GB segments (between triple points) are marked with yellow and when IGC stops at a triple point, the adjacent uncorroded grain boundaries are marked with cyan. The grain boundaries are then grouped into their respective category and the ratio of corroded grain boundaries to the total number of grain boundaries in contact with the IGC fissure is obtained. A total of 1396 grain boundaries from 10 EBSD maps were counted. This gives an indication of the IGC susceptibility for a given GB category.

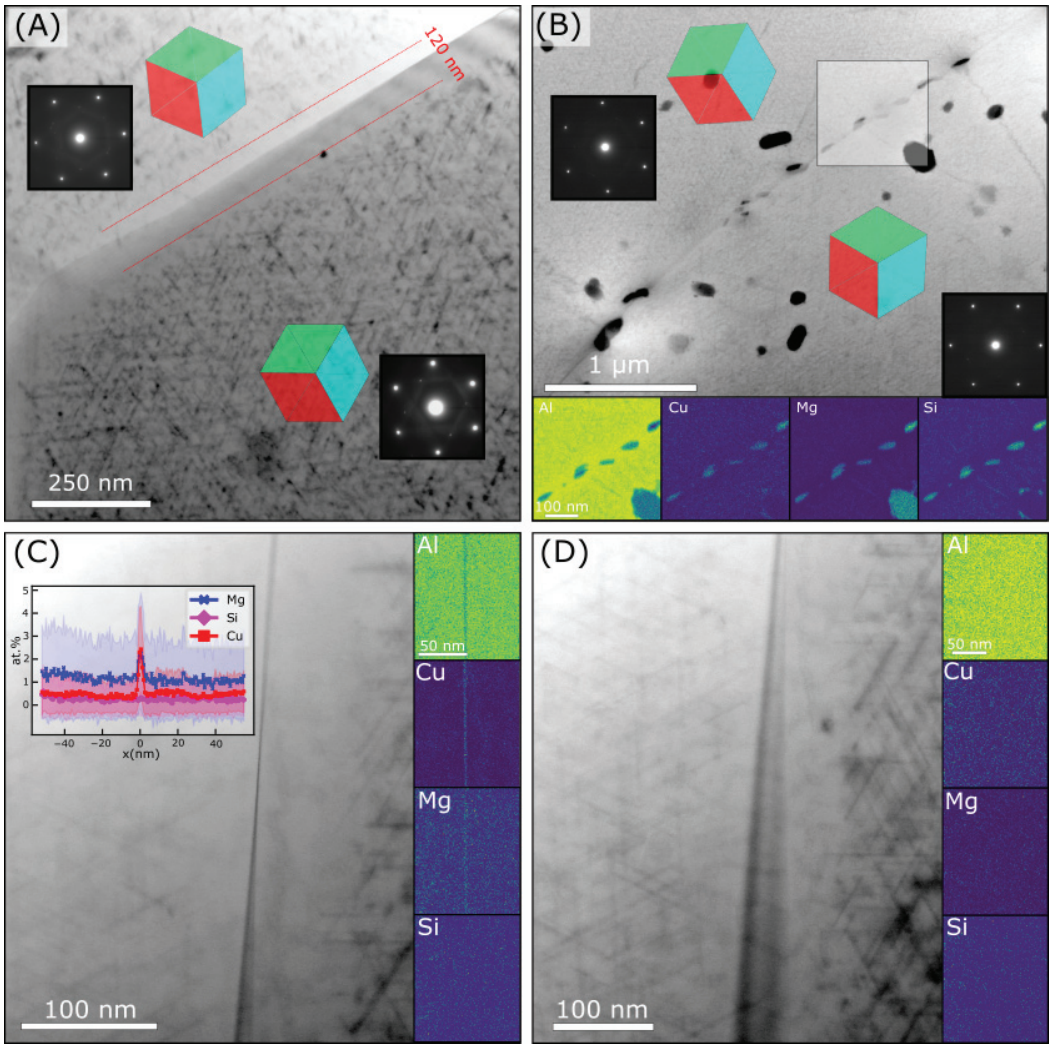

Figure 3: Two different $[111]_{Al}//[111]_{Al}$ type grain boundaries in (A) and (B). (C) Show the grain boundary in (A) aligned parallel with the electron beam. Clear indications of Cu and Mg segregation is seen in the EDS maps. (D) The same grain boundary after tilting away from its parallel alignment. The segregated elements are no longer observed.

Corroded/uncorroded grain boundaries were counted and the results are presented in table 2 according to their adjacent grain orientation and misorientation angle. The most apparent trend is that IGC fissures are more likely to follow grain boundaries with misorientations over 15°. The grain boundaries are also more likely to be attacked if one of the grains has a $<111>_{Al}$ direction parallel to the extrusion direction. Although the differences in the corroded fractions are small, the trends are consistent through each of the 10 corroded EBSD maps.

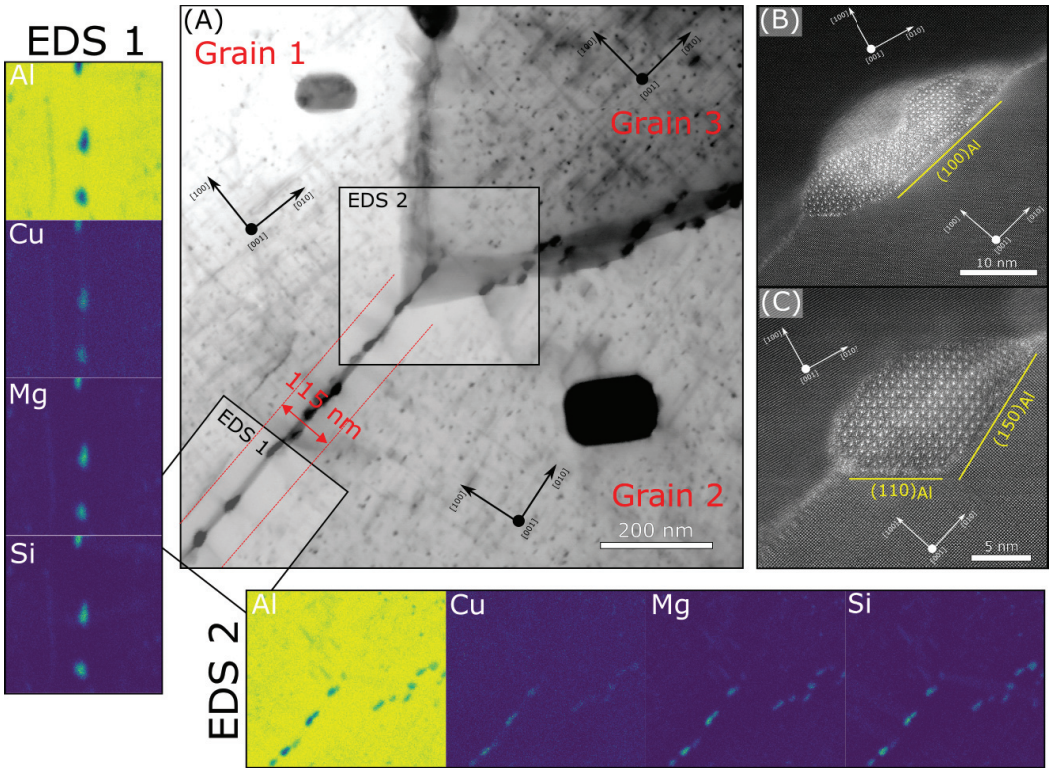

Figure 4: (A) BF-STEM image of grain boundaries between three grains oriented along $[001]_{Al}$. The misorientations between grains 1-2 and 2-3 are ~15° and ~5°, respectively. EDS maps acquired from the regions 'EDS 1' and 'EDS 2' are shown. (B) and (C) are high resolution HAADF-STEM images of particles demonstrating that they are the metastable Q′-phase with defined orientation relationship with (at least) one grain.

Table 2: Fraction of corroded grain boundary segments after a 2 hour exposure to the IGC test solution. Grain boundaries are separated into high- (HA, >15°), medium- (MA, 5–15°) and low- (LA, <5°) angle grain boundaries. The axis between the adjacent grains along the extrusion direction (ED) is indicated.

Direction (ED)	<001>//<111>	<001>//<001>			<111>//<111>		
GB type	HA	HA	MA	LA	HA	MA	LA
Corroded	269	58	46	31	116	61	86
Adjacent and intact	190	62	100	65	84	72	156
Total counted	459	120	146	96	200	133	242
Fraction corroded	59%	48%	32%	32%	58%	46%	36%

4. Discussion

In this work a method for statistical analysis of corroded grain boundaries has been presented. The results shown in table 2 demonstrate that the high-angle grain boundaries have a higher fraction of corrosion attacks than the medium- and low-angle grain boundaries. The combination of corrosion and TEM data indicates that grain boundaries with a high density of Q′-phase particles, are less prone to IGC attacks than boundaries where no particles are present.

A limitation of the method is that only the 2D dimensional corrosion paths are accounted for, while propagation

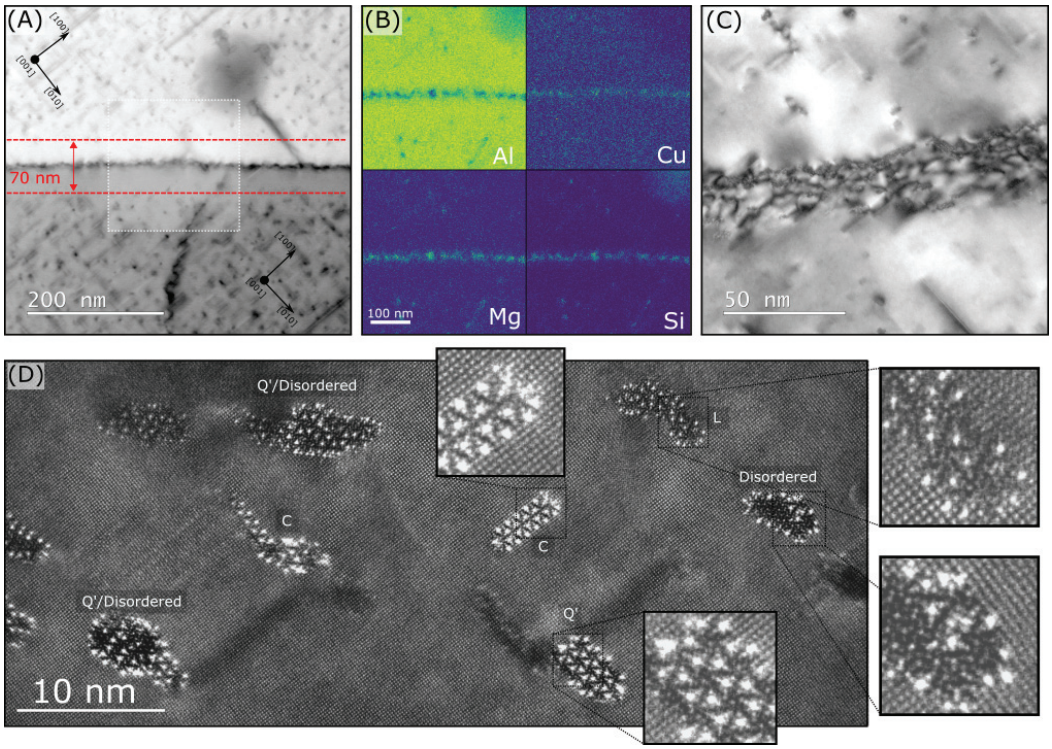

Figure 5: (A) BF-STEM image of a sub-grain boundary in a $[001]_{Al}$ oriented grain distinguished by an in-plane rotation of $< 0.5°$. (B) Shows the EDS results from the indicated region in (A). (C) BF-TEM image demonstrating that dislocations are associated with the grain boundary. (D) High resolution HAADF-STEM image of the particles present on the sub-grain boundary.

also proceeds to a depth of many tens of μm. The 3D path of the corrosion filaments may be complicated, e.g. in some cases two neighbouring attacks are not connected by IGC fissures along the surface, but may be connected deeper into the material. Furthermore, some uncorroded low-angle grain boundaries (<5°) may be overlooked as they must be inferred by small orientation changes or appearances in the image quality map. This might lead to an overestimation in the corroded fraction of low-angle grain boundaries. Despite these limitations, the present work provides statistical insights into grain boundary corrosion.

The classification scheme of the grain boundaries used in this study, enables a more fundamental understanding of the grain boundaries that are present in the alloy and highlights the statistical relevance of the insight gained from TEM studies. High-angle grain boundaries, represented by figure 2, always demonstrate Cu segregation and a few, large Q-phase particles. It is likely that the true Cu segregated layer is confined to 1-3 atomic layers and that the measured extended width is due to beam broadening effects [32]. Based on the high-resolution image presented in figure 2C, one may wonder how Cu atoms are situated at the grain boundary core. It may stabilise as a segregated layer in the form of a 'complexions' [33]. Another explanation is that the atoms find interstitial sites along the grain boundary, which may appear as a continuous layer when projected through the thickness (cf. figure 2C). This has, using ab-initio calculations, been shown to be the case for Cu in typical symmetric tilt (CSL) grain boundaries [34, 35]. A direct observation of ordered Cu was demonstrated at symmetric tilt boundaries in an AA7075 thin film alloy [36, 37]. With increasing misorientation, the distance between segregated Cu-sites decreased [37]. It is however uncertain as to what extent the knowledge obtained from symmetric tilt boundaries can be transferred to the general case of high-angle grain boundaries found in industrial Al alloys. Nevertheless, only one of the two grains in figure 2C is resolvable due

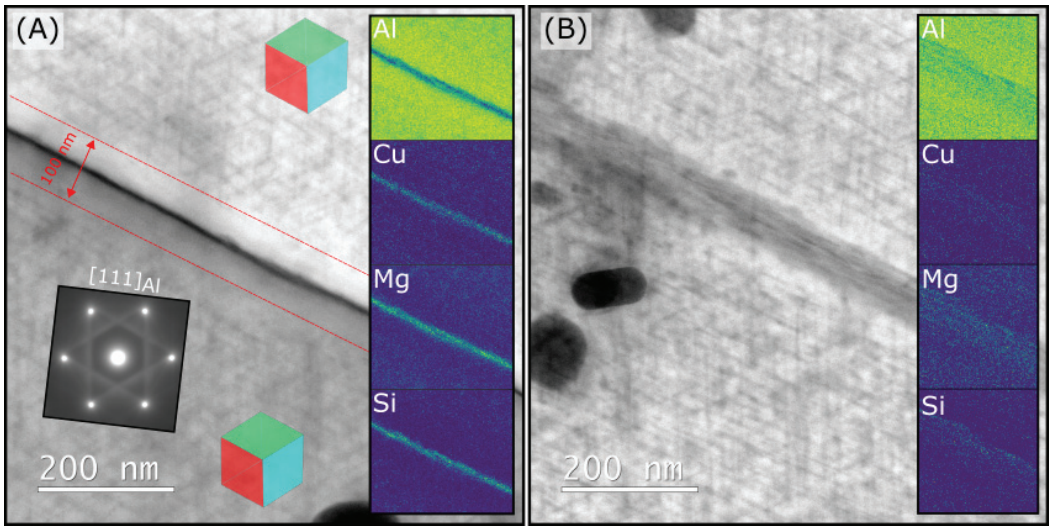

Figure 6: (A) BF-STEM image of a sub-grain boundary aligned parallel to the electron beam, in a grain oriented along the $[111]_{Al}$ axis separated by an in-plane rotation of $< 1.0°$. (B) Shows the same grain boundary inclined with respect to the electron beam. EDS maps of Al, Cu, Mg and Si are shown in both projections.

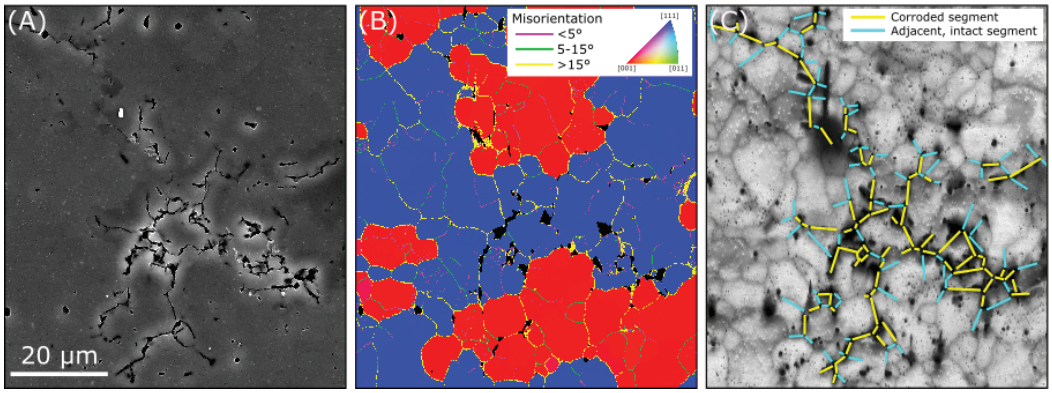

Figure 7: Methodology for studying IGC using EBSD. (A) Shows a secondary electron SEM image after 2 h exposure to the IGC test solution. (B) Inverse pole figure map with grain boundaries separated by misorientation angle. (C) EBSD image quality map, overlaid with corroded (yellow) and uncorroded (cyan) grain boundary segments.

to their orientation with respect to the electron beam, which is typically the case in these materials.

There are grain boundaries both with- and without particles, as demonstrated by figure 3. The fundamental reason for this must be related to GBPs interface plane and growth direction. If this follows a similar manner as the bulk hardening precipitates, the <001>//<001> grain boundaries are preferred over <111>//<111>, as the adjacent grains can rotate freely around the common <001> direction. This will generate both low- and high-angle grain boundaries with a common <001> direction, where metastable Q′-phase needle-like particles can grow. In the <111>//<111> case, a common <001> direction is only possible if the grain boundary plane is $\{110\}_{Al}$ for both adjacent grains. This might be an explanation for the slightly lower fraction of corroded grain boundaries between (<001>//<001>) as to

the (<111>//<111>) grain boundaries, cf. table 2.

Grain boundaries classified as sub-grain boundaries were shown in two different projections in figures 5 and 6. These exhibit the most dense distribution of GBPs, which are likely to have nucleated on dislocations arranged into cell-walls. In both cases, a solute depleted zone (PFZ) is observable. In principle, the galvanic coupling between the cathodic GBPs and anodic PFZ should provide the necessary electrochemical conditions for corrosion to occur.

The importance of grain boundary planes was recently elucidated further by Zhao et al., who reported that a grain boundary may decompose into different facets to reduce the total interface energy [38]. The different facets may lead to local segregated regions or preferential precipitation. This is in agreement with our observations and clearly emphasis the importance of high-resolution work to study interface planes, elemental segregation and grain boundary precipitation. Studies have previously been conducted in the Al-Zn-Mg (7xxx) [39–42] and Al-Cu (2xxx) [43, 44] alloy systems, and have demonstrated orientation dependent grain boundary precipitation. This work contributes with new insights of grain boundaries in Al-Mg-Si alloys, their different appearances and ways of studying them. However, more studies are needed to further understand grain boundary segregation and ways to exploit it through grain boundary engineering aluminium alloys [45]. An in-situ TEM study of grain boundary precipitation in these alloys is a suggested approach [39].

The study herein provides further insights into grain boundary structures in extruded aluminium alloys. Future studies should focus on quantifying the width and amount of Cu segregation in well defined grain boundaries using a correlative TEM and atom probe tomography (ATP) approach [46]. It is also important to understand 'large' scale grain boundary precipitation and IGC propagation. Further understanding may develop methods for engineering alloys having grain boundaries with lower susceptibility to IGC.

5. Conclusion

A detailed analysis of the grain boundaries in a highly textured Al-Mg-Si-Cu alloy has been presented and correlated with a statistical 2D analysis of corroded grain boundaries. The most important findings are:

- Corrosion data shows that intergranular corrosion is less likely to propagate at low-angle grain boundaries. Combined with the microstructural characterisation, the results suggest a reduced susceptibility to IGC with increasing density of metastable particles on the grain boundaries.
- There are large variations in particle densities along boundaries of the same type, most likely caused by changes in interface plane and growth direction.
- Low-angle sub-grain boundaries have an associated PFZ and the most dense distribution of GBPs.
- The GBPs found in this work are predominantly the metastable Q′-phase with defined orientation relationships with the Al matrix. Along sub-grain boundaries the Q′, C, L and disordered phases are found.

Acknowledgements

This work was supported by the KPN project 'FICAL' (NFR: 247598), co-financed by The Research Council of Norway (NFR), and the industrial partners Norsk Hydro ASA, Gränges, Benteler Automotive Raufoss AS and Steertec Raufoss. The (S)TEM work was conducted on the NORTEM (NFR: 197405) infrastructure at the TEM Gemini Centre, Trondheim, Norway.

References

[1] O. Reiso, Extrusion of AlMgSi alloys, Materials Forum 28 (2004) 32–46.

[2] J. Hirsch, Recent development in aluminium for automotive applications, Transactions of Nonferrous Metals Society of China 24 (2014) 1995–2002. doi:10.1016/S1003-6326(14)63305-7.

[3] J. K. Sunde, C. D. Marioara, A. T. J. van Helvoort, R. Holmestad, The evolution of precipitate crystal structures in an Al-Mg-Si(-Cu) alloy studied by a combined HAADF-STEM and SPED approach, Materials Characterization 142 (2018) 458 – 469. doi:10.1016/j.matchar.2018.05.031.

[4] W. F. Miao, D. E. Laughlin, Effects of Cu content and preaging on precipitation characteristics in aluminum alloy 6022, Metallurgical and Materials Transactions A 31 (2000) 361–371. doi:10.1007/s11661-000-0272-2.
[5] M. Murayama, K. Hono, W. Miao, D. E. Laughlin, The effect of Cu additions on the precipitation kinetics in an Al-Mg-Si alloy with excess Si, Metallurgical and Materials Transactions A 32 (2001) 239–246. doi:10.1007/s11661-001-0254-z.
[6] J. Man, L. Jing, S. G. Jie, The effects of Cu addition on the microstructure and thermal stability of an Al-Mg-Si alloy, Journal of Alloys and Compounds 437 (2007) 146–150. doi:10.1016/j.jallcom.2006.07.113.
[7] C. D. Marioara, S. J. Andersen, T. N. Stene, H. Hasting, J. Walmsley, A. T. J. Van Helvoort, R. Holmestad, The effect of Cu on precipitation in Al–Mg–Si alloys, Philosophical Magazine 87 (2007) 3385–3413. doi:10.1080/14786430701287377.
[8] T. Saito, C. D. Marioara, J. Røyset, K. Marthinsen, R. Holmestad, The effects of quench rate and pre-deformation on precipitation hardening in Al-Mg-Si alloys with different Cu amounts, Materials Science and Engineering A 609 (2014) 72–79. doi:10.1016/j.msea.2014.04.094.
[9] M. W. Zandbergen, A. Cerezo, G. D. W. Smith, Study of precipitation in Al-Mg-Si Alloys by atom probe tomography II. Influence of Cu additions, Acta Materialia 101 (2015) 149–158. doi:10.1016/j.actamat.2015.08.018.
[10] Q. Xiao, H. Liu, D. Yi, D. Yin, Y. Chen, Y. Zhang, B. Wang, Effect of Cu content on precipitation and age-hardening behavior in Al-Mg-Si-xCu alloys, Journal of Alloys and Compounds 695 (2017) 1005–1013. doi:10.1016/j.jallcom.2016.10.221.
[11] J. K. Sunde, C. D. Marioara, R. Holmestad, The effect of low cu additions on precipitate crystal structures in overaged al-mg-si(-cu) alloys, Materials Characterization 160 (2020) 110087. doi:10.1016/j.matchar.2019.110087.
[12] G. Svenningsen, M. H. Larsen, J. C. Walmsley, J. H. Nordlien, K. Nisancioglu, Effect of artificial aging on intergranular corrosion of extruded AlMgSi alloy with small Cu content, Corrosion Science 48 (2006) 1528–1543. doi:10.1016/j.corsci.2005.05.045.
[13] M. H. Larsen, J. C. Walmsley, O. Lunder, R. H. Mathiesen, K. Nisancioglu, Intergranular Corrosion of Copper-Containing AA6xxx AlMgSi Aluminum Alloys, Journal of The Electrochemical Society 155 (2008) C550. doi:10.1149/1.2976774.
[14] M. H. Larsen, J. C. Walmsley, O. Lunder, K. Nisancioglu, Effect of Excess Silicon and Small Copper Content on Intergranular Corrosion of 6000-Series Aluminum Alloys, Journal of The Electrochemical Society 157 (2010) C61–C68. doi:10.1149/1.3261804.
[15] S. K. Kairy, T. Alam, P. A. Rometsch, C. H. J. Davies, R. Banerjee, N. Birbilis, Understanding the Origins of Intergranular Corrosion in Copper-Containing Al-Mg-Si Alloys, Metallurgical and Materials Transactions A 47 (2016) 985–989. doi:10.1007/s11661-015-3296-3.
[16] C. D. Marioara, A. Lervik, J. Grønvold, O. Lunder, S. Wenner, T. Furu, R. Holmestad, The Correlation Between Intergranular Corrosion Resistance and Copper Content in the Precipitate Microstructure in an AA6005A Alloy, Metallurgical and Materials Transactions A 49 (2018) 5146–5156. doi:10.1007/s11661-018-4789-7.
[17] S. Kumari, S. Wenner, J. C. Walmsley, O. Lunder, K. Nisancioglu, Progress in Understanding Initiation of Intergranular Corrosion on AA6005 Aluminum Alloy with Low Copper Content, Journal of The Electrochemical Society 166 (2019) C3114–C3123. doi:10.1149/2.0211911jes.
[18] J. Holmestad, M. Ervik, C. D. Marioara, J. C. Walmsley, Investigation of Grain Boundaries in an Al-Mg-Si-Cu Alloy, Materials Science Forum 794-796 (2014) 951–956. doi:10.4028/www.scientific.net/MSF.794-796.951.
[19] S. H. Kim, U. Erb, K. T. Aust, G. Palumbo, Grain boundary character distribution and intergranular corrosion behavior in high purity aluminum, Scripta Materialia 44 (2001) 835 – 839. doi:10.1016/S1359-6462(00)00682-5.
[20] A. Bałkowiec, J. Michalski, H. Matysiak, K. J. Kurzydlowski, Influence of grain boundaries misorientation angle on intergranular corrosion in 2024-T3 aluminium, Materials Science- Poland 29 (2011) 305–311. doi:10.2478/s13536-011-0050-4.
[21] L. H. Chan, H. Weiland, S. Cheong, G. S. Rohrer, A. D. Rollett, The Correlation between Grain Boundary Character and lntergranular Corrosion Susceptibility of 2124 Aluminum Alloy, John Wiley & Sons, Ltd, 2008, pp. 261–267. doi:10.1002/9780470444214.ch28.
[22] T. Minoda, H. Yoshida, Effect of grain boundary characteristics on intergranular corrosion resistance of 6061 aluminum alloy extrusion, Metallurgical and Materials Transactions A 33 (2002) 2891–2898. doi:10.1007/s11661-002-0274-3.
[23] S. K. Kairy, P. A. Rometsch, C. H. J. Davies, N. Birbilis, On the Intergranular Corrosion and Hardness Evolution of 6xxx Series Al Alloys as a Function of Si:Mg Ratio, Cu Content, and Aging Condition, Corrosion 9312 (2017) 1280–1296. doi:10.5006/2506.
[24] W. Chrominski, M. Lewandowska, Precipitation phenomena in ultrafine grained Al-Mg-Si alloy with heterogeneous microstructure, Acta Materialia 103 (2016) 547–557. doi:10.1016/j.actamat.2015.10.030.
[25] T. Saito, E. A. Mørtsell, S. Wenner, C. D. Marioara, S. J. Andersen, J. Friis, K. Matsuda, R. Holmestad, Atomic Structures of Precipitates in Al-Mg-Si Alloys with Small Additions of Other Elements, Advanced Engineering Materials 1800125 (2018) 1–18. doi:10.1002/adem.201800125.
[26] W. Yang, S. Ji, Z. Li, M. Wang, Grain boundary precipitation induced by grain crystallographic misorientations in an extruded Al-Mg-Si-Cu alloy, Journal of Alloys and Compounds 624 (2015) 27–30. doi:10.1016/j.jallcom.2014.10.206.
[27] C. D. Marioara, S. J. Andersen, J. Røyset, O. Reiso, S. Gulbrandsen-Dahl, T. E. Nicolaisen, I. E. Opheim, J. F. Helgaker, R. Holmestad, Improving thermal stability in Cu-containing Al-Mg-Si alloys by precipitate optimization, Metallurgical and Materials Transactions A 45 (2014) 2938–2949. doi:10.1007/s11661-014-2250-0.
[28] F. Bachmann, R. Hielscher, H. Schaeben, Texture analysis with mtex – free and open source software toolbox, in: Texture and Anisotropy of Polycrystals III, volume 160 of *Solid State Phenomena*, Trans Tech Publications Ltd, 2010, pp. 63–68. doi:10.4028/www.scientific.net/SSP.160.63.
[29] R. Krakow, R. J. Bennett, D. N. Johnstone, Z. Vukmanovic, W. Solano-Alvarez, S. J. Lainé, J. F. Einsle, P. A. Midgley, C. M. Rae, R. Hielscher, On three-dimensional misorientation spaces, Proceedings of the Royal Society A: Mathematical, Physical and Engineering Sciences 473 (2017). doi:10.1098/rspa.2017.0274.
[30] L. Jones, H. Yang, T. J. Pennycook, M. S. J. Marshall, S. Van Aert, N. D. Browning, M. R. Castell, P. D. Nellist, Smart align - a new tool for robust non-rigid registration of scanning microscope data, Advanced Structural and Chemical Imaging 1 (2015) 8. doi:10.1186/s40679-015-0008-4.
[31] F. de la Peña, E. Prestat, V. T. Fauske, P. Burdet, P. Jokubauskas, M. Nord, T. Ostasevicius, K. E. MacArthur, M. Sarahan, D. N. Johnstone, J. Taillon, J. Lähnemann, V. Migunov, A. Eljarrat, J. Caron, T. Aarholt, S. Mazzucco, M. Walls, T. Slater, F. Winkler, pquinn dls, B. Martineau, G. Donval, R. McLeod, E. R. Hoglund, I. Alxneit, D. Lundeby, T. Henninen, L. F. Zagonel, A. Garmannslund, hyperspy/hyperspy: Hyperspy v1.5.2, 2019. doi:10.5281/zenodo.3396791.

[32] J. D. Robson, Analytical electron microscopy of grain boundary segregation: Application to Al-Zn-Mg-Cu (7xxx) alloys, Materials Characterization 154 (2019) 325–334. doi:10.1016/j.matchar.2019.06.016.
[33] P. R. Cantwell, M. Tang, S. J. Dillon, J. Luo, G. S. Rohrer, M. P. Harmer, Grain boundary complexions, Acta Materialia 62 (2014) 1 – 48. doi:10.1016/j.actamat.2013.07.037.
[34] R. Mahjoub, K. J. Laws, N. Stanford, M. Ferry, General trends between solute segregation tendency and grain boundary character in aluminum - An ab inito study, Acta Materialia 158 (2018) 257–268. doi:10.1016/j.actamat.2018.07.069.
[35] D. Zhao, O. M. Løvvik, K. Marthinsen, Y. Li, Segregation of Mg, Cu and their effects on the strength of Al Σ5 (210)[001] symmetrical tilt grain boundary, Acta Materialia 145 (2018) 235–246. doi:10.1016/j.actamat.2017.12.023.
[36] P. Parajuli, R. Mendoza-Cruz, A. Hurtado-Macias, U. Santiago, M. J. Yacamán, A Direct Observation of Ordered Structures Induced by Cu Segregation at Grain Boundaries of Al 7075 Alloys, Physica Status Solidi (A) Applications and Materials Science 215 (2018) 1–8. doi:10.1002/pssa.201800240.
[37] P. Parajuli, D. Romeu, V. Hounkpati, R. Mendoza-Cruz, J. Chen, M. J. Yacamán, J. Flowers, A. Ponce, Misorientation dependence grain boundary complexions in <111> symmetric tilt Al grain boundaries, Acta Materialia 181 (2019) 216–227. doi:10.1016/j.actamat.2019.09.010.
[38] H. Zhao, L. Huber, W. Lu, N. J. Peter, D. An, F. De Geuser, G. Dehm, D. Ponge, J. Neugebauer, B. Gault, D. Raabe, Interplay of Chemistry and Faceting at Grain Boundaries in a Model Al Alloy, Physical Review Letters 124 (2020) 1–6. doi:10.1103/physrevlett.124.106102.
[39] E. P. Butler, P. R. Swann, In situ observations of the nucleation and initial growth of grain boundary precipitates in an Al-Zn-Mg alloy, Acta Metallurgica 24 (1976) 343–352. doi:10.1016/0001-6160(76)90009-2.
[40] R. Gronsky, P. Furrer, Grain Boundary Precipitation in Aluminum Alloys: Effect of Boundary Structure., Metallurgical transactions. A 12 A (1981) 121–127. doi:10.1007/BF02648516.
[41] J. K. Park, A. J. Ardell, Precipitation at grain boundaries in the commercial alloy Al 7075, Acta Metallurgica 34 (1986) 2399–2409. doi:10.1016/0001-6160(86)90143-4.
[42] Czurratis P., Kroggel R. and H. Löffler, Precipitation structure in an Al-2.0at.%Zn-1.0at.%Mg alloy within and close to the grain boundaries and its effects on mechanical properties, Czechoslovak Journal of Physics B 38 (1988) 444–456.
[43] D. Vaughan, Grain boundary precipitation in an AlCu alloy, Acta Metallurgica 16 (1968) 563–577. doi:10.1016/0001-6160(68)90131-4.
[44] D. Vaughan, The precipitation of θ′ at high-angle boundaries in an al-cu alloy, Acta Metallurgica 18 (1970) 183 – 187. doi:10.1016/0001-6160(70)90082-9.
[45] D. Raabe, M. Herbig, S. Sandlöbes, Y. Li, D. Tytko, M. Kuzmina, D. Ponge, P. P. Choi, Grain boundary segregation engineering in metallic alloys: A pathway to the design of interfaces, Current Opinion in Solid State and Materials Science 18 (2014) 253–261. doi:10.1016/j.cossms.2014.06.002.
[46] M. Herbig, D. Raabe, Y. J. Li, P. Choi, S. Zaefferer, S. Goto, Atomic-scale quantification of grain boundary segregation in nanocrystalline material, Physical Review Letters 112 (2013) 1–5. doi:10.1103/PhysRevLett.112.126103.

Paper III

The correlation between intergranular corrosion resistance and copper content in the precipitate microstructure in an AA6005A alloy

Calin Daniel Marioara, Adrian Lervik, Julie Grønvold, Otto Lunder, Sigurd Wenner, Trond Furu, Randi Holmestad

Metallurgical and Materials Transactions. A. **49**, (2018) 5146-5156.
DOI:10.1007/s11661-018-4789-7

Paper IV

Atomic structure of solute clusters in Al-Zn-Mg alloys

Adrian Lervik, Elisabeth Thronsen, Jesper Friis, Calin Daniel Marioara, Sigurd Wenner, Artenis Bendo, Kenji Matsuda, Randi Holmestad, Sigmund Jarle Andersen

To be submitted

Atomic structure of solute clusters in Al-Zn-Mg alloys

A. Lervik[1,*], E. Thronsen[1], J. Friis[1,2], C.D. Marioara[2], S. Wenner[1,2], A. Bendo[3], K. Matsuda[3], R. Holmestad[1] & S.J. Andersen[2]

[1]*Department of Physics, Norwegian University of Science and Technology (NTNU), N-7491 Trondheim, Norway*

[2]*SINTEF Industry, N-7465, Trondheim, Norway*

[3]*Graduate School of Science and Engineering, University of Toyama, 3190 Gofuku, Toyama, 930-8555, Japan*

** Corresponding author*

Scanning transmission electron microscopy imaging of Al-Zn-Mg alloys has provided new information on the atomic structures of solute rich clusters forming from a supersaturated solid solution at low temperatures. A novel type of cluster unit of high Zn/Mg ratio is the fundamental building block in all observed cluster configurations. The unit is essentially a partial substitution by Mg and Zn on the cubic aluminum cell and its surrounding truncated cube octahedral shell. A simple set of principles based on Frank-Kasper structures describes how the basic units arrange with respect to each other to form larger clusters. Density functional theory calculations, atom probe tomography and simulated diffraction patterns support the proposed atomic models. The results are relevant to all Al-Zn-Mg alloys and provide new insight into the very early stages of age-hardening.

1 Main

This work investigates solute clusters forming at low temperature in alloys of the Al-Zn-Mg (7xxx) system. These materials are important in the transportation industry, due to good formability and a high strength-to-weight ratio[1,2]. In order to obtain the strength in age hardenable aluminium alloys, a high temperature solution heat treatment (SHT) is required to dissolve most of the solute. A quenching to room temperature will retain high proportions of solutes and vacancies in the Al face centered cubic (fcc) lattice, leading to a supersaturated, metastable solid solution. By keeping the material at room temperature, the hardness will gradually increase, as first discovered by Alfred Wilm in the early 1900s[3]. This effect is called 'natural ageing (NA)' and is caused by solute atoms aggregating to clusters on the fcc lattice. The solute clusters act as small obstacles in the Al lattice, which will obstruct dislocation movements during plastic deformation and contribute to strength.

Solute clusters with periodic ordering are commonly referred to as 'Guinier-Preston (GP) zones', after their discoverers in 1938[4,5]. In Al-Zn-Mg alloys, two generic types of GP-zones have been suggested: GP(I) related to solute rich clusters[6–10], and GP(II) related to vacancy rich clusters [6–12]. Earlier studies have suggested that both play key roles during the subsequent artificial ageing (AA) stage, typically conducted at temperatures between 120-200 °C, especially in initiating the formation of the coherent, hardening precipitate structures η ($MgZn_2$)[6,13–18]. GP(I) zones have been found to exist even after longer ageing times[6,9,19,20]. The GP(II) zones are suggested as possible precursors of the metastable η' precipitate[6,9]. However, the mechanisms for nucleation and/or structural transformation from clusters to precipitates are not understood[12].

This work focuses on the structure of the solute rich clusters formed at low temperature, i.e. the 'GP(I) zones'. These have previously been reported in studies using transmission electron microscopy (TEM)[8,21–23], X-ray diffraction (XRD)[11,24–26] and positron annihilation spectroscopy (PAS)[11,27]. Up till now, a simple anti-phase ordering of solute has been proposed based on diffraction patterns acquired from large regions[8]. This work shows that the ordering is of a fundamentally different kind, and uncovers the atomic structure of the GP(I) zones with support from experimental techniques, simulations and calculations.

Microstructure overview Two alloys with different composition were investigated in this work. Alloy #1 is an industrial alloy (7046.70), which was stored 17 years at room temperature after extrusion. Alloy #2 is a high purity lab-cast alloy which was both naturally aged and heat treated at various temperatures (cf. Method section for details). Conventional bright field (BF)-TEM imaging along the [001] orientation showed a high density of small (1-2 nm) clusters uniformly distributed within the Al matrix, as demonstrated in Fig. 1**a** for Alloy #1. Fig. 1**b** shows the corresponding selected area diffraction pattern (SADP). Two types of diffraction spots appear between the Al reflections. The set of sharp spots (red discs) on the (forbidden) $\{100\}$ and $\{110\}$ positions in Fig. 1**b** originates from larger Al_3Zr dispersoids[28,29]. The set of diffuse spots (yellow triangles) originates from clusters that can be seen in high-angle annular dark field (HAADF)-scanning transmission electron microscopy (STEM) images as in Fig. 1**c**. The spots are a result of a high density combined with the different crystallographically equivalent orientations the clusters can have with the aluminum, while the spread in intensity is due to their small physical size. The fast Fourier transform (FFT) of the HAADF-STEM image in Fig. 1**c**, is shown in Fig. 1**d**. It is clearly similar

to the SADP in Fig. 1**b**. The diffuse, high-intensity spots at the forbidden $\{110\}$ positions in Fig. 1**d** have a different origin. These are due to an artefact caused by the TEM sample preparation (electropolishing), where a distinct surface layer was formed, which is explained in more detail in the Supplementary Information. It should not be confused with the clear diffraction from the larger Al_3Zr dispersoids (cf. Fig. 1**b**). The weak diffraction spots in the SADPs have previously been associated with GP(I) zones[8–10,21,22,28,30–33]. After 2 weeks and after 8 months NA, as well as for 8 min ageing at 120 °C, Alloy #2 exhibits the same diffuse diffraction spots as Alloy #1 (Fig. 1) with only slight variation in intensities. This is shown in Supplementary Fig. 2.

Cluster statistics and composition by atom probe tomography Alloy #1 was investigated by atom probe tomography (APT). Fig. 2**a** shows the Mg and Zn atoms inside the defined clusters after 17 years NA in an evaporated APT needle. As expected, dense co-clustering of Mg and Zn atoms is present. The composition of each cluster as function of total number of atoms within the cluster is shown in Fig. 2**b**. Large clusters consistently have a higher fraction of Al than the smaller clusters (down to 50 atoms). The mean cluster diameter is 1.45 nm, and the Zn/Mg ratio, which is shown as a function of the cluster diameter in Fig. 2**c**, has an average near 1.8. The average composition of all clusters (with standard deviations) was estimated as 67±6% Al, 22±4% Zn, 12±3% Mg (at.%). Including only clusters larger than 1000 atoms gives: 70±3% Al, 20±2% Zn, 10±1% Mg, which corresponds to approximately Al_7Zn_2Mg. The measured Zn/Mg ratio is slightly higher than values reported in other APT studies[23,28,30,34–36]. However, these studies are not directly comparable as the alloys have different compositions and heat-treatments. Differences in the NA times of the materials can also affect the cluster composition [23]. In Cu-containing alloys,

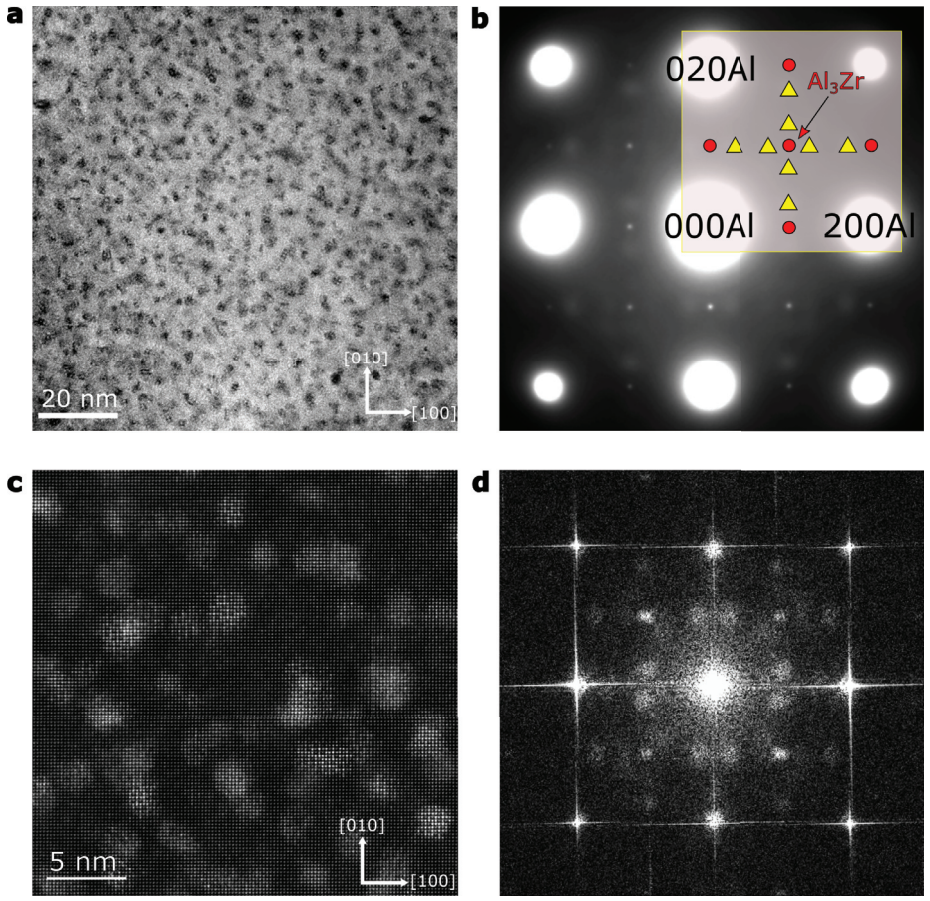

Fig. 1: Alloy #1 after 17 years of natural ageing, oriented along the [001] direction. **a**, BF-TEM micrograph showing a high density of solute clusters (dark contrast). **b**, SADP with diffraction spots of Al_3Zr dispersoids and GP(I) zones, marked by disks and triangles, respectively. **c**, HAADF-STEM image clearly indicating ordering of solute on the fcc lattice. **d**, FFT of **c** where the intensity in the forbidden $\{110\}$ positions are due to a surface layer artefact.

Cu tends to substitute Zn positions in the metastable precipitates as well as in the clusters [14,34]. The high amount of Al measured in the clusters is in agreement with other studies [28,34,36]. Local magnification effects may also cause compositional errors at small scales[37]. In the regions between the clusters, the Al matrix was found to contain 1.65 and 0.54 at.% Zn and Mg, respectively. From the APT dataset, the number density of clusters was determined to be approximately $5.2 \cdot 10^{24}\ \mathrm{m}^{-3}$ with an average nearest neighbor separation of 4.5 $\pm$ 1.0 nm. The obtained values for mean size and number density are in correspondence with other studies using small-angle X-ray scattering (SAXS)[11,26,38].

Cluster units and their stacking principles The APT (Fig. 2**a**) and HAADF-STEM (Fig. 1**c**) results show that the clusters are equiaxed. Along a $\langle 100 \rangle$ orientation, approximately 1/3 of the non-overlapped clusters exhibits a clear atomic structure. Inspecting HAADF-STEM images like Fig. 1**c** at higher magnification, indicates that the atom positions belonging to clusters deviate little from the Al lattice positions. This is shown in Figs. 3**a** and 3**c**, where HAADF-STEM images of two representative single clusters are displayed. Based on the intensities and interatomic distances, suggested atomic motifs of Figs. 3**a** and 3**c** are given in 3**b** and 3**d**, respectively. Blue and red disks correspond to columns with Mg and Zn substitutions, respectively. The analysis demonstrates that the clusters may be simplified in terms of one unit with positions forming a pattern of projected squares and triangles. This unit is identified by a unique high-intensity column, the center where two rows of 5 bright columns along the lateral $\langle 100 \rangle$ Al directions intersect. Together with the observation that the nearest four Zn columns of the center are pushed slightly away, this indicates that the center of the unit contains an interstitial position relative to the FCC Al, i.e. the 'Interstitial

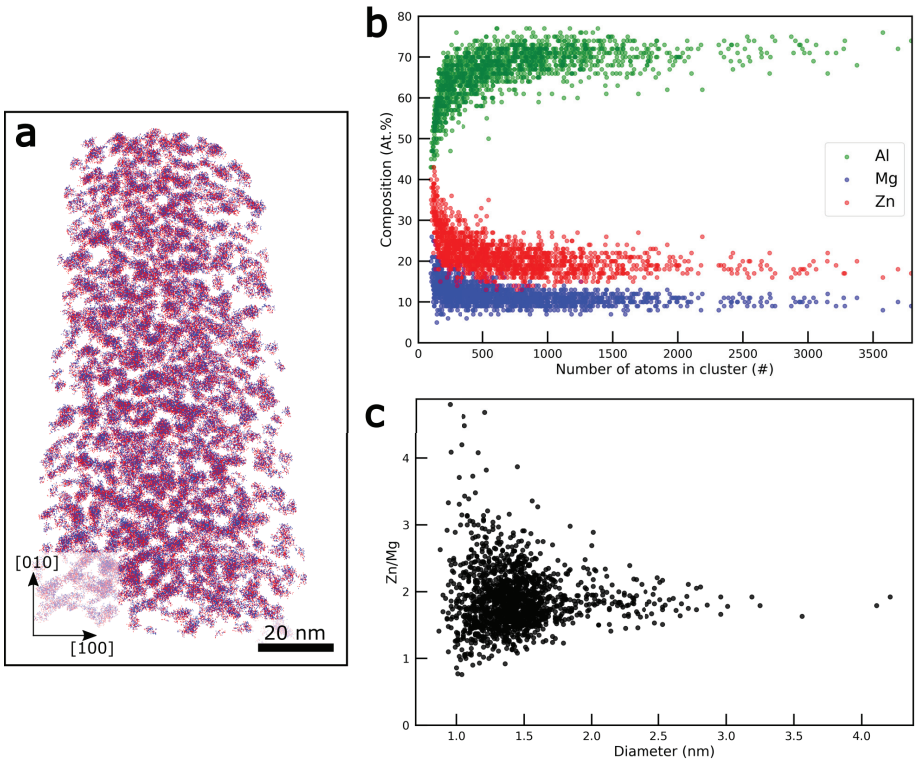

Fig. 2: **a**, Solute atoms inside clusters in Alloy #1 with 17 years NA, as measured by atom probe tomography. Blue is Mg and red is Zn. **b** shows the composition of clusters against the number of atoms in each cluster. **c** shows the Zn/Mg ratio versus the diameter of the cluster.

site' in Fig. 3.

In the HAADF-STEM images along the [001] zone axis, the unit has 4-fold symmetry in projection. The solute arrangement of the unit compatible with the observations is a three-shell structure centered on an Al cube with a possible interstitial. Six Zn atoms occupy the side faces of the FCC cube, forming an octahedron surrounding the interstitial. Eight Mg atoms are the second

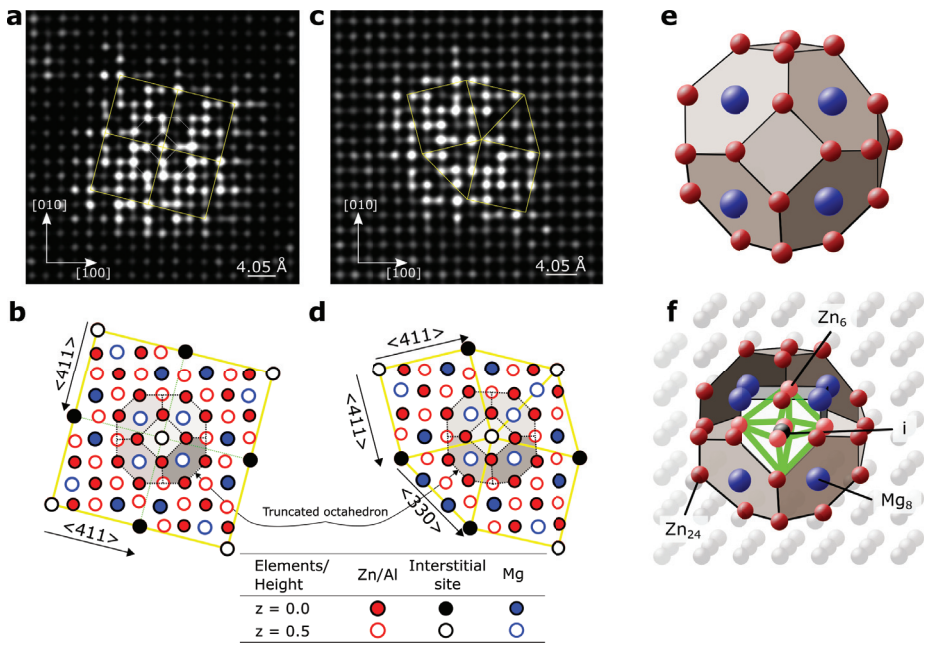

Fig. 3: **a, c**, Filtered HAADF-STEM images of two clusters. **b, d**, Suggested atomic column maps of **a** and **c**, showing connection principles ($\langle 411 \rangle$, $\langle 330 \rangle$) between unit centers, denoted 'Interstital site'. **e**, TCO-shell with Zn on all vertices and Mg on corners. **f**, interior view of cluster unit with interstitial 'i', embedded in Al.

nearest neighbours and occupy the corners of the cube. The outer shell surrounding the inner cube, which is a truncated cube octahedron (TCO), consists of 24 Zn atoms. This suggests that the cluster is composed of three polyhedra (with ideal compositions): the Zn_6 octahedron, the Mg_8 cube and the Zn_{24} TCO around a common interstitial center 'i'. This is illustrated in Figs. 3**e** and 3**f** where the cluster unit can be seen to span two Al-periods (8.1 Å). Thus, along the [001] direction the stacking is abbreviated by '[002]'. The TCO has six square and eight hexagonal faces, coinciding

with the $\{100\}$ and $\{111\}$ Al planes, respectively, as shown in Fig. 3**e**. The 24 vertices are given by permutations of the lattice vector $\frac{1}{2}\langle 120\rangle$ from the center of the cube.

Individual clusters show variations in structure, as in Figs. 3**a** and 3**c**. However, they can always be explained in terms of the described TCO unit stacked according to three principles. The first is that the unit aligns along [002], as stated earlier. The two other principles determine the lateral plane normal to this direction. Both give inter-distance 8.59 Å along $\langle 411\rangle$ and $\langle 330\rangle$, as shown in Fig. 3. The yellow lines connect the distinct 'Interstitial site' center of the units. The analysed images showed that the most common lateral connection was along $\langle 411\rangle$. Many clusters were found to have only this arrangement. In Figs. 3**a** and 3**b** four units arrange in a $\langle 411\rangle$ connected square. This is repeated in the viewing direction by the [002] connection. Figs. 3**c** and 3**d** show that the projected $\langle 330\rangle$ and $\langle 411\rangle$ connections together form squares and triangles in a particular pattern which is called a σ-type Frank-Kasper ordering[39].

Density functional theory calculations In order to elucidate the suggested structure, density functional theory (DFT) calculations of cluster units embedded in 4×4×4 Al cells containing 256 atoms were conducted to check their stability. We describe the unit by the formulae $\mathrm{iZ}_x\mathrm{M}_8\mathrm{Z}_y$, referring to the four constituents: an interstitial and three polyhedra (cf. Fig. 3**f**). The 'i' (= a, z or m) indicates the interstitial atom (Al, Zn or Mg, respectively). If this character is omitted, the cluster has no interstitial center. Z_x ($x = 0, ..., 6$) indicates the number of Zn atoms replacing Al on the cube sides, M_8 = Mg_8 are the corners of the cube and Z_y ($y = 0, ..., 24$) is the number of Zn on the TCO shell. The maximum number of atoms in the cluster unit is 39 including the

interstitial. Fig. 4 shows formation enthalpy versus pressure for a range of configurations of cluster units (given as tables in Supplementary Tabs. 1 and 2).

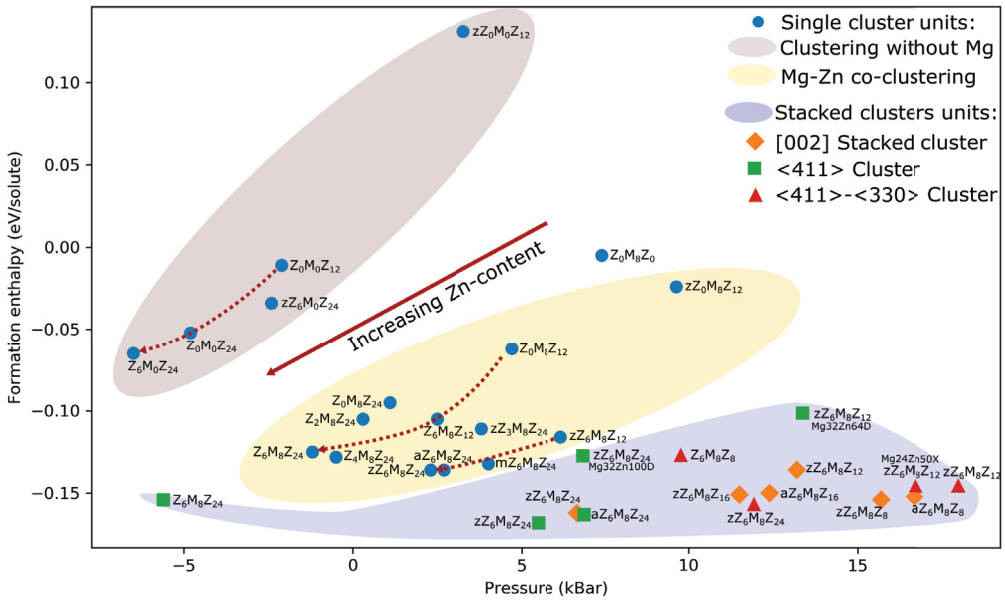

Fig. 4: DFT results showing the formation enthalpy versus pressure for cluster structures with different Al, Zn, and Mg content, showing the advantage of increasing Zn in the structures. Compositions refer to net content in the cluster unit after stacking.

The DFT calculations show that the cluster units prefer high Zn/Mg ratios and the two Zn-containing shells filled by Zn. Fig. 4 shows that a fully occupied TCO ($Z_y, y = 24$) is stabilising giving 9 of the 11 lowest energies with Zn/Mg ratios above 3. The best energies are obtained when both the Zn shells are fully occupied ($Z_x, x = 6$ and $Z_y, y = 24$). Furthermore, fully occupied Zn shells are preferred also with no Mg (M_0) in the clusters. For example, the energy improves as $Z_0M_0Z_{12} \rightarrow Z_0M_0Z_{24} \rightarrow Z_6M_0Z_{24}$ while pressure falls. The pressure is a measure of the misfit

volume with respect to a supercell only containing Al. Adding an interstitial ($zZ_6M_0Z_{24}$) improves pressure, but gives more unfavourable formation enthalpy. An interstitial Zn atom in $Z_0M_0Z_{12}$ ($zZ_0M_0Z_{12}$) is directly unfavourable. Thus, there is a preference for an interstitial only if the cube corners are filled with Mg, and at least one of the polyhedra are filled with Zn, but preferably both.

Almost any symmetrical ordering of the solute atoms compatible with fcc symmetry reduces energy, compared to having the Mg and Zn atoms in solid solution. For example, $Z_0M_8Z_0$ demonstrates that a small energy gain is achieved if the eight Mg atoms take the corners of an Al cell instead of remaining in arbitrary solid solution. Configurations $Z_0M_8Z_{24}$, $Z_2M_8Z_{24}$, $Z_4M_8Z_{24}$ and $Z_6M_8Z_{24}$ improve the formation enthalpy when the inner octahedron (Z_x) fills up as 0, 2, 4 and 6, respectively. The small increase in energy from $Z_6M_8Z_{24}$ to $Z_4M_8Z_{24}$ corresponds with a sign change in pressure. However, when an interstitial is added to $Z_6M_8Z_{24}$, three configurations of $iZ_6M_8Z_{24}$ are obtained with the overall lowest formation enthalpies and nearly similar energies. With a filled Mg cube (Mg_8), the calculations show that energy decreases with more Zn. However, $zZ_3M_8Z_{24}$ shows similar energy gain per solute as $zZ_6M_8Z_{12}$ despite a high Zn/Mg ratio. The reason is likely due to lower symmetry: the distribution of Zn atoms in the inner octahedron conserves one 3-fold axis, but destroys the 4- and 2-fold axes. With $zZ_6M_8Z_{12}$ the inner shell is filled, while the TCO conserves the 3- and 2-fold axes. Lower symmetry increases pressure and impedes the stacking.

Stacking of cluster units Having established that the three most energetically favourable cluster units are of $iZ_6M_8Z_{24}$ type, they were subsequently used to investigate the stability of larger clus-

ters. Two different types of stacking principles were used to build the models, (1): cluster units stacked along [002] and (2): four cluster units in a ring created by $\langle 411 \rangle$ connections. It is shown illustratively how the cluster base unit stacks in Fig. 5 and the $\langle 411 \rangle$ ring is shown in projection in Fig. 6**a**. Two consistent calculation supercells, 4×4×2 and 6×6×2 Al cells, were used for the [002] and the $\langle 411 \rangle$ stacked clusters, respectively. The calculations were done with Zn both fully and semi-occupied in the TCO shells. The results are marked by crosses in Fig. 4 and labeled '[002] Stacked clusters' and '$\langle 411 \rangle$ Cluster'. Based on the calculations, it can be concluded that clusters stacked along [002] are more energetically favourable than single cluster units embedded in the Al matrix. Moreover, by connecting the [002] stacked clusters in a $\langle 411 \rangle$ manner the lowest formation enthalpies are obtained for models containing an interstitial, which is in accordance with the analysis of HAADF-STEM images presented in Fig. 3.

The Zn/Mg ratio in the APT measurements was seen to approach 2 for larger cluster sizes. In an infinite string of [002] connected units every unit shares 8 positions. Thus, for the Zn completed cluster with Zn interstitial ($zZ_6M_8Z_{24}$), the number of Zn in the outer shell (Z_y) is reduced to 20, which results in an overall composition Mg_8Zn_{27}. The sharing of atoms due to the stacking of cluster base units is emphasised in Fig. 5 where the shared Zn atoms are surrounded by black disks. Connecting four $zZ_6M_8Z_{24}$ units in a $\langle 411 \rangle$ square, means for each unit that 4 TCO positions are shared through the edges. Therefore, a TCO unit $zZn_6M_8Z_{24}$ in an infinite stack of rings shares 12 atoms with neighbors and 'reduces' to $zZ_6M_8Z_{18}$ (Mg_8Zn_25). The Zn/Mg ratio (3.1) is still too high compared to APT measurements. Although the calculations showed that single clusters prefer high Zn/Mg ratios, this suggests that the TCO and/or inner octahedron contain Al. HAADF-STEM

image simulations show that this is a real possibility, since the intensity of the columns pertaining to the TCO and octahedron varies in the real images, whereas in the simulated image the intensity is constant due to the constant amount of Zn in each column. This is shown in Supplementary Fig. 4. Moreover, the presented atomic models do not account properly for the cluster-matrix interface. By comparing the simulated image to the real image, it becomes clear that our models overestimate the Zn as they do not properly account for the cluster-matrix interface atomic columns. This is shown in Supplementary Fig. 4.

Phases taking Frank-Kasper structures are known to have flexible compositions [39]. The APT data and simulated HAADF-STEM images suggest that the Zn shells contain substantial amounts of Al. Larger clusters are likely to contain more Al according to the APT measurements. Thus, we suggest that the TCO clusters start with full shells and higher Zn/Mg ratios, as is supported by the DFT calculations and APT measurments. The sharing of the Zn rich TCO shell also contributes to a lower Zn/Mg ratio.

Diffraction from a single cluster The contribution from a single cluster to the weak SADP diffraction spots (cf. Fig. 1**b**), was investigated. To the authors' knowledge, diffraction patterns from single clusters in these alloys have never before been published. Using the models evaluated by DFT calculations, nanobeam diffraction (NBD) patterns were simulated. The $\langle 411 \rangle$ connected $zZ_6M_8Z_{24}$ cluster with the lowest formation enthalpy was selected. It is shown as embedded in the Al matrix in Fig. 6**a**. A corresponding simulated NBD pattern for $t = 40\,\text{Å}$ is given in Fig. 6**b**. A montage of diffraction patterns ranging from 4 to 340 monolayers (0.8 to 69 nm), is shown in

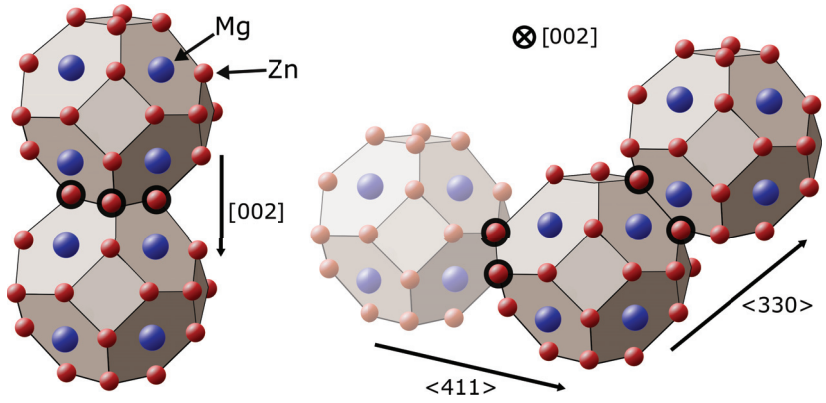

Fig. 5: Schematic ilustration of the TCO unit stacking principles [002], $\langle 330 \rangle$ and $\langle 411 \rangle$ observed in the clusters. Note that the stacking causes certain atoms to be shared: two TCOs share 4, 2 and 2 positions, respectively, lowering overall Zn/Mg ratio as compared to one TCO unit embedded in an Al matrix alone. The shared atoms are emphasised in the figure. Both DFT calculations and APT suggest a considerable amount of Al in the TCO.

Supplementary Fig. 5. NBD patterns were also simulated for clusters buried by Al (Supplementary Fig. 6). In Fig. 6**c**, a 'Smart Aligned'[40] HAADF-STEM image of a large $\langle 411 \rangle$ connected cluster is shown, acquired in Alloy #2 after 400 min artificial ageing (cf. Supplementary Fig. 1). The $zZ_6M_8Z_{24}$ model (c.f. Fig. 6**a**) appears as a square of four units connected edge-to-edge along $\langle 410 \rangle$ directions in the [001] projection. The angle between the [410] and [100] directions is $14.04°$. This is also the rotation between the two square reciprocal lattices as seen in Fig. 6**d**, which shows the FFT of Fig. 6**c**. By comparing the FFT in Fig. 6**d** with the simulated NBD pattern in 6**b**, a strong correlation both in position and intensity is evident. Note that, even though Alloy #2 has been artificially aged, clusters are still present. This is in accordance with previous

studies[6,9,19,20,36] and emphasises the importance of these clusters.

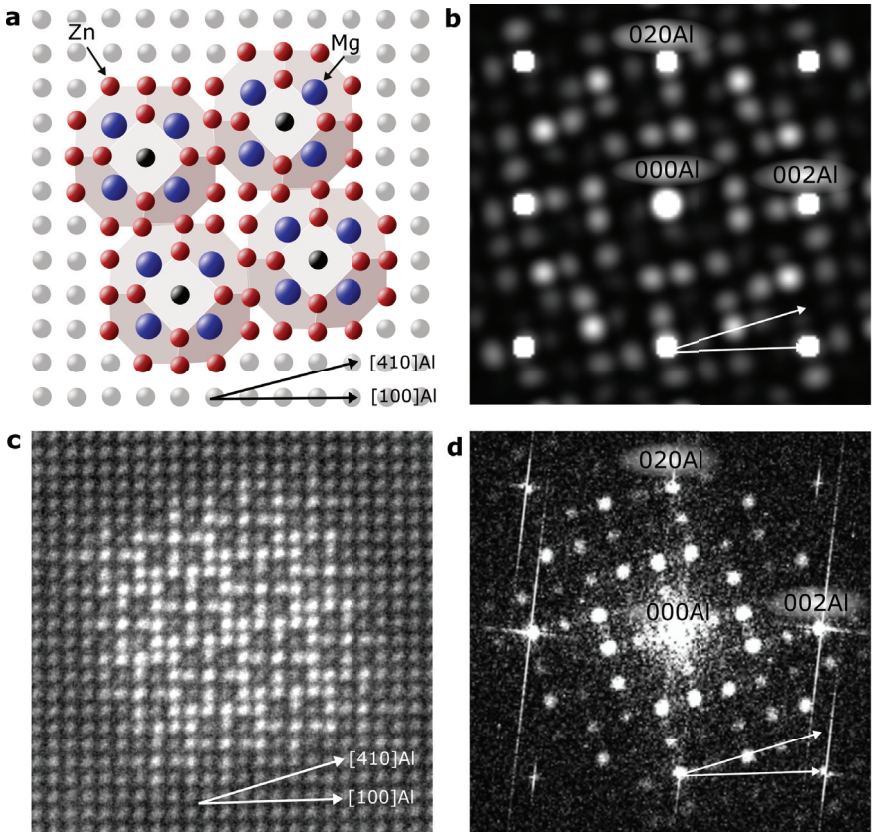

Fig. 6: **a**, [001] projection of the $zZ_6M_8Z_{24}$ cluster unit connected in a $\langle 411 \rangle$ square embedded in Al. **b**, Simulated NBD pattern of **a**. **c**, HAADF-STEM of a single cluster in Alloy #2. **d**, FFT of **c**. The intensities of the simulated diffraction pattern in (**b**) correspond strongly to intensities in the FFT (**d**) of observed cluster (**c**).

The lower cluster symmetry along [001] relative to Al, is obvious in Fig. 6**a**. The cluster belongs to space group P41 (#76), with a 4-fold screw axis, which projects to a pure rotational

axis, without parallel mirror planes. It means that the cluster, as well as the diffraction pattern, will reverse the rotation as viewed from the other side. By taking the average from the two orientations, the resultant diffraction pattern is similar to the SADP in Fig. 1**b**. This is shown in Supplementary Fig. 7.

The hardening precipitates in the 7xxx system and the incoherent equilibrium phase $MgZn_2$ have similar structures[14,16], facilitating transformation to the latter. This work finds no structural similarities between the GP(I) clusters and precipitates. The clusters can be nucleation sites for the precipitates, but are likely to dissolve once hardening precipitates are established to fuel further precipitate growth. Thus, a low formation enthalpy associated with a cluster may delay rather than assist precipitation. It is shown that the clusters, albeit built by the same basis unit, have varying structures. Future work will investigate how effective the different clusters are in forming the hardening phases. Better control of clustering has potential benefits for improving mechanical properties. It should be noted that an interstitial in the TCO produces a vacancy in the surrounding matrix. In principle, this makes the cluster more costly to produce. In the calculations, this is not accounted for. It is likely that the basic unit starts building from the centre, i.e. with an interstitial atom. The inner TCO-composition (iZ_6M_8) is Mg-rich, and expansive, and might therefore encourage the smaller Zn atoms to occupy the TCO shell. It has been suggested before that some form of Mg clustering surrounding a vacancy is crucial in the earliest stages[6,11].

To conclude, we have derived the structure of the clusters formed during natural ageing in Al-Zn-Mg alloys. They are solute orderings on the FCC aluminium and are essentially Frank-Kasper

σ-type structures. The orderings have been explained as stackings in terms of a near spherical solute-ordered unit. The unit is a three-layered shell structure around a common interstitial centre in the Al cell. The first shell is the octahedron formed by the six side centres. The second shell is the cube with the eight corners, preferred by Mg. Surrounding the cube, the immediate truncated cube octahedral shell with 24 positions constitutes the outer boundary. The octahedron and the outer TCO shell are partially or fully occupied by Zn, while the interstitial can take all three species. Three stacking principles are sufficient to explain all observed larger clusters. The partial occupancy of Zn means that a range of different compositions has favourable energies, which is expected based on the Frank-Kasper type of ordering. We expect our result to be significant in further understanding and optimization of age hardening in Al-Zn-Mg alloys, but also relevant to other Al alloy series.

Methods

Materials The data in this work has been obtained from two Al-Zn-Mg alloys. The industrial Alloy #1 (in at.%: 95.40% Al, 0.08% Fe, 1.42% Mg, 0.08% Si, 2.98% Zn and 0.04% Zr) was air cooled after extrusion and left to NA for 17 years. The lab cast Alloy #2 (in at.%: 1.89% Mg and 3.49% Zn) was SHT at 475 °C for 1 hour before it was quenched into water and left for NA. A group of samples were directly aged at 150 °C, while some were aged at 120 °C after 4 days of NA. The Vickers hardness (HV0.1) curve for Alloy #2 obtained during NA reaches a hardness of ∼110 HV0.1 after ∼10 days. This does not increase remarkably with further NA times. A similar hardness value is obtained after 4 days NA and 8 minutes ageing at 120 °C. This is shown in Supplementary Fig. 1.

Transmission Electron Microscopy TEM specimens were prepared by grinding bulk samples with SiC abrasive paper to ∼60 μm foil thickness, punched into 3 mm discs and thereafter electropolished with a Struers TenuPol-5 machine using an electrolyte mixture of 1/3 HNO_3 and 2/3 CH_3OH at temperatures between -30 and -20 °C and an applied potential of 20 V. High-resolution HAADF-STEM images were acquired using an image- and probe Cs-corrected JEOL ARM200CF operated at 200 kV with convergence semi-angle and inner collector angle 28 mrad and 48 mrad, respectively. Smart Align (HREM research) was used in the acquisition, which involves acquiring a stack of successive low-dose images and afterwards aligning them to correct both rigid- and non-rigid scan distortions[40].

Atom Probe Tomography APT samples were prepared according to the conventional focused ion beam (FIB) lift-out method[41], using a FEI Helios G2 dual-beam instrument. The tips were oriented along the [001] direction, and were sharpened to apex diameters of $<$50 nm, finishing with a 5 kV Ga+ ion beam. APT was performed with a Cameca LEAP 5000XS in voltage pulse mode, with the sample cooled to 50 K. A volume of 20 million atoms was evaporated with a pulse fraction of 25%, a pulse rate of 500 kHz, and 0.3% of the pulses leading to a detected atom. A detection efficiency of 77% and evaporation field of 20 eV/nm were assumed in the data reconstruction. Poles and lattice spacings in the [001] directions were visible, allowing a fit of the image compression factor and tip radius to obtain the correct scaling in all directions. The maximum separation algorithm was used[42], with d_{max} and N_{min} values that gave the highest ratio of real to random clusters (0.45 nm and 50). Enveloping and erosion of 0.45 nm was applied to defined the cluster-matrix interface and improve composition quantification[42]. Since we are averaging the chemical composition over a large amount of small clusters, the statistical deviation of the composition in this set is expected to be large and is used as an error estimate. Expected measurement errors include detection efficiency errors (the average error is roughly 1% in compositional fraction), uneven chemical distributions due to crystallographic poles, as well as background events. All these are random errors and is reflected in the statistically determined error.

Density Functional Theory The DFT calculations of the formation enthalpies for the structures were performed at 0 K with the Vienna ab initio Simulation Package (VASP)[43,44], using the Perdew-Burke-Ernzerhof (PBE) gradient approximation[45]. A gamma-centered k-point mesh was used in all calculations with a plane wave energy cut-off above 400 eV and a maximal k-point

distance of 0.18 Å^{-1}. The Methfessel-Paxton method[46] of 1st order was applied for atomic position relaxations with maximum force of 0.001 eV/Å and a smearing factor of 0.2. For accurate energies, all relaxations were followed by a static calculation using the tetrahedron method with Bloch corrections. The formation enthalpies for the different configurations were calculated as

$$\Delta H = E - \sum_i E_{X_i}, \tag{1}$$

where E is the total energy of the configuration in question and i is an index running over all atoms in the structure. E_X is the energy of one element X, embedded in the matrix ($X = \mathrm{Al}, \mathrm{Mg}, \mathrm{Zn}$). For consistency E_X is calculated from bulk Al supercells of the same size as the configuration in question with a single Al substituted with X[14];

$$E_X = E_{XAl_{N\ 1}} - \frac{N-1}{N} E_{Al_N}, \tag{2}$$

where N is the number of atoms in the supercell.

Diffraction pattern and image simulations The NBD patterns were simulated using the μSTEM simulation software in the position-averaged convergent beam electron diffraction (PACBED) mode[47]. The calculations were carried out on a 512x512 pixel mesh grid with 10 layers of Al unit cells surrounding the cluster model on each side forming a supercell with dimensions approximately $97\,\mathrm{x}97$ Å to avoid wrap-around errors due to the Al-cluster interface. The probe forming aperture was set to $0.75\,\mathrm{mrad}$ to avoid overlap of the diffraction spots. The model was periodic in the z-direction and the simulations were carried out over a thickness interval of $12-700$ Å. For the HAADF-STEM image simulations, the MULTEM simulation software was used [48]. The caulculations were carried out on a 1024x1024 pixel mesh grid. The supercell dimensions were

approximately $40\,\mathrm{x}40\,$Å. The convergence angle was set to $27.78\,\mathrm{mrad}$ and the inner and outer collection angles were $48\,\mathrm{mrad}$ and $206\,\mathrm{mrad}$, respectively. The thickness of the model was approximately $405\,$Å.

References

1. Jensrud, O. High Strength Aluminium Alloys Extrusions - A Review of the Thermo-Mechanical-Process in High Performance Profile Manufacturing. *Key Engineering Materials* **491**, 11–18 (2011).

2. Dursun, T. & Soutis, C. Recent developments in advanced aircraft aluminium alloys. *Materials & Design* **56**, 862–871 (2014).

3. Hornbogen, E. Hundred years of precipitation hardening. *Journal of Light Metals* **1**, 127 – 132 (2001).

4. Guinier, A. Structure of age-hardened aluminium-copper alloys. *Nature* **142**, 569–570 (1938).

5. Preston, G. LXXIV. The diffraction of X-rays by an age-hardening alloy of aluminium and copper. The structure of an intermediate phase. *The London, Edinburgh, and Dublin Philosophical Magazine and Journal of Science* **26**, 855–871 (1938).

6. Löffler, H., Kovács, I. & Lendvai, J. Decomposition processes in Al-Zn-Mg alloys. *Journal of Materials Science* **18**, 2215–2240 (1983).

7. Dlubek, G., Krause, R., Brümmer, O. & Plazaola, F. Study of formation and reversion of Guinier-Preston zones in Al-4.5 at%Zn-x at%Mg alloys by positrons. *Journal of Materials Science* **21**, 853–858 (1986).

8. Berg, L. K. *et al.* GP-zones in Al–Zn–Mg alloys and their role in artificial aging. *Acta Materialia* **49**, 3443 – 3451 (2001).

9. Hansen, V., Karlsen, O. B., Langsrud, Y. & Gjønnes, J. Precipitates, zones and transitions during aging of Al-Zn-Mg-Zr 7000 series alloy. *Materials Science and Technology* **20**, 185–193 (2004).

10. Buha, J., Lumley, R. N. & Crosky, A. G. Secondary ageing in an aluminium alloy 7050. *Materials Science and Engineering: A* **492**, 1–10 (2008).

11. Dupasquier, A. *et al.* Hardening nanostructures in an AlZnMg alloy. *Philosophical Magazine* **87**, 3297–3323 (2007).

12. Chung, T.-F. *et al.* Transmission electron microscopy investigation of separated nucleation and in-situ nucleation in AA7050 aluminium alloy. *Acta Materialia* **149**, 377–387 (2018).

13. Gjønnes, J. & Simensen, C. J. An electron microscope investigation of the microstructure in an aluminium-zinc-magnesium alloy. *Acta Metallurgica* **18**, 881–890 (1970).

14. Marioara, C. D., Lefebvre, W., Andersen, S. J. & Friis, J. Atomic structure of hardening precipitates in an Al-Mg-Zn-Cu alloy determined by HAADF-STEM and first-principles calculations: Relation to η-MgZn2. *Journal of Materials Science* **48**, 3638–3651 (2013).

15. Bendo, A. *et al.* Atomic scale HAADF-STEM study of η' and η_1 phases in peak-aged Al–Zn–Mg alloys. *Journal of Materials Science* **53**, 4598–4611 (2018).

16. Lervik, A. *et al.* Precipitation in an extruded AA7003 aluminium alloy: Observations of 6xxx-type hardening phases. *Materials & Design* **186**, 108204 (2020).

17. Chung, T.-F. *et al.* An atomic scale structural investigation of nanometre-sized η precipitates in the 7050 aluminium alloy. *Acta Materialia* **174**, 351 – 368 (2019).

18. Bendo, A. *et al.* Characterisation of structural similarities of precipitates in Mg–Zn and Al–Zn–Mg alloys systems. *Philosophical Magazine* **99**, 2619–2635 (2019).

19. Inoue, H., Sato, T., Kojima, Y. & Takahashi, T. The Temperature Limit for GP Zone Formation in an Al-Zn-Mg Alloy. *Metallurgical and Materials Transactions A* **12**, 1429–1434 (1981).

20. Akuata, C. K. *et al.* Age hardening response of AA7108A investigated by means of Synchrotron-based X-ray Absorption Spectroscopy (XAS) measurements. *Materials Science and Engineering: A* **747**, 42–52 (2019).

21. Jiang, X. J., Taftø, J., Noble, B., Holme, B. & Waterloo, G. Differential scanning calorimetry and electron diffraction investigation on low-temperature aging in Al-Zn-Mg alloys. *Metallurgical and Materials Transactions A* **31**, 339–348 (2000).

22. Sun, W. *et al.* Precipitation strengthening of aluminum alloys by room-temperature cyclic plasticity. *Science* **363**, 972–975 (2019).

23. Liu, J. *et al.* Formation of solute nanostructures in an Al–Zn–Mg alloy during long-term natural aging. *Journal of Alloys and Compounds* **821**, 153572 (2019).

24. Deschamps, A., Bréchet, Y. & Livet, F. Influence of copper addition on precipitation kinetics and hardening in Al–Zn–Mg alloy. *Materials Science and Technology* **15**, 993–1000 (1999).

25. Deschamps, A. *et al.* Low-temperature dynamic precipitation in a supersaturated Al-Zn-Mg alloy and related strain hardening. *Philosophical Magazine A* **79**, 2485–2504 (1999).

26. Schloth, P. *et al.* Early precipitation during cooling of an Al-Zn-Mg-Cu alloy revealed by *in situ* small angle X-ray scattering. *Applied Physics Letters* **105**, 101908 (2014).

27. Ferragut, R., Somoza, A. & Tolley, A. Microstructural evolution of 7012 alloy during the early stages of artificial ageing. *Acta Materialia* **47**, 4355–4364 (1999).

28. Stiller, K., Warren, P. J., Hansen, V., Angenete, J. & Gjønnes, J. Investigation of precipitation in an Al-Zn-Mg alloy after two-step ageing treatment at 100° and 150°C. *Materials Science and Engineering: A* **270**, 55–63 (1999).

29. Cassell, A. *et al.* Dispersoid composition in zirconium containing Al-Zn-Mg-Cu (AA7010) aluminium alloy. *Acta Materialia* **169**, 135 – 146 (2019).

30. Sha, G. & Cerezo, A. Early-stage precipitation in Al-Zn-Mg-Cu alloy (7050). *Acta Materialia* **52**, 4503–4516 (2004).

31. Chen, J., Zhen, L., Yang, S., Shao, W. & Dai, S. Investigation of precipitation behavior and related hardening in AA 7055 aluminum alloy. *Materials Science and Engineering: A* **500**, 34–42 (2009).

32. Liu, D. *et al.* Quantitative study of nanoscale precipitates in Al-Zn-Mg-Cu alloys with different chemical compositions. *Materials Science and Engineering: A* **639**, 245–251 (2015).

33. Matsuda, K. *et al.* Extra electron diffraction spots caused by fine precipitates formed at the early stage of aging in Al–Mg–X (X=Si, Ge, Zn)-Cu alloys. *Materials Transactions* **58**, 167–175 (2017).

34. Hono, K., Sano, N. & Sakurai, T. Quantitative atom-probe analysis of some aluminum alloys. *Surface Science* **266**, 350 – 357 (1992).

35. Maloney, S. K., Hono, K., Polmear, I. J. & Ringer, S. P. The chemistry of precipitates in an aged Al-2.1Zn-1.7Mg at.% alloy. *Scripta Materialia* **41**, 1031–1038 (1999).

36. Wang, Y. L. *et al.* Variation of nanoparticle fraction and compositions in two-stage double peaks aging precipitation of Al-Zn-Mg alloy. *Nanoscale Research Letters* **13**, 131 (2018).

37. Philippe, T., Gruber, M., Vurpillot, F. & Blavette, D. Clustering and local magnification effects in atom probe tomography: A statistical approach. *Microscopy and Microanalysis* **16**, 643–648 (2010).

38. Gupta, R. K., Deschamps, A., Cavanaugh, M. K., Lynch, S. P. & Birbilis, N. Relating the Early Evolution of Microstructure with the Electrochemical Response and Mechanical Performance of a Cu-Rich and Cu-Lean 7xxx Aluminum Alloy. *Journal of The Electrochemical Society* **159**, C492–C502 (2012).

39. Joubert, J.-M. & Crivello, J.-C. Non-Stoichiometry and Calphad Modeling of Frank-Kasper Phases. *Applied Sciences* **2**, 669–681 (2012).

40. Jones, L. *et al.* Smart Align - a new tool for robust non-rigid registration of scanning microscope data. *Advanced Structural and Chemical Imaging* **1**, 8 (2015).

41. Prosa, T. J. & Larson, D. J. Modern focused-ion-beam-based site-specific specimen preparation for atom probe tomography. *Microscopy and Microanalysis* **23**, 194–209 (2017).

42. Jägle, E. A., Choi, P.-P. & Raabe, D. The maximum separation cluster analysis algorithm for atom-probe tomography: Parameter determination and accuracy. *Microscopy and Microanalysis* **20**, 1662–1671 (2014).

43. Kresse, G. & Hafner, J. Ab initio molecular dynamics for open-shell transition metals. *Physical review B* **48**, 13115–13118 (1993).

44. Kresse, G. & Joubert, D. From ultrasoft pseudopotentials to the projector augmented-wave method. *Physical review B* **59**, 1758–1775 (1999).

45. Perdew, J. P., Burke, K. & Ernzerhof, M. Generalized gradient approximation made simple. *Physical review letters* **77**, 3865–3868 (1996).

46. Methfessel, M. & Paxton, A. T. High-precision sampling for Brillouin-zone integration in metals. *Physical review B* **40**, 3616–3621 (1989).

47. Allen, L. J., D'Alfonso, A. J. & Findlay, S. D. Modelling the inelastic scattering of fast electrons. *Ultramicroscopy* **151**, 11–22 (2015).

48. Lobato, I. & Dyck, D. V. MULTEM: A new multislice program to perform accurate and fast electron diffraction and imaging simulations using Graphics Processing Units with CUDA. *Ultramicroscopy* **156**, 9–17 (2015).

Acknowledgements This work was supported by the The Research Council of Norway (NFR) through

the projects 'FICAL' (NFR: 247598) (A.L. & R.H.), support by the industrial partners Hydro, Gränges, Benteler Automotive Raufoss AS and Steertec Raufoss, and 'SumAl' (NFR: 294933) (J.F., C.D.M., S.W., R.H. & S.J.A.), supported by Hydro, Benteler Automotive Raufoss AS and Neuman Aluminium. E.T. and R.H. are supported by the NTNU Digital Transformation initiative 'Alldesign'. The international collaboration was made possible through INTPART (NFR: 249698). The (S)TEM work was conducted on the NORTEM (NFR: 197405) infrastructure at the TEM Gemini Centre, Trondheim, Norway. The DFT calculations were performed on resources provided by UNINETT Sigma2 - the National Infrastructure for High Performance Computing and Data Storage in Norway (NN8068K). K.M. and A.B. acknowledges the Japan Science and Technology Agency (JST) under Collaborative Research Based on Industrial Demand "Heterogeneous Structure Control: Towards Innovative Development of Metallic Structural Materials".

Competing Interests The authors declare that they have no competing financial interests.

Correspondence Correspondence should be addressed to A. Lervik. (E-mail: Adrian.lervik@ntnu.no).

Author contribution A.L., A.B., K.M., R.H. and S.J.A. conceived, designed and supervised the research. A.L. conducted the (S)TEM experiments. S.W. conducted the APT measurements and analysis. J.F. prepared the models and conducted the DFT modelling. E.T. conducted the image and diffraction simulations. S.J.A. and C.D.M. analysed the data and deduced the structure. A.L. and E.T. prepared the figures. A.L., E.T. and S.J.A wrote the manuscript with input from all the authors.

Paper V

Precipitation in an extruded AA7003 aluminium alloy: Observations of 6xxx-type hardening phases

Adrian Lervik, Calin Daniel Marioara, Maria Kadanik,
John Charles Walmsley, Benjamin Milkereit, Randi Holmestad

Materials & Design **186** (2020) 108204
DOI:10.1016/j.matdes.2019.108204

Materials and Design 186 (2020) 108204

Contents lists available at ScienceDirect

Materials and Design

journal homepage: www.elsevier.com/locate/matdes

Precipitation in an extruded AA7003 aluminium alloy: Observations of 6xxx-type hardening phases

A. Lervik[a,*], C.D. Marioara[b], M. Kadanik[d,e], J.C. Walmsley[c], B. Milkereit[d,e], R. Holmestad[a]

[a] Department of Physics, Norwegian University of Science and Technology (NTNU), Trondheim N-7491, Norway
[b] SINTEF Industry, N-7465 Trondheim, Norway
[c] Department of Materials Science and Metallurgy, University of Cambridge, CB2 3QZ, UK
[d] Chair of Materials Science, Faculty of Marine Technology and Mechanical Engineering, University of Rostock, Albert-Einstein-Str. 2, Rostock 18059, Germany
[e] Competence Centre ◦CALOR, Department Life, Light & Matter, Faculty of Interdisciplinary Research, University of Rostock, Albert-Einstein-Str. 25, Rostock 18059, Germany

HIGHLIGHTS

- Air cooling results in heterogenous nucleation of β-Mg_2Si and η-$MgZn_2$ on grain boundaries and dispersoids.
- Artificial ageing temperature influences the Mg-Zn (η) hardening phases orientation relationship with the aluminium matrix.
- 6xxx type hardening phases are found to coexist with the 7xxx type hardening in the T7 temper if water quenched.

GRAPHICAL ABSTRACT

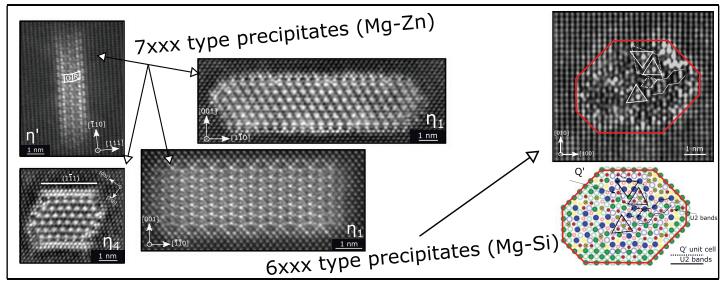

ARTICLE INFO

Article history:
Received 18 June 2019
Received in revised form 8 August 2019
Accepted 10 September 2019
Available online 24 October 2019

Keywords:
Aluminium alloys
Scanning transmission electron microscopy
Heterogeneous nucleation
Differential scanning calorimetry
η-$MgZn_2$
Precipitation

ABSTRACT

Precipitation behavior in an industrially extruded AA7003 alloy has been studied using Transmission Electron Microscopy (TEM) together with Differential Scanning Calorimetry (DSC). Air Cooling (AC) after solution heat treatment results in quench induced heterogeneous precipitation of both β-Mg_2Si and η-$MgZn_2$ phases. Detailed TEM characterisation of resulting nanoscale precipitates after AC, or Water Quenching (WQ), and subsequent artificial ageing demonstrate that η' and η_2 hardening precipitates dominate in T6, whereas the overaged T7 state contains η_2 and η_1, where the latter accounts for approximately 50% of the relative phase fraction. The T7 state in addition forms 6xxx-type hardening precipitates only after WQ. Results presented here are expected to be relevant for any Si containing 7xxx alloy and open new possibilities for development of hybrid 6xxx- and 7xxx series aluminium alloys. This is discussed with respect to potential influence on mechanical- and corrosion properties.

1. Introduction

Age hardenable Al-Zn-Mg alloys are of great importance in automotive- and aerospace applications due to their high strength to weight ratio [1-4]. High Zn/Mg ratio alloys, such as AA7003, are of particular interest due to increased extrusion speed while maintaining a yield strength of ~330 MPa [4-7]. These alloys are generally subjected to a Solution Heat Treatment (SHT) after extrusion, followed by a quench to room temperature, before Artificial Ageing (AA) at temperatures between 100 and 200 ◦C. Variations in mechanical processing, SHT- and AA temperatures, along with alloy composition and potential quench-induced precipitation, strongly influence the resulting mechanical- and corrosion properties. Balancing these

* Corresponding author.
E-mail address: adrian.lervik@ntnu.no (A. Lervik).

https://doi.org/10.1016/j.matdes.2019.108204
0264-1275/

parameters has been a challenge for decades and generally one sacrifices mechanical properties to increase Stress Corrosion Cracking (SCC) resistance in 7xxx alloys, by AA to tempers other than the maximum strength yielding condition [8].

One way of measuring quench sensitivity in aluminium alloys is by Differential Scanning Calorimetry (DSC) measurement of excess specific heat capacity curves for precipitation reactions over a wide range of cooling rates [9,10]. The minimum cooling rate at which no precipitation enthalpy is detected gives the Critical Cooling Rate (CCR). All solute will thus remain in Supersaturated Solid Solution (SSSS) upon reaching room temperature, and not be precipitated on e.g. Al_3Zr dispersoids [11-16], and grain boundaries [14,15,17], which both are reported nucleation sites for the hexagonal equilibrium phase η-$MgZn_2$. DSC, in combination with Transmission Electron Microscopy (TEM), can be used to construct Continuous Cooling Precipitation (CCP) diagrams, predicting domains in which certain phases form with respect to temperature and cooling rates [18]. One example from an alloy (AA7020) with nearly similar composition to the one in the present study, revealed quench-induced precipitation of equilibrium η-$MgZn_2$ and β-Mg_2Si phases, both along grain boundaries and within the grains, by Scanning Electron Microscopy (SEM) after DSC-cooling experiments [17]. β-Mg_2Si was deduced to be the high temperature reaction occurring during slow cooling rates, disappearing when cooling >0.3 K/s. The η-$MgZn_2$ particles, observed at slightly lower temperatures disappear at cooling rates >3 K/s, thus indicating the CCR for this alloy.

In the beginning of the subsequent AA stage, coherent solute-rich Guinier-Preston (GP) zones are formed from the SSSS [19-22]. GP(I) zones, made up from Al, Mg and Zn, are fully coherent with the aluminium matrix and described as an elongated anti-phase structure with alternating arrangement of Zn and Mg rich planes [21,23,24]. GP(II) zones are described as ordering of Zn-rich layers on $\{111\}_{Al}$ with internal ordering as elongated $\langle 110\rangle_{Al}$ domains [21]. Maximum hardness is achieved by the formation of nanoscale semi-coherent metastable Mg-Zn precipitates, denoted η', while further ageing results in decreasing hardness due to coarsening, and a corresponding depletion in volume fraction of η'.

All together, there are thirteen reported orientation relationships which the nanoscale η-phase may form with the Al matrix [25-30,59]. The ones relevant for this study are summarised in Table 1. η' and η_2, which are plates on $\{111\}_{Al}$, were explained in detail as the Type 1 and Type 2 precipitate by Marioara et al. [30]. Type 1 consists of a rhomobohedral- (R) and an orthorombic unit (O), while Type 2 plates consist of R-units stacked pairwise or rotated 180° with respect to one another [30]. Similar stacking of R-units has been observed in the plate shaped η_1 precipitate [29,31,32]. It has recently been demonstrated that the η-precipitates may incorporate an additional flattened hexagonal sub-unit giving rise to internal stacking faults [29,31]. This sub-unit can also be described through the O- and R-units [33]. It is identical to a sub-unit found within the monoclinic Mg_4Zn_7 phase in Mg-Zn-X alloys [32,34], if the O-unit replaces its internal Zn sites with Mg. This was calculated to be as energetically favourable [30]. Incorporation of these sub-units results in a quasi-crystal like internal structure giving uncommon morphologies, making it difficult to classify their habit planes in a Bright Field (BF)-TEM image. High-Angle Annular Dark Field (HAADF) Scanning Transmission Electron Microscopy (STEM) has proven to be a more accurate method for determining the structure of these small-scale precipitate structures [29-33,35,59].

The general precipitation sequence may be written as:

$$SSSS \rightarrow GP(I)/GP(II) \rightarrow \eta' + \eta_{(1-13)} \rightarrow \eta(MgZn_2), \quad (1)$$

where the exact phase fraction heavily depends on the applied thermomechanical treatment. More in-depth summaries related to the nanoscale η-precipitates can be found elsewhere [29,31].

Table 1
Orientation relationships between nanoscale η-precipitates and the Al matrix demonstrated in this study. These notations are used throughout the article.

	Orientation relationship	Habit plane
η' (Type 1)	$[100]_\eta//[11\bar{2}]_{Al}$, $[120]_\eta//[\bar{1}10]_{Al}$	$(001)_\eta//(111)_{Al}$
η_2 (Type 2)	$[100]_\eta//[11\bar{2}]_{Al}$, $[120]_\eta//[\bar{1}10]_{Al}$	$(001)_\eta//(111)_{Al}$
η_1	$[100]_\eta//[\bar{1}\bar{1}0]_{Al}$, $[120]_\eta//[001]_{Al}$, $(010)_\eta//(001)_{Al}$	$(001)_\eta//(110)_{Al}$
η_4	$[100]_\eta//[\bar{1}\bar{1}\bar{1}]_{Al}$, $[120]_\eta//[\bar{1}\bar{1}2]_{Al}$, $(001)_\eta//(110)_{Al}$	$(2\bar{1}0)_\eta//(\bar{1}\bar{1}\bar{1})_{Al}$

In this work, we aim for a systematic study of the microstructure in an industrially extruded AA7003. Microstructural response to variation in quench rate and AA temperature is investigated, with particular emphasis on bulk (within the grain) precipitation.

2. Material and methods

2.1. Material

The composition of the investigated AA7003 alloy, provided by Benteler Automotive Raufoss AS, is given in Table 2. The alloy was extruded into hollow rectangular profiles with dimensions 68 × 85 mm and wall thickness of 2.4 mm. The profiles were thereafter SHT at 480 °C for 30 min, followed by either a aWater Quench (WQ) or Air Cooling (AC) to room temperature. Cooling rates during AC were measured to drop from 4 to 2 K/s and 2 to 1 K/s in the temperature ranges 480–300 °C and 300–100 °C, respectively. The samples were subsequently AA at 140 °C for 17 h or 170 °C for 6 h, which are designated as the T6 and T7 tempers, respectively. Vickers hardness (HV10) values for AC-T6, AC-T7, WQ-T6 and WQ-T7 are 121, 112, 127 and 118, respectively.

2.2. Transmission electron microscopy

TEM specimens were prepared by grinding with SiC abrasive paper to ~100 μ m foil thickness, punched into 3 mm discs and thereafter electropolished with a Struers TenuPol-5 machine. An electrolyte consisting of 1/3 HNO_3 and 2/3 CH_3OH was used, and kept at temperatures between −30 and −20 °C with an applied potential of 18 V.

Precipitate crystal structures were studied in high-resolution HAADF-STEM mode using an image- and probe Cs-corrected JEOL ARM200CF operated at 200 kV, with 0.08 nm probe size, convergence semi-angle of 28 mrad and 35 mrad inner collector angle. High-resolution HAADF-STEM images were acquired using Smart Align, which involves acquiring a stack of successive low-dose images and afterwards aligning them to correct both rigid- and non-rigid scan distortions in the micrographs [36]. Energy-Dispersive X-ray Spectroscopy (EDS) spectrum imaging was performed with an Oxford X-max 80 silicon drift detector with a detector solid angle of 0.23 sr on a JEOL JEM-2100F operated at 200 kV in analytical STEM mode with a 1.0 nm probe size.

Table 2
Alloy composition of the investigated alloy (in wt% and at.%) measured using optical emission spectroscopy.

	Fe	Mg	Si	Zn	Cu	Zr	Ti	Al	Zn/Mg
wt%	0.20	0.68	0.11	5.56	0.01	0.17	0.02	Bal.	8.20
at.%	0.10	0.78	0.11	2.37	0.00(4)	0.05	0.01	Bal.	3.04

2.3. Differential scanning calorimetry

The precipitation behavior during cooling from solution annealing was analysed by DSC as described by Milkereit et al. [9]. Two DSC devices were used, namely a Setaram Sensys heat flux DSC for cooling rates of 0.01 to 0.1 K/s and a PerkinElmer Pyris DSC for cooling rates of 0.3 to 3 K/s. In the first device, two sample scans and one related baseline scan were measured, while in the PerkinElmer four and two sample and baseline scans were measured, respectively. The measured heat flow signal was normalised by the scanning rates and sample masses. Measured curves were averaged and the scatter plotted as introduced in Ref. [37].

3. Results

3.1. Precipitation during quenching

Fig. 1 shows excess specific heat curves for AA7003 after cooling from 480 °C with linear cooling rates from 0.01 K/s to 3 K/s. A high temperature reaction, denoted A, starts immediately at the onset of cooling in the two slowest cooling rates and is visible until ~430 °C. The peak labeled C at ~400 °C shifts towards lower temperatures and becomes increasingly suppressed with higher cooling rates. There is hint of another reaction, seen as a shoulder on its high temperature side labeled B. B & C are visible in all cooling conditions up to 1 K/s and may still be present at the highest cooling rate of 3 K/s.

At least two overlapping peaks (D & E) are observed in the region 315–150 °C. These also become suppressed at higher cooling rates and seem to nearly disappear already at 1 K/s. The peaks shift towards higher temperatures with increasing cooling rates and, consequently, overlap with the previously mentioned high temperature peaks. A low temperature peak, F, is observed at <100 ° C.

TEM observations of AC cooled samples before AA reveal quench induced precipitates, of both η-$MgZn_2$ and β-Mg_2Si, nucleating heterogeneously on grain boundaries, Al_3Zr dispersoids and Al-Fe-Si particles. Representative BS-STEM micrographs are shown in Fig. 2. Fig. 2A and B shows precipitation on two grain boundaries. In Fig. 2A, there are two β-Mg_2Si particles present together with Al_3Zr dispersoids, while in Fig. 2 B there is a fine population of small η-$MgZn_2$ precipitates. Fig. 2 C and D shows typical observations made in the bulk where Fig. 2C shows nucleation of β-Mg_2Si on an Al-Fe-Si particle and Fig. 2D shows a complex nucleation cluster, where Al_3Zr, β-Mg_2Si, η-$MgZn_2$ and dislocations are present. It is not clear which are the nucleation sites for each phase in Fig. 2 D. Notice the low contrast from the β-Mg_2Si particle. The chemical compositions of the phases present were verified using EDS (not shown). No evidence of homogeneous nucleation of hardening phases was observed during AC.

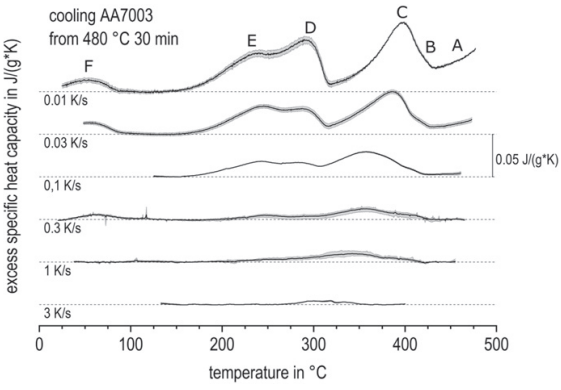

Fig. 1. DSC cooling curves for AA7003 with varying cooling rates from 0.01 to 3 K/s. The alloy was subjected to a solution heat treatment at 480 °C for 30 min prior to cooling.

3.2. Microstructure in aged tempers

Similar to the AC-T4 temper, the final AC-T6/T7 tempers have significant amounts of heterogeneous nucleated precipitates. Fig. 3 shows an example of a typical bulk microstructure acquired by HAADF-STEM. Multiple heterogeneous nucleation sites amid the bulk hardening phases are observed. Precipitate Free Zones (PFZ) are found to form around these nucleation sites. In Fig. 3, taken in the AC-T6 temper, both β-Mg_2Si and η-$MgZn_2$ are found together with two Al_3Zr particles. It is not clear whether Al_3Zr is the primary nucleation site, or if η-$MgZn_2$ can serve as a nucleation site for β-Mg_2Si, or vice versa. Another example, from the overaged AC-T7 condition, is shown in Fig. 4, where three η-particles and one β-Mg_2Si are nucleated onto a Al-Fe-Si particle. In both Figs. 3 and 4, the β-Mg_2Si particles are not distinguishable solely from the HAADF- and BF-STEM micrographs. This emphasises the difficulty of observing this phase in this system, unless it is explicitly searched for.

Bulk microstructures in T6 and T7 after WQ appear similar to the AC and aged tempers, as in Fig. 3, apart from the heterogeneous nucleation. No observations of β-Mg_2Si were made on the typical nucleation sites demonstrated in Fig. 2. However, η-$MgZn_2$ particles were occasionally observed on Al_3Zr and Al-Fe-Si dispersoids. It is possible that these have formed during AA as they were not observed in the as-WQ samples. On grain boundaries, η-$MgZn_2$ particles were observed in a similar manner as for the AC tempers.

Only the η-precipitates described in Table 1 were observed in the present work. BF-TEM micrographs along $[110]_{Al}$ are shown for all four final tempers in Fig. 5. In this projection, 2/4, 1/3 and 1/6 of the precipitates with habit planes $\{111\}_{Al}$, $\{100\}_{Al}$ and $\{110\}_{Al}$, respectively, are observed edge on. The remaining precipitates are projections of equivalent precipitates on similar family planes, undefined faulted phases and in some rare cases the cross-section of η_4. In order to obtain a relative fraction of phases present, the number of precipitates with habit planes $\{111\}_{Al}$, $\{100\}_{Al}$ and $\{110\}_{Al}$ were counted and multiplied by 2, 3 and 6, respectively. This means only counting the edge-on precipitates and multiplying in order to account for the identical precipitates lying on equivalent planes not observed in the zone axis. As summarised in Table 3, both the T6 tempers are dominated by η' and η_2, while the T7 tempers are dominated by η_1 and η_2. Due to uncertainties when measuring the dimensions of particles from BF-TEM images, such as in Fig. 5, an upper threshold for the minor dimension (thickness) of measured particles with $\{111\}_{Al}$ habit plane was set to 20 Å, slightly higher than its distinct thickness of $7\times\{111\}_{Al}$ (≈16.4 Å) as shown in Fig. 6A [30], in order to separate η' from η_2. It is then observed that in both T7 states, η' is non-existent. Several authors have suggested the reaction $\eta' \rightarrow \eta_2$ as a possible transformation [26,38-40]. Furthermore, from Table 3 and Fig. 5 it is clear that both dimensions of the precipitates are larger when aged at 170 °C.

The phase with habit plane $\{110\}_{Al}$, marked with question marks in Fig. 5B and D, was not observed by high-resolution HAADF-STEM when imaging along $[110]_{Al}$ or $[100]_{Al}$ axis. It is likely to be another orientation relation which η may form with aluminium or a faulted structure growing along the $[100]_{Al}$ direction.

η' hardening precipitates with structures similar to those reported before were observed in all conditions. An example is

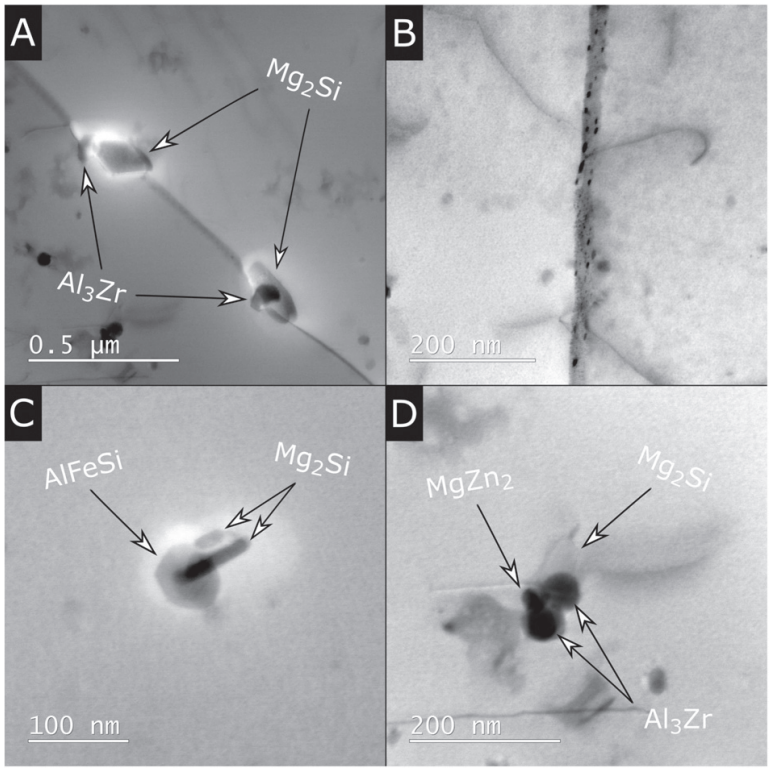

Fig. 2. BF-STEM micrographs from the AC-T4 condition, showing typical heterogeneous nucleation sites. A) Two β-Mg_2Si phases on a grain boundary, with an Al_3Zr particle in the nucleation site. B) A grain boundary with fine population of small η-$MgZn_2$ precipitates. C) Two β-Mg_2Si particles nucleated on a Al-Fe-Si particle. D) A nucleation site including Al_3Zr dispersoids, η-$MgZn_2$, β-Mg_2Si and dislocation lines. Notice the low contrast from the β-Mg_2Si phase. The chemical composition of the phases in all micrographs has been verified using EDS.

shown in Fig. 6A, and is the η' (Type 1) precipitate [30]. This precipitate can also incorporate defects, such as a roto-inversion center, shown in Fig. 6B. η_2 (Type 2) is also frequently observed, although not shown here.

η_1 was observed along the two axis: $[001]_\eta//[110]_{Al}$ and $[100]_\eta//[1\bar{1}0]_{Al}$, shown in Fig. 6C and D, respectively. Fig. 6C and D shows the habit interface created by the $(010)_\eta$ plane aligned with the $(001)_{Al}$ plane, rotated 90° across $[001]_{Al}$. This phase is a plate shaped precipitate with habit plane $(010)_\eta//(001)_{Al}$.

Furthermore, cross-sections with orientation relationship corresponding to those reported for η_4 [26], were observed in the T7 tempers, and one is shown in Fig. 6E. It has been proposed as a rod/lath with habit planes on $\{111\}_{Al}$ with the following orientation relationship: $(2\bar{1}0)_\eta//(\bar{1}1\bar{1})_{Al}$ and $[001]_\eta//[110]_{Al}$, which is in agreement with the presented micrograph. Two $\{111\}_{Al}$ planes enriched with high Z elements (Zn or Cu) are observed on both sides of the precipitate.

A range of faulted structures were observed in the present work, and one is shown Fig. 6F. Orientation relationships for these precipitates cannot be simply defined. They do however stack the same R-unit, but do addition incorporate the flattened hexagonal sub-units indicated as the white hexagon, separating regions of well ordered structures. In the given example, there is a previously unreported semi-coherent interface present along the $[1\bar{1}\bar{4}]_{Al}$ direction, which connects to the unfaulted structure marked in the figure. The orientation can thus be written as $[100]_\eta//[110]_{Al}$ and $(010)_\eta//(2\bar{2}1)_{Al}$. This has never been observed for a free-standing non-faulted precipitate. Similar faulted structures have been observed within the η_1 and η_2 precipitates [29,31-33].

3.3. Observation of 6xxx hardening phases

As no Mg_2Si-phases were observed in the T6 and T7 tempers at the typical heterogeneous nucleation sites after WQ, this would suggest that Si still remains in solid solution. However, STEM-EDS of WQ-T7 revealed a fine population of small Mg-Si precipitates between the slightly larger η precipitates. This is shown in Fig. 7, where EDS spectrum images are obtained across a grain boundary. The Si signal correlates with some Mg sites, but not with Zn. They do however appear close to each other, since the Mg-Si particles are observed to occasionally nucleate on the η-particles, or vice-versa, as demonstrated by HAADF-STEM in Fig. 7.

High-resolution observations along $[100]_{Al}$ reveal Mg-Si phases with disordered crystal structures, similar to what has been observed in the 6xxx aluminium system [41,42]. These are small needles, distributed homogeneously within a grain. The cross-section of one

example is shown in Fig. 8. It consists of Q' and U2 building blocks connected by a near hexagonal Si network [43], demonstrated by the overlaid atomic positions in Fig. 8. Furthermore, there are indications of either Zn or Cu enrichment at the interface which gives localised bright atomic columns. Based on the atomic overlay the composition of the precipitate in Fig. 8 results in $Al_{0.27}(Cu,Zn)_{0.17}Mg_{0.29}Si_{0.27}$ giving a Mg/Si ratio close to 1 which is typical for 6xxx type hardening phases [33,44].

4. Discussion

During AC from solution annealing, there are multiple heterogeneous precipitation reactions occurring. Observed nucleation sites are grain boundaries in addition to Al_3Zr and Al-Fe-Si dispersoids. Both η-$MgZn_2$ and β-Mg_2Si were found on these sites, as demonstrated in Fig. 2. These precipitation events must be related to the observed peaks in the DSC cooling curves in Fig. 1, where at least 6 precipitation reactions are occurring.

A complete understanding of the peaks denoted A–F in Fig. 1, would require extensive TEM investigations following interrupted quenching. However, a qualitative discussion is possible based on previous work. The origin of peak A, directly visible at the onset of cooling in the two slowest cooling rates, is unclear. It may be related to the formation of Al-Fe-Si dispersoids or β-Mg_2Si. Kemsies et al. demonstrated that the previously described "stable" Al-Fe-Mn-Si dispersoids can partially dissolve at temperatures above ~450 °C, giving a substantial signal in the DSC curves [37]. As the reaction is diffusion driven, it may become suppressed with higher cooling rates, which is similar to what is observed in present work.

Two peaks, B & C, are observed in the region 430–320 °C, with B appearing as a shoulder on the high temperature side in the range 430–400 °C. These may correspond to β-Mg_2Si, which is suggested to occur in this temperature region in AA7020 [17]. The formation enthalpies of β-Mg_2Si and η-$MgZn_2$ are about one order of magnitude apart [10,45]. This might suggest that β-Mg_2Si can appear significant in the DSC cooling curves, although it is lower in volume fraction. In the region 350–170 °C, there are two peaks, D & E, where at least one should correspond to η-$MgZn_2$, as has been reported to precipitate within a very similar temperature range in other Al-Zn-Mg alloys [15,10,17,46]. The reason for the two peaks in this region is unclear. The final peak observed at <100 ° C most likely corresponds to homogeneous distribution of cluster nucleation [47].

As discussed, there are more peaks in the DSC cooling curves than observed phases. One possible explanation for this is the undetected presence of other phases such as T-$Al_2Mg_3Zn_3$. Another explanation could be that the same phase may yield different peaks in the DSC curves owing to different nucleation sites and/or morphology. In binary Al-Si, it was demonstrated that the same Si-phase resulted in two observable peaks in the DSC curves due to different aspect ratios [48]. Similar observations were made for Mg_2Si in a ternary Al-Mg-Si alloy [49].

It is evident from the DSC curves that precipitation may occur if the cooling rate is insufficient to suppress all the reaction events occurring. In this alloy it is made clear by TEM, and supported by DSC, that the material is quench sensitive during AC. From Fig. 1, precipitation enthalpy is still detected at the highest measured cooling rate of 3 K/s, indicating that the CCR for our alloy is higher than this.

With regard to the nanoscale η-phases it seems that the artificial ageing temperature is the controlling parameter for both precipitate orientation and size. The hardness in the T7 tempers is 9 (HV10) less than for their T6 counterparts due to coarser precipitates. The two prior cooling conditions seem to have minimal influence on bulk precipitate size and orientation, although some solute is consumed in heterogeneous precipitation during AC reducing the hardness by 6 (HV10) when comparing the AC and WQ tempers. As shown in Fig. 6, there are many orientations which the nanoscale η precipitates

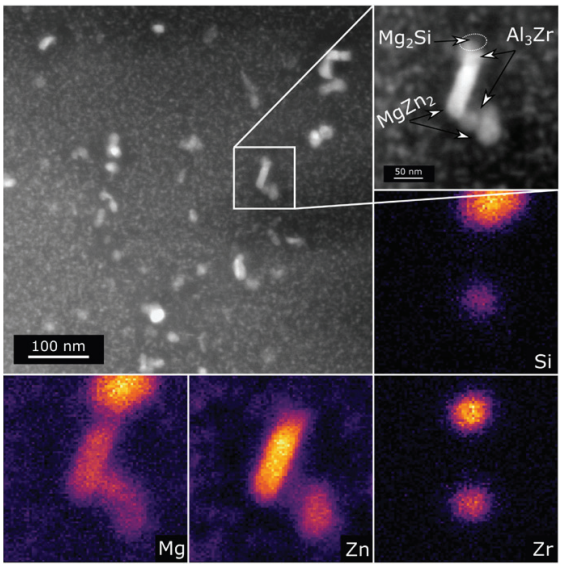

Fig. 3. HAADF-STEM micrograph showing heterogeneous nucleation in the bulk microstructure of the AC-T6 temper. The corresponding EDS spectrum images for Mg, Si, Zn and Zr from the indicated area are shown. β-Mg_2Si, η-$MgZn_2$ and Al_3Zr are observed in the particle agglomerate.

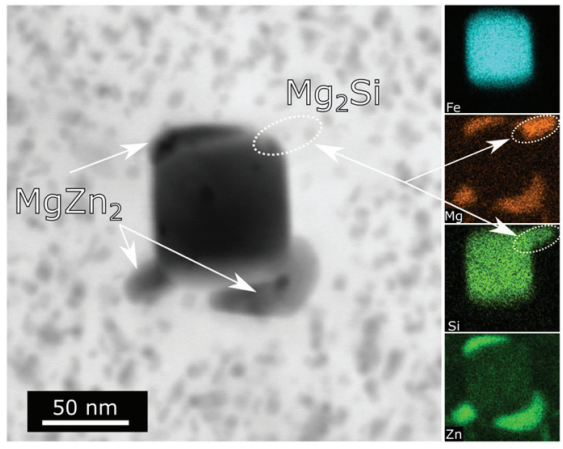

Fig. 4. STEM-BF micrograph of a Al-Fe-Si particle in the AC-T7 condition. Three η-$MgZn_2$ precipitates can clearly be observed in the micrograph and the corresponding EDS map. A smaller β-Mg_2Si particle is also nucleated on the particle, but cannot be seen in the STEM image. As indicated, this is only revealed in the corresponding Mg and Si EDS spectrum images.

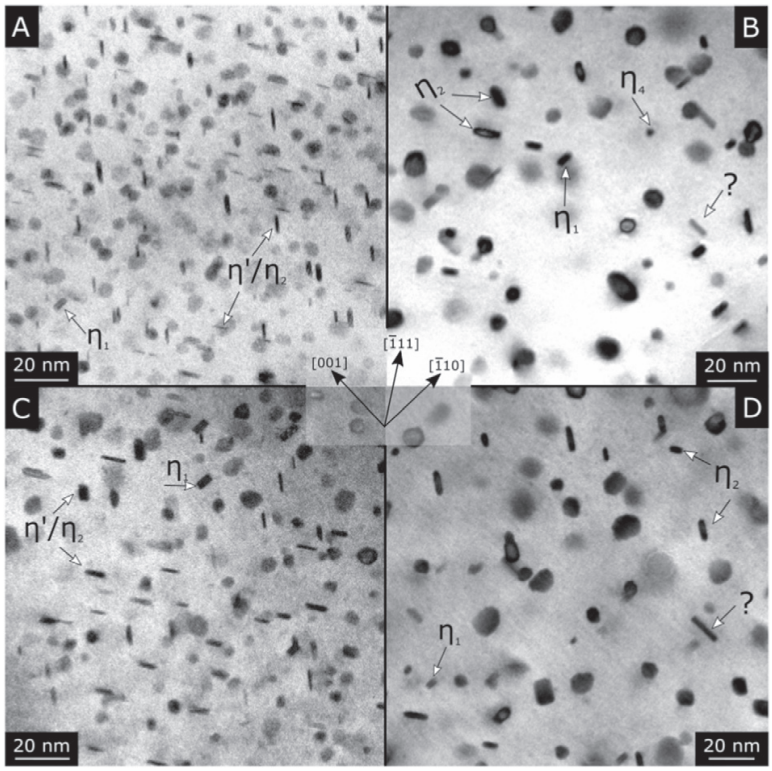

Fig. 5. BF-TEM micrographs of bulk precipitates oriented along the $[110]_{Al}$ direction with the same indicated coordinate system. (A) AC sample in T6 and T7 (B). (C) WQ sample in T6 and T7 (D). The precipitates are generally larger in the T7 conditions which contains ~50% η_1 precipitates growing on the $\{100\}_{Al}$ planes, in addition to η'/η_2 on $\{111\}_{Al}$. '?' with habit plane $\{110\}_{Al}$ has not been identified.

can form with respect to the aluminium matrix. Introducing exact 3D models for η_1 and η_4 is outside the scope of present work, but should be conducted in future and calculated using Density Functional Theory (DFT) calculations in a similar manner as for η' and η_2 [30].

A homogeneous distribution of 6xxx hardening phases were only observed in the WQ-T7 state. Extensive STEM work was carried out to determine if these phases were present in WQ-T6 (ageing at 140 °C), but none were observed. This could indicate that these phases only form when ageing at relatively high temperatures with respect to what is typical in 7xxx alloys. In alloys subjected to Retrogression and Reageing (RRA), this may be important when performing the retrogression stage at elevated temperatures if the alloy contains Si. More work needs to be done in order to understand the kinetics of the observed concurrent precipitation and its influence on hardness. Comparing hardening kinetics in a similar alloy like the present but with 0.0 wt.% Si is a possible approach.

To the authors knowledge, there is only one report on precipitation of nanoscale 6xxx type hardening phases in 7xxx alloys. Hansen et al. studied Cu-free high Zn/Mg ratio 7xxx alloys with varying Si amounts and compared microstructures after SHT at 450 and 550 °C [50]. The higher SHT temperature dissolved primary Mg_2Si-phases resulting in precipitation of Mg-Si hardening phases during the subsequent AA, contributing to the overall hardness.

There are, on the other hand, reports on the effect of adding Zn to 6xxx alloys. Saito et al. demonstrated that Zn can be incorporated into 6xxx hardening phases without disrupting the underlying Si-network [51]. Partial substitution both on and between Si-network columns was observed, as well as a tendency for Zn to segregate at particle/matrix interfaces. No η-phases were observed in the bulk microstructure, even with up to 1 wt.% Zn addition. By adding up to 3 wt.% Zn in an Al-Mg-Si alloy, Ding et al. were able to precipitate η in the bulk microstructure [52].

With respect to material properties, Gong et al. reported improvements in fatigue strength with increasing Si content in a 7xxx alloy [53]. She et al. reported a decrease in SCC susceptibility and decrease in tensile strength with increasing Si content [54]. The role of 6xxx precipitates on such properties could be explored further by optimising composition and thermal treatments. In relation to SCC, authors have claimed hardening phases (or their interfaces), as well as β-Mg_2Si, as important hydrogen trapping sites [55-58]. Modelling of these properties requires accurate knowledge of the precipitates present in the microstructure. However, it is unclear how the η-phase(s), β-Mg_2Si and 6xxx hardening phases compare with respect to hydrogen trapping energies and

Table 3
Relative fraction of identifiable plate shaped η hardening phases. The average minor dimension (thickness) and major dimension (diameter) and corresponding standard deviation are given as sorted based on the precipitate orientation. In addition, the upper and lower value within the measured population for the two dimensions is given.

	AC								WQ							
	T6			T7					T6				T7			
	η'	η_2	η_1	?	η'	η_2	η_1	?	η'	η_2	η_1	?	η'	η_2	η_1	?
Measurements (#)	62	22	2	0	0	55	46	8	24	29	5	0	1	47	29	8
Relative fraction (%)	71	25	4	0	0	37	47	16	40	48	12	0	0	41	38	21
Avg. thickness (nm)	1.40 ± 0.21	2.25 ± 0.43	–	–	–	3.55 ± 0.86	3.87 ± 1.48	3.73 ± 1.93	1.59 ± 0.21	2.49 ± 0.45	3.33 ± 0.39	–	–	3.33 ± 0.80	3.84 ± 1.18	2.89 ± 1.18
Upper/lower thickness (nm)	1.88/1.04	3.34/2.01	–	–	–	6.67/1.95	9.06/1.77	8.79/2.50	1.98/1.04	4.06/2.07	3.82/2.68	–	–	6.49/2.45	6.30/2.32	3.82/2.12
Avg. diameter (nm)	5.42 ± 1.19	6.08 ± 1.19	–	–	–	8.84 ± 2.23	7.27 ± 1.96	10.25 ± 3.04	6.16 ± 1.38	6.44 ± 1.29	4.92 ± 0.78	–	–	8.13 ± 2.00	7.41 ± 1.77	10.24 ± 2.20
Upper/lower diameter (nm)	8.32/2.58	8.67/4.38	–	–	–	13.73/4.82	12.10/4.21	15.59/6.14	9.51/3.56	9.08/3.68	6.30/3.95	–	–	13.72/4.58	11.05/3.39	14.39/7.12

Fig. 6. HAADF-STEM micrographs of η type precipitates in the WQ samples. A–B: η' (Type 1) precipitate along $[11\bar{2}]_{Al}$, showing a defect free (A) and a faulted variant (B). C–D: η_1 along $[001]_\eta//[110]_{Al}$ and $[010]_\eta//[\bar{1}10]_{Al}$ in (C) and (D), respectively. (E) is a micrograph of the cross-section of η_4 with the interface relation as $(2\bar{1}0)_\eta//(\bar{1}1\bar{1})_{Al}$. (F) Shows a highly disordered η precipitate. Notice the similar R- and O-units as in η', in addition to the flattened hexagon which can be described in two ways. A and B are obtained in WQ–T6, while the rest are from WQ–T7.

this should be explored further. Understanding hydrogen partition within the microstructure may suggest ways to reduce hydrogen concentration at grain boundaries and alleviate SCC susceptibility.

Optimising thermomechanical treatments could make use of the excess Si commonly found in 7xxx alloys by ensuring complete dissolution of the β-Mg_2Si with respect to the SHT and limiting quench induced precipitation. This may open possibilities for development of new hybrid 6xxx/7xxx series aluminium alloys.

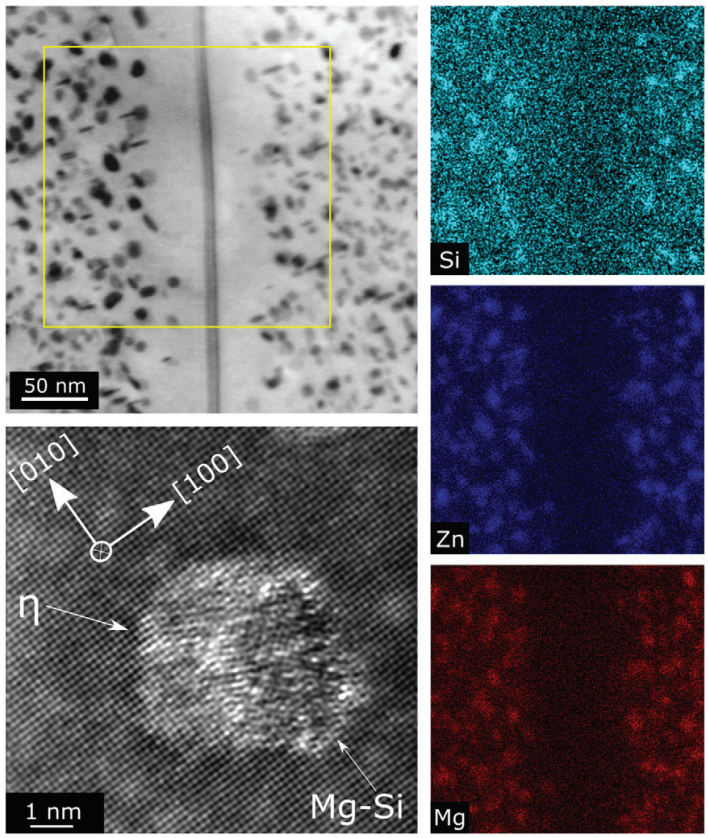

Fig. 7. BF-STEM image of a grain boundary in WQ-T7. The yellow square indicate where the corresponding Si, Zn and Mg EDS spectrum images are obtained. There are small regions in which Mg correlates with Si, but not with Zn. The Si and Zn signal may overlap since the 6xxx type hardening precipitate often are observed together with an η-type precipitate as shown by the high-resolution HAADF-STEM micrograph taken along $[100]_{Al}$.

5. Conclusion

An industrially extruded AA7003 alloy is investigated after different thermal treatments following either air cooling or water quenching from solution heat treatment. The main findings are:

1. Air cooling results in heterogeneous nucleation of β-Mg_2Si and η-$MgZn_2$ particles on grain boundaries and dispersoids.
2. The critical cooling rate for this alloy is higher than 3 K/s.
3. Bulk microstructures are dominated by η' & η_2 and η_1 & η_2 hardening precipitates after artificially ageing at 140 and 170 °C, respectively. This is independent of the prior water- or air cooling.
4. In the WQ-T7 state, 6xxx-type hardening precipitates coexist with the 7xxx hardening precipitates.

The results presented provide important fundamental insight into bulk microstructures, which are important for optimisation of thermomechanical treatments in 7xxx alloys containing Si.

CRediT authorship contribution statement

A. Lervik: Conceptualization, Data curation, Formal Analysis, Investigation, Writing - original draft. **C.D. Marioara:** Formal Analysis, Investigation, Writing - review & editing. **M. Kadanik:** Data Curation, Investigation. **J.C. Walmsley:** Funding acquisition, Supervision, Writing - review & editing. **B. Milkereit:** Formal analysis, Investigation, Supervision, Writing - review & editing. **R. Holmestad:** Funding acquisition, Supervision, Writing - review & editing.

Acknowledgments

L. Lodgaard and Benteler Automotive Raufoss AS is greatly acknowledged for providing the material and being involved in the discussions. This work was supported by the KPN project "FICAL" (Research Council of Norway (NFR):247598), co-financed by The Research Council of Norway (NFR), and the industrial partners Hydro, Gränges, Benteler Automotive Raufoss AS and Steertec Raufoss. The (S)TEM work was conducted on the NORTEM (Research Council of Norway (NFR):197405) infrastructure at the TEM Gemini Centre, Trondheim, Norway.

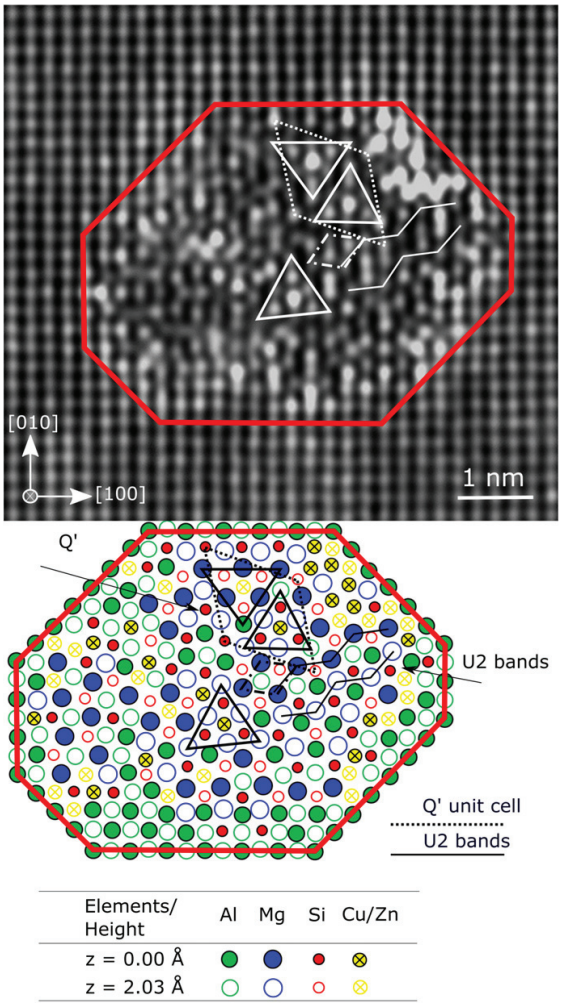

Fig. 8. HAADF-STEM micrograph of a disordered 6xxx type precipitate (top) and suggested atomic overlay (bottom). The micrograph has been fast Fourier transformed with a circular mask removing periods shorter than 0.15 nm. The micrograph is obtained in the WQ–T7 condition along the $[100]_{Al}$ direction.

References

[1] G. Totten, D. MacKenzie, Handbook of Aluminum, Marcel Dekker, New York, 2003.

[2] T. Shikama, S. Yoshihara, Highly SCC resistant 7000-series aluminum alloy extrusion, KOBELCO Technol. Rev. (2017) 65–68. http://www.kobelco.co.jp/english/ktr/pdf/ktr_35/065-068.pdf.

[3] T. Dursun, C. Soutis, Recent developments in advanced aircraft aluminium alloys, Mater. Des. 56 (2014) 862–871. https://doi.org/10.1016/j.matdes.2013.12.002.

[4] A. Reyes, O.S. Hopperstad, O.G. Lademo, M. Langseth, Modeling of textured aluminum alloys used in a bumper system: material tests and characterization, Comput. Mater. Sci. 37 (2006) 246–268. https://doi.org/10.1016/j.commatsci.2005.07.001.

[5] O. Jensrud, High Strength Aluminium Alloys Extrusions — A Review of the Thermo-Mechanical-Process in High Performance Profile Manufacturing, Progress in Extrusion Technology and Simulation of Light Metal Alloys, Key Engineering Materials, 491, Trans Tech Publications. 2012, pp. 11–18. https://doi.org/10.4028/www.scientific.net/KEM.491.11.

[6] M.C. Paulisch, N. Wanderka, M. Haupt, S. Selve, I. Driehorst, W. Reimers, The influence of heat treatments on the microstructure and the mechanical properties in commercial 7020 alloys, Mater. Sci. Eng. A 626 (2015) 254–262. https://doi.org/10.1016/j.msea.2014.12.040.

[7] M.C. Paulisch, M. Lentz, H. Wemme, A. Andrich, I. Driehorst, W. Reimers, The different dependencies of the mechanical properties and microstructures on hot extrusion and artificial aging processing in case of the alloys Al 7108 and Al 7175, J. Mater. Process. Technol. 233 (2016) 68–78. https://doi.org/10.1016/j.jmatprotec.2016.02.012.

[8] A.C.U. Rao, V. Vasu, M. Govindaraju, K.V.S. Srinadh, Stress corrosion cracking behaviour of 7xxx aluminum alloys: a literature review, Trans. Nonferrous Metals Soc. China (English Edition) 26 (2016) 1447–1471. https://doi.org/10.1016/S1003-6326(16)64220-6.

[9] B. Milkereit, O. Kessler, C. Schick, Recording of continuous cooling precipitation diagrams of aluminium alloys, Thermochim. Acta 492 (2009) 73–78. https://doi.org/10.1016/j.tca.2009.01.027.

[10] M.J. Starink, B. Milkereit, Y. Zhang, P.A. Rometsch, Predicting the quench sensitivity of Al-Zn-Mg-Cu alloys: a model for linear cooling and strengthening, Mater. Des. 88 (2015) 958–971. https://doi.org/10.1016/j.matdes.2015.09.058.

[11] M. Conserva, E. Di Russo, O. Caloni, Comparison of the influence of chromium and zirconium on the quench sensitivity of Al-Zn-Mg-Cu alloys, Metall. Trans. 2 (1971) 1227–1232. https://doi.org/10.1007/BF02664256.

[12] A. Deschamps, Y. Bréchet, Influence of quench and heating rates on the ageing response of an Al-Zn-Mg-(Zr) alloy, Mater. Sci. Eng. A 251 (1998) 200–207. https://doi.org/10.1016/S0921-5093(98)00615-7.

[13] A. Deschamps, Y. Bréchet, Nature and distribution of quench-induced precipitation in an Al-Zn-Mg-Cu alloy, Scr. Mater. 39 (1998) 1517–1522. https://doi.org/10.1016/S1359-6462(98)00357-1.

[14] D. Godard, P. Archambault, E. Aeby-Gautier, G. Lapasset, Precipitation sequences during quenching of the AA 7010 alloy, Acta Mater. 50 (2002) 2319–2329. https://doi.org/10.1016/S1359-6454(02)00063-0.

[15] A. Deschamps, G. Texier, S. Ringeval, L. Delfaut-Durut, Influence of cooling rate on the precipitation microstructure in a medium strength Al-Zn-Mg alloy, Mater. Sci. Eng. A 501 (2009) 133–139. https://doi.org/10.1016/j.msea.2008.09.067.

[16] Y. Zhang, C. Bettles, P.A. Rometsch, Effect of recrystallisation on Al3Zr dispersoid behaviour in thick plates of aluminium alloy AA7150, J. Mater. Sci. 49 (2014) 1709–1715. https://doi.org/10.1007/s10853-013-7856-x.

[17] Y. Zhang, B. Milkereit, O. Kessler, C. Schick, P.A. Rometsch, Development of continuous cooling precipitation diagrams for aluminium alloys AA7150 and AA7020, J. Alloys Compd. 584 (2014) 581–589. https://doi.org/10.1016/j.jallcom.2013.09.014.

[18] B. Milkereit, N. Wanderka, C. Schick, O. Kessler, Continuous cooling precipitation diagrams of Al-Mg-Si alloys, Mater. Sci. Eng. A 550 (2012) 87–96. https://doi.org/10.1016/j.msea.2012.04.033.

[19] H. Inoue, T. Sato, Y. Kojima, T. Takahashi, The temperature limit for GP zone formation in an Al-Zn-Mg alloy, Metall. Mater. Trans. A 12 (1981) 1429–1434. https://doi.org/10.1007/BF02643687.

[20] X.J. Jiang, B. Noble, B. Holme, G. Waterloo, J. Taftø, Differential scanning calorimetry and electron diffraction investigation on low-temperature aging in Al-Zn-Mg alloys, Metall. Mater. Trans. A 31 (2000) 339–348. https://doi.org/10.1007/s11661-000-0269-x.

[21] L.K. Berg, J. Gjønnes, V. Hansen, X.Z. Li, M. Knutson-Wedel, G. Waterloo, D. Schryvers, L.R. Wallenberg, GP-zones in Al-Zn-Mg alloys and their role in artificial aging, Acta Mater. 4 (2001) 3443–3451. https://doi.org/10.1016/S1359-6454(01)00251-8.

[22] G. Sha, A. Cerezo, Early-stage precipitation in Al-Zn-Mg-Cu alloy (7050), Acta Mater. 52 (2004) 4503–4516. https://doi.org/10.1016/j.actamat.2004.06.025.

[23] C. Wolverton, Crystal structure and stability of complex precipitate phases in Al-Cu-Mg-(Si) and Al-Zn-Mg alloys, Acta Mater. 49 (2001) 3129–3142. https://doi.org/10.1016/S1359-6454(01)00229-4.

[24] K. Matsuda, A. Kawai, K. Watanabe, S. Lee, C.D. Marioara, S. Wenner, K. Nishimura, T. Matsuzaki, N. Nunomura, T. Sato, R. Holmestad, S. Ikeno, Extra electron diffraction spots caused by fine precipitates formed at the early stage of aging in Al-Mg-X (X = Si, Ge, Zn)-Cu alloys, J. Jpn. Inst. Light Met. 58 (2017) 167–175. https://doi.org/10.2464/jilm.67.186.

[25] P. Thackary, The nature and morphology of precipite in Al-Zn-Mg alloys, J. Inst. Met. 96 (1968) 7.

[26] J. Gjønnes, C.J. Simensen, An electron microscope investigation of the microstructure in an aluminium-zinc-magnesium alloy, Acta Metall. 18 (1970) 881–890. https://doi.org/10.1016/0001-6160(70)90016-7.

[27] H.P. Degischer, W. Lacom, A. Zahra, Y.C. Zahra, Decomposition processes in an Al-5% Zn-1% Mg alloy — part II: electron microscopic investigations, Zeitschrift Z. Metallkd. 71 (1980) 213–238.

[28] H. Löffler, I. Kovács, J. Lendvai, Review decomposition processes in Al-Zn-Mg alloys, J. Mater. Sci. 18 (1983) 2215–2240. https://doi.org/10.1007/BF00541825.

[29] T.-F. Chung, Y.-L. Yang, M. Shiojiri, C.-N. Hsiao, W.-C. Li, C.-S. Tsao, Z. Shi, J. Lin, J.-R. Yang, An atomic scale structural investigation of nanometre-sized η precipitates in the 7050 aluminium alloy, Acta Mater. (2019) https://doi.org/10.1016/j.actamat.2019.05.041.

[30] C.D. Marioara, W. Lefebvre, S.J. Andersen, J. Friis, Atomic structure of hardening precipitates in an Al-Mg-Zn-Cu alloy determined by HAADF-STEM and first-principles calculations: relation to η-MgZn2, J. Mater. Sci. 48 (2013) 3638–3651. https://doi.org/10.1007/s10853-013-7158-3.

[31] A. Bendo, K. Matsuda, S. Lee, K. Nishimura, N. Nunomura, H. Toda, M. Yamaguchi, T. Tsuru, K. Hirayama, K. Shimizu, H. Gao, K. Ebihara, M. Itakura, T.

Yoshida, S. Murakami, Atomic scale HAADF-STEM study of η and η_1 phases in peak-aged Al-Zn-Mg alloys, J. Mater. Sci. 53 (2018) 4598–4611. https://doi.org/10.1007/s10853-017-1873-0.

[32] A. Bendo, T. Maeda, K. Matsuda, A. Lervik, R. Holmestad, C.D. Marioara, K. Nishimura, N. Nunomura, H. Toda, M. Yamaguchi, K.-i. Ikeda, T. Homma, Characterisation of structural similarities of precipitates in Mg-Zn and Al-Zn-Mg alloys systems, Philos. Mag. 0 (2019) 1–17. https://doi.org/10.1080/14786435.2019.1637032.

[33] S.J. Andersen, C.D. Marioara, J. Friis, S. Wenner, R. Holmestad, Precipitates in aluminium alloys, Adv. Phys. X 3 (2018) 790–813. https://doi.org/10.1080/23746149.2018.1479984.

[34] A. Singh, J. Rosalie, Lattice correspondence and growth structures of monoclinic Mg4Zn7 phase growing on an icosahedral quasicrystal, Crystals 8 (2018) 194. https://doi.org/10.3390/cryst8050194.

[35] Y.Y. Li, L. Kovarik, P.J. Phillips, Y.F. Hsu, W.H. Wang, M.J. Mills, High-resolution characterization of the precipitation behavior of an Al-Zn-Mg-Cu alloy, Philos. Mag. Lett. 92 (2012) 166–178. https://doi.org/10.1080/09500839.2011.652682.

[36] L. Jones, H. Yang, T.J. Pennycook, M.S.J. Marshall, S. Van Aert, N.D. Browning, M.R. Castell, P.D. Nellist, Smart Align — a new tool for robust non-rigid registration of scanning microscope data, Adv. Struct. Chem. Imaging 1 (2015) 8. https://doi.org/10.1186/s40679-015-0008-4.

[37] R.H. Kemsies, B. Milkereit, S. Wenner, R. Holmestad, O. Kessler, In situ DSC investigation into the kinetics and microstructure of dispersoid formation in Al-Mn-Fe-Si(-Mg) alloys, Mater. Des. 146 (2018) 96–107. https://doi.org/10.1016/j.matdes.2018.03.007.

[38] A.J. De Ardo, C.J. Simensen, A structural investigation of multiple aging of Al-7 wt pct Zn-2.3 wt pct Mg, Metall. Trans. 4 (1973) 2413–2421. https://doi.org/10.1007/BF02669384.

[39] V. Hansen, O.B. Karlsen, Y. Langsrud, J. Gjønnes, Precipitates, zones and transitions during aging of Al-Zn-Mg-Zr 7000 series alloy, Mater. Sci. Technol. 20 (2004) 185–193. https://doi.org/10.1179/026708304225010424.

[40] T.-F. Chung, Y.-L. Yang, B.-M. Huang, Z. Shi, J. Lin, T. Ohmura, J.-R. Yang, Transmission electron microscopy investigation of separated nucleation and in-situ nucleation in AA7050 aluminium alloy, Acta Mater. 149 (2018) 377–387. https://doi.org/10.1016/j.actamat.2018.02.045.

[41] T. Saito, C.D. Marioara, S.J. Andersen, W. Lefebvre, R. Holmestad, Aberration-corrected HAADF-STEM investigations of precipitate structures in Al-Mg-Si alloys with low Cu additions, Philos. Mag. 94 (2014) 520–531. https://doi.org/10.1080/14786435.2013.857051.

[42] J.K. Sunde, C.D. Marioara, A.T. van Helvoort, R. Holmestad, The evolution of precipitate crystal structures in an Al-Mg-Si(-Cu) alloy studied by a combined HAADF-STEM and SPED approach, Mater Charact 142 (2018) 458–469. https://doi.org/10.1016/j.matchar.2018.05.031.

[43] S.J. Andersen, C.D. Marioara, J. Friis, R. Bjørge, Q. Du, I. Ringdalen, S. Wenner, E.A. Mørtsell, R. Holmestad, T. Saito, J. Røyset, O. Reiso, Directionality and column arrangement principles of precipitates in Al-Mg-Si-(Cu) and Al-Mg-Cu linked to line defect in Al, Mater. Sci. Forum 877 (2016) 461–470. https://doi.org/10.4028/www.scientific.net/MSF.877.461.

[44] T. Saito, E.A. Mørtsell, S. Wenner, C.D. Marioara, S.J. Andersen, J. Friis, K. Matsuda, R. Holmestad, Atomic structures of precipitates in Al-Mg-Si alloys with small additions of other elements, Adv. Eng. Mater. 1800125 (2018) 1–18. https://doi.org/10.1002/adem.201800125.

[45] B. Milkereit, M.J. Starink, Quench sensitivity of Al-Mg-Si alloys: a model for linear cooling and strengthening, Mater. Des. 76 (2015) 117–129. https://doi.org/10.1016/j.matdes.2015.03.055.

[46] B. Milkereit, M. Österreich, P. Schuster, G. Kirov, E. Mukeli, O. Kessler, Dissolution and precipitation behavior for hot forming of 7021 and 7075 aluminum alloys, Metals 8 (2018) 531. https://doi.org/10.3390/met8070531.

[47] P. Schloth, J.N. Wagner, J.L. Fife, A. Menzel, J.M. Drezet, H. Van Swygenhoven, Early precipitation during cooling of an Al-Zn-Mg-Cu alloy revealed by in situ small angle X-ray scattering, Appl. Phys. Lett. 105 (2014) 9–12. https://doi.org/10.1063/1.4894768.

[48] P. Schumacher, S. Pogatscher, M.J. Starink, C. Schick, V. Mohles, B. Milkereit, Quench-induced precipitates in Al-Si alloys: calorimetric determination of solute content and characterisation of microstructure, Thermochim. Acta 602 (2015) 63–73. https://doi.org/10.1016/j.tca.2014.12.023.

[49] P. Schumacher, Plastisches Verformungsverhalten unterkühlter Aluminiumlegierungen im System Al-Mg-Si,Ph.D. thesis. Universität Rostock. 2018.

[50] V. Hansen, A. Vevecka-Priftaj, J. Fjerdingen, Y. Langsrud, J. Gjønnes, The influence of silicon on age hardening kinetics and phase precipitations in Al-Mg-Zn alloys, Mater. Sci. Forum 519-521 (2006) 579–584. https://doi.org/10.4028/www.scientific.net/MSF.519-521.579.

[51] T. Saito, S. Wenner, E. Osmundsen, C.D. Marioara, S.J. Andersen, J. Røyset, W. Lefebvre, R. Holmestad, The effect of Zn on precipitation in Al-Mg-Si alloys, Philos. Mag. 94 (2014) 2410–2425. https://doi.org/10.1080/14786435.2014.913819.

[52] X.P. Ding, H. Cui, J.X. Zhang, H.X. Li, M.X. Guo, Z. Lin, L.Z. Zhuang, J.S. Zhang, The effect of Zn on the age hardening response in an Al-Mg-Si alloy, Mater. Des. 65 (2015) 1229–1235. https://doi.org/10.1016/j.matdes.2014.09.086.

[53] B.S. Gong, Z.J. Liu, Y.L. Wang, Z.J. Zhang, P. Zhang, H.C. Jiang, L.J. Rong, Z.F. Zhang, Improving the fatigue strength of A7N01 aluminum alloy by adjusting Si content, Mater. Sci. Eng. A 742 (2019) 15–22. https://doi.org/10.1016/j.msea.2018.10.085.

[54] H. She, W. Chu, D. Shu, J. Wang, B.-d. Sun, Effects of silicon content on microstructure and stress corrosion cracking resistance of 7050 aluminum alloy, Trans. Nonferrous Metals Soc. China 24 (2014) 2307–2313. https://doi.org/10.1016/S1003-6326(14)63349-5.

[55] H. Saitoh, Y. Iijima, K. Hirano, Behaviour of hydrogen in pure aluminium, Al-4 mass% Cu and Al-1 mass% Mg2Si alloys studied by tritium electron microautoradiography, J. Mater. Sci. 29 (1994) 5739–5744. https://doi.org/10.1007/BF00349974.

[56] X.Y. Sun, B. Zhang, H.Q. Lin, Y. Zhou, L. Sun, J.Q. Wang, E.H. Han, W. Ke, Atom probe tomographic study of elemental segregation at grain boundaries for a peak-aged Al-Zn-Mg alloy, Corros. Sci. 79 (2014) 1–4. https://doi.org/10.1016/j.corsci.2013.10.027.

[57] L. Oger, M.C. Lafouresse, G. Odemer, L. Peguet, C. Blanc, Hydrogen diffusion and trapping in a low copper 7xxx aluminium alloy investigated by Scanning Kelvin Probe Force Microscopy, Mater. Sci. Eng. A 706 (2017) 126–135. https://doi.org/10.1016/j.msea.2017.08.119.

[58] T. Tsuru, M. Yamaguchi, K. Ebihara, M. Itakura, Y. Shiihara, K. Matsuda, H. Toda, First-principles study of hydrogen segregation at the MgZn2 precipitate in Al-Mg-Zn alloys, Comput. Mater. Sci. 148 (2018) 301–306. https://doi.org/10.1016/j.commatsci.2018.03.009.

[59] A. Bendo, K. Matsuda, A. Lervik, T. Tsuru, K. Nishimura, N. Nunomura, R. Holmestad, C.D. Marioara, K. Shimizu, H. Toda, M. Yamaguchi, An unreported precipitate orientation relationship in Al-Zn-Mg based alloys, Mater. Charact. 158 (2019)109958.

Paper VI

Stress corrosion cracking in an extruded Cu-free Al-Zn-Mg alloy

Adrian Lervik, John Charles Walmsley, Lars Lodgaard, Calin Daniel Marioara, Roy Johnsen, Otto Lunder, Randi Holmestad

In preparation

Article

Stress corrosion cracking in an extruded Cu-free Al-Zn-Mg alloy

Adrian Lervik [1,*], John C. Walmsley [2], Lars Lodgaard [3], Calin D. Marioara [4], Roy Johnsen [5], Otto Lunder [4], and Randi Holmestad [1]

1 Department of Physics, Norwegian University of Science and Technology (NTNU), N-7491 Trondheim, Norway
2 Department of Materials Science and Metallurgy, University of Cambridge, CB2 3QZ, U.K.
3 Benteler Automotive, 2830, Raufoss, Norway
4 SINTEF Industry, N-7465, Trondheim, Norway
5 Department of Mechanical and Industrial Engineering, NTNU, Richard Birkelands vei 2b, 7491, Trondheim, Norway
* Correspondence: adrian.lervik@ntnu.no

Received: date; Accepted: date; Published: date

Abstract: Stress corrosion cracking (SCC) in Cu-free Al-Zn-Mg (7xxx) aluminium alloys is not fully understood and is a limiting factor that prevents usage in many applications. In the present work, this phenomenon has been studied using the double cantilever beam method and slow strain rate tensile tests for a peak- and slightly overaged temper in a AA7003 alloy. Microstructural features including grain boundary particles, precipitate free zones and matrix precipitates have been studied using transmission- and scanning electron microscopy. A difference in the SCC properties is established between the two tempers. The dominating difference in microstructure is the size and orientation of hardening phases. Possible explanations relating the microstructural observations and SCC properties are discussed.

Keywords: Aluminium alloys; Stress corrosion cracking; Transmission electron microscopy; EBSD; Microstructure; Grain boundaries

1. Introduction

Wrought Al-Zn-Mg-(Cu) (7xxx) aluminium alloys are of great interest in automotive- and aerospace application due to their high strength-to-weight ratio and formability [1,2]. Replacing heavy components with lighter aluminium alloys will allow for longer travel distance on the same amounts of energy, effectively reducing green house gas emissions. However, the 7xxx alloy series is known for their susceptibility to stress corrosion cracking (SCC) which limits the use of these alloys in many applications [3]. Both the understanding and the suggested ways to mitigate SCC have been reviewed several times [3–8]. However, there are still many unanswered questions concerning the phenomenon.

SCC in aluminium usually occurs along grain boundaries when a susceptible material is stressed above some critical value in a corrosive environment. Cracking is initiated due to mechanical surface defects or from areas corroded by pitting and/or intergranular corrosion (IGC) [4]. The propagation mechanism is a subject of controversy as the fundamental mechanism(s) is not fully understood. Commonly proposed propagation mechanisms include hydrogen embrittlement (HE), anodic dissolution and passive film rupture [3,4,9]. It is not unlikely that several of these mechanisms may occur simultaneously and effect one another, as suggested by Najjar *et al.* [10]. In the vicinity of the crack tip the pH is low and the dominating cathodic reaction is proton reduction [11]. This results in hydrogen evolution and diffusion ahead of the crack, promoting conditions for local embrittlement [9,10].

Microstructural features often discussed in relation to SCC include grain boundary particles (GBPs) [12–17], widths and solute concentration in the precipitate free zones (PFZs) [12], and elemental

segregation to grain boundaries [18–21]. Also, bulk (matrix) precipitates and their interactions with dislocations have been suggested to influence the SCC, as their size and shape may influence the slip characteristics and affect strain localisation at the grain boundaries [15,22–27]. All these microstructural features are strongly affected by the thermo-mechanical processing of the alloy. Especially, variations in the final age hardening (artificial ageing) stage, can drastically change the SCC properties. As such, it is common that a slightly overaged condition has higher SCC resistance than the highest strength peak aged temper in the same alloy [4].

Sarkar *et al.* demonstrated that with increasing Cu addition to an Al-Zn-Mg alloy, the crack growth rate decreased accordingly [15]. Correspondingly, much work has been conducted in order to understand why Cu additions have such positive effects at reducing SCC susceptibility. It is now generally accepted that Cu is substituted into the η-$MgZn_2$ GBPs, changing the composition to η-$MgZn_{(2-x)}Cu_x$, and that is the main reason for the improved SCC resistance by adding Cu [15,28–31]. The equilibrium η-$MgZn_2$ phase is highly anodic with respect to the aluminium matrix [32], and with increasing Cu substitution the potential difference between particle and matrix decreases. This understanding is however not applicable to Cu-free systems.

In a previous study, the bulk (in grain) microstructure of the same alloy used herein, was studied in detail after both air cooling and water quenching from solution heat treatment (SHT), and aged to a T6 and T7 temper [33]. Heterogeneous nucleation of β-Mg_2Si and η-$MgZn_2$ particles on grain boundaries and dispersoids was observed after air cooling. Part of the motivation for this work is to see if small variation in Si content, and thus the presence of β-Mg_2Si particles at grain boundaries may have any influence on the SCC properties. Furthermore, the nanoscale η hardening precipitates had different size and orientation relationships with the Al matrix in the T6 and T7 tempers, independent of the prior cooling method from SHT. Here, the characterisation focuses on the grain boundary microstructure in addition to SCC testing. This is done in a commercial Cu-free aluminium alloy with variations in Si content, quench rates and artificial aging parameters.

2. Experimental

2.1. Materials

Two AA7003 alloys with composition given in table 1 were cast and homogenized, before they were pre-heated to 480 °C and extruded at ∼11 mm/s into a solid rectangular profile with dimensions 20×25 mm. A subsequent SHT at 480 °C for 30 min was conducted, before either water quench (WQ) or air cooling (AC) to room temperature was performed. Subsequent artificial ageing (AA) was carried out at 140 °C for 17 h or 170 °C for 6 h, which are designated as the peak- (T6) and slightly overaged (T7) tempers, respectively. Samples are further referred to as '*x*-*yy*-*zz*', where *x* indicate high (H) or low (L) Si content, *yy* is the quench rate (WQ or AC) and *zz* is the artificial ageing temper (T6 or T7).

Table 1. Alloy compositions (in wt.%) measured using optical emission spectroscopy.

Alloy	Fe	Mg	Si	Zn	Cu	Zr	Ti	Al	Zn/Mg
7003-H	0.20	0.68	0.11	5.56	0.01	0.17	0.02	Bal.	8.20
7003-L	0.20	0.71	0.05	5.65	<0.01	0.15	0.01	Bal.	8.20

2.2. Double cantilever beam

Specimens for double cantilever beam (DCB) testing were machined from the extruded profiles. into the geometry initially suggested by Hyatt [34], with some modifications. In the schematic drawing in figure 1, the v-notch was removed by spark erosion as it was deemed unnecessary for the test. One third of the samples were subjected to fatigue pre-cracking before bolt loading, while the rest were bolt loaded directly. The initial notch condition had no influence on the measured properties. Crack-tip stress intensity was calculated using the formula:

$$K_I = \frac{\Delta E h [3h(a+0.6h)^2 + h^3]^{1/3}}{4[(a+0.6h)^3 + h^2 a]} \quad (1)$$

where Δ, E, h, and a are the deflection at the load point, elastic modulus (70 GPa), half the specimen height and the crack length measured from the load point, respectively. An initial loading to 25 MPa$\sqrt{\text{m}}$ was applied. The crack tip was kept wet by dripping a few drops of 3.5 wt.% NaCl solution once per day, for a total duration of 1500 h. The crack evolution was measured using an optical microscope. Crack velocity in the stress independent 'Region II (plateau)' [4], was interpolated to obtain a mean value with corresponding standard deviation. SCC threshold stress intensities, K_{ISCC}, were determined from the points with the lowest crack velocity and K_I value, and represented in a similar manner. In order to study the fracture surfaces, specimens were cooled in liquid nitrogen and pulled apart using rapid tensile overload. Three parallels for each temper were measured.

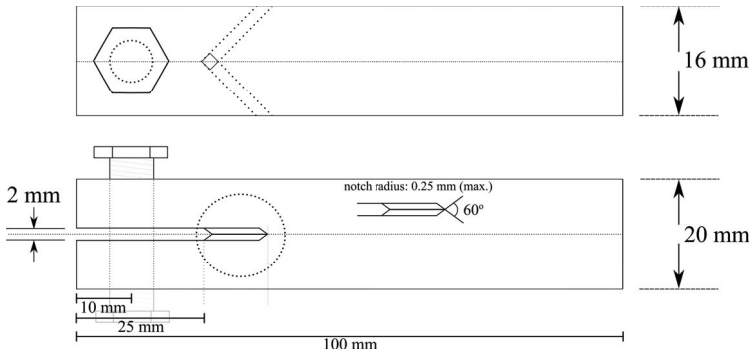

Figure 1. Schematic drawing of the DCB specimens used in this work. Originally from [34].

2.3. Slow strain rate testing

Specimens for slow strain rate testing (SSRT) were machined from the same extruded profile into the geometry given in figure 2. The samples were washed in ethanol in an ultrasonic bath for 2.5 min prior to testing. Test environments used were air and 3.5 wt.% NaCl solution with neutral pH and pH 3. An initial strain rate of 1.2×10^{-8} ms^{-1} was applied in all cases. Plastic insulators were mounted between the clamps and the sample in order to prevent galvanic effects when testing in solution. The pH and open circuit potential (OCP) were measured during and after each test. One tensile test for each temper in each environment was conducted. The fracture surfaces were observed in scanning electron microscopy (SEM) and from such images the reduction in area (RA) was estimated according to:

$$\text{RA} = \frac{(Z_0 - Z_f)}{Z_0} \times 100, \quad (2)$$

where Z_0 and Z_f are the initial and final cross-section area after fracture, respectively. The reduction in area ratio (RRA) was used as a measure to deduce susceptibility to the environment. This was done by dividing the RA value obtained in the test solution on the RA acquired in air:

$$\text{RRA} = \frac{\text{RA}_{\text{sol}}}{\text{RA}_{\text{air}}}. \quad (3)$$

2.4. Potentiodynamic polarisation

Samples for potentiodynamic polarisation were cut to 25×20×3.5 mm. An electrical contact was soldered to the back of the specimen, before it was embedded in epoxy and ground to a mirror finish

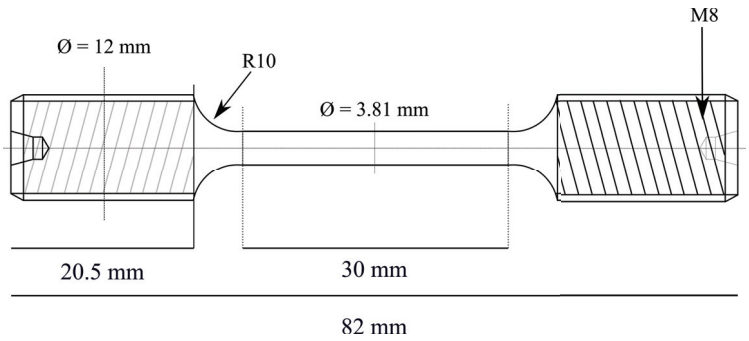

Figure 2. Schematic drawing of the round tensile specimens used for slow strain rate testing.

using 4000 grit SiC abrasive paper. Samples were left at OCP in 3.5 wt.% NaCl for 1 hour. Polarisation was started at 100 mV below OCP and increased at a rate of 0.1 mV/s to a maximum current density of 0.05 A/cm^2, and then back down to OCP.

2.5. Electrical conductivity

Electrical conductivity was measured using Sigmatest 2.069 unit on samples that were polished with 2000 grit SiC paper. Five measurements on each of the four samples were conducted.

2.6. Electron microscopy

Samples for electron backscattered diffraction (EBSD) were mechanically polished down to 0.02 μm colloidal silica suspension before a final argon ion thinning step. EBSD scans were conducted on a Hitachi SU-6600 FEG-SEM using a Nordif EBSD detector with a working distance of 24 mm, sample tilt of 70°, and <0.3 μm step size. Nordif3.0 was used to index the acquired patterns and all subsequent analysis was conducted using MTEX [35].

Specimens for transmission electron microscopy (TEM) were prepared by grinding using SiC abrasive paper to ~100 μm foil thickness, punched into 3 mm discs and thereafter electropolished with a Struers TenuPol-5 machine. An electrolyte consisting of 1/3 HNO_3 and 2/3 CH_3OH kept at temperatures between -30 and -20 °C with an applied potential of 18 V was used. Lastly, a final Ar ion milling step in a PIPS II instrument was applied to remove the outer layers exposed to the electrolyte. Typical conditions for this were 3 kV for 5 min at ±3°, followed by stepwise reduction in potential down to 0.5 kV for similar durations and angles.

Two TEMs were used in this work. (i) a JEOL JEM-2100F operated at 200 kV, equipped with an Oxford X-Max 80 silicon drift detector with solid angle of 0.23 sr for energy-dispersive X-ray spectroscopy (EDS). (ii) A double Cs-corrected JEOL ARM200CF operated at at 200 kV using convergence semi-angle of 28 and 48 mrad inner collector angle for high-angle annular dark-field (HAADF)-scanning transmission electron microscopy (STEM) imaging. The microscope is equipped with a Centurio EDS detector (solid angle: 0.98 sr). EDS data were post-processed using the open-source python package HyperSpy [36].

3. Results

3.1. Microstructure

Representative backscattered electron (BSE)-SEM images at two different magnifications are shown in figure 3. The images are acquired both parallel (3**a** & 3**b**) and normal to the extrusion direction (3**c** & 3**d**). The large particles visible in the low-magnification images in figures 3**a** & 3**c**, are α-Al(FeMn)Si phase primary constituents. In figures 3**b** & 3**d**, the grain structure is visible, with

presence of very small η-$MgZn_2$ particles (<0.5 μm). The images are from the H-AC-T6 condition. In all AC conditions, β-Mg_2Si particles are also present on grain boundaries, visible as dark regions in figures 3**b** & 3**d**. This is the only observable difference between the WQ and AC samples. No variation in GBPs size or distribution, between the T6 and T7 tempers, could be established using SEM.

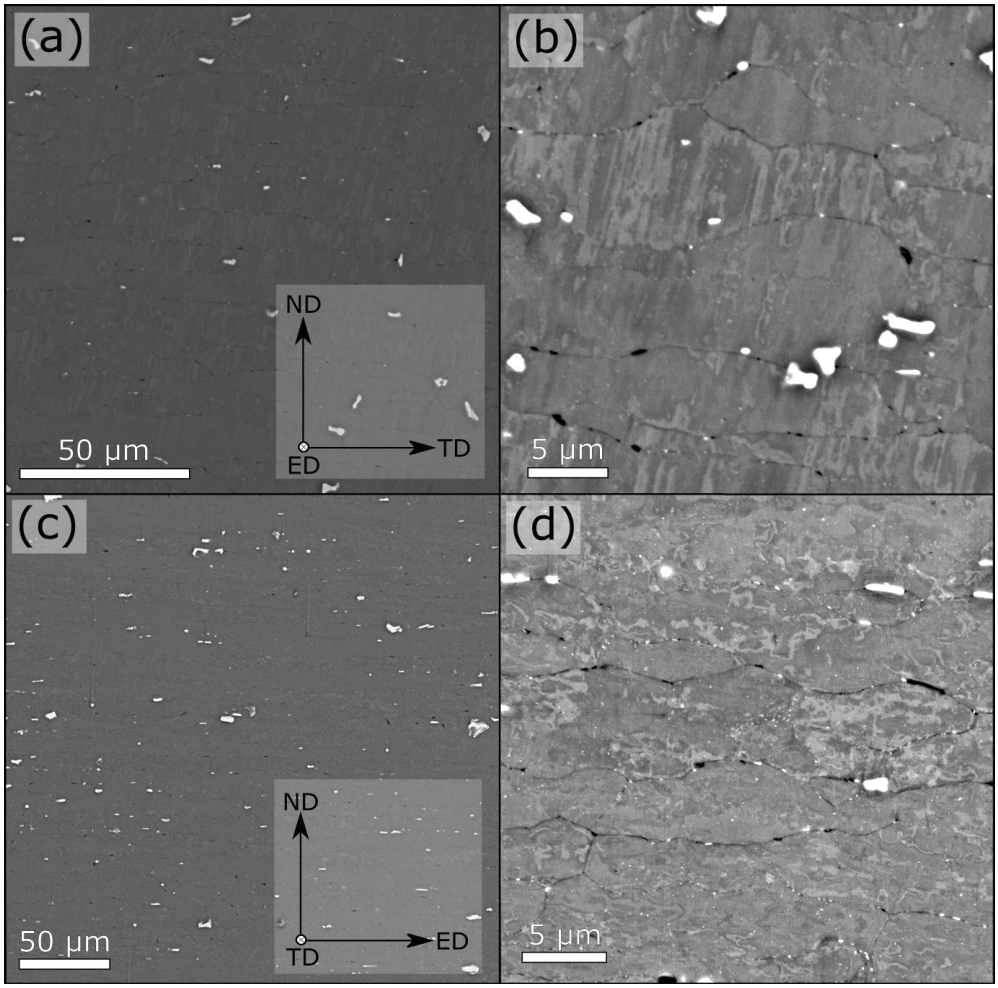

Figure 3. Representative BSE-SEM images from sample H-AC-T6, acquired both parallel (3**a** & 3**b**) and normal to the extrusion direction (3**c** & 3**d**). Large α-Al(FeMn)Si primary particles can be seen in **a** and **c**, and tiny η-$MgZn_2$ particles are visible on the grain boundaries in **b** and **d**. The black regions on the grain boundaries in **b** and **d**, are β-Mg_2Si particles, which are only present in AC samples.

EBSD images acquired along two different orientations are shown in figure 4. In both figures 4**a** and 4**b** the grains are coloured according to the inverse pole figure in figure 4**c**, and the grain boundary misorientations are coloured according to the scale in figure 4**b**. Figure 4**a** shows the cross-section of the extrusion direction (ED) where most of the grains are oriented close to either the $[111]_{Al}$ or $[100]_{Al}$ directions. Large amounts of low-angle grain boundaries are found between grains with close to similar orientation, and high-angle grain boundaries are typically found between grains with dissimilar orientations. Most of the grain boundaries are aligned nearly parallel with the transverse direction (TD). In figure 4**b**, the cross-section of the TD is shown. It can be seen that the grains adapt a more scattered distribution of orientations. A clear extrusion texture is visible, where large fibrous

grains are aligned parallel to the extrusion direction. These grains are separated by high-angle grain boundaries and within the fibers there are mostly low-angle and sub-grain boundaries. The sub-grain boundaries are best defined by the change in colour within each grain and not by the misorientation lines separating individual grains, as the threshold in the analysis was set to >3° to define grain boundaries. Both EBSD images are from the H-WQ-T6 sample, but the texture is representative for all the tempers in this study.

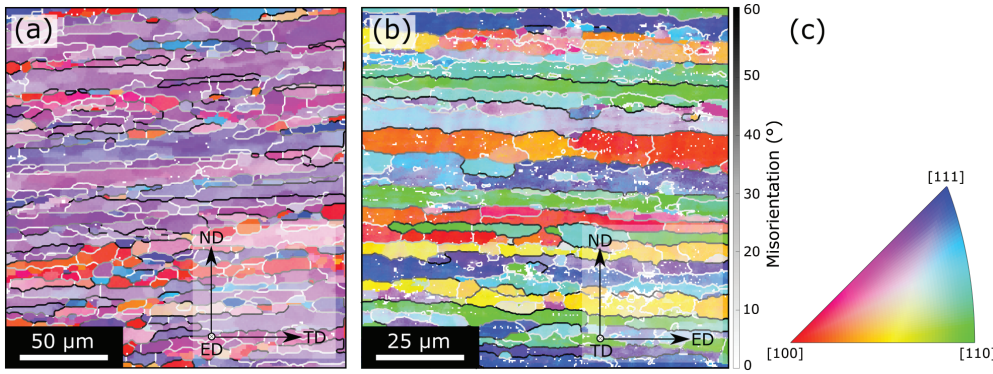

Figure 4. Representative EBSD images acquired along two different directions in **a** and **b**. The grains are coloured according to the inverse pole figure in **c**. Grain boundary misorientations are colour coded according to the scale in **b**.

3.2. Grain boundaries in TEM

Three distinct grain boundary 'types' were observed in all tempers and are represented in the HAADF-STEM image acquired parallel with the extrusion direction in sample H-AC-T7, shown in figure 5. Type 1 are sub-grain boundaries with <2° in misorientation, and are clearly distinguishable by their high density of small particles. These are likely to have formed due to preferential nucleation on dislocations. Type 2 and 3 grain boundaries are not distinguished by misorientation angle, but rather by the presence of particles or not. Type 2 contains precipitated particles, which are larger than those found on the sub-grain boundaries, while type 3 has very few or no particles present. The size of 40-60 grain boundary particles on both type 1 and type 2 grain boundaries was measured for two tempers, and is presented in table 2. The average value of the particle size increases slightly in the T7 condition. However, there are large variations in the measured data which is manifested in the standard deviations. Large scatter in particle sizes and densities are found within the same material, and even along the same grain boundary segment. This is likely related to the particles nucleation plane and/or coherency of the adjourning grains.

A typical cell structure with high density of grain boundary particles is shown in figures 6**a-c**. These bright-field (BF)-STEM images were acquired viewing perpendicular to the extrusion direction for sample H-WQ-T6. In figure 6**c**, the GBPs are seen from different projections and demonstrate their puck-like shape. Type 2 grain boundaries with particles of different size and morphology are shown in the two BF-STEM images in figure 6**d** & 6**e**. In figure 6**d** the long axes of the particles are aligned in the same direction and show a similar strong diffraction contrast. This indicates that they are all nucleated relative to one of the grains. In 6**e** the particles appear more randomly oriented. Figure 6**f** shows a HAADF-STEM image of a type 3 grain boundary with no particles present. Similar observations were made in all the conditions studied in this work.

The average widths of PFZss, measured from 10 type 2 and type 3 grain boundaries, are given in table 2 with corresponding standard deviations. The H-WQ-T6 condition has an average width of 80 nm, which is slightly smaller than the three other tempers with PFZs similar at around 110 nm.

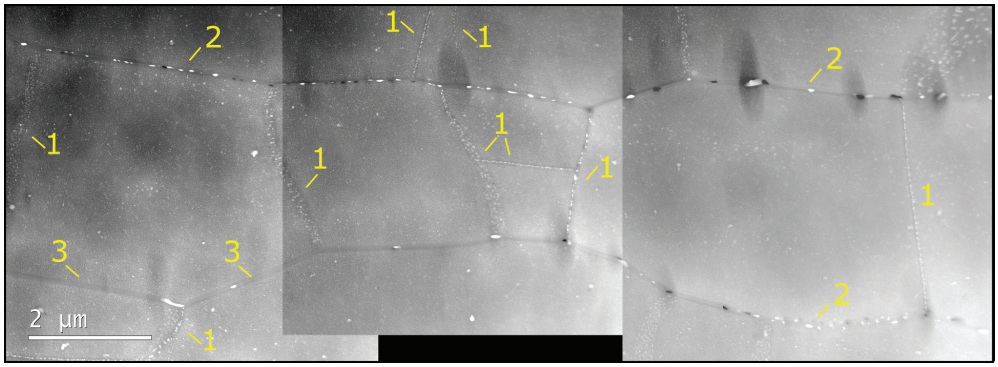

Figure 5. HAADF-STEM image showing the typical microstructure found in TEM. Three distinct types of grain boundaries are observed. (1) Low-angle sub-grain boundaries with high number densities of particles. (2) Grain boundaries with fewer, but larger particles and (3) grain boundaries with no or very few particles. The image is acquired parallel to the extrusion direction for sample H-AC-T7. Similar observations were made in all temperrs.

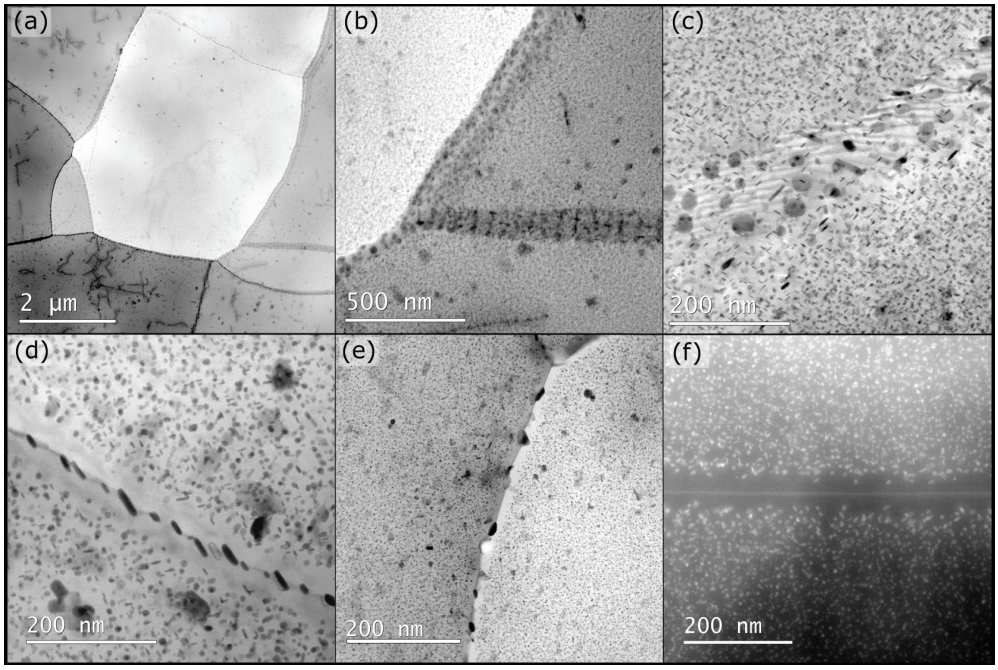

Figure 6. BF-STEM images of a cell structure consisting of sub-grain boundaries (type 1) with high density of grain boundary particles in **a-c**. **d** & **e** shows two type 2 grain boundaries with particles of different size, shape and distance between. **f** is a HAADF-STEM image of a type 3 grain boundary where no particles are present and the PFZs are clearly visible.**c** is acquired in sample H-AC-T6, while the rest is from H-WQ-T6, all parallel to the extrusion direction.

Composition of approximately 150 grain boundary particles for each temper of the high Si alloy, was measured using EDS spot analysis in microscope (i), and the average Zn/Mg ratio is shown in table 2. Particles in the T7 tempers exhibit a higher average Zn/Mg ratio regardless of the cooling method from SHT. The T6-AC temper has the lowest average Zn/Mg ratio of 1.64. Note that within the same temper there are large variations in the GBP compositions, which can be seen in the scattered

plots shown in Supplementary figure A1. In addition, a particle composition analysis from one GBP in each condition was obtained from microscope (ii) and is given table 2. No clear difference can be deduced from these results. The Al amount is likely to be overestimated due to the surrounding matrix. All the particles represented in table 2 are some variant of $MgZn_{2-x}Al_x$.

Table 2. Compositional analysis using TEM-EDS of GBPs in each temper acquired in microscope (ii). Average Zn/Mg ratio of ∼150 GBPs acquired using microscope (i) represented in the column named 'multiple'. Average GBP size with corresponding standard deviation measured for grain boundaries with dense and non-dense particle distribution in the two conditions with the largest difference in measured SCC properties. Average width of PFZs acquired from 10 grain boundaries in each temper.

	Single GBP composition			Multiple	GBP size (nm)		PFZ (nm)
	Al	Zn	Mg	Avg. Zn/Mg	Type 1 (Sub GB)	Type 2	
H-WQ-T6	47.0 ± 4.4	36.7 ± 3.1	16.5 ± 2.1	2.21	23.0 ± 8.9	65.1 ± 30.2	80 ± 6
H-WQ-T7	49.5 ± 10.4	36.5 ± 7.6	13.9 ± 3.7	2.56			107 ± 15
H-AC-T6	60.4 ± 5.2	28.2 ± 3.9	11.2 ± 2.4	1.64			103 ± 13
H-AC-T7	53.9 ± 7.9	32.9 ± 5.9	13.0 ± 3.3	2.57	34.9 ± 8.2	88.9 ± 27.0	116 ± 10

In addition, there are β-Mg_2Si particles present along grain boundaries for the AC tempers. This is shown in figure 7, where large β-Mg_2Si and two $MgZn_{2-x}Al_x$ particles are present. Note that there are also Al_3Zr dispersoids close to the β-Mg_2Si particles in figure 7, which makes it uncertain what the nucleation site is in this example.

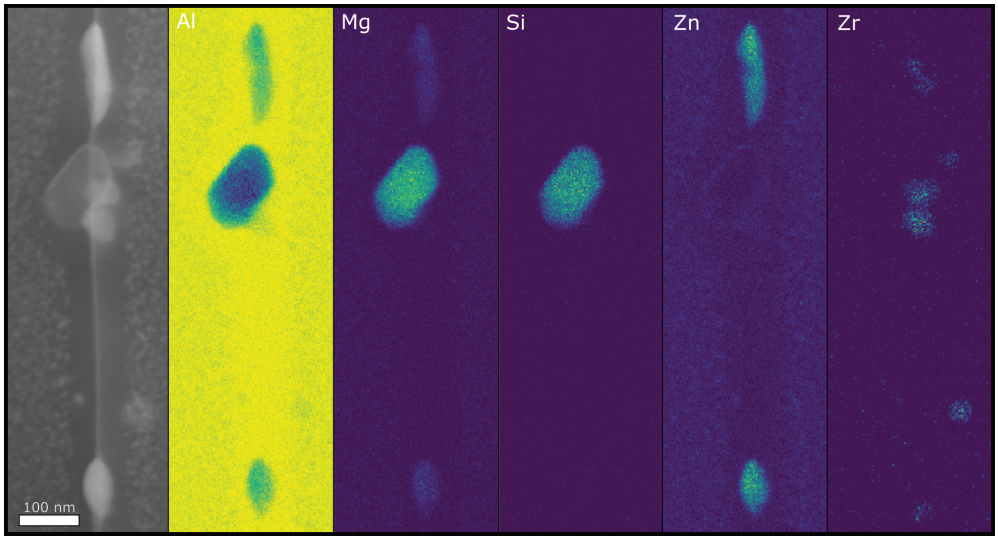

Figure 7. A HAADF-STEM image and corresponding EDS maps from a grain boundary in the sample H-AC-T6. Both $MgZn_{2-x}Al_x$ and β-Mg_2Si particles are present if the material has been AC from SHT. Al_3Z dispersoids are also found in connection this grain boundary.

The concentrations of the PFZs were measured using EDS on type 3 grain boundaries. Data from an EDS map is represented as a linescan where each point represents the average and corresponding standard error of the mean as a function of distance from the boundary. This is shown in figure 8 for H-AC-T6, H-WQ-T6 and H-AC-T7. The in PFZs are mostly composed of Al in addition to reduced levels of Mg and Zn. The H-WQ-T6 sample has a Zn/Mg ratio closer to one, than the AC and T7 tempers. Moreover, sample H-WQ-T6 consistently demonstrated enhanced Si signal. In some cases an enhanced Cu signal was found at grain boundaries, but no indications of Mg or Zn segregation were observed in any of the tempers.

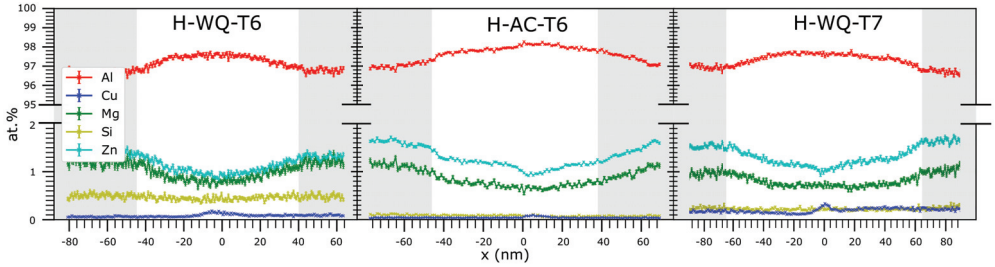

Figure 8. Elemental composition profiles across a type 3 grain boundary in three selected tempers. The relative solute level is similar, but the H-WQ-T6 condition exhibits a Zn/Mg ratio closer to one in addition to an enhanced Si level.

3.3. Matrix precipitates

In our previous work, we demonstrated that the T6 and T7 tempers consisted of bulk precipitates that differed both in orientation relationship and size, ndependent of the prior cooling rate from SHT [33]. The T6 temper consisted of η' and η_2 precipitates, while the T7 temper had η_1 and η_2 precipitates. Precipitates in the T7 temper are larger both in thickness and diameter. This is shown in figure 9, where figure 9**a** is the η' precipitate imaged along $[11\bar{2}]_{Al}$ in H-WQ-T6. Figures 9**b** and 9**c** are the η_2 and η_1 precipitates, respectively, projected along $[110]_{Al}$ in sample H-WQ-T7. η_1 has a $(110)_{Al}$ interface plane, while the two others lie on the $(111)_{Al}$ plane.

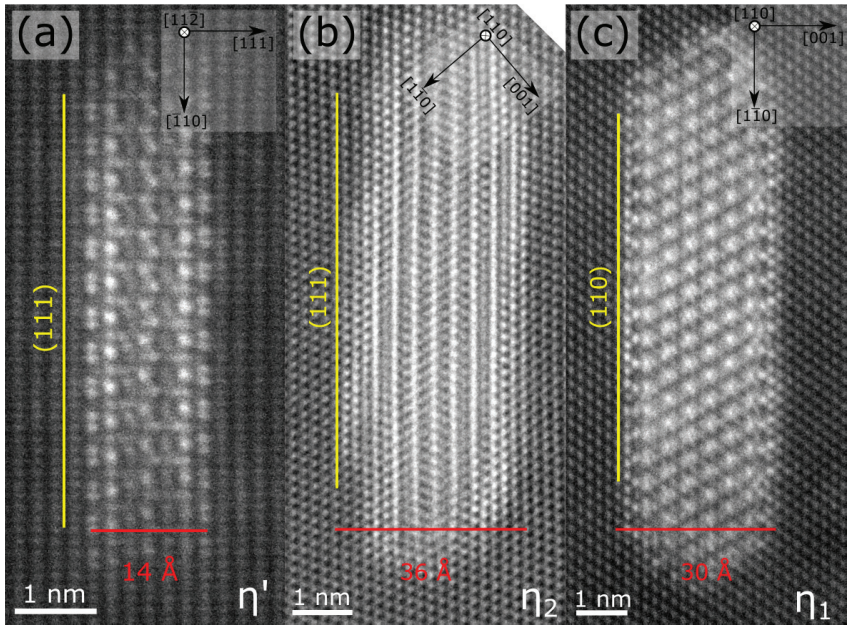

Figure 9. HAADF-STEM images of the different precipitates present in the tempers studied. **a** shows the η' precipitate acquired in H-WQ-T6 along $[11\bar{2}]_{Al}$. **b** and **c** are the η_2 and η_1 precipitates, respectively, projected along $[110]_{Al}$ in sample H-WQ-T7. η' & and η_2 are present in T6. η_1 and η_2 are present in T7.

3.4. Electrical conductivity

The electrical conductivity of the different conditions was measured and the results are given in table 3. The measured values are slightly higher for the T7 tempers. There is no measurable effect between the two different cooling methods from SHT.

Table 3. Electrical conductivity measurements of the four studied tempers, represented by the average value and standard deviation of 5 independent measurements.

	H-WQ-T6	H-WQ-T7	H-AC-T6	H-AC-T7
MS/m	26.15 ± 0.16	27.15 ± 0.13	26.13 ± 0.11	27.23 ± 0.09

3.5. DCB testing

Results from the DCB tests are shown in figure 10, where the region II (plateau) crack velocity is shown together with the estimated K_{ISCC} values. Region II crack velocities are all within the same order of magnitude (10^{-9} ms^{-1}), with the lowest values in the T7 tempers. A higher K_{ISCC} value is found in the T7 tempers. AC increases the K_{ISCC} value to slightly higher values than their WQ counterparts. All conditions, except L-T7-AC, exhibit a clear drop in crack velocity at lower K_{ISCC} values. The difference in Si levels does not show any clear trend and has limited effect on the properties measured here. The conventional crack velocity vs. stress intensity figure, from which the data presented in figure 10 is obtained, is found in Supplementary figure A2.

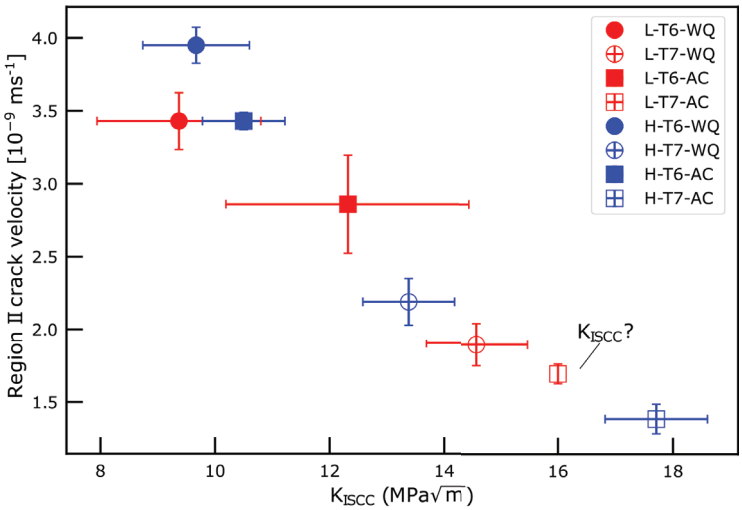

Figure 10. Results from the DCB tests. Average region II crack velocity and K_{ISCC} value from three samples with corresponding standard deviation. The K_{ISCC} value of the L-T7-AC temper is uncertain as it did not demonstrate a clear drop in crack velocity at low K_i values, which all other conditions did. There is a clear trend that the K_{ISCC} values are higher for the T7 tempers.

The cracks on the DCB specimens were studied in SEM in the directions both parallel- and normal to the extrusion direction. A schematic figure is shown in figure 11**a**, where the red lines indicate the cracks. Along the extrusion direction the cracks follow nearly a straight line as shown in figure 11**b**. Higher magnification images of the crack tip region are shown in figures 11**c** and 11**d**, demonstrating that the cracks follow the grain boundaries between the fibrous grains aligned along ED direction. In order to see the cracks in the transverse cross-section, DCB samples were cut along the transverse direction as the crack had not passed through the entire specimen during the test period. This crack

is demonstrated in figure 11**e**, where two selected secondary electron (SE)-SEM images are shown in figures 11**f** and 11**g**. It can be seen that the cracks are not as straight as along the extrusion direction, and more cracks branching from the main crack can be seen clearly in figures 11**f** and 11**g**.

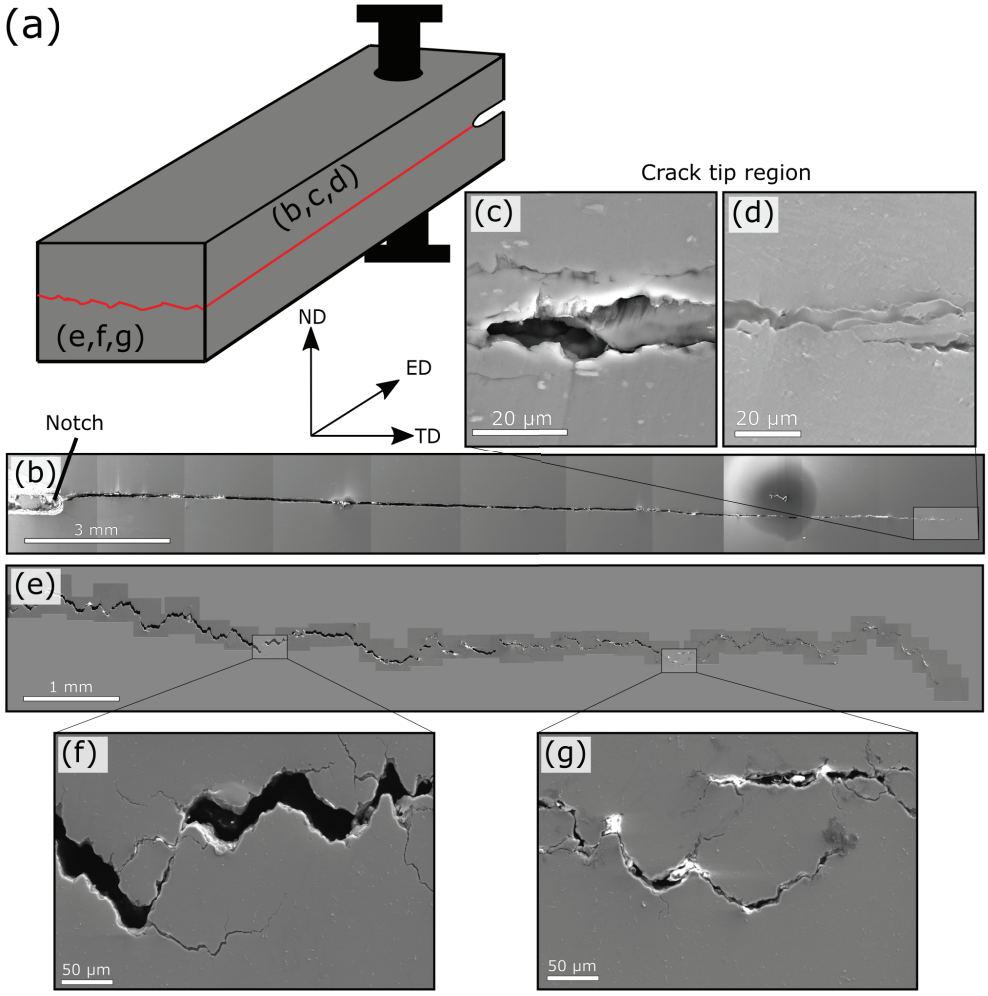

Figure 11. A schematic figure of a cracked DCB specimen in **a**, where the base has been cut along the transverse direction to reveal the crack. SE-SEM images of the crack along the extrusion direction and the transverse directions are shown in figures **b** and **e**, respectively. **b** and **c** are higher magnification SE-SEM images of the crack tip along the extrusion direction. **f** and **g** are two higher magnification images of cracks in the transverse direction.

Some of the samples were pulled apart and the fracture surface of two are shown in figure 12. As may be seen in figures 12**a** and 12**b**, the crack front is slightly deeper in the center of the specimens than at the edges. SE-SEM images of the fracture surfaces are shown in figures 12**c** and 12**d**, where the fibrous grains are seen to remain along the extrusion direction. The fracture surfaces clearly demonstrate that the cracks are intergranular in nature. Note that the SEM images do not capture the depth of field, which is more clear in the earlier presented figure 11**e**.

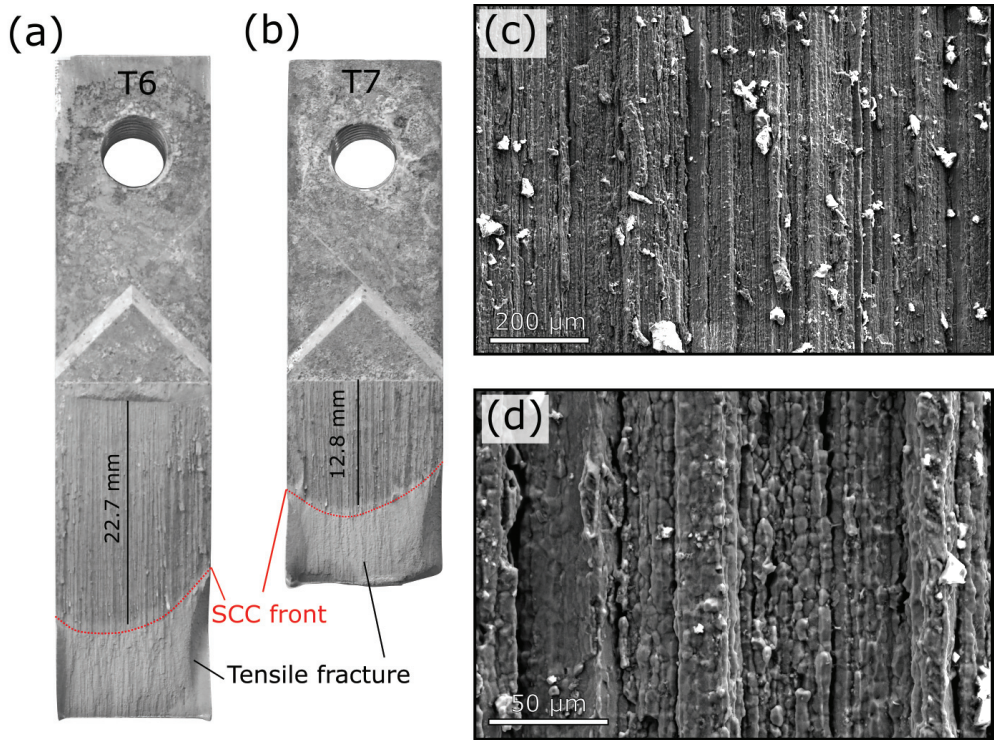

Figure 12. DCB specimen pulled apart using a tensile overload for tempers H-WQ-T6 and H-WQ-T7 in **a** and **b**, respectively. **c** and **d** are SE-SEM images at different magnification of the fracture surface within the SCC front area in **a**.

EBSD was conducted on the cracked DCB specimens in order to reveal which grain boundaries are susceptible to SCC. This is shown in figure 13. The cracks seem to predominately follow the high-angle grain boundaries which separate the long fibrous grains.

3.6. Slow strain rate tests

Results from SSRT are summarised in table 4. The T7 tempers exhibit lower ultimate tensile strength (UTS) and yield strength (YS) than the T6 tempers, but have higher total elongation and reduction in area (RA) values. The UTS values for all samples are similar when tested in air or solution. No clear trends in the total elongation can be established when testing in solution. In certain cases the total elongation is longer in solution than in air. All T7 tempers demonstrate a higher RRA value (less change) compared to the T6 tempers in both test solutions. The two different Si levels do not demonstrate any clear difference in the measured properties. The stress-strain curves are given in Supplementary figure A3 for the interested reader.

Representative fracture surfaces of the SSRT specimens are shown in figure 14. Samples fractured in air, regardless of temper, all demonstrate a ductile failure in the center of the specimen. A flat fracture region is found closer to the edge. Samples stressed in 3.5 wt.% NaCl at pH 7 similarly have ductile failure in the centre of the specimen with some corrosion products between. However, there is an apparent difference between the T6 and T7 samples, regardless of the pH in the test solution. This is the appearance of cracks, always present close to the edge in the T6 specimens. These may penetrate up to $\sim$600 μm into the specimen from the outer surface. In one case, the crack penetrated through the entire cross-section (Supplementary figure A4). It is important to emphasise that this cracking

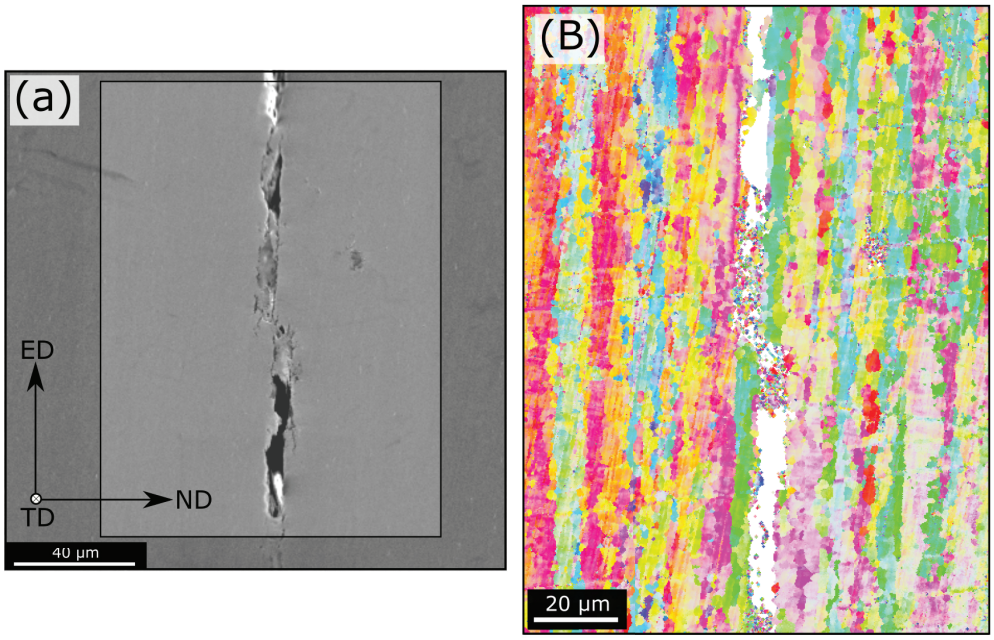

Figure 13. SE-SEM image of a DCB crack and the corresponding EBSD map from the indicated region. The crack predominantly follows the high-angle grain boundaries separating the long fibrous grains along the extrusion direction (ED).

Table 4. Results from SSRT in air and 3.5 wt.% NaCl with pH 7 and pH 3. The yield strength (YS), ultimate tensile strength (UTS), total elongation and reduction in area (RA) are given. The reduction in area ratio (RRA) are calculated based from the RA values, and demonstrate less change for the T7 tempers.

	YS (MPa)	UTS (MPa)			Total Elongation (%)			RA (%)			RRA (%)	
ID	Air	Air	pH 7	pH 3	Air	pH 7	pH 3	Air	pH 7	pH 3	pH 7	pH 3
L-WQ-T6	362	376	379	380	14.4	17.8	13.7	49.3	32.4	36.6	0.66	0.74
H-WQ-T6	357	374	379	386	15.5	15.6	14.4	56.4	44.5	40.9	0.79	0.72
L-WQ-T7	311	322	335	328	15.7	14.4	14.9	63.7	61.1	49.2	0.96	0.77
H-WQ-T7	322	333	327	332	15.9	15.2	15.4	65.0	56.8	46.2	0.87	0.71
L-AC-T6	354	372	380	384	14.4	15.6	14.5	56.9	44.5	40.9	0.71	0.78
H-AC-T6	358	375	373	373	16.1	14.7	14.9	58.8	40.6	34.9	0.69	0.59
L-AC-T7	315	326	329	329	14.7	16.4	16.3	57.6	58.1	59.7	1.01	1.03
H-AC-T7	313	324	322	328	14.7	16.1	14.5	60.6	50.7	57.9	0.84	0.95

behaviour was not observed in the T7 tempers, and also not when the T6 tempers were strained in air. The cracks observed in figure 14 have a depth along the tensile axis (extrusion direction) of up to 1 mm. This is revealed by embedding the whole specimen in epoxy and polishing the sample in towards the center of the round tensile specimen. This crack shown in Supplementary figure A5 for a T6 sample using optical microscopy and SEM.

3.7. Polarisation curves

Two of the tempers which demonstrated clear difference in the measured SCC properties were subjected to potentiodynamic polarisation. This is shown in figure 15, where the T6 and the T7 tempers exhibit similar behaviour. The corrosion potential is ∼10 mV lower for the T7 temper.

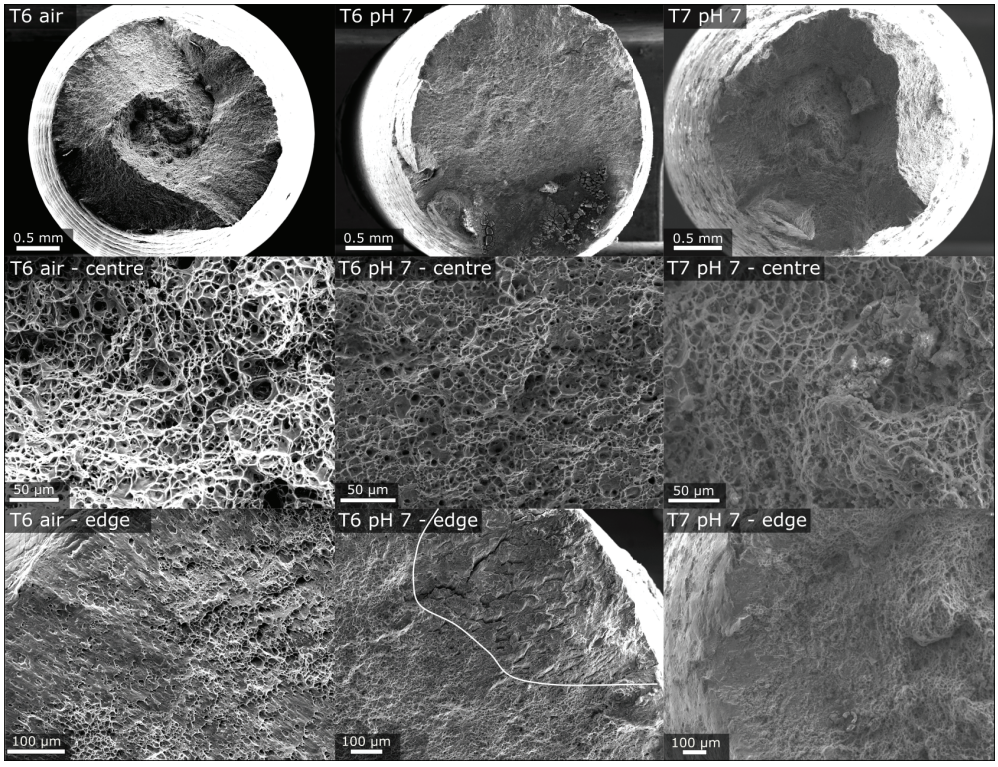

Figure 14. Fracture surfaces of selected samples in air and in solution, with highlighted features in the centre and close to the edge. The main difference is the cracking behaviour observed in the T6 tempers when testing in solution.

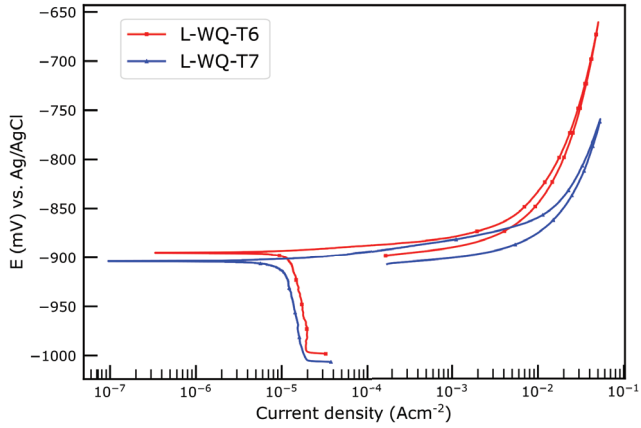

Figure 15. Potentiodynamic polarisation curves of two selected samples.

4. Discussion

In the present work, nearly all the microstructural features believed to have an effect on SCC have been studied. The only clear observation established is a difference in the bulk hardening phases, which changes in size and orientation relationship with the Al matrix. If this is the primary reason for the increased SCC resistance in the T7 tempers is somewhat uncertain. However, our results are in

agreement with other studies which previously have suggested that bulk hardening phases alter the deformation mode (slip characteristics) and influence the strain localisation at the grain boundaries [23,37]. Higher strain localisation is likely to influence the crack propagation, but also influence hydrogen diffusion and trapping. Guyot & Cottignies suggested that the yield stress decrease due to overageing was associated with coarsening of precipitates resulting in a transition from shearing to Orowan by-passing at a critical precipitate radius of 3 nm [38]. This fits well with our observations. In recent years, the hydrogen distribution within Cu-free Al-Zn-Mg alloys has been studied and it has been suggested that the bulk precipitates are important in hydrogen trapping [39–41] and also motionless dislocations [42]. A relative study of the hydrogen trapping ability of the η hardening precipitates with different interface planes is yet to be carried out and may give further insights into the difference between the T6 and T7 temper.

Comparing the DCB results for the T6 and T7 tempers, there are little differences in the region II crack velocities (cf. figure 10). This may be an indication that there are little or no changes in the grain boundary chemistry. This is supported by the microstructural characterisation, where only limited differences in concentration of solute element in the PFZs, PFZs widths, electrical conductivity, polarisation behaviour or in the grain boundary particle compositions, could be established. The average Zn/Mg ratio for grain boundary particles in H-AC-T6 was lower than for the other tempers. A lower Zn content in the GBPs should provide a lower potential difference between the $MgZn_2$ phases and surrounding PFZs. However, this temper did not exhibit greater SCC resistance than any of the T7 tempers. The PFZs solute concentrations presented are likely to be subjected to errors in the absolute value. However, the relative difference between the tempers should, provide an indication of differences between the samples. Comparing the results in figure 8 to the SCC results, is seems unlikely that PFZs solute content will have any significant influence on the SCC properties of the tempers studied here. The flat Si curve across the GB in sample H-WQ-T6 is questionable, but similar curves were observed several times only for this condition.

Type 2 and type 3 grain boundaries show no clear correlation between particle distribution and misorientation angles. It is more likelyrelated to grain boundary termination plane. That is, if one of the adjacent grains terminates with a $\{111\}_{Al}$ plane, it is more likely to precipitate the equilibrium η-$MgZn_2$ phase. This has been reported by others [43,44]. However, as the η-$MgZn_2$ hardening precipitates have several possible interface planes for nucleation in bulk Al [33,45,46], it is not unlikely that other boundary termination planes also play a role for these grain boundary particles. This may cause large variations even along the same grain boundary, as suggested by Butler & Swan [47]. Grain boundary defects such as ledges may also act as preferential nucleation sites [44,47]. Zhao *et al.* demonstrated how a grain boundary may decompose into facets with different segregation and precipitation behaviour [48]. The spacing between GBPs may have influence on the presented SCC results, but the statistics from the methods used in this work could not be used in drawing any conclusions related to this due to the enormous variations between grain boundaries within the same sample. More statistical methods, such as 3D focused ion beam (FIB) [49] or X-ray based methods are suitable for this purpose.

In agreement with the work of others, we find that that the cracks predominately follow the high-angle grain boundaries which separates the large fibrous grains. Tang *et al.* found that the cracks tend to propagate at high-angle grain boundaries with a large difference in the Schmid Factor of the neighbouring grains [50]. Day & Dent studied SCC and reported that cracks propagated along high-angle grain boundaries decorated with fewer, larger particles than the low-angle sub-grain boundaries [51]. The grain boundaries presented here must act differently with respect to a potential SCC propagation mechanism. The low-angle grain boundaries have a near continuous distribution of anodic $MgZn_2$ type particles, which may facilitate a dissolution type failure. High-angle grain boundaries are likely to be more susceptible to stress-localisation, as larger differences between adjourning grains may limit slip across the interface. Strain localisation may again increase the hydrogen segregation and thus promote local conditions for embrittlement. More site specific grain

boundary analysis should be applied in future work. A possible approach is by using FIB to carve out a region in front of the crack tip to understand which types of grain boundaries are susceptible to cracking.

Air cooling from SHT results in heterogeneous nucleation of β-Mg_2Si particles on grain boundaries. She *et al.* reported an improved SCC with increasing Si content and higher area fraction of β-Mg_2Si particles [52]. Singh *et al.* reported hydrogen bubble formation within the crack tip, which was associated with the anodic dissolution of the β-Mg_2Si particles [53]. The differences in Si level for the two alloys studied here did not show any clear difference. Higher differences in the Si level may have displayed other results.

It is likely that stressing the specimens along the TD direction (as apposed to the ED direction done here) would have resulted in clear differences in elongation before failure. However, the SSRT test is a 'fast' test, in comparison to other more static long exposure tests. The corrosion processes may not have time to occur prior to fracture. Alternative approaches with SSRT could have been to: (1) apply a load to some % of the YS, and immerse the samples for longer periods. (2) Hydrogen pre-charging of the samples prior to tensile tests. Regardless, there are clear difference in the SCC between the T6 and T7 tempers with respect to observations in cracking behaviour and the retrogression and reageing (RRA) values. Other testing methods are also possible and must be considered in future works. Some testing methods has been reviewed for EN AW-7075 by Magaji *et al.* [54].

Although not studied here, residual stresses may have effect on the measured results. Robinson *et al.* demonstrated large residual stresses associated with water quenching an AA7075 alloy, which could be reduced by 25-40% after overageing [55]. However, in this work, its influence should be limited as there were little difference between the water quenched and air samples.

5. Conclusions

In the present work, the SCC properties of an extruded Al-Zn-Mg alloys with two different Si contents have been studied in two tempers following two different quenching conditions from SHT. The main findings are:

- Overageing (T7) both increases the K_{ISCC} value and decreases the region II crack velocity. This is likely related to differences in bulk precipitates which may change the slip characteristics from shearing in T6 to looping in T7, and ultimately affect the degree of strain localisation at the grain boundaries.
- Low-angle sub-grain boundaries have a near continuous distribution of small grain boundary particles, while other grain boundaries vary greatly in particle density and may have none, few or many particles present.
- The cracks follow predominantly the high-angle grain boundaries between the fibrous grains.
- Cracking behaviour observed in SSRT, only occurred in the T6 tempers.
- The small variations in Si content between the alloys here have little or no influence on the measured SCC properties.

These finding are expected to be relevant in future studies concerning properties in similar extruded Cu-free Al-Zn-Mg alloys.

Author Contributions: "Conceptualization, A.L. and L.L.; Methodology, A.L.; Formal analysis, A.L.; Investigation, A.L.; Resources, L.L. and R.J.; Data curation, A.L.; Writing–original draft preparation, A.L.;Writing–review and editing, A.L.; visualization, A.L.; Supervision, J.C.W., R.H., O.L., R.J. and C.D.M.; project administration, R.H.; Funding acquisition, J.C.W. and R.H."

Funding: This work was supported by the KPN project "FICAL" (NFR: 247598), co-financed by The Research Council of Norway (NFR), and the industrial partners Hydro, Gränges, Benteler Automotive Raufoss AS and Steertec Raufoss. The (S)TEM work was conducted on the NORTEM (NFR: 197405) infrastructure at the TEM Gemini Centre, Trondheim, Norway.

Acknowledgments: Benteler Automotive Raufoss AS is greatly acknowledged for providing the material. Ellen S. Skilbred is greatly acknowledges for assisting with the SSRT experiments.

Conflicts of Interest: The authors declare no conflict of interest.

References

1. Dursun, T.; Soutis, C. Recent developments in advanced aircraft aluminium alloys. *Materials and Design* **2014**, *56*, 862–871. doi:10.1016/j.matdes.2013.12.002.
2. Jensrud, O. High Strength Aluminium Alloys Extrusions - A Review of the Thermo-Mechanical-Process in High Performance Profile Manufacturing. Progress in Extrusion Technology and Simulation of Light Metal Alloys. Trans Tech Publications, 2012, Vol. 491, *Key Engineering Materials*, pp. 11–18. doi:10.4028/www.scientific.net/KEM.491.11.
3. Speidel, M.O. Stress corrosion cracking of aluminum alloys. *Metallurgical Transactions A* **1975**, *6*, 631–651. doi:10.1007/BF02672284.
4. Rao, A.C.U.; Vasu, V.; Govindaraju, M.; Srinadh, K.V.S. Stress corrosion cracking behaviour of 7xxx aluminum alloys: A literature review. *Transactions of Nonferrous Metals Society of China (English Edition)* **2016**, *26*, 1447–1471. doi:10.1016/S1003-6326(16)64220-6.
5. Holroyd, N.J.H.; Scamans, G.M. Stress corrosion cracking in Al-Zn-Mg-Cu aluminum alloys in saline environments. *Metallurgical and Materials Transactions A* **2013**, *44*, 1230–1253. doi:10.1007/s11661-012-1528-3.
6. Holroyd, N.J.; Scamans, G.M. Crack propagation during sustained-load cracking of Al-Zn-Mg-Cu aluminum alloys exposed to moist air or distilled water. *Metallurgical and Materials Transactions A* **2011**, *42*, 3979–3998. doi:10.1007/s11661-011-0793-x.
7. Braun, R. Environmentally assisted cracking of aluminium alloys. *Materialwissenschaft und Werkstofftechnik* **2007**, *38*, 674–689. doi:10.1002/mawe.200700204.
8. Burleigh, T.D. The Postulated Mechanisms for Stress Corrosion Cracking of Aluminum Alloys: A Review of the Literature 1980-1989. *CORROSION* **1991**, *47*, 89–98. doi:10.5006/1.3585235.
9. Lynch, S. Hydrogen embrittlement phenomena and mechanisms. *Corrosion Reviews* **2012**, *30*, 105 – 123.
10. Najjar, D.; Magnin, T.; Warner, T. Influence of critical surface defects and localized competition between anodic dissolution and hydrogen effects during stress corrosion cracking of a 7050 aluminium alloy. *Materials Science and Engineering A* **1997**, *238*, 293–302. doi:10.1016/S0921-5093(97)00369-9.
11. Bland, L.G.; Locke, J.S. Chemical and electrochemical conditions within stress corrosion and corrosion fatigue cracks. *npj Materials Degradation* **2017**, *1*, 12. doi:10.1038/s41529-017-0015-0.
12. Cornish, A.; Day, M.K.B. The effect of variable quenching condition on the relationship between the stress-corrosion resistance, tensile properties, and microstructure of high-purity Al-Zn-Mg alloy. *Journal of the institute of metals* **1971**, *99*, 377–384.
13. Poulose, P.K.; Morral, J.E.; McEvily, A.J. Stress corrosion crack velocity and grain boundary precipitates in an Al-Zn-Mg alloy. *Metall Trans* **1974**, *5*, 1393–1400. doi:10.1007/BF02646625.
14. Christodoulou, L.; Flower, H.M. Hydrogen embrittlement and trapping in Al6%Zn-3%Mg. *Acta Metallurgica* **1980**, *28*, 481–487. doi:10.1016/0001-6160(80)90138-8.
15. Sarkar, B.; Marek, M.; Starke, E.A. The effect of copper content and heat treatment on the stress corrosion characteristics of Ai-6Zn-2Mg-X Cu alloys. *Metallurgical Transactions A* **1981**, *12*, 1939–1943. doi:10.1007/BF02643806.
16. Puiggali, M.; Zielinski, A.; Olive, J.; Renauld, E.; Desjardins, D.; Cid, M. Effect of microstructure on stress corrosion cracking of an Al-Zn-Mg-Cu alloy. *Corrosion Science* **1998**, *40*, 805 – 819. doi:10.1016/S0010-938X(98)00002-X.
17. Sun, X.; Zhang, B.; Lin, H.; Zhou, Y.; Sun, L.; Wang, J.; Han, E.H.; Ke, W. Correlations between stress corrosion cracking susceptibility and grain boundary microstructures for an Al–Zn–Mg alloy. *Corrosion Science* **2013**, *77*, 103 – 112. doi:10.1016/j.corsci.2013.07.032.
18. Viswanadham, R.K.; Sun, T.S.; Green, J.A. Grain boundary segregation in Al-Zn-Mg alloys-Implications to stress corrosion cracking. *Metallurgical and Materials Transactions A* **1980**, *11*, 85–89. doi:10.1007/BF02700441.
19. Scamans, G.M.; Holroyd, N.J.H.; Tuck, C.D.S. The role of magnesium segregation in the intergranular stress corrosion cracking of aluminium alloys. *Corrosion Science* **1987**, *27*, 329–347. doi:10.1016/0010-938X(87)90076-X.

20. Song, R.G.; Tseng, M.K.; Zhang, B.J.; Liu, J.; Jin, Z.H.; Shin, K.S. Grain boundary segregation and hydrogen-induced fracture in 7050 aluminium alloy. *Acta Materialia* **1996**, *44*, 3241–3248. doi:10.1016/1359-6454(95)00406-8.
21. Song, R.; Dietzel, W.; Zhang, B.; Liu, W.; Tseng, M.; Atrens, A. Stress corrosion cracking and hydrogen embrittlement of an Al–Zn–Mg–Cu alloy. *Acta Materialia* **2004**, *52*, 4727 – 4743. doi:10.1016/j.actamat.2004.06.023.
22. Vasudevan, A.K.; Sadananda, K. Role of slip mode on stress corrosion cracking behavior. *Metallurgical and Materials Transactions A: Physical Metallurgy and Materials Science* **2011**, *42*, 405–414. doi:10.1007/s11661-010-0471-4.
23. Wu, L.M.; Wang, W.H.; Hsu, Y.F.; Trong, S. Effects of Microstructure on the Mechanical Properties and Stress Corrosion Cracking of an Al-Zn-Mg-Sc-Zr Alloy by Various Temper Treatments. *Materials Transactions* **2007**, *48*, 600–609. doi:10.2320/matertrans.48.600.
24. Baumgartner, M.; Kaesche, H. Intercrystalline Corrosion and Stress Corrosion Cracking of AlZnMg Alloys. *Corrosion* **1988**, *44*, 231–239. doi:10.5006/1.3583931.
25. Hardwick, D.A.; Thompson, A.W.; Bernstein, I.M. The effect of copper content and microstructure on the hydrogen embrittlement of Al-6Zn-2Mg alloys. *Metallurgical Transactions A* **1983**, *14*, 2517–2526. doi:10.1007/BF02668893.
26. Albrecht, J.; Thompson, A.W.; Bernstein, I.M. The role of microstructure in hydrogen-assisted fracture of 7075 aluminum. *Metallurgical Transactions A* **1979**, *10*, 1759–1766. doi:10.1007/BF02811712.
27. Cornish, A.J.; Day, M. The effect of variable quenching conditions on the relationship between stress-corrosion resistance, tensile properties, and microstructure of high purity Al-Zn-Mg alloy. *Journal of the institute of metals* **1971**, *99*, 377–384.
28. Knight, S.P.; Birbilis, N.; Muddle, B.C.; Trueman, A.R.; Lynch, S.P. Correlations between intergranular stress corrosion cracking, grain-boundary microchemistry, and grain-boundary electrochemistry for Al-Zn-Mg-Cu alloys. *Corrosion Science* **2010**, *52*, 4073–4080. doi:10.1016/j.corsci.2010.08.024.
29. Goswami, R.; Lynch, S.; Holroyd, N.J.; Knight, S.P.; Holtz, R.L. Evolution of grain boundary precipitates in Al 7075 upon aging and correlation with stress corrosion cracking behavior. *Metallurgical and Materials Transactions A: Physical Metallurgy and Materials Science* **2013**, *44*, 1268–1278. doi:10.1007/s11661-012-1413-0.
30. Gupta, R.K.; Deschamps, A.; Cavanaugh, M.K.; Lynch, S.P.; Birbilis, N. Relating the Early Evolution of Microstructure with the Electrochemical Response and Mechanical Performance of a Cu-Rich and Cu-Lean 7xxx Aluminum Alloy. *Journal of the Electrochemical Society* **2012**, *159*, C492–C502. doi:10.1149/2.062211jes.
31. Chen, J.; Zhang, X.; Zou, L.; Yu, Y.; Li, Q. Effect of precipitate state on the stress corrosion behavior of 7050 aluminum alloy. *Materials Characterization* **2016**, *114*, 1–8. doi:10.1016/j.matchar.2016.01.022.
32. Birbilis, N.; Buchheit, R.G. Electrochemical Characteristics of Intermetallic Phases in Aluminum Alloys An Experimental Survey and Discussion. *Journal of The Electrochemical Society* **2005**, *152*, B140–B151. doi:10.1149/1.1869984.
33. Lervik, A.; Marioara, C.; Kadanik, M.; Walmsley, J.; Milkereit, B.; Holmestad, R. Precipitation in an extruded AA7003 aluminium alloy: Observations of 6xxx-type hardening phases. *Materials & Design* **2019**, *186*, 108204. doi:10.1016/j.matdes.2019.108204.
34. Hyatt, M.V. Use of Precracked Specimens in Stress Corrosion Testing of High Strength Aluminum Alloys. *CORROSION* **1970**, *26*, 487–503. doi:10.5006/0010-9312-26.11.487.
35. Bachmann, F.; Hielscher, R.; Schaeben, H. Texture Analysis with MTEX – Free and Open Source Software Toolbox. Texture and Anisotropy of Polycrystals III. Trans Tech Publications Ltd, 2010, Vol. 160, *Solid State Phenomena*, pp. 63–68. doi:10.4028/www.scientific.net/SSP.160.63.
36. de la Peña, F.; Prestat, E.; Fauske, V.T.; Burdet, P.; Jokubauskas, P.; Nord, M.; Ostasevicius, T.; MacArthur, K.E.; Sarahan, M.; Johnstone, D.N.; Taillon, J.; Lähnemann, J.; Migunov, V.; Eljarrat, A.; Caron, J.; Aarholt, T.; Mazzucco, S.; Walls, M.; Slater, T.; Winkler, F.; pquinn dls.; Martineau, B.; Donval, G.; McLeod, R.; Hoglund, E.R.; Alxneit, I.; Lundeby, D.; Henninen, T.; Zagonel, L.F.; Garmannslund, A. hyperspy/hyperspy: HyperSpy v1.5.2, 2019. doi:10.5281/zenodo.3396791.
37. Wu, H.; Fan, G. An overview of tailoring strain delocalization for strength-ductility synergy. *Progress in Materials Science* **2020**, p. 100675. doi:10.1016/j.pmatsci.2020.100675.
38. Guyot, P.; Cottignies, L. Precipitation kinetics, mechanical strength and electrical conductivity of AlZnMgCu alloys. *Acta Materialia* **1996**, *44*, 4161–4167. doi:10.1016/S1359-6454(96)00033-X.

39. Oger, L.; Lafouresse, M.C.; Odemer, G.; Peguet, L.; Blanc, C. Hydrogen diffusion and trapping in a low copper 7xxx aluminium alloy investigated by Scanning Kelvin Probe Force Microscopy. *Materials Science and Engineering A* **2017**, *706*, 126–135. doi:10.1016/j.msea.2017.08.119.
40. Tsuru, T.; Yamaguchi, M.; Ebihara, K.; Itakura, M.; Shiihara, Y.; Matsuda, K.; Toda, H. First-principles study of hydrogen segregation at the $MgZn_2$ precipitate in Al-Mg-Zn alloys. *Computational Materials Science* **2018**, *148*, 301–306. doi:10.1016/j.commatsci.2018.03.009.
41. Tsuru, T.; Shimizu, K.; Yamaguchi, M.; Itakura, M.; Ebihara, K.; Bendo, A.; Matsuda, K.; Toda, H. Hydrogen-accelerated spontaneous microcracking in high-strength aluminium alloys. *Scientific Reports* **2020**, *10*, 1–8. doi:10.1038/s41598-020-58834-6.
42. Oger, L.; Malard, B.; Odemer, G.; Peguet, L.; Blanc, C. Influence of dislocations on hydrogen diffusion and trapping in an Al-Zn-Mg aluminium alloy. *Materials & Design* **2019**, *180*, 107901. doi:10.1016/j.matdes.2019.107901.
43. Unwin, P.N.; Nicholson, R.B. The nucleation and initial stages of growth of grain boundary precipitates in Al-Zn-Mg and Al-Mg alloys. *Acta Metallurgica* **1969**, *17*, 1379–1393. doi:10.1016/0001-6160(69)90155-2.
44. Gronsky, R.; Furrer, P. Grain Boundary Precipitation in Aluminum Alloys: Effect of Boundary Structure. *Metallurgical transactions. A* **1981**, *12 A*, 121–127. doi:10.1007/BF02648516.
45. Chung, T.F.; Yang, Y.L.; Shiojiri, M.; Hsiao, C.N.; Li, W.C.; Tsao, C.S.; Shi, Z.; Lin, J.; Yang, J.R. An atomic scale structural investigation of nanometre-sized η precipitates in the 7050 aluminium alloy. *Acta Materialia* **2019**. doi:10.1016/j.actamat.2019.05.041.
46. Bendo, A.; Matsuda, K.; Lervik, A.; Tsuru, T.; Nishimura, K.; Nunomura, N.; Holmestad, R.; Marioara, C.D.; Shimizu, K.; Toda, H.; Yamaguchi, M. An unreported precipitate orientation relationship in Al-Zn-Mg based alloys. *Materials Characterization* **2019**, *158*, 109958. doi:10.1016/j.matchar.2019.109958.
47. Butler, E.P.; Swann, P.R. In situ observations of the nucleation and initial growth of grain boundary precipitates in an Al-Zn-Mg alloy. *Acta Metallurgica* **1976**, *24*, 343–352. doi:10.1016/0001-6160(76)90009-2.
48. Zhao, H.; Huber, L.; Lu, W.; Peter, N.J.; An, D.; De Geuser, F.; Dehm, G.; Ponge, D.; Neugebauer, J.; Gault, B.; Raabe, D. Interplay of Chemistry and Faceting at Grain Boundaries in a Model Al Alloy. *Phys. Rev. Lett.* **2020**, *124*, 106102. doi:10.1103/PhysRevLett.124.106102.
49. Singh, S.S.; Loza, J.J.; Merkle, A.P.; Chawla, N. Three dimensional microstructural characterization of nanoscale precipitates in AA7075-T651 by focused ion beam (FIB) tomography. *Materials Characterization* **2016**, *118*, 102–111. doi:10.1016/j.matchar.2016.05.009.
50. Tang, J.; Zhang, Y.; Ye, L.; Qu, M.; Wu, J.; Zhang, Z.; Liu, S.; Deng, Y. Effect of Grain Boundary and Crystallographic Orientation on the Stress Corrosion Behavior of an Al-Zn-Mg Alloy. *Journal of Materials Engineering and Performance* **2019**, *28*, 2954–2966. doi:10.1007/s11665-019-04050-x.
51. Day, M.K.B.; Cornish, A.J.; Dent, T. The relationship between structure and stress-corrosion life in Al-Zn-Mg alloy. *Metal Science Journal* **1969**, *3*, 175–182.
52. She, H.; Chu, W.; Shu, D.; Wang, J.; Sun, B.d. Effects of silicon content on microstructure and stress corrosion cracking resistance of 7050 aluminum alloy. *Transactions of Nonferrous Metals Society of China* **2014**, *24*, 2307–2313. doi:10.1016/S1003-6326(14)63349-5.
53. Singh, S.S.; Stannard, T.J.; Xiao, X.; Chawla, N. In Situ X-ray Microtomography of Stress Corrosion Cracking and Corrosion Fatigue in Aluminum Alloys. *Jom* **2017**, *69*, 1404–1414. doi:10.1007/s11837-017-2413-8.
54. Magaji, N.; Mayrhofer, R.; Kröger, B.; Schnatterer, C.; Zander, D. Comparison of test methods used to analyze stress corrosion cracking of differently tempered 7xxx alloys. *Materials and Corrosion* **2019**, *70*, 1192–1204. doi:10.1002/maco.201810717.
55. Robinson, J.S.; Pirling, T.; Truman, C.E.; Panzner, T. Residual stress relief in the aluminium alloy 7075. *Materials Science and Technology* **2017**, *33*, 1765–1775. doi:10.1080/02670836.2017.1318243.

Part III

Summary and Outlook

Chapter 6

General Discussion and Outlook

The main results of the thesis were divided into two main parts which consist of microstructure and corrosion properties in Al-Mg-Si-Cu and Al-Zn-Mg alloys, respectively. In this chapter the research is put into a broader context with respect to other relevant works published within the field and the author's thoughts for future work are presented.

6.1 Optimising IGC resistance

*This discussion relates to the work presented in Papers **I-III**.*

The results from Paper **I** showed that removing the primary particles present on the surface influences the intergranular corrosion properties. This can perhaps be implemented into industrial processing by conducting a surface etch using a similar solution as presented by Larsen *et al.* [135]. This will of course need to be optimised. Our results only assess how these particles behave in the accelerated IGC ISO standard test. This behaviour may be different in other solutions and in 'real' exposure conditions. A comparison of test methods was conducted by Cornejo *et al.* where it was demonstrated that the more realistic test (ASTM G85 A2) compared better to the outdoor exposure test [154]. A future work thus needs to evaluate how removing these surface particles effect samples that are exposed to 'real' conditions. Within the FICAL project, some work has been done in order to evaluate the ISO test. The differences, from a round robin test involving several labs, were mainly due to i) variation in solution to exposed area ratio and ii) if the cut edges were left exposed or not. As a matter of fact, the ISO standard does not specify a fixed solution to exposed area ratio, but rather that it should be $5 \geq$ ml/cm^2.

The work further demonstrates that the surface particles are important in defining the initiation and resulting distribution of corroded grain boundaries. However, they are not essential when IGC propagates through the material, as the maximum penetration depths reached similar values for the two alloys, after prolonged exposure. This means that the grain boundary properties and/or bulk properties are more important in the propagation stage. It was observed that Cu-rich particles could be found at the corroded grain boundaries, which in turn will act as internal cathodes and increase the cathodic activity. These Cu particles were never found when studying the microstructure prior to exposure. This demonstrates how dynamic this process is; the Cu remnants must come from either selectively dissolved particles, segregated Cu or from the matrix itself. Understanding the processes and kinetics of what is occurring in the crack tip is important considering important in order to further establish knowledge concerning the mechanism.

The basis of Paper **II** was to obtain insights into grain boundary structures and their correlation to IGC. This work present methodology in how to better represent grain boundary textures from EBSD data, without having to conduct much extra analysis. It does not include all 5 degrees of freedom, which would mean also including the grain boundary planes. The reasons for this is that: i) the grain boundary plane can decompose into facets at the atomic scale, which would not be captured in the EBSD anyhow, and ii) to the best of the author's knowledge, there exists only one analysis method to obtain this information (in EBSD), and this is a statistical method only applicable to random textures [227]. Statistically analysing grain boundaries using a 5-parameter scheme is probably the most important topic to solve in order to be able to conduct grain boundary engineering. Nevertheless, the work presented in Paper **II** is on a more fundamental level with respect to characterisation. The distinct differences between grain boundaries typically observed were presented and are likely to be useful to understand what to expect when observing using TEM, but also important for modelling work. The methodology can be applied in future work. Studying a similarly textured alloy and the statistical time development of corroded grain boundary types would be an interesting study.

Paper **III** directly investigates how to improve IGC resistance by playing with thermo-mechanical processing steps. Three clear methods were shown: slow cooling from SHT, higher artificial ageing temperatures and pre-deformation. Draining Cu from solid solution by forcing both heterogeneous and/or homogeneous nucleation of Cu-containing particles seem to be the common factor in achieving better IGC resistance. Pre-deformation will of course impact mechanical properties. The methodology developed for analysing the EDS maps provides significantly more statistical accurate results than what is obtained from a single linescan.

A combination of the results from papers **I-III** indicates that it is possible to ob-

tain corrosion resistance Al-Mg-Si-Cu alloys by: reducing the amount of high-angle grain boundaries, removing surface particles and optimising the thermo-mechanical treatment.

These results are likely to useful in future models in order to predict IGC susceptibility. By understanding the kinetics of what is occurring within the IGC filaments, and how the relative rates of propagation compare between the different grain boundary types (Paper **II**), one may improve empirical models [228–230]. This can further be tuned to include the distribution of α-phase particles (particularly those in connection to grain boundaries) and import real grain structures directly from EBSD data. However, correctly modelling IGC is a complicated matter due to all the variables and the dynamics of the process; and is a project on its own.

6.2 Al-Zn-Mg alloys and SCC properties

*This discussion relates to the work presented in Papers **IV-VI**.*

Most of the mechanical and corrosion properties are closely linked to the thermo-mechanical treatments these alloys are subjected to. As introduced in section 3.4, slight variations in artificial ageing parameters can have large effects on the SCC properties. Therefore, it has been extremely important to revisit the precipitation sequence in this alloy system (cf. precipitation sequence 2.3). In paper **IV** we started from the earliest stages (natural ageing) and found that the solute clusters that forms (i.e. 'GP(I)-zones') can be described through a fundamental unit which is a truncated cube octahedron. This unit can stack in certain directions to form larger clusters. This works demonstrate how a combination using several state-of-the-art methodologies can be used to support and supplement each other. Without these methods it would not have been possible to deduce the results of this work. As these clusters are important for the subsequent artificial ageing, it is clear that the newfound understanding concerning the structure will be important in future work. It is believed that a large amount of modelling work will initiate from this work: both in understanding how they contribute to mechanical properties and how they are related to transformations to hardening phases.

In Paper **V** we investigated microstuctures in two tempers in a commercial alloy, in addition to how the quenching rate effects the microstructure. For the latter, the cooling differential scanning calorimetry method was applied. Interrupting at different temperatures during cooling and studying the microstructure in TEM (not done in Paper **V**) is a suggestion for further study, as it would enable deconvolution of the measured peaks. The work shows that following a typical air-cooling, dispersoids, grain boundaries and primarily particles all serve as heterogeneous

nucleation sites. We further investigated the hardening phases in the T6 and T7 tempers, which had clear differences in both precipitate size and orientation relationship with the Al matrix. This is important to emphasise as both the size and orientation may influence the material response to plastic deformation, SCC and even hydrogen partitioning (trapping). Using HAADF-STEM we also show that the η_1 and η_4 precipitates are semi-coherent particles. Many studies do the work to separate the orientation relationship of these precipitates, while many others simply assign everything except η' as the equilibrium η phase. Future studies must go further in quantifying the volume fraction of the different orientation relationship as function of artificial ageing conditions. This might be possible using a scanning precession electron diffraction (SPED) approach when imaging along the $[110]_{\mathrm{Al}}$ direction [40]. It would also be interesting to be able to do the same using APT. Due to the very close relation with overageing and SCC properties, presented in paper **VI** and in other works, there must be a connection here that is yet to be clearly understood.

With nearly 75% of all aluminium still in its first time use, there will be an increase in the recycling of these alloys. As introduced earlier, there are strict composition ranges for different alloys for different applications. As accidentally found in Paper **V**, in the alloy with a very small amount of Si (0.11 at.%), Mg-Si hardening precipitate phases typically formed in 6xxx (cf. table 2.3) were observed. This opens a new room for development of Si-containing Al-Zn-Mg alloys, wherein optimising the thermo-mechanical to make use of this excess Si is the goal. It is likely to become more important in recycled alloys. Based on the observations made, it seem that the alloy must be water-quenched from SHT in order to keep the excess vacancies and that the artificial ageing must be conducted at high temperatures (relative to what is common in Al-Zn-Mg alloys). The findings from Paper **V**, also suggest that the retrogression and reageing (RRA) heat treatment should be revisited using modern experimental techniques. The reason for suggesting this is that the hardening precipitate phases have not been studied adequately in literature during this heat treatment as it mostly focuses on grain boundary particles. The high temperature part (retrogression. i.e. short holding at 'high' temperature) probably does not dissolve hardening phases, while they coarsen the grain boundary particles (which is what is currently believed). It seems more likely that the retrogression stage forms Mg-Zn hardening phases, with different habit planes, in a similar manner to what has been presented in Paper **V**. It might also nucleate the Mg-Si precipitate phases. However, such a study must also account for grain boundary microstructures.

Paper **VI** revisits SCC in Cu-free Al-Zn-Mg alloys and provides insights into the grain boundary microstructure. From the DCB results there are differences, most

noteworthy in the K_{iscc} values, between the two tempers. With the methods used, there were however no striking difference between the cooling methods. The study would, perhaps, been more complete if the SSRT experiments were conducted in the transverse direction and not only along the extrusion direction. It is likely that a more clear trend in susceptibility would have been deduced in this case. The SSRT results are still interesting, as they demonstrate differences in tempers both with respect to the reduction in area ratio and the secondary cracking only observed in one of the two temper states. Moreover, the microstructure study is complete and the findings are expected to be relevant to others.

Future work must also consider whether the tests conducted in Paper **VI** are suitable to evaluate the SCC properties in these materials. This is a study in itself, but is an important topic in the whole SCC debate. Especially, SSRT is a relatively fast test in the way used here. Applying a fixed load and keeping samples longer in the solution might have given other results. Alternatively, hydrogen pre-charging and then conducting the tests similar, as to here, might have given other results. Other test method must also be considered, some of which were reviewed by Magaji *et al.* [231].

Possible suggestions for future work are: i) look at the microstructure and SCC properties in the same alloy, but with additions of Cu. The reason for this is that many have reported higher SCC resistance when overageing and addressed this the to the composition of the grain boundary particles. However, many of these studies only consider the GBPs and forget the bulk microstructure. ii) Take a second look at RRA procedures. The reason for this is again that many studies only focus on GBPs and forget about the bulk microstructure. As a matter of fact, the earlier work of Talianker & Cina (who first suggested the RRA procedure) they suggested that the dislocation structures (or dislocations in connection to grain boundaries) disappeared in the heat RRA treatment and attributed this to the improved resistance to SCC [232]. Park & Ardel also suggested that bulk hardening precipitate size and orientation relationships may influence SCC in RRA treated samples [191]. More recent works also show that a slow cooling and/or step quenching may positively influence SCC properties [233, 234]. Investigating more 'exotic' thermal treatments is interesting as they are likely to become more applicable in industry with increasing development in processing equipment.

6.3 From 2D to 3D

A limitation in the studies concerning grain boundaries presented in this thesis is that the grain boundary particles have not been statistically studied. This is a topic with room for improvement using 3D methods such as e.g. focused ion beam (FIB) tomography [235] or X-ray based methods. The same goes for both IGC and SCC,

which are 3D phenomena that are only studied in 2D in this work. With respect to data analysis, more sophisticated methods using e.g. machine learning approaches in extracting useful information from the EDS data, could be looked more into. Combining this with accounting for beam broadening effects may lead to more accurate quantification of the amount of segregated solute at a particular grain boundary. Nevertheless, it is believed that the results presented in this thesis are relevant in many aspects of aluminium alloys. The applied methodologies, and the combination between them, as well as the analysis conducted will be imprortant in future works.

Chapter 7

Conclusion

In the work presented in thesis, several microstructural aspects related to grain boundary corrosion phenomena in aluminium alloys, have been studied. Detailed analysis of grain boundary particles and bulk precipitate microstructures, and their correlation with corrosion properties, have been the underlying motivation. TEM has been the main tool to provide the detailed information required to further understanding with respect to corrosion related phenomena. Much of the presented work is expected to be useful both for industry and as inspiration for further scientific work to solve many of the unsolved questions and also new questions that have emerged from the results presented here.

References

1. Hirsch, J. Recent development in aluminium for automotive applications. *Transactions of Nonferrous Metals Society of China* **24,** 1995–2002. doi:10.1016/S1003-6326(14)63305-7 (2014).
2. Polmear, I., John, D. S., Nie, J.-F. & Qian, M. in *Light Alloys* (eds Polmear, I., John, D. S., Nie, J.-F. & Qian, M.) Fifth Edition (Butterworth-Heinemann, Boston, 2017). doi:10.1016/B978-0-08-099431-4.00002-6.
3. Totten, G. . & MacKenzie, D. S. *Handbook of Aluminum. Vol. I and II* (Marcel Dekker, New York, 2003).
4. Dursun, T. & Soutis, C. Recent developments in advanced aircraft aluminium alloys. *Materials & Design* **56,** 862–871. doi:10.1016/j.matdes.2013.12.002 (2014).
5. EU commission. *Reducing CO2 emissions from passenger cars - before 2020* (accessed 2020-04-17). https://ec.europa.eu/clima/policies/transport/vehicles/cars_en.
6. Schlesinger, M. *Aluminum Recycling* doi:10.1201/b16192 (CRC Press, Boca Raton, 2013).
7. Statistics Norway. *Metalleksport i tollmurenes tid (Norwegian only)* (accessed 2020-03-15). www.ssb.no/energi-og-industri/artikler-og-publikasjoner/metalleksport-i-tollmurenes-tid.
8. Statistics Norway. *External trade in goods* (accessed 2020-03-15). www.ssb.no/en/utenriksokonomi/statistikker/muh/aar.
9. Walmsley J. C. *et al.* FICAL project description (2014).
10. Zajac, S., Hutchinson, B., Johansson, A. & Gullman, L.-O. Microstructure control and extrudability of Al–Mg–Si alloys microalloyed with manganese. *Materials Science and Technology* **10,** 323–333. doi:10.1179/mst.1994.10.4.323 (1994).

11. Tanihata, H., Sugawara, T., Matsuda, K. & Ikeno, S. Effect of casting and homogenizing treatment conditions on the formation of Al-Fe-Si intermetallic compounds in 6063 Al-Mg-Si alloys. *Journal of Materials Science* **34,** 1205–1210. doi:10.1023/A:1004504805781 (1999).

12. Kuijpers, N. C. W. *et al.* The dependence of the β-AlFeSi to α-Al(FeMn)Si transformation kinetics in Al-Mg-Si alloys on the alloying elements. *Materials Science and Engineering A* **394,** 9–19. doi:10.1016/j.msea.2004.09.073 (2005).

13. Lodgaard, L. & Ryum, N. Distribution of Mn- and Cr-Containing Dispersoids in Al-Mg-Si-Alloys. *Materials Science Forum* **331-337,** 945–950. doi:10.4028/www.scientific.net/msf.331-337.945 (2000).

14. Lodgaard, L. & Ryum, N. Precipitation of dispersoids containing Mn and/or Cr in Al–Mg–Si alloys. *Materials Science and Engineering: A* **283,** 144–152. doi:10.1016/s0921-5093(00)00734-6 (2000).

15. Hu, R., Ogura, T., Tezuka, H., Sato, T. & Liu, Q. Dispersoid formation and recrystallization behavior in an Al-Mg-Si-Mn alloy. *Journal of Materials Science and Technology* **26,** 237–243. doi:10.1016/S1005-0302(10)60040-0 (2010).

16. Bayat, N., Carlberg, T. & Cieslar, M. In-situ study of phase transformation during homogenization 6005 and 6082 Al alloys. *Journal of Alloys and Compounds* **725,** 504–509. doi:10.1016/j.jallcom.2017.07.149 (2017).

17. Zheng, K., Politis, D. J., Wang, L. & Lin, J. A review on forming techniques for manufacturing lightweight complex—shaped aluminium panel components. *International Journal of Lightweight Materials and Manufacture* **1,** 55–80. doi:10.1016/j.ijlmm.2018.03.006 (2018).

18. Humphreys, F. J. & Hatherly, M. *Recrystallization and Related Annealing Phenomena* Second Edition (Elsevier, Oxford, 2004).

19. Embury, J. D. & Nicholson, R. B. The nucleation of precipitates: The system Al-Zn-Mg. *Acta Metallurgica* **13,** 403–417. doi:10.1016/0001-6160(65)90067-2 (1965).

20. Milkereit, B., Starink, M. J., Rometsch, P. A., Schick, C. & Kessler, O. Review of the Quench Sensitivity of Aluminium Alloys: Analysis of the Kinetics and Nature of Quench-Induced Precipitation. *Materials* **12.** doi:10.3390/ma12244083 (2019).

21. Godard, D., Archambault, P., Aeby-Gautier, E. & Lapasset, G. Precipitation sequences during quenching of the AA 7010 alloy. *Acta Materialia* **50.** Computational Thermodynamics and Materials Design, 2319–2329. doi:10.1016/S1359-6454(02)00063-0 (2002).

22. Deschamps, A., Texier, G., Ringeval, S. & Delfaut-Durut, L. Influence of cooling rate on the precipitation microstructure in a medium strength Al–Zn–Mg alloy. *Materials Science and Engineering: A* **501,** 133–139. doi:10.1016/j.msea.2008.09.067 (2009).

23. Hornbogen, E. Hundred years of precipitation hardening. *Journal of Light Metals* **1,** 127–132. doi:10.1016/S1471-5317(01)00006-2 (2001).

24. Guinier, A. Structure of age-hardened aluminium-copper alloys. *Nature* **142,** 569–570. doi:10.1038/142569b0 (1938).

25. Preston, G. D. The Diffraction of X-Rays by Age-Hardening Aluminium Copper Alloys. *Proceedings of the Royal Society of London. Series A (1934-1990)* **167,** 526–538 (1938).

26. Preston, G. D. The diffraction of X-rays by an age-hardening alloy of aluminium and copper. The structure of an intermediate phase. *The London, Edinburgh, and Dublin Philosophical Magazine and Journal of Science* **26,** 855–871. doi:10.1080/14786443808562177 (1938).

27. Andersen, S. J. *et al.* The crystal structure of the β'' phase in Al–Mg–Si alloys. *Acta Materialia* **46,** 3283–3298. doi:10.1016/S1359-6454(97)00493-X (1998).

28. Hasting, H. S. *et al.* Composition of β'' precipitates in Al–Mg–Si alloys by atom probe tomography and first principles calculations. *Journal of Applied Physics* **106,** 123527. doi:10.1063/1.3269714 (Dec. 2009).

29. Marioara, C. D., Andersen, S. J., Zandbergen, H. W. & Holmestad, R. The influence of alloy composition on precipitates of the Al-Mg-Si system. *Metallurgical and Materials Transactions A* **36,** 691–702. doi:10.1007/s11661-005-1001-7 (2005).

30. Sunde, J. K., Marioara, C. D., van Helvoort, A. T. & Holmestad, R. The evolution of precipitate crystal structures in an Al-Mg-Si(-Cu) alloy studied by a combined HAADF-STEM and SPED approach. *Materials Characterization* **142,** 458–469. doi:10.1016/j.matchar.2018.05.031 (2018).

31. Edwards, G. A., Stiller, K., Dunlop, G. L. & Couper, M. J. The precipitation sequence in Al–Mg–Si alloys. *Acta Materialia* **46,** 3893–3904. doi:10.1016/S1359-6454(98)00059-7 (1998).

32. Saito, T. *et al.* Atomic Structures of Precipitates in Al-Mg-Si Alloys with Small Additions of Other Elements. *Advanced Engineering Materials* **1800125,** 1–18. doi:10.1002/adem.201800125 (2018).

33. Miao, W. F. & Laughlin, D. E. Effects of Cu content and preaging on precipitation characteristics in aluminum alloy 6022. *Metallurgical and Materials Transactions A* **31,** 361–371. doi:10.1007/s11661-000-0272-2 (2000).

34. Murayama, M., Hono, K., Miao, W. & Laughlin, D. E. The effect of Cu additions on the precipitation kinetics in an Al-Mg-Si alloy with excess Si. *Metallurgical and Materials Transactions A* **32,** 239–246. doi:10.1007/s11661-001-0254-z (2001).

35. Man, J., Jing, L. & Jie, S. G. The effects of Cu addition on the microstructure and thermal stability of an Al-Mg-Si alloy. *Journal of Alloys and Compounds* **437,** 146–150. doi:10.1016/j.jallcom.2006.07.113 (2007).

36. Marioara, C. D. *et al.* The effect of Cu on precipitation in Al–Mg–Si alloys. *Philosophical Magazine* **87,** 3385–3413. doi:10.1080/14786430701287377 (2007).

37. Saito, T., Marioara, C. D., Røyset, J., Marthinsen, K. & Holmestad, R. The effects of quench rate and pre-deformation on precipitation hardening in Al-Mg-Si alloys with different Cu amounts. *Materials Science and Engineering A* **609,** 72–79. doi:10.1016/j.msea.2014.04.094 (2014).

38. Zandbergen, M. W., Cerezo, A. & Smith, G. D. Study of precipitation in Al-Mg-Si Alloys by atom probe tomography II. Influence of Cu additions. *Acta Materialia* **101,** 149–158. doi:10.1016/j.actamat.2015.08.018 (2015).

39. Xiao, Q. *et al.* Effect of Cu content on precipitation and age-hardening behavior in Al-Mg-Si-xCu alloys. *Journal of Alloys and Compounds* **695,** 1005–1013. doi:10.1016/j.jallcom.2016.10.221 (2017).

40. Sunde, J. K., Marioara, C. D. & Holmestad, R. The effect of low Cu additions on precipitate crystal structures in overaged Al-Mg-Si(-Cu) alloys. *Materials Characterization* **160,** 110087. doi:10.1016/j.matchar.2019.110087 (2020).

41. Wenner, S., Jones, L., Marioara, C. D. & Holmestad, R. Atomic-resolution chemical mapping of ordered precipitates in Al alloys using energy-dispersive X-ray spectroscopy. *Micron* **96,** 103–111. doi:10.1016/j.micron.2017.02.007 (2017).

42. Marioara, C. D. *et al.* The Correlation Between Intergranular Corrosion Resistance and Copper Content in the Precipitate Microstructure in an AA6005A Alloy. *Metallurgical and Materials Transactions A* **49,** 5146–5156. doi:10.1007/s11661-018-4789-7 (2018).

43. Andersen, S. J. *et al.* Directionality and Column Arrangement Principles of Precipitates in Al-Mg-Si-(Cu) and Al-Mg-Cu Linked to Line Defect in Al. *Materials Science Forum* **877,** 461–470. doi:10.4028/www.scientific.net/MSF.877.461 (2016).

44. Murayama, M. & Hono, K. Pre-precipitate clusters and precipitation processes in Al-Mg-Si alloys. *Acta Materialia* **47,** 1537–1548. doi:10.1016/S1359-6454(99)00033-6 (1999).

45. Serizawa, A., Hirosawa, S. & Sato, T. Three-dimensional atom probe characterization of nanoclusters responsible for multistep aging behavior of an Al-Mg-Si alloy. *Metallurgical and Materials Transactions A* **39,** 243–251. doi:10.1007/s11661-007-9438-5 (2008).

46. Torsæter, M. *et al.* The influence of composition and natural aging on clustering during preaging in Al-Mg-Si alloys. *Journal of Applied Physics* **108.** doi:10.1063/1.3481090 (2010).

47. Marioara, C. D., Andersen, S. J., Jansen, J. & Zandbergen, H. W. Atomic model for GP-zones in a 6082 Al-Mg-Si system. *Acta Materialia* **49,** 321–328. doi:10.1016/S1359-6454(00)00302-5 (2001).

48. Chen, J. H., Costan, E., van Huis, M. A., Xu, Q. & Zandbergen, H. W. Atomic Pillar-Based Nanoprecipitates Strengthen AlMgSi Alloys. *Science* **312,** 416–419. doi:10.1126/science.1124199 (2006).

49. Zandbergen, H. W., Andersen, S. J. & Jansen, J. Structure Determination of Mg_5Si_6 Particles in Al by Dynamic Electron Diffraction Studies. *Science* **277,** 1221–1225. doi:10.1126/science.277.5330.1221 (1997).

50. Cayron, C. & Buffat, P. A. Transmission electron microscopy study of the β' phase (Al-Mg-Si alloys) and QC phase (Al-Cu-Mg-Si alloys): ordering mechanism and crystallographic structure. *Acta Materialia* **48,** 2639–2653. doi:10.1016/S1359-6454(00)00057-4 (2000).

51. Vissers, R. *et al.* The crystal structure of the β' phase in Al-Mg-Si alloys. *Acta Materialia* **55,** 3815–3823. doi:10.1016/j.actamat.2007.02.032 (2007).

52. Teichmann, K., Marioara, C. D., Andersen, S. J. & Marthinsen, K. TEM study of β' precipitate interaction mechanisms with dislocations and β' interfaces with the aluminium matrix in Al–Mg–Si alloys. *Materials Characterization* **75,** 1–7. doi:10.1016/j.matchar.2012.10.003 (2013).

53. Andersen, S. J., Marioara, C. D., Vissers, R., Frøseth, A. & Zandbergen, H. W. The structural relation between precipitates in Al-Mg-Si alloys, the Al-matrix and diamond silicon, with emphasis on the trigonal phase U1-MgAl2Si2. *Materials Science and Engineering A* **444,** 157–169. doi:10.1016/j.msea.2006.08.084 (2007).

54. Andersen, S. J., Marioara, C. D., Frøseth, A., Vissers, R. & Zandbergen, H. W. Crystal structure of the orthorhombic U2-Al4Mg4 Si4 precipitate in the Al-Mg-Si alloy system and its relation to the β' and β'' phases. *Materials Science and Engineering A* **390,** 127–138. doi:10.1016/j.msea.2004.09.019 (2005).

55. R. Vissers C. D. Marioara, S. J. A. & Holmestad, R. *Crystal structure determination of the B′ phase in Al-Mg-Si alloys by combining quantitative electron diffraction and ab-initio calculations* in *Aluminium Alloys. The Physical and Mechanical Properties* Proceedings of ICAA11. 22nd–26th Sept. 2008 (eds Hirsch J., S. B. & Gottstein, G.) (Wiley, 2008), 1263–1269.

56. Cayron, C., Sagalowicz, L., Beffort, O. & Buffat, P. A. Structural phase transition in Al-Cu-Mg-Si alloys by transmission electron microscopy study on an Al-4 wt% Cu-1 wt% Mg-Ag alloy reinforced by SiC particles. *Philosophical Magazine A* **79,** 2833–2851. doi:10.1080/01418619908212027 (1999).

57. Marioara, C. D. *et al.* HAADF-STEM study of β'-type precipitates in an over-aged Al–Mg–Si–Ag alloy. *Philosophical Magazine* **92,** 1149–1158. doi:10.1080/14786435.2011.642319 (2012).

58. Torsæter, M., Ehlers, F. J. H., Marioara, C. D., Andersen, S. J. & Holmestad, R. Applying precipitate-host lattice coherency for compositional determination of precipitates in Al-Mg-Si-Cu alloys. *Philosophical Magazine* **92,** 3833–3856. doi:10.1080/14786435.2012.693214 (2012).

59. Arnberg, L. & Aurivillius, B. The Crystal Structure of $Al_xCu_2Mg_{(12-x)}Si_7$, (h-AlCuMgSi). *Acta Chemica Scandinavica* **34a,** 1–5. doi:10.3891/acta.chem.scand.34a-0001 (1980).

60. Wolverton, C. Crystal structure and stability of complex precipitate phases in Al-Cu-Mg-(Si) and Al-Zn-Mg alloys. *Acta Materialia* **49,** 3129–3142. doi:10.1016/S1359-6454(01)00229-4 (2001).

61. Matsuda, K., Ikeno, S., Sato, T. & Uetani, Y. Metastable phases in an Al-Mg-Si alloy containing copper. *Metallurgical and Materials Transactions A* **32,** 1293–1299. doi:10.1007/s11661-001-0219-2 (2001).

62. Chakrabarti, D. J. & Laughlin, D. E. Phase relations and precipitation in Al-Mg-Si alloys with Cu additions. *Progress in Materials Science* **49,** 389–410. doi:10.1016/S0079-6425(03)00031-8 (2004).

63. Jacobs, M. H. The structure of the metastable precipitates formed during ageing of an Al-Mg-Si alloy. *The Philosophical Magazine: A* **26,** 1–13. doi:10.1080/14786437208221015 (1972).

64. Inoue, H., Sato, T., Kojima, Y. & Takahashi, T. The Temperature Limit for GP Zone Formation in an Al-Zn-Mg Alloy. *Metallurgical and Materials Transactions A* **12,** 1429–1434. doi:10.1007/BF02643687 (1981).

65. Jiang, X. J., Noble, B., Holme, B., Waterloo, G. & Taftø, J. Differential scanning calorimetry and electron diffraction investigation on low-temperature aging in Al-Zn-Mg alloys. *Metallurgical and Materials Transactions A* **31,** 339–348. doi:10.1007/s11661-000-0269-x (2000).

66. Berg, L. K. *et al.* GP-zones in Al-Zn-Mg alloys and their role in artificial aging. *Acta Materialia* **4,** 3443–3451. doi:10.1016/S1359-6454(01)00251-8 (2001).

67. Sha, G. & Cerezo, A. Early-stage precipitation in Al-Zn-Mg-Cu alloy (7050). *Acta Materialia* **52,** 4503–4516. doi:10.1016/j.actamat.2004.06.025 (2004).

68. Stiller, K., Warren, P. J., Hansen, V., Angenete, J. & Gjønnes, J. Investigation of precipitation in an Al-Zn-Mg alloy after two-step ageing treatment at 100° and 150°C. *Materials Science and Engineering A* **270,** 55–63. doi:10.1016/S0921-5093(99)00231-2 (1999).

69. Engdahl, T., Hansen, V., Warren, P. J. & Stiller, K. Investigation of fine scale precipitates in Al-Zn-Mg alloys after various heat treatments. *Materials Science and Engineering A* **327,** 59–64. doi:10.1016/S0921-5093(01)01876-7 (2002).

70. Hansen, V., Karlsen, O. B., Langsrud, Y. & Gjønnes, J. Precipitates, zones and transitions during aging of Al-Zn-Mg-Zr 7000 series alloy. *Materials Science and Technology* **20,** 185–193. doi:10.1179/026708304225010424 (2004).

71. Buha, J., Lumley, R. N. & Crosky, A. G. Secondary ageing in an aluminium alloy 7050. *Materials Science and Engineering A* **492,** 1–10. doi:10.1016/j.msea.2008.02.039 (2008).

72. Chen, J., Zhen, L., Yang, S., Shao, W. & Dai, S. Investigation of precipitation behavior and related hardening in AA 7055 aluminum alloy. *Materials Science and Engineering A* **500,** 34–42. doi:10.1016/j.msea.2008.09.065 (2009).

73. Liu, D. *et al.* Quantitative study of nanoscale precipitates in Al-Zn-Mg-Cu alloys with different chemical compositions. *Materials Science and Engineering A* **639,** 245–251. doi:10.1016/j.msea.2015.04.104 (2015).

74. Matsuda, K. *et al.* Extra electron diffraction spots caused by fine precipitates formed at the early stage of aging in Al–Mg–X (X=Si, Ge, Zn)-Cu alloys. *Journal of Japan Institute of Light Metals* **58,** 167–175. doi:10.2464/jilm.67.186 (2017).

75. Löffler, H., Kovács, I. & Lendvai, J. Review Decomposition processes in Al-Zn-Mg alloys. *Journal of Materials Science* **18,** 2215–2240. doi:10.1007/BF00541825 (1983).

76. Dlubek, G., Krause, R., Brümmer, O. & Plazaola, F. Study of formation and reversion of Guinier-Preston zones in Al-4.5 at%Zn-x at%Mg alloys by positrons. *Journal of Materials Science* **21,** 853–858. doi:10.1007/BF01117364 (1986).

77. Akuata, C. K. *et al.* Age hardening response of AA7108A investigated by means of Synchrotron-based X-ray Absorption Spectroscopy (XAS) measurements. *Materials Science and Engineering A* **747,** 42–52. doi:10.1016/j.msea.2019.01.052 (2019).

78. Chung, T. F. *et al.* Transmission electron microscopy investigation of separated nucleation and in-situ nucleation in AA7050 aluminium alloy. *Acta Materialia* **149,** 377–387. doi:10.1016/j.actamat.2018.02.045 (2018).

79. Bendo, A. *et al.* Microstructure evolution in a hydrogen charged and aged Al–Zn–Mg alloy. *Materialia* **3,** 50–56. doi:10.1016/j.mtla.2018.09.035 (2018).

80. Li, Y.-Y. *et al.* High-resolution characterization of the precipitation behavior of an Al-Zn-Mg-Cu alloy. *Philosophical Magazine Letters* **92,** 166–178. doi:10.1080/09500839.2011.652682 (2012).

81. Marioara, C. D., Lefebvre, W., Andersen, S. J. & Friis, J. Atomic structure of hardening precipitates in an Al-Mg-Zn-Cu alloy determined by HAADF-STEM and first-principles calculations: Relation to η-$MgZn_2$. *Journal of Materials Science* **48,** 3638–3651. doi:10.1007/s10853-013-7158-3 (2013).

82. Friauf, J. B. Crystal structure of magnesium di-zincide. *Physical Review* **29,** 34–40 (1927).

83. Komura, Y. & Tokunaga, K. Structural studies of stacking variants in Mg-base Friauf–Laves phases. *Acta Crystallographica Section B* **36,** 1548–1554. doi:10.1107/S0567740880006565 (1980).

84. Thackary, P. The Nature and Morphology of precipitate in Al-Zn-Mg Alloys. *Journal of the Institute of Metals* **96,** 7 (1968).

85. Gjønnes, J. & Simensen, C. J. An electron microscope investigation of the microstructure in an aluminium-zinc-magnesium alloy. *Acta Metallurgica* **18,** 881–890. doi:10.1016/0001-6160(70)90016-7 (1970).

86. Degischer, H. P., Lacom, W., Zahra, A. & Zahra, Y. C. Decomposition Processes in an Al-5% Zn-1% Mg alloy - Part II: Electronmicroscopic Investigations. *Zeitschrift für Metallkunde* **71,** 213–238 (1980).

87. Chung, T.-F. *et al.* An atomic scale structural investigation of nanometre-sized η precipitates in the 7050 aluminium alloy. *Acta Materialia.* doi:10.1016/j.actamat.2019.05.041 (2019).

88. Bendo, A. *et al.* An unreported precipitate orientation relationship in Al-Zn-Mg based alloys. *Materials Characterization* **158,** 109958. doi:10.1016/j.matchar.2019.109958 (2019).

89. Bendo, A. *et al.* Atomic scale HAADF-STEM study of η' and η_1 phases in peak-aged Al–Zn–Mg alloys. *Journal of Materials Science* **53,** 4598–4611. doi:10.1007/s10853-017-1873-0 (2018).

90. Bendo, A. *et al.* Characterisation of structural similarities of precipitates in Mg–Zn and Al–Zn–Mg alloys systems. *Philosophical Magazine* **99,** 2619–2635. doi:10.1080/14786435.2019.1637032 (2019).

91. Dumont, M., Lefebvre, W., Doisneau-Cottignies, B. & Deschamps, A. Characterisation of the composition and volume fraction of η' and η precipitates in an Al-Zn-Mg alloy by a combination of atom probe, small-angle X-ray scattering and transmission electron microscopy. *Acta Materialia* **53,** 2881–2892. doi:10.1016/j.actamat.2005.03.004 (2005).

92. Andersen, S. J., Marioara, C. D., Friis, J., Wenner, S. & Holmestad, R. Precipitates in aluminium alloys. *Advances in Physics: X* **3,** 790–813. doi:10.1080/23746149.2018.1479984 (2018).

93. Singh, A. & Rosalie, J. Lattice Correspondence and Growth Structures of Monoclinic Mg_4Zn_7 Phase Growing on an Icosahedral Quasicrystal. *Crystals* **8,** 194. doi:10.3390/cryst8050194 (2018).

94. Liu, C. *et al.* In-situ STEM imaging of growth and phase change of individual $CuAl_X$ precipitates in Al alloy. *Scientific Reports* **7,** 1–8. doi:10.1038/s41598-017-02081-9 (2017).

95. De Ardo, A. J. & Simensen, C. J. A structural investigation of multiple aging of Al-7 wt pct Zn-2.3 wt pct Mg. *Metallurgical Transactions* **4,** 2413–2421. doi:10.1007/BF02669384 (1973).

96. Wu, H. & Fan, G. An overview of tailoring strain delocalization for strength-ductility synergy. *Progress in Materials Science,* 100675. doi:10.1016/j.pmatsci.2020.100675 (2020).

97. Verhoeven, J. D. *Fundamentals of physical metallurgy* (Wiley New York, 1975).

98. Hull, D. & Bacon, D. J. *Introduction to Dislocations* Fifth Edition (Butterworth-Heinemann, Oxford, 2011).

99. Teichmann, K., Marioara, C. D., Andersen, S. J. & Marthinsen, K. The effect of preaging deformation on the precipitation behavior of an Al-Mg-Si alloy. *Metallurgical and Materials Transactions A* **43,** 4006–4014. doi:10.1007/s11661-012-1235-0 (2012).

100. Wenner, S. *Transmission Electron Microscopy and Muon Spin Relaxation Studies of Precipitation in Al-Mg-Si Alloys* PhD thesis (Dept. of Physics, Norwegian university of science and technology, 2014).

101. Embury, J. D., Lloyd, D. J. & Ramacachandran, T. R. in *Aluminum Alloys —Contemporary Research and Applications* (eds Vasudevan, A. K. & Doherty, R. D.) 579–601 (Elsevier, 1989). doi:10.1016/B978-0-12-341831-9.50027-9.

102. Myhr, O. R., Grong, Ø. & Andersen, S. J. Modelling of the age hardening behaviour of Al–Mg–Si alloys. *Acta Materialia* **49,** 65–75. doi:10.1016/S1359-6454(00)00301-3 (2001).

103. Myhr, O. R., Grong, Ø. & Schäfer, C. An Extended Age-Hardening Model for Al-Mg-Si Alloys Incorporating the Room-Temperature Storage and Cold Deformation Process Stages. *Metallurgical and Materials Transactions A* **46,** 6018–6039. doi:10.1007/s11661-015-3175-y (2015).

104. Sabirov, I., Murashkin, M. & Valiev, R. Nanostructured aluminium alloys produced by severe plastic deformation: New horizons in development. *Materials Science and Engineering: A* **560,** 1–24. doi:10.1016/j.msea.2012.09.020 (2013).

105. Jones, L. *et al.* Optimising multi-frame ADF-STEM for high-precision atomic-resolution strain mapping. *Ultramicroscopy* **179,** 57–62. doi:10.1016/j.ultramic.2017.04.007 (2017).

106. Guyot, P. & Cottignies, L. Precipitation kinetics, mechanical strength and electrical conductivity of AlZnMgCu alloys. *Acta Materialia* **44,** 4161–4167. doi:10.1016/S1359-6454(96)00033-X (1996).

107. Christiansen, E. *Nanoscale Characterisation of Deformed Aluminium Alloys* PhD thesis (Dept. of Physics, Norwegian university of science and technology (NTNU), 2019).

108. Lejček, P. *Grain Boundary Segregation in Metals* doi:10.1007/978-3-642-12505-8_1 (Springer, Berlin, Heidelberg, 2010).

109. Priester, L. *Grain Boundaries: From Theory to Engineering* 1–442. doi:10.1007/978-94-007-4969-6 (Springer, Dordrecht, 2013).

110. Wolf, D. & Lutsko, J. F. On the geometrical relationship between tilt and twist grain-boundaries. *Zeitschrift für Kristallographie* **189,** 239–262 (1989).

111. Brandon, D. G. The structure of high-angle grain boundaries. *Acta Metallurgica* **14,** 1479–1484. doi:10.1016/0001-6160(66)90168-4 (1966).

112. Read, W. T. & Shockley, W. Dislocation Models of Crystal Grain Boundaries. *Physical Review* **78,** 275–289. doi:10.1103/PhysRev.78.275 (1950).

113. Kronberg, M. L. & Wilson, F. H. Secondary recrystallization in copper. *Metals Transaction* **185,** 501–514 (1949).

114. Ashby, M. F., Spaepen, F. & Williams, S. The structure of grain boundaries described as a packing of polyhedra. *Acta Metallurgica* **26,** 1647–1663. doi:10.1016/0001-6160(78)90075-5 (1978).

115. Raabe, D. *et al.* Grain boundary segregation engineering in metallic alloys: A pathway to the design of interfaces. *Current Opinion in Solid State and Materials Science* **18,** 253–261. doi:10.1016/j.cossms.2014.06.002 (2014).

116. Luo, J., Cheng, H., Asl, K. M., Kiely, C. J. & Harmer, M. P. The Role of a Bilayer Interfacial Phase on Liquid Metal Embrittlement. *Science* **333,** 1730–1733. doi:10.1126/science.1208774 (2011).

117. Unwin, P. N. T., Lorimer, G. W. & Nicholson, R. B. The origin of the grain boundary precipitate free zone. *Acta Metallurgica* **17,** 1363–1377. doi:10.1016/0001-6160(69)90154-0 (1969).

118. Tang, M., Carter, W. C. & Cannon, R. M. Diffuse interface model for structural transitions of grain boundaries. *Physical Review B* **73,** 024102. doi:10.1103/PhysRevB.73.024102 (2006).

119. Cantwell, P. R. *et al.* Grain boundary complexions. *Acta Materialia* **62,** 1–48. doi:10.1016/j.actamat.2013.07.037 (2014).

120. Balluffi, R. W. Grain Boundary Diffusion Mechanisms in Metals. *Metallurgical transactions B* **13 B,** 527–553. doi:10.1007/BF02648378 (1982).

121. Zhao, H. *et al.* Interplay of Chemistry and Faceting at Grain Boundaries in a Model Al Alloy. *Physical Review Letters* **124,** 1–6. doi:10.1103/physrevlett.124.106102 (2020).

122. Raghavan, M. Microanalysis of precipitate free zones (PFZ) in Al-Zn-Mg and Cu-Ni-Nb alloys. *Metallurgical Transactions A* **11,** 993–999. doi:10.1007/BF02654713 (1980).

123. Zhao, H. *et al.* Segregation assisted grain boundary precipitation in a model Al-Zn-Mg-Cu alloy. *Acta Materialia* **156,** 318–329. doi:10.1016/j.actamat.2018.07.003 (2018).

124. Ogura, T., Hirosawa, S. & Sato, T. Quantitative characterization of precipitate free zones in Al-Zn-Mg(-Ag) alloys by microchemical analysis and nanoindentation measurement. *Science and Technology of Advanced Materials* **5,** 491–496. doi:10.1016/j.stam.2004.02.007 (2004).

125. Radmilovic, V. *et al.* Nanoindentation properties and the microstructure of grain boundary precipitate-free zones (PFZs) in an AlCuSiGe alloy. *Philosophical Magazine* **87,** 3905–3919. doi:10.1080/14786430601153414 (2007).

126. Vasudévan, A. K. & Doherty, R. D. Grain boundary ductile fracture in precipitation hardened aluminum alloys. *Acta Metallurgica* **35,** 1193–1219. doi:10.1016/0001-6160(87)90001-0 (1987).

127. Matsuda, K. *et al.* Effect of Copper Addition on Precipitation Behavior near Grain Boundary in Al–Zn–Mg Alloy. *Materials Transactions* **60,** 1688–1696. doi:10.2320/matertrans.L-M2019828 (2019).

128. Reboul, M. C. & Baroux, B. Metallurgical aspects of corrosion resistance of aluminium alloys. *Materials and Corrosion* **62,** 215–233. doi:10.1002/maco.201005650 (2011).

129. Frankel, G. S. & Landolt, D. in *Encyclopedia of Electrochemistry* (American Cancer Society, 2007). doi:10.1002/9783527610426.bard040101.

130. Birbilis, N. & Buchheit, R. G. Electrochemical Characteristics of Intermetallic Phases in Aluminum Alloys An Experimental Survey and Discussion. *Journal of The Electrochemical Society* **152,** B140–B151. doi:10.1149/1.1869984 (2005).

131. Birbilis, N. & Buchheit, R. G. Investigation and Discussion of Characteristics for Intermetallic Phases Common to Aluminum Alloys as a Function of Solution pH. *Journal of The Electrochemical Society* **155,** C117–C126. doi:10.1149/1.2829897 (2008).

132. Li, J. & Dang, J. A Summary of Corrosion Properties of Al-Rich Solid Solution and Secondary Phase Particles in Al Alloys. *Metals* **7,** 84. doi:10.3390/met7030084 (2017).

133. Zhu, Y., Sun, K. & Frankel, G. S. Intermetallic Phases in Aluminum Alloys and Their Roles in Localized Corrosion. *Journal of The Electrochemical Society* **165,** C807–C820. doi:10.1149/2.0931811jes (2018).

134. Gharbi, O. & Birbilis, N. Clarifying the Dissolution Mechanisms and Electrochemistry of Mg2Si as a Function of Solution pH. *Journal of The Electrochemical Society* **165,** C497–C501. doi:10.1149/2.1061809jes (2018).

135. Larsen, M. H., Walmsley, J. C., Lunder, O. & Nisancioglu, K. Effect of Excess Silicon and Small Copper Content on Intergranular Corrosion of 6000-Series Aluminum Alloys. *Journal of The Electrochemical Society* **157,** C61–C68. doi:10.1149/1.3261804 (2010).

136. Kairy, S. K. & Birbilis, N. Clarifying the Role of Mg2Si and Si in Localized Corrosion of Aluminum Alloys by Quasi In Situ Transmission Electron Microscopy. *Corrosion* **76,** 464–475. doi:10.5006/3457 (2020).

137. Eckermann, F., Suter, T., Uggowitzer, P. J., Afseth, A. & Schmutz, P. The influence of MgSi particle reactivity and dissolution processes on corrosion in Al–Mg–Si alloys. *Electrochimica Acta* **54,** 844–855. doi:10.1016/j.electacta.2008.05.078 (2008).

138. Han, J. & Ogle, K. Dealloying of $MgZn_2$ Intermetallic in Slightly Alkaline Chloride Electrolyte and Its Significance in Corrosion Resistance. *Journal of The Electrochemical Society* **164,** C952–C961. doi:10.1149/2.0341714jes (2017).

139. Shimizu, K. & Nisancioglu, K. High Resolution SEM Investigation of Intercrystalline Corrosion on 6000-Series Aluminum Alloy with Low Copper Content. *ECS Electrochemistry Letters* **3,** C29–C31. doi:10.1149/2.0041409eel (2014).

140. Kumari, S., Wenner, S., Walmsley, J. C., Lunder, O. & Nisancioglu, K. Progress in Understanding Initiation of Intergranular Corrosion on AA6005 Aluminum Alloy with Low Copper Content. *Journal of The Electrochemical Society* **166,** C3114–C3123. doi:10.1149/2.0211911jes (2019).

141. Kairy, S. K., Rometsch, P. A., Davies, C. H. J. & Birbilis, N. On the electrochemical and quasi in-situ corrosion response of the Q-phase ($Al_xCu_yMg_zSi_w$) intermetallic particle in 6xxx series Al-alloys. *Corrosion* **73,** 1–29. doi:10.5006/2249 (2017).

142. Ikeuba, A. I., Zhang, B., Wang, J., Han, E. H. & Ke, W. Electrochemical, TOF-SIMS and XPS studies on the corrosion behavior of Q-phase in NaCl solutions as a function of pH. *Applied Surface Science* **490,** 535–545. doi:10.1016/j.apsusc.2019.06.089 (2019).

143. Svenningsen, G., Larsen, M. H., Walmsley, J. C., Nordlien, J. H. & Nisancioglu, K. Effect of artificial aging on intergranular corrosion of extruded AlMgSi alloy with small Cu content. *Corrosion Science* **48,** 1528–1543. doi:10.1016/j.corsci.2005.05.045 (2006).

144. Larsen, M. H., Walmsley, J. C., Lunder, O., Mathiesen, R. H. & Nisancioglu, K. Intergranular Corrosion of Copper-Containing AA6xxx AlMgSi Aluminum Alloys. *Journal of The Electrochemical Society* **155,** C550. doi:10.1149/1.2976774 (2008).

145. Holmestad, J., Ervik, M., Marioara, C. D. & Walmsley, J. C. Investigation of Grain Boundaries in an Al-Mg-Si-Cu Alloy. *Materials Science Forum* **794-796,** 951–956. doi:10.4028/www.scientific.net/MSF.794-796.951 (2014).

146. Kairy, S. K. *et al.* Understanding the Origins of Intergranular Corrosion in Copper-Containing Al-Mg-Si Alloys. *Metallurgical and Materials Transactions A* **47,** 985–989. doi:10.1007/s11661-015-3296-3 (2016).

147. Kairy, S. K., Rometsch, P. A., Davies, C. H. J. & Birbilis, N. On the Intergranular Corrosion and Hardness Evolution of 6xxx Series Al Alloys as a Function of Si:Mg Ratio, Cu Content, and Aging Condition. *Corrosion* **73,** 1280–1295. doi:10.5006/2506 (2017).

148. Svenningsen, G. *et al.* Effect of low copper content and heat treatment on intergranular corrosion of model AlMgSi alloys. *Corrosion Science* **48,** 226–242. doi:10.1016/j.corsci.2004.11.025 (2006).

149. Zhan, H. *et al.* The influence of copper content on intergranular corrosion of model AlMgSi(Cu) alloys. *Materials and Corrosion* **59,** 670–675. doi:10.1002/maco.200804110 (2008).

150. Dong, P., Sun, D., Wang, B., Zhang, Y. & Li, H. Microstructure, microhardness and corrosion susceptibility of friction stir welded AlMgSiCu alloy. *Materials & Design* **54,** 760–765. doi:10.1016/j.matdes.2013.09.001 (2014).

151. Li, H. *et al.* The intergranular corrosion susceptibility of a heavily overaged Al-Mg-Si-Cu alloy. *Corrosion Science* **107,** 113–122. doi:10.1016/j.corsci.2016.02.025 (2016).

152. Zou, Y. *et al.* The intergranular corrosion behavior of 6000-series alloys with different Mg/Si and Cu content. *Applied Surface Science* **405,** 489–496. doi:10.1016/j.apsusc.2017.02.045 (2017).

153. Liang, W. J., Rometsch, P. A., Cao, L. F. & Birbilis, N. General aspects related to the corrosion of 6xxx series aluminium alloys: Exploring the influence of Mg/Si ratio and Cu. *Corrosion Science* **76,** 119–128. doi:10.1016/j.corsci.2013.06.035 (2013).

154. Cornejo, M. *et al.* A comparison of accelerated corrosion tests for the assessment of the intergranular corrosion susceptibility of bare 6000 aluminum sheets. *Materials and Corrosion* **70,** 623–632. doi:10.1002/maco.201810493 (2019).

155. Svenningsen, G., Larsen, M. H., Nordlien, J. H. & Nisancioglu, K. Effect of thermomechanical history on intergranular corrosion of extruded AlMgSi(Cu) model alloy. *Corrosion Science* **48,** 3969–3987. doi:10.1016/j.corsci.2006.03.018 (2006).

156. Svenningsen, G., Larsen, M. H., Nordlien, J. H. & Nisancioglu, K. Effect of high temperature heat treatment on intergranular corrosion of AlMgSi(Cu) model alloy. *Corrosion Science* **48,** 258–272. doi:10.1016/j.corsci.2004.12.003 (2006).

157. Kumari, S., Wenner, S., Walmsley, J. C., Lunder, O. & Nisancioglu, K. Copper enriched by dealloying as external cathode in intergranular corrosion of aluminium alloy AA6005. *Corrosion Science* **158,** 108090. doi:10.1016/j.corsci.2019.07.014 (2019).

158. Lebouil, S., Tardelli, J., Rocca, E., Volovitch, P. & Ogle, K. Dealloying of Al_2Cu, Al_7Cu_2Fe, and Al_2CuMg intermetallic phases to form nanoparticulate copper films. *Materials and Corrosion* **65,** 416–424. doi:10.1002/maco.201307550 (2014).

159. Wang, S.-S. *et al.* Effect of Cu Content and Aging Conditions on Pitting Corrosion Damage of 7xxx Series Aluminum Alloys. *Journal of The Electrochemical Society* **162,** C150–C160. doi:10.1149/2.0301504jes (2015).

160. Nisancioglu, K. Electrochemical Behavior of Aluminum-Base Intermetallics Containing Iron. *Journal of The Electrochemical Society* **137,** 69. doi:10.1149/1.2086441 (1990).

161. Zander, D., Schnatterer, C., Altenbach, C. & Chaineux, V. Microstructural impact on intergranular corrosion and the mechanical properties of industrial drawn 6056 aluminum wires. *Materials & Design* **83,** 49–59. doi:10.1016/j.matdes.2015.05.079 (2015).

162. Schnatterer, C. & Zander, D. Influence of the grain boundary chemistry on the intergranular corrosion mechanisms of a high-strength Al-Mg-Si alloy. *Surface and Interface Analysis* **48,** 750–754. doi:10.1002/sia.5859 (2016).

163. Minoda, T. & Yoshida, H. Effect of grain boundary characteristics on intergranular corrosion resistance of 6061 aluminum alloy extrusion. *Metallurgical and Materials Transactions A* **33,** 2891–2898. doi:10.1007/s11661-002-0274-3 (2002).

164. Kim, S. H., Erb, U., Aust, K. T. & Palumbo, G. Grain boundary character distribution and intergranular corrosion behavior in high purity aluminum. *Scripta Materialia* **44,** 835–839. doi:10.1016/S1359-6462(00)00682-5 (2001).

165. Bałkowiec, A., Michalski, J., Matysiak, H. & Kurzydlowski, K. J. Influence of grain boundaries misorientation angle on intergranular corrosion in 2024-T3 aluminium. *Materials Science-Poland* **29,** 305–311. doi:10.2478/s13536-011-0050-4 (2011).

166. Chan, L. H., Weiland, H., Cheong, S., Rohrer, G. S. & Rollett, A. D. in *Applications of Texture Analysis* 261–267 (John Wiley & Sons, Ltd, 2008). doi:10.1002/9780470444214.ch28.

167. Scamans, G. M., Alani, R. & Swann, P. R. Pre-exposure embrittlement and stress corrosion failure in AlZnMg Alloys. *Corrosion Science* **16.** doi:10.1016/0010-938X(76)90065-2 (1976).

168. Holroyd, N. J. H. & Scamans, G. M. Crack propagation during sustained-load cracking of Al-Zn-Mg-Cu aluminum alloys exposed to moist air or distilled water. *Metallurgical and Materials Transactions A* **42,** 3979–3998. doi:10.1007/s11661-011-0793-x (2011).

169. Holroyd, N. J. H. & Scamans, G. M. Stress corrosion cracking in Al-Zn-Mg-Cu aluminum alloys in saline environments. *Metallurgical and Materials Transactions A* **44,** 1230–1253. doi:10.1007/s11661-012-1528-3 (2013).

170. Speidel, M. O. Stress corrosion cracking of aluminum alloys. *Metallurgical Transactions A* **6,** 631–651. doi:10.1007/BF02672284 (1975).

171. Rao, A. C. U., Vasu, V., Govindaraju, M. & Srinadh, K. V. S. Stress corrosion cracking behaviour of 7xxx aluminum alloys: A literature review. *Transactions of Nonferrous Metals Society of China (English Edition)* **26,** 1447–1471. doi:10.1016/S1003-6326(16)64220-6 (2016).

172. Kannan, M. B., Srinivasan, P. B. & Raja, V. S. in *Stress Corrosion Cracking* (eds Raja, V. & Shoji, T.) 307–340 (Woodhead Publishing, 2011). doi:10.1533/9780857093769.3.307.

173. Braun, R. Environmentally assisted cracking of aluminium alloys. *Materialwissenschaft und Werkstofftechnik* **38,** 674–689. doi:10.1002/mawe.200700204 (2007).

174. Burleigh, T. D. The Postulated Mechanisms for Stress Corrosion Cracking of Aluminum Alloys: A Review of the Literature 1980-1989. *Corrosion* **47,** 89–98. doi:10.5006/1.3585235 (1991).

175. Sarkar, B., Marek, M. & Starke, E. A. The effect of copper content and heat treatment on the stress corrosion characteristics of Ai-6Zn-2Mg-X Cu alloys. *Metallurgical Transactions A* **12,** 1939–1943. doi:10.1007/BF02643806 (1981).

176. Knight, S. P., Birbilis, N., Muddle, B. C., Trueman, A. R. & Lynch, S. P. Correlations between intergranular stress corrosion cracking, grain-boundary microchemistry, and grain-boundary electrochemistry for Al –Zn–Mg–Cu alloys. *Corrosion Science* **52,** 4073–4080. doi:10.1016/j.corsci.2010.08.024 (2010).

177. Goswami, R., Lynch, S., Holroyd, N. J., Knight, S. P. & Holtz, R. L. Evolution of grain boundary precipitates in Al 7075 upon aging and correlation with stress corrosion cracking behavior. *Metallurgical and Materials Transactions A* **44,** 1268–1278. doi:10.1007/s11661-012-1413-0 (2013).

178. Chen, J., Zhang, X., Zou, L., Yu, Y. & Li, Q. Effect of precipitate state on the stress corrosion behavior of 7050 aluminum alloy. *Materials Characterization* **114,** 1–8. doi:10.1016/j.matchar.2016.01.022 (2016).

179. Lynch, S. . in *Stress Corrosion Cracking* (eds Raja, V. & Shoji, T.) 3–89 (Woodhead Publishing, 2011). doi:10.1533/9780857093769.1.3.

180. Djukic, M. B., Bakic, G. M., Zeravcic, V. S., Sedmak, A. & Rajicic, B. The synergistic action and interplay of hydrogen embrittlement mechanisms in steels and iron: Localized plasticity and decohesion. *Engineering Fracture Mechanics* **216,** 106528. doi:10.1016/j.engfracmech.2019.106528 (2019).

181. Najjar, D., Magnin, T. & Warner, T. J. Influence of critical surface defects and localized competition between anodic dissolution and hydrogen effects during stress corrosion cracking of a 7050 aluminium alloy. *Materials Science and Engineering: A* **238,** 293–302. doi:10.1016/S0921-5093(97)00369-9 (1997).

182. Lynch, S. P. in *Stress Corrosion Cracking* (eds Raja, V. S. & Shoji, T.) 90–130 (Woodhead Publishing, 2011). doi:10.1533/9780857093769.1.90.

183. Hardwick, D. A., Thompson, A. W. & Bernstein, I. M. The effect of copper content and microstructure on the hydrogen embrittlement of Al-6Zn-2Mg alloys. *Metallurgical Transactions A* **14,** 2517–2526. doi:10.1007/BF02668893 (1983).

184. Young, G. A. & Scully, J. R. The effects of test temperature, temper, and alloyed copper on the hydrogen-controlled crack growth rate of an Al-Zn-Mg-(Cu) alloy. *Metallurgical and Materials Transactions A* **33,** 1297–1297. doi:10.1007/s11661-002-0233-z (2002).

185. Christodoulou, L. & Flower, H. M. Hydrogen embrittlement and trapping in Al6%Zn-3%Mg. *Acta Metallurgica* **28,** 481–487. doi:10.1016/0001-6160(80)90138-8 (1980).

186. Puiggali, M. *et al.* Effect of microstructure on stress corrosion cracking of an Al-Zn-Mg-Cu alloy. *Corrosion Science* **40,** 805–819. doi:10.1016/S0010-938X(98)00002-X (1998).

187. Ji, Y. *et al.* Discontinuous model combined with an atomic mechanism simulates the precipitated η' phase effect in intergranular cracking of 7-series aluminum alloys. *Computational Materials Science* **166,** 282–292. doi:10.1016/j.commatsci.2019.05.008 (2019).

188. Wu, L.-M., Wang, W.-H., Hsu, Y.-F. & Trong, S. Effects of Microstructure on the Mechanical Properties and Stress Corrosion Cracking of an Al-Zn-Mg-Sc-Zr Alloy by Various Temper Treatments. *Materials Transactions* **48,** 600–609. doi:10.2320/matertrans.48.600 (2007).

189. Cornish, A. J. & Day, M. K. B. The effect of variable quenching conditions on the relationship between stress-corrosion resistance, tensile properties, and microstructure of high purity Al-Zn-Mg alloy. *Journal of the Institute of Metals* **99,** 377–384 (1971).

190. Albrecht, J., Thompson, A. W. & Bernstein, I. M. The role of microstructure in hydrogen-assisted fracture of 7075 aluminum. *Metallurgical Transactions A* **10,** 1759–1766. doi:10.1007/BF02811712 (1979).

191. Park, J. K. & Ardell, A. J. Effect of Retrogression and Reaging Treatments on the Microstructure of Al-7075-T651. *Metallurgical Transactions A* **15A,** 1531–1543 (1984).

192. Baumgartner, M. & Kaesche, H. Intercrystalline Corrosion and Stress Corrosion Cracking of AlZnMg Alloys. *Corrosion* **44,** 231–239. doi:10.5006/1.3583931 (1988).

193. Oger, L., Lafouresse, M. C., Odemer, G., Peguet, L. & Blanc, C. Hydrogen diffusion and trapping in a low copper 7xxx aluminium alloy investigated by Scanning Kelvin Probe Force Microscopy. *Materials Science and Engineering A* **706,** 126–135. doi:10.1016/j.msea.2017.08.119 (2017).

194. Tsuru, T. *et al.* First-principles study of hydrogen segregation at the $MgZn_2$ precipitate in Al-Mg-Zn alloys. *Computational Materials Science* **148,** 301–306. doi:10.1016/j.commatsci.2018.03.009 (2018).

195. Tsuru, T. *et al.* Hydrogen-accelerated spontaneous microcracking in high-strength aluminium alloys. *Scientific Reports* **10,** 1–8. doi:10.1038/s41598-020-58834-6 (2020).

196. Viswanadham, R. K., Sun, T. S. & Green, J. A. S. Grain boundary segregation in Al-Zn-Mg alloys-Implications to stress corrosion cracking. *Metallurgical and Materials Transactions A* **11,** 85–89. doi:10.1007/BF02700441 (1980).

197. Scamans, G. M., Holroyd, N. J. H. & Tuck, C. D. S. The role of magnesium segregation in the intergranular stress corrosion cracking of aluminium alloys. *Corrosion Science* **27,** 329–347. doi:10.1016/0010-938X(87)90076-X (1987).

198. Song, R. G. *et al.* Grain boundary segregation and hydrogen-induced fracture in 7050 aluminium alloy. *Acta Materialia* **44,** 3241–3248. doi:10.1016/1359-6454(95)00406-8 (1996).

199. Song, R. G. *et al.* Stress corrosion cracking and hydrogen embrittlement of an Al–Zn–Mg–Cu alloy. *Acta Materialia* **52,** 4727–4743. doi:10.1016/j.actamat.2004.06.023 (2004).

200. Singh, S. S., Stannard, T. J., Xiao, X. & Chawla, N. In Situ X-ray Microtomography of Stress Corrosion Cracking and Corrosion Fatigue in Aluminum Alloys. *Jom* **69,** 1404–1414. doi:10.1007/s11837-017-2413-8 (2017).

201. Stannard, T. J. *et al.* 3D time-resolved observations of corrosion and corrosion-fatigue crack initiation and growth in peak-aged Al 7075 using synchrotron X-ray tomography. *Corrosion Science* **138,** 340–352. doi:10.1016/j.corsci.2018.04.029 (2018).

202. Altenbach, C. *et al.* Synchrotron-based holotomography and X-ray fluorescence study on the stress corrosion cracking behavior of the peak-aged 7075 aluminum alloy. *Journal of Alloys and Compounds* **817,** 152722. doi:10.1016/j.jallcom.2019.152722 (2020).

203. Su, H. *et al.* Influence of hydrogen on strain localization and fracture behavior in Al–Zn–Mg–Cu aluminum alloys. *Acta Materialia* **159,** 332–343. doi:10.1016/j.actamat.2018.08.024 (2018).

204. Robinson, J. S., Pirling, T., Truman, C. E. & Panzner, T. Residual stress relief in the aluminium alloy 7075. *Materials Science and Technology* **33,** 1765–1775. doi:10.1080/02670836.2017.1318243 (2017).

205. Williams, D. B. & Carter, C. B. *Transmission Electron Microscopy- A Textbook for Materials Science* doi:10.1007/978-0-387-76501-3 (Springer, Boston, MA, 2009).

206. The Kavli Price. *2020 Kavli Prize Laurates* (accessed 2020-05-28). http://kavliprize.org/prize-landing/laureates/2020.

207. Fultz, B. & Howe, J. M. *Transmission electron microscopy and diffractometry of materials* 1–758. doi:10.1007/978-3-540-73886-2 (Springer, Berlin, Heidelberg, 2008).

208. Zuo, J. M. & Spence, J. C. H. *Advanced transmission electron microscopy: Imaging and diffraction in nanoscience* 1–729. doi:10.1007/978-1-4939-6607-3 (Springer, New York, 2016).

209. Williams, D. B. & Carter, C. B. *Transmission Electron Microscopy Diffraction, Imaging, and Spectrometry* doi:10.1007/978-3-319-26651-0 (Springer, Cham, 2016).

210. Erni, R. *Aberration-Corrected Imaging in Transmission Electron Microscopy* doi:10.1142/p703 (Imperial College Press, 2010).

211. Treacy, M. M. J. Z Dependence of Electron Scattering by Single Atoms into Annular Dark-Field Detectors. *Microscopy and Microanalysis* **17,** 847–858. doi:10.1017/S1431927611012074 (2011).

212. Findlay, S. *et al.* Dynamics of annular bright field imaging in scanning transmission electron microscopy. *Ultramicroscopy* **110,** 903–923. doi:10.1016/j.ultramic.2010.04.004 (2010).

213. Uhlemann, S. & Haider, M. Residual wave aberrations in the first spherical aberration corrected transmission electron microscope. *Ultramicroscopy* **72,** 109–119. doi:10.1016/S0304-3991(97)00102-2 (1998).

214. Haider, M. *et al.* A spherical-aberration-corrected 200 kV transmission electron microscope. *Ultramicroscopy* **75,** 53–60. doi:10.1016/S0304-3991(98)00048-5 (1998).

215. Wang, Z., Lv, K., Zheng, J. K. & Chen, B. Atomic-scale characterization of interfaces between 2A70 aluminum alloy matrix and Cu-enriched layer after electropolishing. *Materials Characterization* **150,** 150–154. doi:10.1016/j.matchar.2019.02.028 (2019).

216. Jones, L. *et al.* Smart Align - a new tool for robust non-rigid registration of scanning microscope data. *Advanced Structural and Chemical Imaging* **1,** 8. doi:10.1186/s40679-015-0008-4 (2015).

217. Nylund, I.-E. *Project thesis: Evaluation of energy-dispersive spectroscopy characteristics for improved compositional analysis* (Dept. of Physics, Norwegian university of science and technology (NTNU), 2017).

218. Cliff, G. & Lorimer, G. W. The quantitative analysis of thin specimens. *Journal of Microscopy* **103,** 203–207. doi:10.1111/j.1365-2818.1975.tb03895.x (1975).

219. Watanabe, M. & Williams, D. B. The quantitative analysis of thin specimens: A review of progress from the Cliff-Lorimer to the new ζ-factor methods. *Journal of Microscopy* **221,** 89–109. doi:10.1111/j.1365-2818.2006.01549.x (2006).

220. Faulkner, R. G., Morgan, T. S. & Little, E. A. Analytical electron microscopy of thin segregated layers. *X-Ray Spectrometry* **23,** 195–202. doi:10.1002/xrs.1300230503 (1994).

221. Robson, J. Analytical electron microscopy of grain boundary segregation: Application to Al-Zn-Mg-Cu (7xxx) alloys. *Materials Characterization* **154,** 325–334. doi:10.1016/j.matchar.2019.06.016 (2019).

222. De la Peña, F. *et al. HyperSpy v1.5.2* version v1.5.2. Sept. 2019. doi:10.5281/zenodo.3396791.

223. Leng, Y. *Materials Characterization: Introduction to Microscopic and Spectroscopic Methods* (John Wiley & Sons, 2008).

224. Bachmann, F., Hielscher, R. & Schaeben, H. *Texture Analysis with MTEX – Free and Open Source Software Toolbox* in *Texture and Anisotropy of Polycrystals III* **160** (Trans Tech Publications Ltd, Mar. 2010), 63–68. doi:10.4028/www.scientific.net/SSP.160.63.

225. Schwartz, A. J., Kumar, M., Adams, B. L. & Field, D. P. *Electron Backscatter Diffraction in Materials Science* doi:10.1007/978-0-387-88136-2 (Springer-Verlag, 2009).

226. Hyatt, M. V. Use of Precracked Specimens in Stress Corrosion Testing of High Strength Aluminum Alloys. *Corrosion* **26,** 487–503. doi:10.5006/0010-9312-26.11.487 (1970).

227. Saylor, D. M., El-Dasher, B. S., Adams, B. L. & Rohrer, G. S. Measuring the five-parameter grain-boundary distribution from observations of planar sections. *Metallurgical and Materials Transactions A* **35 A,** 1981–1989. doi:10.1007/s11661-004-0147-z (2004).

228. Huang, T.-S., Zhao, S., Frankel, G. S. & Wolfe, D. A. A Statistical Model for Localized Corrosion in 7xxx Aluminum Alloys. *Corrosion* **63,** 819–827. doi:10.5006/1.3278431 (2007).

229. Lim, M. L. C. *et al.* Model to predict intergranular corrosion propagation in three dimensions in AA5083-H131. *Materials & Design* **96,** 131–142. doi:10.1016/j.matdes.2016.01.089 (2016).

230. Zhao, S., Wolfe, D. A., Huang, T.-S. & Frankel, G. S. Generalized model for IGC growth in aluminum alloys. *Journal of Statistical Planning and Inference* **137,** 2405–2412. doi:10.1016/j.jspi.2006.09.021 (2007).

231. Magaji, N., Mayrhofer, R., Kröger, B., Schnatterer, C. & Zander, D. Comparison of test methods used to analyze stress corrosion cracking of differently tempered 7xxx alloys. *Materials and Corrosion* **70,** 1192–1204. doi:10.1002/maco.201810717 (2019).

232. Talianker, M. & Cina, B. Retrogression and reaging and the role of dislocations in the stress corrosion of 7000-type aluminum alloys. *Metallurgical Transactions A* **20,** 2087–2092. doi:10.1007/BF02650294 (1989).

233. Xie, P. *et al.* Enhancing the stress corrosion cracking resistance of a low-Cu containing Al-Zn-Mg-Cu aluminum alloy by step-quench and aging heat treatment. *Corrosion Science* **161,** 108184. doi:10.1016/j.corsci.2019.108184 (2019).

234. Yuan, D. *et al.* Enhancing stress corrosion cracking resistance of low Cu-containing Al-Zn-Mg-Cu alloys by slow quench rate. *Materials & Design* **164,** 107558. doi:10.1016/j.matdes.2018.107558 (2019).

235. Singh, S. S., Loza, J. J., Merkle, A. P. & Chawla, N. Three dimensional microstructural characterization of nanoscale precipitates in AA7075-T651 by focused ion beam (FIB) tomography. *Materials Characterization* **118,** 102–111. doi:10.1016/j.matchar.2016.05.009 (2016).

Appendices

Appendix A

Poster on the η_1 precipitate interface

Presented at 'The 61st Symposium of The Japanese Society of Microscopy' in Toyama, Japan. 1st-3rd November 2018.

Structure and interface of the η_1-$MgZn_2$ precipitate studied using TEM and DFT calculations

A. Lervik[1,*], C.D. Marioara[2], S.J. Andersen[2], J. Friis[2] and R. Holmestad[1]
[1]Department of Physics, Norwegian University of Science and Technology (NTNU), Trondheim, Norway.
[2]SINTEF Industry, Trondheim, Norway.

* Corresponding author.
adrian.lervik@ntnu.no

Background and motivation

- Age-hardenable AlMgZn alloys are of great interest in automotive and aerospace structural products, particularly due to their high strength/weight ratio. The strength is achieved due to formation of nanoscale coherent $MgZn_2$ (η') precipitates, formed on the {111} Al planes [1].
- The η-phase has been reported to form with additionally 9 orientation relations with Al [2], many of which the interface structure remains unresolved.
- In the overaged T7 state of an investigated 7003 alloy the η_1, growing along the {100} Al planes, has been found to account for approximately 50% of the relative fraction of precipitates.
- A correct interface model of η_1 is essential for accurate description of material properties.

Methods

- HAADF-STEM micrographs obtained along $[100]_{Al}$ using a probe corrected Jeol ARM 200CF.
- Bulk structure similar to the hexagonal C14 Laves structure [3], and interface is highly coherent in the $[1\bar{2}10]_\eta$ projection [4].
- Interface mismatch in the $[0001]_\eta$ projection is caused by an Al/Zn ratio of 11/6.
  - Results in interface defect(s) and a small zig-zag rotation of the internal structure.
  - Segregation of Zn and/or Cu at interface.
- Theoretical supercell, consisting of 845 atoms, determined using blob-detection of the HAADF-STEM images.
- Initial relaxation using LAMMPS Molecular Dynamics (MD) [5], before proceeding with DFT using VASP [6].

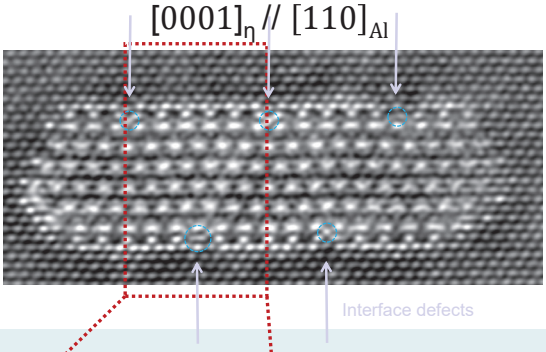

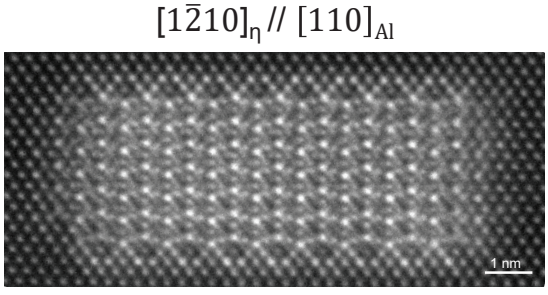

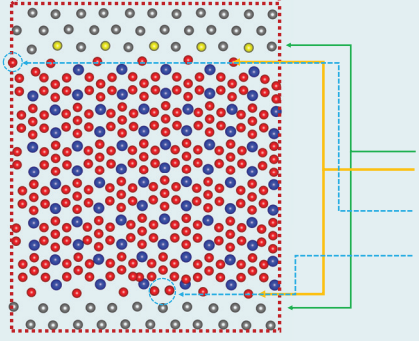

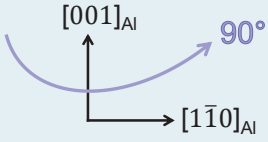

Interface model

1. Replace 1/2 Al with Cu in interface.
2. Add double-occupancy of Zn columns in interface.
   This is the misfit accommodating layer.
3. Remove Mg, and add Zn in the interface layer causing the defect.
4. Accommodate the double defect position in the bottom interface. Incorporated as two Zn atoms.

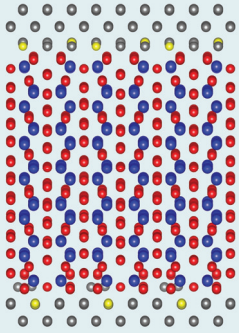

Status

An accurate atomistic structure of interfaces is essential in order to study mechanical properties, but also hydrogen trapping in relation to corrosion properties. Using a combination of aberration corrected HAADF-STEM images and DFT, we are close to providing a generalised model for η_1.

Al
Cu
Mg
Zn

References

[1] C.D. Marioara *et.al,* Journal of Material Science 48, (**2013**), 3638-3651.
[2] J. Gjønnes & C.J. Simensen, Acta Metallurgica 18, (**1970**), 881-890.
[3] Komura *et.al,* Acta Crystallographica Section B 36, (**1980**) 1548-1554.
[4] A. Bendo *et.al,* Journal of Material Science 53, (**2018**) 4598-4611.
[5] S. Plimpton, J. Comp. Phys. 117, (**1995**), 1-42
[6] G. Kresse & J. Furthmuller, Phys. Rev. B 54, (**1996**), 11169

Acknowledgements

I. G. Ringdalen is greatly acknowledges for running the LAMMPS relaxations. This work was supported by the KPN project FICAL (247598), co-financed by The Research Council of Norway (RCN), and the industrial partners Norsk Hydro, Gränges, Benteler, and Steertec. The (S)TEM work was carried out on the NORTEM (197405) infrastructure at the TEM Gemini Centre, Trondheim, Norway.

TEM Gemini Centre
FICAL
NTNU Norwegian University of Science and Technology

Appendix B

Paper III: Supplementary information

Supplementary material

The following details the methodology used to calculate the amount of solutes absorbed into hardening precipitates and precipitates nucleated on dispersoids (the so-called precipitate solute fraction), given in Table 4. Condition 185°C_2h_AC is used for the exemplification.

First, we assume we have an equal mix of three compositions in the β" precipitates: Mg_5Si_6, $Mg_5Al_2Si_4$ and $Mg_4Al_3Si_4$ [1]. That results in an average composition of $Mg_{9.33}Al_{3.33}Si_{9.33}$ for the 22 atoms containing β" unit cell. Taking into account the Al content and the fact that 22 Mg, Si and Al atoms in one β" unit cell displace a volume occupied by 24 Al atoms, we can equate that:

VF (β") = SF (β") x (24/22) x (22/18.67) = SF (β") x 1.286, where VF is volume fraction and SF is solute fraction.

We also assume a Q' composition of $Mg_6Al_6Si_7Cu_2$ [2], a β'_{Cu} composition of $Mg_3Al_3Si_2Cu$ [3,4] and an equal mix of both phases in the non- β" Cu-containing parts (in the β'_{Cu} and Q' parts). Therefore the average composition of (β'_{Cu} and Q') particles is (%) 27.5Si, 31Mg, 31 Al and 10.5Cu. Taking into consideration the Al content in the unit cells of both phases and the unit cell parameters [2-4] we can calculate that VF (Q') = SF (Q') x 22.49/15 and VF (β'_{Cu}) = SF (β'_{Cu}) x 10.055/6. On average:

VF (Cu-containing) = SF x 1.588.

Analysis of 50 HAADF-STEM images concluded that 10 are perfect β" (20%) and the rest (80%) are with various mix of β"/ Q'/ β'_{Cu} (see Table 3). In total, 23 Cu columns in the Si3/Al sites are counted in the perfect β" precipitates (=> **approx. 2.3 Cu columns per β" precipitate**), while 303 Cu columns were counted in the rest of the precipitates (=> **7.575 Cu columns per mixed, β" and Cu-containing precipitate**).

In the β'_{Cu} phase one unit cell has a cross section area of 0.4123 nm^2 and it contains 1 Cu atomic column; in Q' one unit cell has a cross-section area of 0.9223 nm^2 and it contains 2 Cu atomic columns, therefore we get an area of 0.4612 nm^2 for 1 Cu column. **On average (β'_{Cu} and Q') we have a Cu density of 0.43675 nm^2 per 1 Cu column**.

We assume all bulk precipitates have the measured average cross-section (CS) area of 7.23 nm^2 and the total VF of 0.653% from Table 2. Because 20% of all precipitates were found to be perfect β", it results **VF (β") = 0.131**, and **VF (mixed, β" and Cu-containing precipitates) = 0.522**.

One β" unit cell has 22 atoms and 0.9856 nm^2 CS area, therefore one β" precipitate (CS = 7.23 nm^2) contains 161.38 atomic columns => ~ 68.46Mg, 68.46Si and 24.45Al. But 2.3 columns per precipitate is Cu on Si3/Al sites, therefore **the true perfect β" composition is 68.46Mg (42.42%), 68.46Si (42.42%), 22.15Al (13.73%) and 2.3Cu (1.43%)**.

One mixed (β" and Cu-containing) precipitate (with CS = 7.23 nm^2) contains on average 7.575 Cu columns, therefore the average CS for such a precipitate can split as 3.31 nm^2 (Cu-containing β'_{Cu} and Q') (45.78%) and 3.92 nm^2 perfect β" (54.22%).

From Table 3 we have 20% fraction of perfect β". Therefore: VF (perfect β") = 0.131% equals SF (β") = 0.102% divided as 0.0433%Mg, 0.0433Si, 0.0140Al and 0.0014586Cu.

VF (mixed) = 0.522% splits as VF (β") = 0.283% and VF (β'_{Cu} and Q') = 0.239%.

Therefore SF (β" from the mixed particles) = 0.220% splits into 0.0934Mg, 0.0934Si, 0.0302Al and 0.0031469Cu.

And VF (β'_{Cu} and Q' parts of the mixed precipitates) = 0.522 x 0.4578 = 0.239%, therefore SF (β'_{Cu} and Q') = 0.239/1.588 = 0.1505% splits into 0.0467Mg, 0.0467Al, 0.0414Si and 0.0158Cu.

When we sum up the solute fractions of perfect β", β" from mixed precipitates and the Cu-containing parts of the mixed precipitates we obtain the total solute level absorbed into bulk precipitates (at%):

0.182 Mg, 0.178 Si, 0.091 Al and 0.020 Cu.

In addition, if we assume that all precipitates nucleated on dispersoids are Q' with composition $Mg_6Al_6Si_7Cu_2$ and with parameters given in Table 2 (assuming that one dispersoid nucleates on average one Q') we calculate a total precipitate solute fraction (where the solute fraction of bulk precipitates and of the Q' nucleated on dispersoids is added) of (at%) 0. 200 Mg, 0.197 Si, 0.107 Al and 0.026 Cu. A graphical summary of the methodology is given in Figure S1.

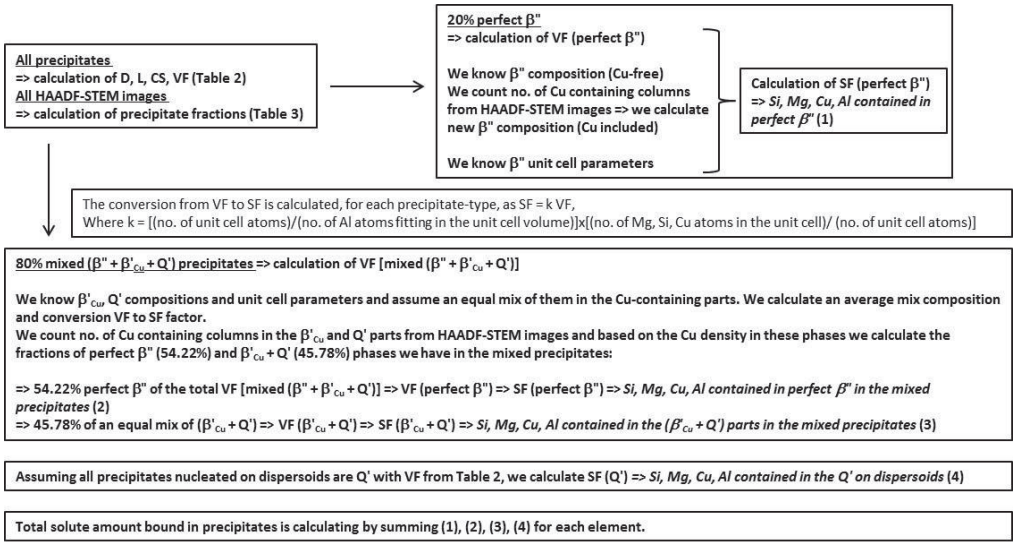

Figure S1 Summary of methodology for calculation of solute amounts bound into precipitates, with exemplification for condition 185°C_2h_AC.

References for the supplementary material

1. H. S. Hasting, A. G. Frøseth, S. J. Andersen, R. Vissers, J. C. Walmsley, C. D. Marioara, F. Danoix, W. Lefebvre and R. Holmestad, *Journal of Applied Physics*, 2009, vol. 106, article number 123527.
2. S. Wenner, L. Jones, C. D. Marioara and R. Holmestad, *Micron*, 2017, vol. 96, pp. 103-11.
3. C. D. Marioara, J. Nakamura, K. Matsuda, S. J. Andersen, R. Holmestad, T. Sato, T. Kawabata and S. Ikeno, *Philos. Mag.*, 2012, vol. 92/9, pp. 1149-1158.
4. T. Saito, C. D. Marioara, S. J. Andersen, W. Lefebvre and R. Holmestad, *Philos. Mag.*, vol. 94, 2014, pp. 520-31.

Appendix C

Paper IV: Supplementary information

Supplementary material to: Atomic structure of solute clusters in Al-Zn-Mg alloys

A. Lervik[1,*], E. Thronsen[1], J. Friis[1,2], C.D. Marioara[2], S. Wenner[1,2], A. Bendo[3], K. Matsuda[3], R. Holmestad[1] & S.J. Andersen[2]

[1]*Department of Physics, Norwegian University of Science and Technology (NTNU), N-7491 Trondheim, Norway*

[2]*SINTEF Industry, N-7465, Trondheim, Norway*

[3]*Graduate School of Science and Engineering, University of Toyama, 3190 Gofuku, Toyama, 930-8555, Japan*

** Corresponding author*

1 Supplementary hardness curves

The hardness curve for Alloy #2 after different ageing treatments is shown in Fig. 1. The alloy was either 1) artificially aged at 120 °C after 4 days of natural ageing where it was investigated in transmission electron microscopy (TEM) after 8 minutes ageing. 2) Directly artificially aged at 150 °C where it was studied in its peak hardness condition. 3) Naturally aged for two weeks and studied in TEM after 2 weeks natural ageing.

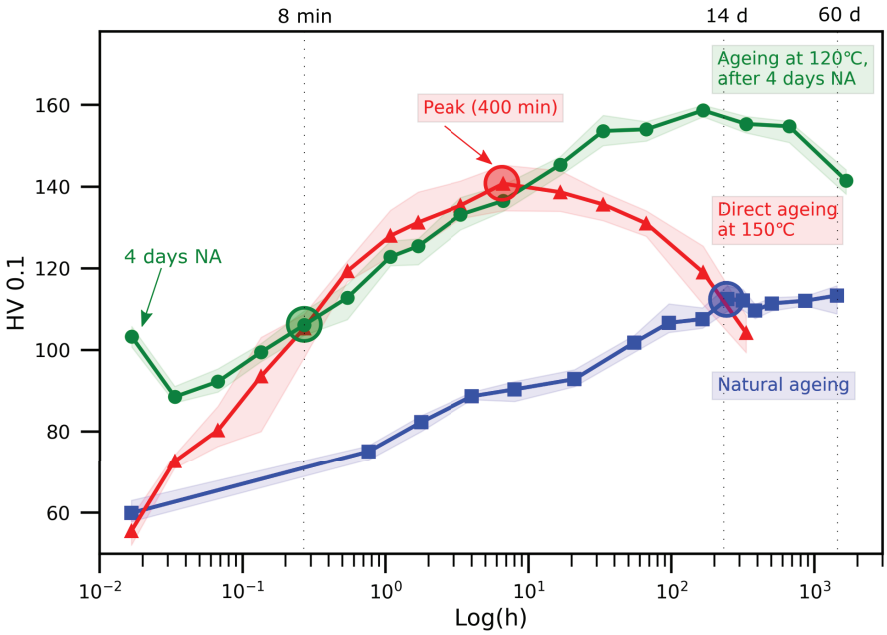

Figure 1: HV0.1 curves for Alloy #2 used in this study. TEM samples were prepared at the regions indicated by the shaded circle. The hardness is equal for 2 weeks natural ageing and after 8 minutes artificial ageing at 120 °C.

2 Supplementary TEM data

Additional high-angle annular dark field (HAADF)-scanning transmission electron microscopy (STEM) images, corresponding fast Fourier transform (FFT) and selected area diffraction pattern (SADP) of alloy #2 naturally aged for 2 weeks is shown in Figs. 2**a**, 2**b**, 2**c** and after 8 minutes artificial ageing at 120 °C in Figs. 2**d**, 2**e**, 2**f**.

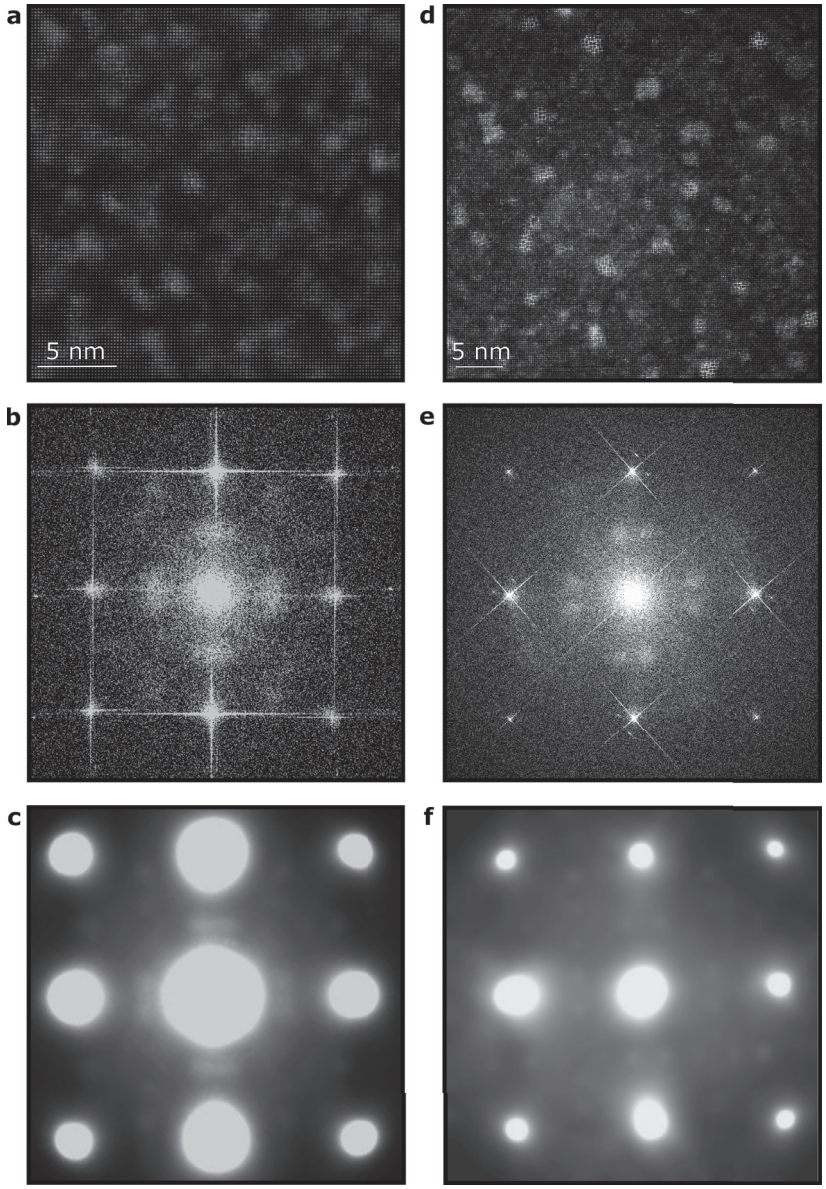

Figure 2: **a,b,c**, HAADF-STEM, corresponding FFT and a SADP for alloy #2 after 2 weeks natural ageing. **d,e,f**, Similar images for alloy #2 after 8 minutes ageing at 120 °C.

3 Supplementary surface layer

Fig. 3 shows the presence of a high Z-contrast layer of $\sim$4 nm thickness close to the vacuum, but below the outermost aluminium oxide layer. Chemical analysis indicate the layer to be rich in Cu, with presence of both Al and O. Similar observation was reported by Weng et al.[1]. It is likely that this layer covers the entire surface of the TEM specimen, resulting in the unwanted extra diffraction spots as shown in the FFT of the surface in Fig. 3. This was only observed for Alloy #1 in this study, where the TEM specimens were prepared at NTNU (Trondheim, Norway). TEM specimens of Alloy #2 were prepared at Toyama University (Toyama, Japan).

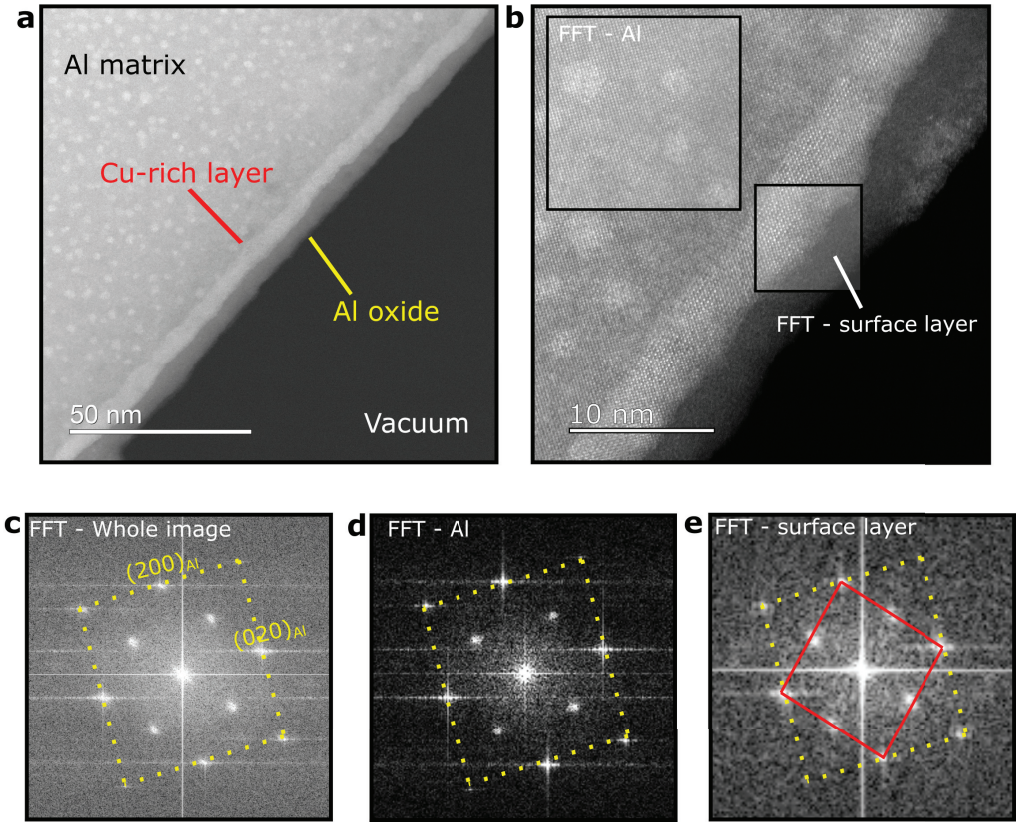

Figure 3: **a**, A HAADF-STEM image taken close to the edge of the specimen demonstrating an additional layer. **b**, high-resolution image of **a**. **c,d,e**, are FFT of the entire image **b** and from the two regions indicated in **b**.

4 Supplementary DFT data

The composition, formation enthalpy, pressure and Zn/Mg ratio for the density functional theory (DFT) calculations shown in Fig. 5 in the main text for single cluster units and stacked clusters are given in Tab. 1 and 2, respectively.

Table 1: Cluster single unit i$Z_x M_8 Z_y$ formation enthalpy and pressure in a 4×4×4 Al calculation cell. Sorted according to the lowest formation enthalpy per solute. See the main text and Fig. 3 for explanation of the cluster configurations.

Configuration/composition			Formation enthalpy [eV] per			Pressure	Ratio
No	Cluster	Calculation cell	total	atom	solute	kBar	Zn/Mg
1	$aZ_6M_8Z_{24}$	$Mg_8Zn_{30}Al_{219}$	-5.170	-0.020	-0.136	2.7	3.8
2	$zZ_6M_8Z_{24}$	$Mg_8Zn_{31}Al_{218}$	-5.284	-0.021	-0.136	2.3	3.9
3	$mZ_6M_8Z_{24}$	$Mg_9Zn_{30}Al_{218}$	-5.139	-0.020	-0.132	4.0	3.3
4	$Z_4M_8Z_{24}$	$Mg_8Zn_{28}Al_{220}$	-4.621	-0.018	-0.128	-0.5	3.5
5	$Z_6M_8Z_{24}$	$Mg_8Zn_{30}Al_{218}$	-4.731	-0.019	-0.125	-1.2	3.8
6	$zZ_6M_8Z_{12}$	$Mg_8Zn_{19}Al_{230}$	-3.120	-0.012	-0.116	6.2	2.4
7	$zZ_3M_8Z_{24}$	$Mg_8Zn_{28}Al_{221}$	-3.981	-0.016	-0.111	3.8	3.5
8	$Z_6M_8Z_{12}$	$Mg_8Zn_{18}Al_{230}$	-2.731	-0.011	-0.105	2.5	2.3
9	$Z_2M_8Z_{24}$	$Mg_8Zn_{26}Al_{222}$	-3.562	-0.014	-0.105	0.3	3.3
10	$Z_0M_8Z_{24}$	$Mg_8Zn_{24}Al_{224}$	-3.024	-0.012	-0.095	1.1	3
11	$Z_6M_0Z_{24}$	$Mg_8Zn_{30}Al_{226}$	-1.935	-0.008	-0.065	-6.5	3.8
12	$Z_0M_8Z_{12}$	$Mg_8Zn_{12}Al_{236}$	-1.232	-0.005	-0.062	4.7	1.5
13	$Z_0M_0Z_{24}$	$Zn_{24}Al_{232}$	-1.229	-0.005	-0.052	-4.8	-
14	$zZ_6M_0Z_{24}$	$Zn_{31}Al_{226}$	-1.057	-0.004	-0.034	-2.4	-
15	$zZ_0M_8Z_{12}$	$Mg_8Zn_{13}Al_{236}$	-0.508	-0.002	-0.024	9.6	1.6
16	$Z_0M_0Z_{12}$	$Zn_{12}Al_{244}$	-0.132	-0.001	-0.011	-2.1	-
17	$Z_0M_8Z_0$	Mg_8Al_{248}	-0.043	-0.000	-0.005	7.4	0
18	$zZ_0M_0Z_{12}$	$Zn_{13}Al_{244}$	1.707	0.007	0.131	3.3	-

Table 2: Formation enthalpy and pressure of [002] connected $\mathrm{iZ}_x\mathrm{M}_8\mathrm{Z}_y$ (except conf. 7). Confs. 1-6: single column of units (in 4×4×2 Al cells). Conf. 7: Solitary cluster (See Tab. 1). Confs. 8-12: clusters stacked in $\langle 411 \rangle$ squares (in 6×6×2 and 8×8×2 Al cells for confs. 8-10 and confs. 11-12, respectively). Conf. 10: Interstitial by shifted column, normal occupancy. Confs. 13-15: cluster stacked in $\langle 411 \rangle$ connections (in 6×6×2 Al cells).

Configuration/unit/composition			Formation enthalpy [eV] per			Pressure	Ratio	Comments
No	Unit	Composition/shared	total	atom	solute	kBar	Zn/Mg	
1	$\mathrm{zZ_6M_8Zn_{24}}$	$\mathrm{Mg_8Zn_{27}Al_{94}}$ / [002]	-5.681	-0.044	-0.162	6.7	3.4	-
2	$\mathrm{zZ_6M_8Z_8}$	$\mathrm{Mg_8Zn_{11}Al_{110}}$ / [002]	-2.916	-0.023	-0.154	15.7	1.4	-
3	$\mathrm{aZ_6M_8Z_8}$	$\mathrm{Mg_8Zn_{10}Al_{111}}$ / [002]	-2.740	-0.021	-0.152	16.7	1.3	-
4	$\mathrm{zZ_6M_8Z_{16}}$	$\mathrm{Mg_8Zn_{19}Al_{102}}$ / [002]	-4.065	-0.032	-0.151	11.5	2.1	-
5	$\mathrm{aZ_6M_8Z_{16}}$	$\mathrm{Mg_8Zn_{18}Al_{103}}$ / [002]	-3.903	-0.030	-0.150	12.4	2.3	-
6	$\mathrm{zZ_6M_8Z_{12}}$	$\mathrm{Mg_8Zn_{17}Al_{104}}$ / [002]	-3.394	-0.026	-0.136	13.2	2.4	-
7	$\mathrm{zZ_6M_8Z_{24}}$	$\mathrm{Mg_8Zn_{31}Al_{218}}$ / none	-5.284	-0.021	-0.136	2.3	3.9	-
8	$\mathrm{zZ_6M_8Z_{24}}$	$\mathrm{Mg_{32}Zn_{124}Al_{136}}$ / $\langle 411 \rangle$	-26.261	-0.090	-0.168	5.5	3.9	-
9	$\mathrm{aZ_6M_8Z_{24}}$	$\mathrm{Mg_{32}Zn_{120}Al_{140}}$ / $\langle 411 \rangle$	-24.721	-0.085	-0.163	6.9	3.8	-
10	$\mathrm{Z_6M_8Z_{24}}$	$\mathrm{Mg_{32}Zn_{120}Al_{136}}$ / $\langle 411 \rangle$	-23.444	-0.081	-0.154	-5.6	3.8	-
11	$\mathrm{zZ_6M_8Z_{24}}$	$\mathrm{Mg_{32}Zn_{100}Al_{384}}$ / $\langle 411 \rangle$	-16.812	-0.033	-0.127	6.870	3.1	Alternating Zn/Al in center columns
12	$\mathrm{zn_6M_8Z_{12}}$	$\mathrm{Mg_{32}Zn_{64}Al_{420}}$ / $\langle 411 \rangle$	-9.737	-0.019	-0.101	13.370	2	Alternating Zn/Al in center columns
13	$\mathrm{zZ_6M_8Z_{24}}$	$\mathrm{Mg_{24}Zn_{69}Al_{198}}$ / $\langle 411 \rangle$-$\langle 330 \rangle$	-14.596	-0.050	-0.157	11.930	2.9	-
14	$\mathrm{zZ_6M_8Z_{12}}$	$\mathrm{Mg_{24}Zn_{49}Al_{218}}$ / $\langle 411 \rangle$-$\langle 330 \rangle$	-10.620	-0.04	-0.146	18.000	2	-
15	$\mathrm{zZ_6M_8Z_{12}}$	$\mathrm{Mg_{24}Zn_{50}Al_{216}}$ / $\langle 411 \rangle$-$\langle 330 \rangle$	-10.907	-0.04	-0.145	16.730	2.1	Alternating Zn/vacancies in center columns

5 Supplementary simulated STEM images

In Fig. 4**a**, a simulated high-angle annular dark field scanning transmission electron microscopy (HAADF-STEM) image of the $zZ_6M_8Z_{24}$ model connected in a $\langle 411 \rangle$ manner is shown. Each corner in the square is the center of a single cluster unit. In **b**, an experimental HAADF-STEM image of a cluster connected in a $\langle 411 \rangle$ manner is shown. Note that in **a**, four cluster units are connected, indicated by yellow lines, whereas in **b**, nine cluster units are connected. Note that the cluster-matrix interface is not accounted for properly in the model. By comparing the top left square in **b** with the square in **a**, it is evident that due to the improper description of the interface in our models causes an overestimation of the Zn/Mg content.

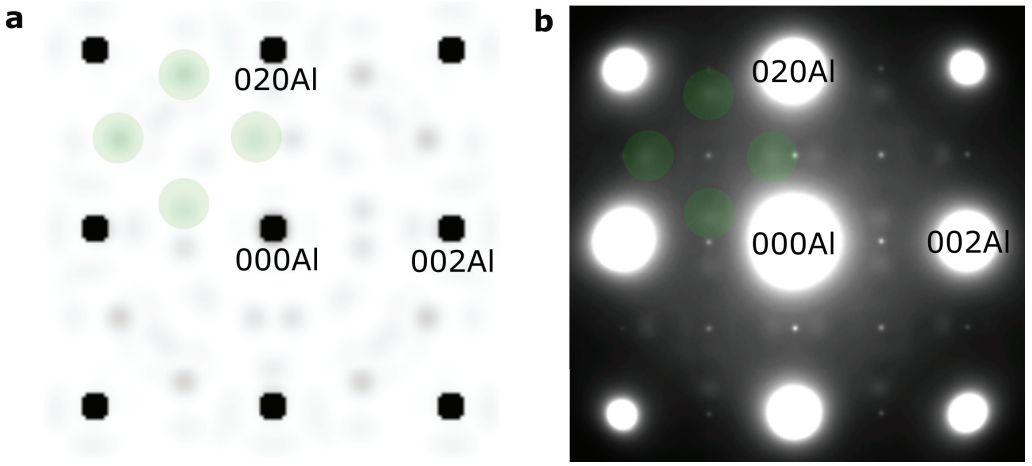

Figure 4: **a**, Simulated HAADF-STEM image of the model $zZ_6M_8Z_{24}$ connected in a $\langle 411 \rangle$ manner, i.e. configuration 8 in Tab. 2. **b**, Experimental HAADF-STEM image of a cluster connected in a $\langle 411 \rangle$ manner. Note that in the simulated image four cluster base units are connected, whereas the real image connects nine cluster units. This is indicated by the yellow lines.

6 Supplementary simulated nanobeam diffraction patterns

Model $zZ_6M_8Z_{24}$ connected in a $\langle 411 \rangle$ manner periodic through the whole thickness Figure 5 shows a montage of simulated nanobeam diffraction (NBD) patterns over a thickness interval of t =8.09 Å to 687.65 Å. The diffraction patterns are adjusted for contrast and brightness.

Cluster embedded in the Al matrix In addition to simulating the NBD pattern from a cluster model that was periodic through the thickness, a model where a cluster was embedded in the Al matrix was also simulated. The result is shown in Figure 6. In **a**, the model $zZ_6M_8Z_{24}$ connected in a $\langle 411 \rangle$ manner periodic through the whole thickness extends through the whole thickness with a periodicity of 8.09 Å as indicated. This is the same model as in Figure 6 in the main text and Figure 5 in this Supplementary text. The corresponding simulated NBD pattern is shown in **b** for t=40.45 Å. The model in **c** is not periodic in the z-direction: it shows the more realistic case where a cluster is embedded in the Al matrix with unit cells of Al both above and below the cluster. In this case, two unit cells of Al are placed above 5 unit cells of $zZ_6M_8Z_{24}$ connected in a $\langle 411 \rangle$ manner periodic through the whole thickness , while there are multiple layers of Al unit cells below to reach a total thickness of t=728 Å. The corresponding simulated NBD pattern is shown in **d** for t=728 Å. By comparing the two simulated diffraction patterns, it is evident that the same spots are present, but the dynamical effects are different in the two cases due to the difference in thickness.

Average diffraction pattern As discussed in the main text, there exists two possible orientations for the $zZ_6M_8Z_{24}$ connected in a $\langle 411 \rangle$ manner periodic through the whole thickness model. The two different orientations are equivalent to a flipping operation, thus the NBD pattern will also

be flipped. By taking the average of simulated NBD patterns of the two possible orientations, the diffraction pattern will appear as in Fig. 7**a**. The experimental SADP in Fig. 7**b** is obtained from a region containing multiple clusters, i.e. it is an average diffraction pattern from multiple clusters. By comparing the average diffraction pattern in 7**a** with the SADP pattern, it is evident that the same spots are visible, indicated by the opaque, green circles in **a** and **b**. Note: the forbidden 100 and 110 reflections in figure 7**b** are due to Al_3Zr dispersoids.

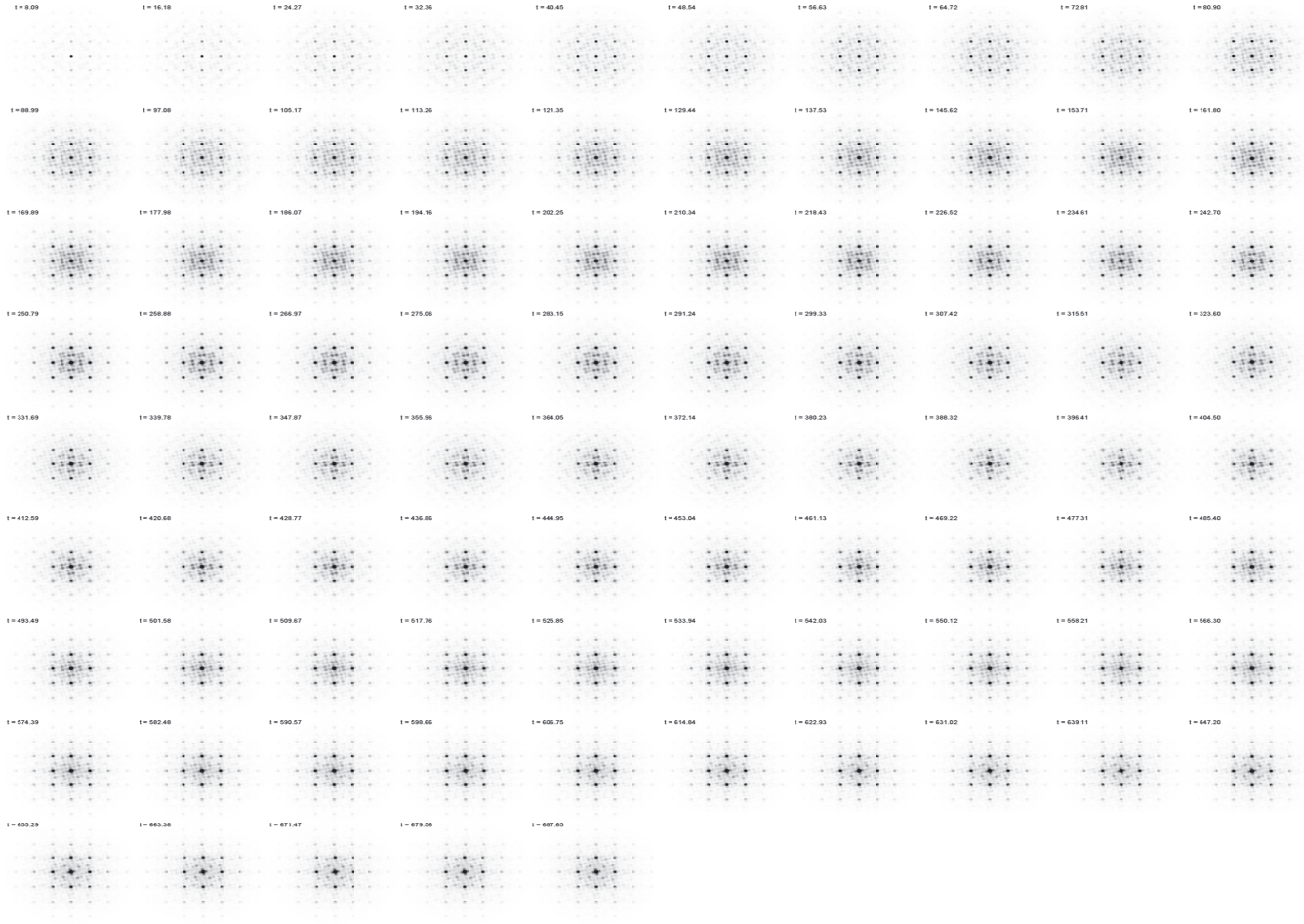

Figure 5: Montage of simulated NBD patterns over a thickness interval of t =8.09 Å to 687.65 Å.

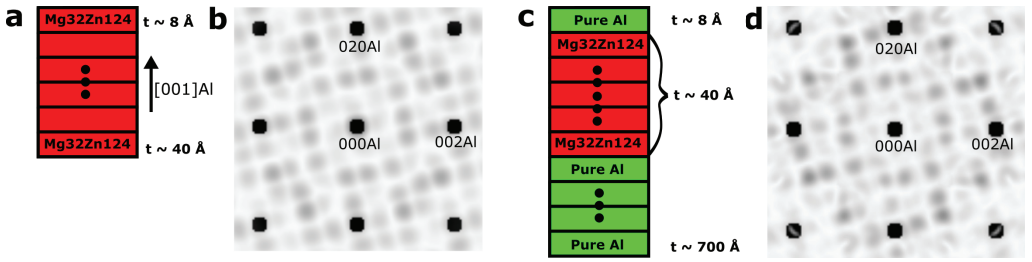

Figure 6: **a**, Model where $zZ_6M_8Z_{24}$ connected in a $\langle 411 \rangle$ manner extends periodically through the whole thickness. **b**, Simulated NBD pattern corresponding to the model in **a**. **c**, Model where $zZ_6M_8Z_{24}$ connected in a $\langle 411 \rangle$ manner is embedded in the Al matrix in the [001]Al-direction. **d**, Simulated NBD pattern corresponding to the model in **c**.

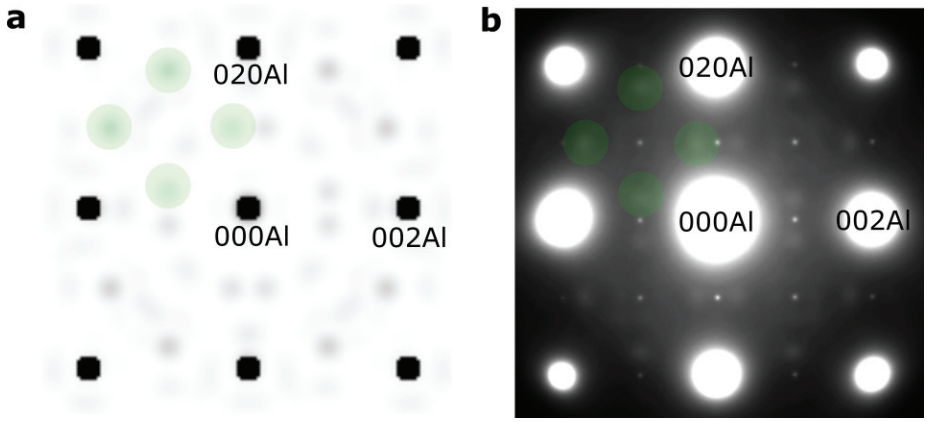

Figure 7: **a**, The average of two NBD patterns in the two possible orientations in the main text. **b**, SADP from a region containing multiple clusters and dispersoids.

References

1. Wang, Z., Lv, K., Zheng, J. K. & Chen, B. Atomic-scale characterization of interfaces between 2A70 aluminum alloy matrix and Cu-enriched layer after electropolishing. *Materials Characterization* **150**, 150 – 154 (2019).

Appendix D

Paper VI: Supplementary information

Supplementary Materials: Stress corrosion cracking in an extruded Cu-free Al-Zn-Mg alloy

Adrian Lervik [1,*], John C. Walmsley [2], Lars Lodgaard [3], Calin D. Marioara [4], Roy Johnsen [5], Otto Lunder [4], and Randi Holmestad [1]

Appendix A Supplementary figures

Appendix A.1 Supplementary EDS data

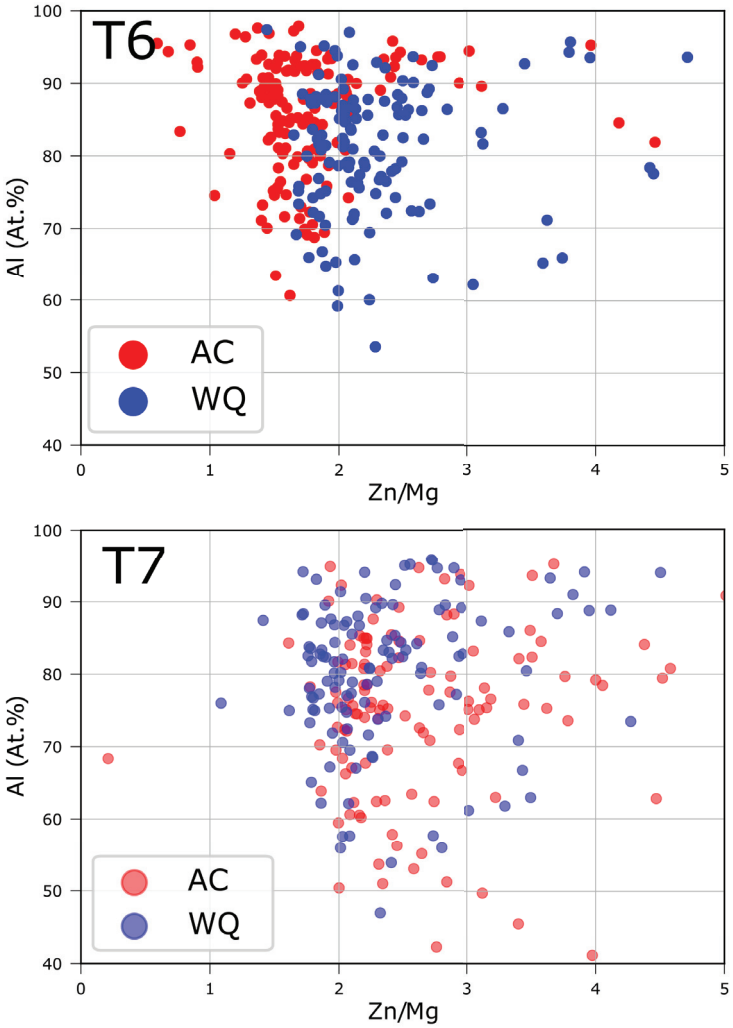

Figure A1. Results from 150 EDS point analysis of grain boundary particles in each temper acquired using microscope (i) (see main text for details). The Al at.% is shown as function of the Zn/Mg ratio, separated into the different tempers.

Appendix A.2 Double cantilever beam results

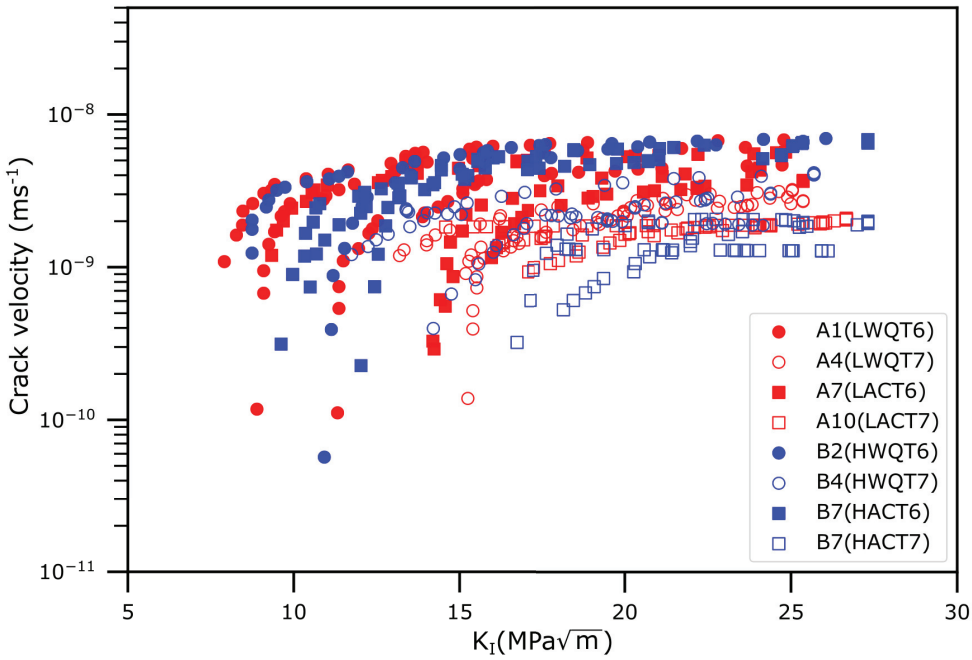

Figure A2. Results from the double cantilever beam tests represented in a conventional crack velocity against stress intensity (K-V) figure.

Appendix A.3 Stress-strain curves

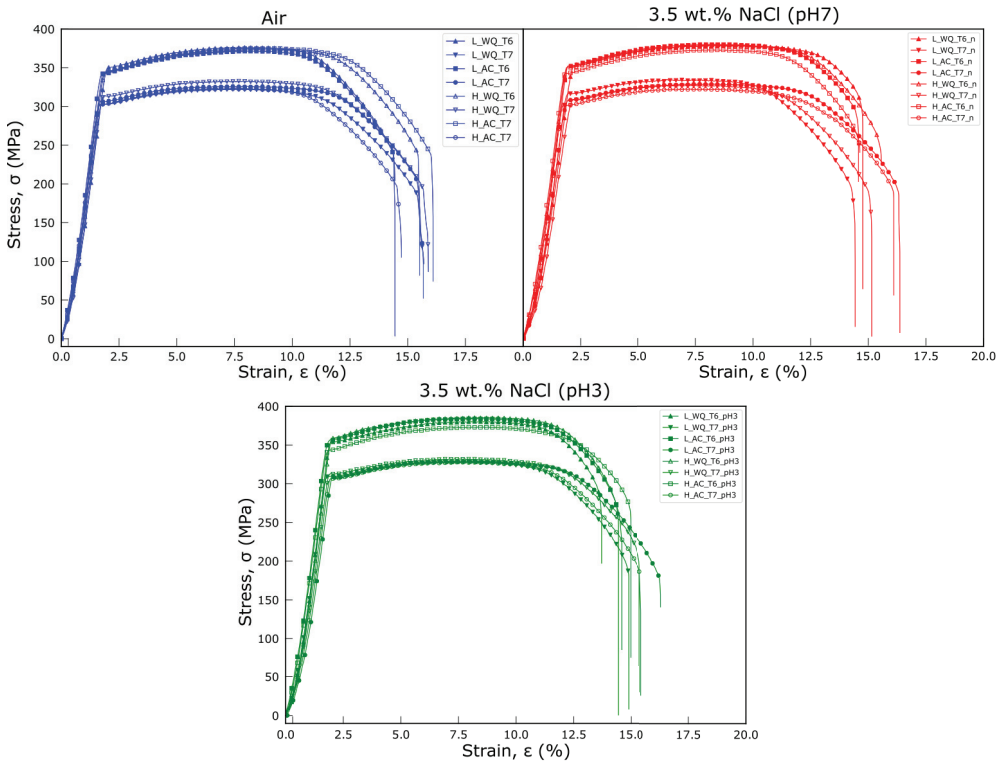

Figure A3. Stress-strain curves for the 4 tempers with two different Si contents in tested in air and 3.5 wt.% NaCl solution with different pH.

Appendix A.4 Cracking in tensile specimens

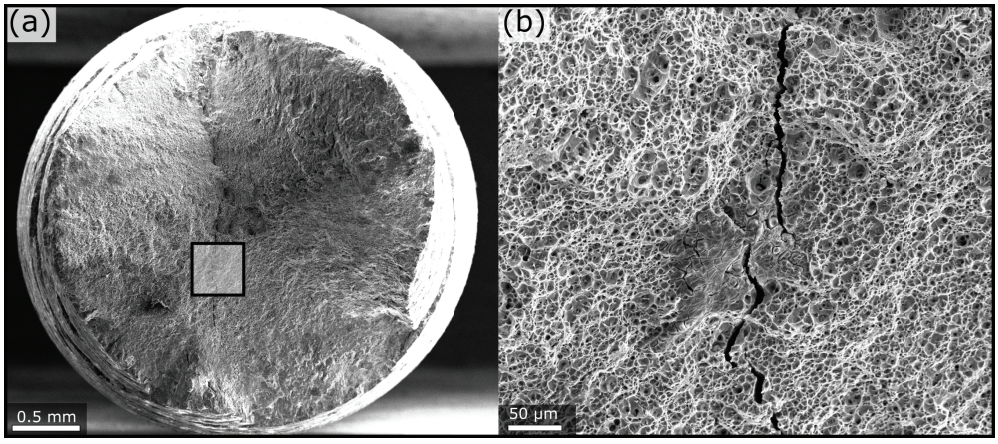

Figure A4. Fracture surface for sample H-AC-T6, demonstrating a crack penetrating the entire cross-section.

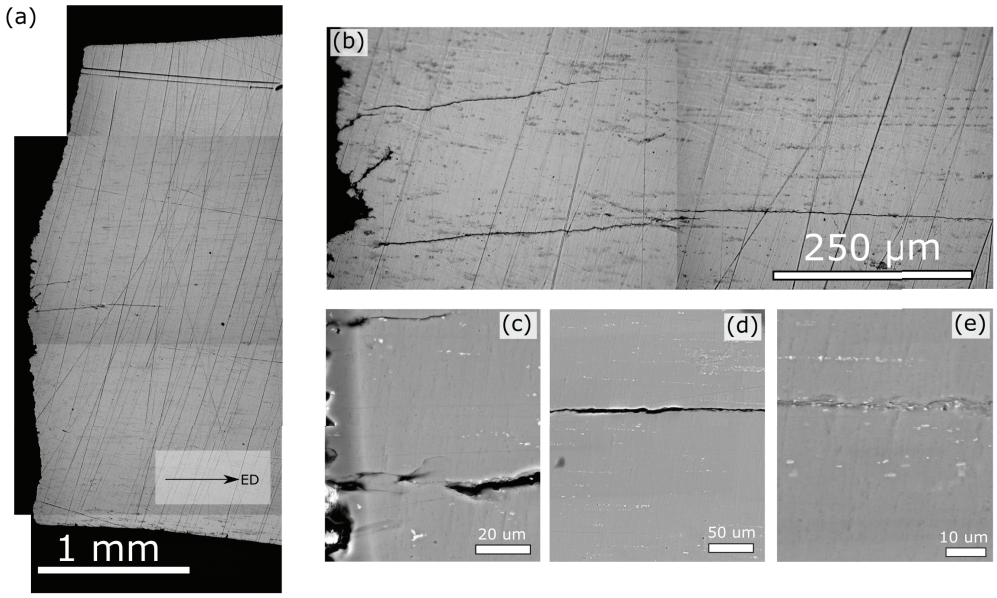

Figure A5. A slow strain rate testing (SSRT) sample embedded in epoxy and polished to reveal the depth extent of the secondary cracks. Figures (a) and (b) are optical microscopy images and (c)-(e) are backscattered electron (BSE)-scanning electron microscopy (SEM) images.

ISBN 978-82-326-4868-9 (printed ver.)
ISBN 978-82-326-4869-6 (electronic ver.)
ISSN 1503-8181

NTNU
Norwegian University of
Science and Technology